UNIVERSITY OF ICELAND

Ph.D. Thesis

Geology

Basalt lava degassing: mechanism and characterisation

Nicolas Levillayer

May 2025

FACULTY OF EARTH SCIENCES

Basalt lava degassing: mechanism and characterisation

Nicolas Levillayer

Dissertation submitted in partial fulfillment of a
Philosophiae Doctor degree in Geology

Advisor
Dr. Olgeir Sigmarsson

Ph.D. Committee
Andri Stefánsson
Sæmundur Ari Halldórsson
Pierre-Jean Gauthier

Opponents
Evgenia Ilyinskaya
Fidel Costa

Faculty of Earth Sciences
School of Engineering and Natural Sciences
University of Iceland
Reykjavik, May 2025

Basalt lava degassing: mechanism, characterisation and consequences
Dissertation submitted in partial fulfillment of a *Ph.D.* degree in Geology

Copyright © 2025 Nicolas Levillayer
All rights reserved

Faculty of Earth Sciences
School of Engineering and Natural Sciences
University of Iceland
Sturlugata 7
102, Reykjavik
Iceland

Telephone: 525 4000

Bibliographic information:
Nicolas Levillayer, 2025, *Basalt lava degassing: mechanism and characterisation*, PhD dissertation, Faculty of Earth Sciences, University of Iceland, 198 pp.

Author ORCID: 0009-0003-5544-491X

Abstract

The volcanic gas composition emitted during basaltic eruptions is relatively well understood, but the emissions from cooling lava fields have been less studied, along with their environmental impacts. The study investigated the gas emission from crystallising lava, as well as the internal structure of lava and associated segregation veins. Gas samples were collected from the eruptive crater, cooling vents, and solidifying lava in Fagradalsfjall. The gas emissions were found rich in sulphur and sulphide-forming elements at the eruptive crater, while post-eruptive gas is richer in halogens, especially chlorine at the crystallising lava and fluorine at the cooling vent. Estimates of emissions from crystallising lava show significant release of metals that form chlorides. The relationship between emission and fractional crystallisation, along with segregation melt formation during lava solidification, was examined. The first minerals to from are anhydrous, forming a fully crystallised framework after 40-50% crystallisation. In the residual melt, volatile elements saturate and form a volume-rich gas phase. The gas presses the melt through the crystal framework, forming segregation veins. Chemical analyses of these veins reveal whether the gas phase escaped into the atmosphere or solidified with the melt. The similar compositions of segregation veins and gas from solidifying lava indicate a relationship between the internal lava evolution and lava degassing. Overall, the results show that gas emissions from lava are distinct from emissions at the vent but correlate well with the fractional emission of basalt melt, both in terms of origin and nature. The environmental impacts of heavy metal gas emissions from basalt lava are a worthy subject for future research.

Útdráttur

Samsetning eldfjallagas samfara myndun basalthrauna er tiltölulega vel þekkt, en eiming frá kólnandi hraunbreiðum hefur lítið verið könnuð sem og umhverfisáhrif. Afgösun á málmum og – málmleysingum frá hrauni við storknun var könnuð, sem og innri uppbygging hrauna og aðskilnaðaræða sem myndast við afgösunina. Gasi frá gosopi, kólnandi gígum og storknandi hrauni var safnað austan Fagradalsfjalls. Efnasamsetning gassýna sannreynir að í gosopi ríkja brennisteinn og málmar í súlfíðsamböndum, á meðan hraun gefa frá sér halógenríkt gas og málma í halíðsamböndum en flúorríkt gas kemur úr kólnandi gíg. Mat á losun þungmálma frá kólnandi hrauni sýnir umtalsverða losun málma sem mynda klóríð.

Tengsl afgösunar við hlutkristöllun og myndun afleiddrar kviku í basalthraunum við storknun var kannaður. Fyrstu steindir sem kristallast eru vatnssnauðar (ólivín, plagióklas og klínópýroxen) og mynda heilsteypta kristalgrind eftir u.þ.b. 50% kristöllun. Inn á milli kristallana er afgangsbráðin þar sem rokgjörnu efnin sem haldast ekki í lausn mynda rúmmálsfrekan gasfasa. Gasið þrýstir bráðinni gegnum kristalgrindina til holrýma ofar í hrauni (svokallað “gas-filter pressing” ferli) og myndar aðskilnaðaræðar eða holufyllingar (segregation veins/vesicles). Efnagreiningar æðanna leiða í ljós hvort gasfasinn hafi sloppið til andrúmslofts eða þést og storknað með síðust bráð hraunkvikunnar. Líkindi efnasamsetninga aðskilnaðaræða og gass frá storknandi hrauni benda til beinna tengsla á milli innri kvikuþróunnar hrauna og losunar afgangsgass frá basaltkvikunni. Í heild sýna niðurstöður að gaslosun frá hrauni er mjög frábrugðin losun við gosop en fellur vel að hlutafgösun basaltkviku, bæði hvað varðar uppruna og eðli. Umhverfisáhrif af gaslosun þungmálma frá basalthraunum er verðugt rannsóknarefni í framtíðinni.

Preface

In this thesis, I will introduce you the research that I conducted during my PhD and its main outcome. In this PhD project, multiple aspects regarding lava degassing are investigated, from its origin, associated with lava emplacement and differentiation, to the characterisation of the emitted gas composition and the potential impact of such gas emission.

The motivation for this project arises from the recent advancements in understanding the origin, characteristics and consequences of volcanic degassing. Such investigations revealed the significant compositional variability exhibited by volcanic gas emissions, both across different volcanoes and during a single eruption. Yet not all volcanic gas types were equally studied and there is limited knowledge about the secondary degassing, with a notable lack of information on the gases released from crystallising lava fields. Filling this gap in information is crucial, as lava degassing may differ significantly from at-vent emissions in both composition and spatiotemporal distribution.

The scarcity of information regarding this gas type combined with the great opportunity offered by the Reykjanes Fires that began in 2021 led to the initiation of this project. The main objective is to thoroughly explore and characterise the degassing occurring at the lava field, investigate its composition, and evaluate its potential hazard. However, not only the features of the gas released by the crystallising lava are poorly constrained but also the origin and mechanism behind such degassing. In order to address this knowledge gap, the segregation process and its products, known to be associated with significant volatile circulation within emplacing and crystallising lava, are studied in detail and related to their key role for lava degassing. The thesis will thus be organised as follows:

In the first chapter of this thesis, I will present a detailed literature review to better apprehend the research conducted during my PhD, its interest and contribution. Thus, I will first describe the state of the art about volcanic degassing, its origin and diversity, together with the major and trace elements involved in such process. Will then be presented the current understanding about the segregation process taking place in crystallising lava bodies along with the resulting products, the segregations, and their features. Finally, I will introduce the state of the art regarding Icelandic volcanism and its products, with a particular focus on the emitted volcanic gas and the volcanic systems investigated in this PhD.

In the second chapter, I will introduce the geological context of the products examined in the project, the sampling campaigns, and the analytical methods used both for gas and lava analyses. Thus, this chapter starts with a broad overview of the Fagradalsfjall eruptive episode and its timeline. I then detail the sampling campaign conducted for gas collection with a quick description of each gas sample and the material used. Following that, the sampling sites, and associated volcanic system are introduced, together with the lava and segregation samples collected at each location. The measurements conducted on the different gas and rocks will then be detailed, first presenting the sample preparation, followed by the analytical methods and instruments used, along with the uncertainties associated with each analysis.

The chapter 3 will detail the results and discussion from the study of the different gas emitted during the Fagradalsfjall eruptions. Such gases were collected between 2021-2023 using a filter pack, allowing collection of both reactive species (such as SO_2, HCl, HF) and aerosols. Following sampling, the filters were leached separately and the reactive species concentration measured by Ion Chromatography while the trace elements composition of the aerosols was measured by ICP-MS. In this chapter is discussed and compared the features of the primary and secondary gas composition in terms of major volatile and trace elements. The volatility changes of trace elements with evolving gas features (relative concentration of S, Cl and F; temperature, etc.) between the primary and secondary degassing are then investigated. Such investigation reveals important change in gas composition, shifting from dominated by S in the primary gas to Cl-rich and the crystallising lava and F-rich at the extinct-crater. This composition shift, along with temperature drop is demonstrated to affect the release of numerous trace elements. As a result, the secondary gas is constantly depleted in elements degassing as sulphide or in their elemental form, whereas enrichments in halide forming species are observed. Finally, a quantification of the amount of volatile trace elements released post-eruptively by the crystallising lava is attempted and compared to such results from the erupting crater and the flowing lava. Such comparison reveals limited liberation of many elements from the crystallising lava but significant emissions of halide-forming species, particularly Zn.

In Chapter 4, I will present the investigation conducted on multiple segregation veins and associated host lava from different Icelandic volcanic systems. Both lavas and segregations were analysed for major element concentration by ICP-OES and trace elements by ICP-MS. Additionally, mineral composition analyses were conducted using microprobe and laser ablation ICP-MS. Through this chapter, I will first detail the whole rock and phase composition of the different segregation veins and their host lava in terms of major, trace and volatile elements. By highlighting the similarities and differences between the segregations, the emplacement model and involved processes will be constrained and described. In particular, the composition of some segregations suggested that processes other than fractional crystallisation takes place during segregation formation. Additionally, the variable maturity stage of the segregations is hypothesised to result from progressive fractional crystallisation of the segregation melt, after its initial escape. The enrichment of certain trace elements known for their volatile behaviour in a few segregations is then used to investigate the volatile circulation through the segregation process and its potential connection with lava degassing. This enrichment is further used to estimate the metal release from the Eldgjá lava field. Such estimation suggests large metal emissions associated with the very large volume of degassing lava.

The last part of my PhD research will be presented in Chapter 5, in which is detailed my attempt to use ion selective electrodes to measure the fluorine and chlorine concentrations of lava samples. In this chapter, I first detail the preparation and analysis procedure, along with the first results obtained and the adaptions needed to obtain satisfying quantifications of both halogens. The revised method is thus used on a set of international and Icelandic standard to assess the potential of this technique, the associated uncertainties and limits. Such analyses reveal that ISE can be used for both F and Cl, but obtaining robust results for the latter is not straight forward as the chlorine selective electrode is much less sensitive than the fluorine one. Finally, results regarding halogen measurements of Fagradalsfjall and Sundhnúksgígar lavas and tephras are presented and interpreted in the light of their major element concentrations and isotope ratios. Results show halogen concentration range that are well explained by an effect of both variable fractional crystallisation and magma source

heterogeneity (especially in F). In contrast, no lava degassing could be identified through analysed products as tephras and lavas showed similar halogen composition.

The thesis will be concluded with a concise chapter summarising the major findings from this PhD. Perspectives on future work related to lava degassing will then be presented, based on the observations, results, and limitations of this thesis.

Table of Contents

List of Figures

List of Tables

List of Publications

Levillayer, N., Mandon, C., & Sigmarsson, O. (2025). Post-eruptive outgassing of heavy metals at Fagradalsfjall, Iceland. Bulletin of Volcanology, 87(8), 1-19.

Levillayer, N. & Sigmarsson, O. Role of segregation processes on volatile degassing during basalt lava crystallisation. Journal of Volcanology and Geothermal Research (submitted).

Levillayer, N. & Sigmarsson, O. Investigating Cl and F concentration in Reykjanes lava using Ion Selective Electrodes (In preparation).

Matthews, S. W., Caracciolo, A., Bali, E., Halldórsson, S. A., Sigmarsson, O., Guðfinnsson, G. H., ... & Drouin, V. (2024). A dynamic mid-crustal magma domain revealed by the 2023 to 2024 Sundhnúksgígar eruptions in Iceland. Science, 386(6719), 309-314.

Acknowledgements

The four years I spent doing this PhD taught me incredible things that could not be learnt in any other way. I want to thank Olgeir Sigmarsson who trusted me enough to select me as PhD student, with an exciting project on lava degassing. Your supervision over these four years was precious, and I will always be grateful for the time you spent with me working on the different projects, switching from endless anecdotes dating forty years back, to hard-core revision of manuscripts.

I also want to acknowledge my committee members Andri Stefánsson, Pierre-Jean Gauthier and Sæmundur A. Halldórsson for all helping me at a different time of the PhD and for responding fasts to my demands, whenever it was needed.

To Jóhann Gunnarsson Robin, I want to say that I am grateful for all our stimulating conversations about lab work and chemistry, which really contributed to show the beauty of testing new analytical methods, sometimes resulting in frustration but others in great satisfaction. To Krzysztof Suchoroski, thanks for showing me how to do rigorous chemistry in the clean lab, explaining step by step the processes involved. Thank you to all other technicians involved in my PhD, Jean-Luc Devidal, Claire Fonquernie, Guðmundur H. Guðfinnsson, Rebekka Hlín Rúnarsdóttir and Sveinbjörn Steinþórsson without which my research would not have been as fruitful.

I am also very grateful for the role of Céline Mandon, whose contribution to my PhD taught me a lot, and who showed me a path on how to be a young scientist in the field of volcanic degassing. Besides, I would like to acknowledge Melissa for allowing me to participate in a project related to volcanic degassing that was not associated with my PhD, thus widening my perspective of that field of research. Likewise, a big thank to the geochemistry and petrology team of the Institute of Earth Sciences (Simon W. Matthews, Alberto Caracciolo, Enikő Bali, etc.) for associated me to fieldwork and investigation on Reykjanes lava composition and origin. This greatly strengthened my understanding of diverse petrological and geochemical tools, that I could apply for my own research.

It is important to me to mention the students and researchers that I had the opportunity to meet in conferences. Discussions with you greatly helped me to keep the flame for research in geoscience.

Thanks a lot to my PhD-twin Garance, who started her PhD with Olgeir at the same time as me but managed to finish it months before. Our mutual help on reviewing each other manuscripts and conference talks greatly improved my work and well-being. I also want to deeply thank Daniel and Noemi for being here from the beginning to the end of the PhD, sharing the worst and best part of our PhD adventures together. I will always remember us as the best PhD trio imaginable. I cannot write this acknowledgment without thanking all my officemates during over three years, who all made, in a different manner this, PhD more pleasant, and my life more enjoyable.

Thanks, Ástrós, for your daily support and curiosity for my PhD project and for broadening my social life by creating so many climbing and hiking groups. This was key for me to keep a balanced life. To my friend of Klífurhúsið, thanks for making my evening more pleasant

and make me forget about the problems faced during some more challenging working days. To the people of Faffarar, thanks for the great company during these diverse hikes and other outdoors activities.

To my parents I would like to say I am very grateful for endless their support since I started my studies in Geology, cheering me for studying in a university 500 km away from home, then to go in Erasmus in Iceland. To my brother, thanks for showing me the way on how to become a scientist and all the ambushes that I could then easily avoid. The three of you made my dream possible, even when I did not believe in it.

Finally, I would like to thank the Reykjanes Peninsula for reawakening the exactly when I started looking for PhD in relation with volcanic degassing.

1 State of the art

1.1 Volcanic degassing and volatile metal emissions

Volcanic gas emissions are essential to the cycle of many chemical species such as carbon dioxide and water (Williams et al. 1992; Burton et al. 2013). The degassing from volcanic eruptions also significantly affects the atmosphere and climate through the release of sulphur-forming aerosols, potentially leading to volcanic winters (Rampino et al. 1988; Robock 2000; Oppenheimer et al. 2018), but also greenhouse gases such as CO_2, H_2O or CH_4 (Cole-Dai 2010; Burton et al. 2013). Volcanic winters can have disastrous impacts on the Earth climate and biosphere (including human society) as demonstrated by historical (Laki, 1783-1784 AD, Tambora, 1815 AD) and prehistorical (Toba, 75 ka) examples (Rampino and Self 1992; Thordarson and Self 2003; Raible et al. 2016). Depending on the eruption scale, volcanic winters last from months up to millennia, thus having an immediate effect on the environment. In contrast, volcanic greenhouse gases rather have a long-term impact (ka to Ma), potentially affecting the overall climate of the planet (Kerrick 2001). In addition to its greenhouse effect, carbon dioxide release can also have local but deadly consequences, the lake Nyos disaster in 1986 being the most dramatic example, with a massive release of CO_2 from the lake taking nearly 2000 lives (Kling et al. 1987). Finally, the recent Hunga Tonga-Hunga Ha'apai 2022 eruption highlighted the climatic effects of water released from large phreatomagmatic eruptions (Schoeberl et al. 2023).

In this section, I will outline the key background to my thesis research. I will first describe the history of volcanic gas sampling and the development of the techniques used in the PhD. Next, a discussion regarding the origin of the volatiles within the Earth is presented, to highlight the elements of interest when investigating volcanic gas emissions. I then describe the processes that lead to formation of the volcanic gas and the behaviour of the different elements that will be studied in this work. A concise overview of the state of the art regarding the volcanic gas features and its variability across the world is then given as a framework for understanding the context of volcanic degassing in Iceland. Finally, I will present the current knowledge and associated research regarding secondary degassing and related processes, emphasising the interest of the work conducted during this PhD.

1.1.1 History of volcanic gas sampling and study

Knowledge regarding the effect of volcanic degassing is relatively recent information. Though volcanic gases have been a subject of attention for centuries, with population in the vicinity of volcanoes early identifying such gas as dangerous, the study of the volcanic gas was hindered until the latest part of the 20th century by the lack of appropriate techniques to sample and analyse it. The first proper volcanic gas collection and analyses were published by Day and Shepherd in 1913 revealed water dominance in the gas (Day and Shepherd 1913). In the following decades, multiple gas sampling were conducted worldwide, identifying

other species released (CO_2, SO_2, H_2, HCl) and first indication that gas emissions have heterogeneous composition (Symonds et al. 1994 and reference therein).

The modern days study of volcanic gas composition started some 50 years ago when the German scientist Werner Giggenbach revolutionised the volcanic gas sampling method in the so-called "A Simple Method for the Collection and Analysis of Volcanic Gas Samples" paper in 1975. In this article and following ones (Giggenbach 1975, 1989), Giggenbach developed the technique to sample simultaneously all the major gases, using pre-evacuated bottles partly filled with NaOH solution, inserted directly in the fumarole vent. In the so-called Giggenbach bottles, the reactive gases are captured by the base while the non-condensable species are trapped in the vacuum (Fig. 1.1).

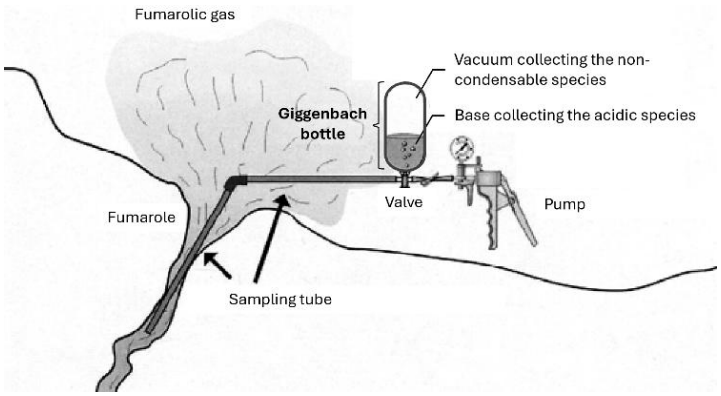

Figure 1.1. Schematic of fumarole sampling using a Giggenbach bottle. *The fumarolic gas is pumped through a tube to the Giggenbach bottle, partially filled with a base and completed by vacuum. The non-condensable species in the gas accumulate in the vacuum whereas the acidic species dissolve in the base. Figure modified from Lee et al. (2005).*

This new sampling method allowed more exhaustive sampling and quantification of the major volatiles that remain gaseous after being released (H_2O, CO_2, CO, CH_4, SO_2, H_2S, HCl, HF, HBr, H_2, etc.), which together make up > 99 % of the volcanic gas (Oppenheimer et al. 2014). However, a second category of elements are released by volcanic degassing: the volatile trace elements. Here are qualified as volatiles elements that significantly partition in the gas phase (gas/melt partition coefficient Kd > 0.01), whereas trace elements refer to elements with concentration of the order of ppms or lower. In most cases, these elements are not released as free elements, instead forming complex species with the major volatiles such as sulphides, halides, oxides and hydroxides (e.g., ReO_3, CuCl, TeS, etc.). Unlike the major volatiles, such complex species do not remain gaseous in the cold and oxidant atmospheric conditions but rather form aerosol by gas-to-solid conversion quickly after their escape. Such conversion is associated with different processes such as gas condensation or adsorption on solid particles (Symonds et al. 1992; Witham et al. 2005; Scholtysik and Canil 2021). The emissions of trace elements, which include toxic heavy metals, could thus not be sampled by Giggenbach bottle and required another collection method.

To fulfill that objective and as the Giggenbach bottles were developed, Naughton et al. (1975) made the first attempt on sampling aerosols, along with major reactive volatile (mainly SO_2). This technique was improved in the following years by Finnegan (1984), Crowe et al. (1987) and Finnegan et al. (1989), giving birth to the filter pack sampling

method (Fig. 1.2). In this method, the volcanic gas is pumped through a series of filters, one Polytetrafluoroethylene (PTFE) laminated filter collecting the particulate matter and two to four base-impregnated filters to collected acidic species (sulphur and halogens).

Though the volatile trace elements only represent a minor part of the gas released by volcanoes, their emissions are a crucial aspect of volcanic degassing (Nriagu 1989; Aiuppa et al. 2003; Allard et al. 2016). Such emission of trace elements is of interest because many classify as heavy metals (As, Cd, Cr, Pb, Hg, etc.; World Health Organisation, 2007). Jerome Nriagu pointed out in 1989 that volcanic degassing represents over 20 % of the total (natural and anthropogenic) emissions of numerous metals such as As, Cd, Cr, Cu, Hg, Ni, Pb and Sb. The release of these pollutants is a significant threat for the local ecosystem, affecting not only the atmosphere but also the hydrosphere, soil and ultimately the biosphere (Allen et al. 2000; Aiuppa et al. 2000; Tam et al. 2016; Ilyinskaya et al. 2017, 2021). Such local pollution can be impactful in the fertile and thus populated areas surrounding volcanoes such as in Indonesia or the Philippines (Shoji and Takahashi 2002; Fiantis et al. 2019).

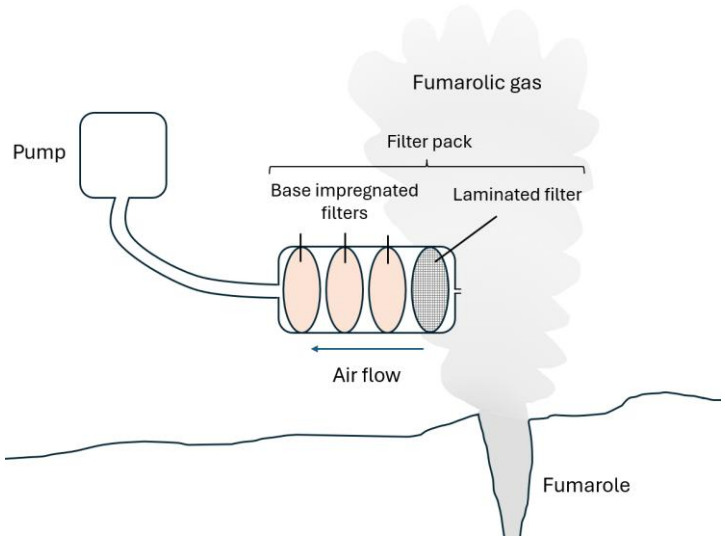

Figure 1.2. Schematic of fumarole sampling using a filter pack. *The fumarolic gas is pumped directly in the filter pack, first through a PTFE laminated filter and then a series (typically two to four) of base impregnated filters. The particulate matter/aerosols are trapped in the laminated filter whereas acidic species are collected by the base impregnated filters.*

1.1.2 Volatile concentrations in the solid Earth

To track the origin of the volcanic degassing, it is necessary to study the presence of volatiles where the magma is formed, in the Earth crust and mantle. Using Mid-oceanic ridge basalt (MORB) melt inclusions, Saal et al. (2002) calculated the volatile concentration in the mantle source of these basalts, assumed to be representative of the depleted upper mantle. The authors thus estimated that the upper mantle contains around 150 ppm of H_2O and S, 70 ppm CO_2, 16 ppm F and one ppm Cl. Slightly lower values were calculated by Salters and Stracke (2004), with estimations of 120 ppm water and sulphur, 50 ppm CO_2, 11 ppm F and 0.5 ppm Cl. The crust is much more heterogeneous than the mantle but is systematically enriched in volatiles. The average continental crust composition was calculated by Hans Wedepohl (1995), with separate estimation of the lower and upper crust, the latter being

more differentiated so richer in volatile, especially CO_2. The average volatile concentrations calculated is around 7000 ppm CO_2, 700 ppm S, 500 ppm Cl and F and only 1 ppm Br and I.

The magma formation (whether at subduction, hotspot or rift) is produced by partial melting of the mantle and/or crust, typically of a few percents (e.g., Schiano et al. 1998). While the mantle (or crust) is melting, the volatiles behave as incompatible elements and thus partition in the silicate melt. Such a process results in the formation of a magma much richer in volatile than its source. Depending on the exact degree of partial melting and the involvement or not of a crustal component, the resulting magma can have a drastically different composition, including in terms of volatiles. Diverse processes can then affect the magma content in volatiles (and other elements), such as crustal contamination/assimilation or crystallisation and thus differentiation of the magma.

The subsequent range of magma volatile content was presented by Oppenheimer et al. (2014), who summed up the average erupted magma composition from the different tectonic settings, from MORBs to rhyolites (Table 1.1). The pre-eruptive volatile content in MORBs is generally 0.1 to 0.2 weight % H_2O, 1500-3000 ppm SO_2, 100-600 ppm F, 50-400 ppm CO_2 and 20-50 ppm Cl. Ocean Island basalts have similar SO_2 and halogen concentrations but higher H_2O and CO_2. Magma in subduction context is richer in water and halogens but poorer in CO_2 and SO_2. Rhyolitic magmas are the richest in volatile (because more differentiated) but low CO_2 and SO_2 content. Such variable volatile concentration will in turn affect the composition of the gas phase issued from the magma.

Table 1.1 Typical major volatile concentrations in the different types of magma as compiled by Oppenheimer et al. (2014)

	H_2O	CO_2	S	Cl	F
MORBs	< 0.5 %	50-400 ppm	800-1500 ppm	20-50 ppm	100-600 ppm
OIBs	0.2-1 %	0.2-0.65 %	< 3000 ppm	20-50 ppm	100-600 ppm
Rhyolite	3-7 %	very low	< 200 ppm	600-2700 ppm	200-1500 ppm

1.1.3 Formation of the gas phase and volatile partition

In a silicate melt, the degassing behaviour of any volatile element can be governed by two different processes: exsolution when saturation is reached or partition in an already existing gas phase. Oppenheimer et al. (2014) described the situation as "In the broadest terms, H_2O and CO_2 exsolution are effectively controlled by the phase diagram, and trace elements by partition coefficients". Carbon dioxide is the least soluble volatile, with a solubility of 0.2 weight percent at 10 km depth (Iacono-Marziano et al. 2012), and therefore reaches first saturation. As the magma rise to lower pressure, CO_2 solubility decreases until carbon dioxide saturates and begins to exsolve, forming a gas phase. Crystallisation can also play a role in CO_2 saturation by increasing its concentration in the residual melt. Water solubility is much higher than CO_2 in the silicate melt (Fig. 1.3), with values above 5 % at 10 km (Dixon et al. 1995). This solubility however also drops as pressure decrease, reaching value below 1 % at depth inferior to a kilometre. Thus, as the magma keep ascending, water also starts to exsolve, increasing the gas phase fraction. Given the much higher water

concentration in the magma, the amount of gas produced by water exsolution largely exceeds the one produced by CO_2.

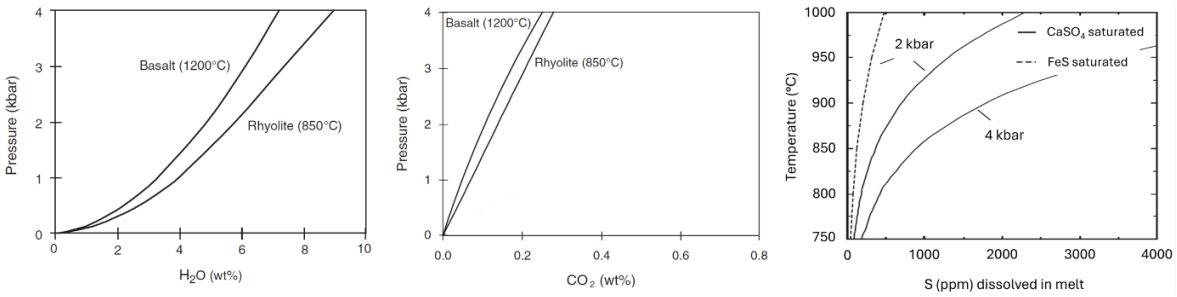

Figure 1.3. Water, carbon dioxide and sulphur solubilities in the silicate melt at variable pressure, temperature and melt composition. *Figure modified from Wallace et al. (2015).*

From that moment, other volatiles such as sulphur, halogens and volatile trace elements can start to enter the already existing gas phase, even if they are still undersaturated in the melt, to an extent governed by their vapour/melt partition coefficient. The major volatiles S, Cl and F could thus degas either by exsolution or partition in the vapour dominated gas. In contrast to H_2O and CO_2, sulphur, chlorine and fluorine solubilities are very complex and poorly constrained, with strong variation depending on the exact magma composition (Scaillet et al. 2004; Shinohara 2009; Wallace et al. 2015). Sulphur saturation, which is highly dependent on oxygen fugacity (Lerner et al. 2021) was occasionally observed, resulting in crystallisation of S-rich minerals and thus S-depletion in the residual melt and associated gas phase (Edmonds et al. 2018; Sigmarsson et al. 2020). Similarly, in a magma with high Cl/H_2O ratio, chlorine could exsolve and form a hydrosaline solution (Webster 2004). Given the high solubility and low concentration of fluorine in magmas, F saturation pre-eruptively is considered unlikely. In most cases however, sulphur and halogen volatile behaviour is approximated by considering simple partitioning in the existing vapor phase (Scaillet et al. 1998; Edmonds and Wallace 2017; Edmonds and Woods 2018). Such partitioning is also rather complex and the partition coefficient variable, but as a general rule and for typical magma, sulphur is the first to partition significantly in the vapor phase, as soon as water exsolve, followed by chlorine whereas limited amount of fluorine partition in the gas phase before the magma is erupted (Carroll and Webster 2018).

The major reactive volatiles are not the only one forming the gas phase in the magma, numerous trace elements following them. These volatile trace elements partly escape the silicate melt, to an extent dependent on their own partition coefficients. Such partition coefficients spans a wide range of values, some elements largely partitioning in the gas phase (Te, Se, Po, Hg) whereas other do not significantly leaves the melt (V, Ce, Hf; Zelenski et al. 2021). The erupted gas is thus the results of the multiple processes and element behaviour taking place at depth and its composition records numerous information regarding the magma composition, its origin, depth and dynamics.

1.1.4 Features and variability of volcanic gas

Because of the difference in magmatic processes occurring at depths (associated with each tectonic settings), the volcanic gas released is by no mean homogeneous. Differentiation prior to eruption (by fractional crystallisation) will also affect the magma composition and gas phase escaping from it. Since most volatile remain widely incompatible until the late

stage of crystallisation (amphibole, apatite, etc.), differentiation generally results in similar enrichment in the different volatiles and thus does not affect the subsequent gas composition. Sulphur is however not always incompatible as the formation of S-rich minerals is frequent at depth resulting in a sulphur-depleted differentiated magma and gas. Additional complexity regarding gas composition arises from the fact that the magmatic gas can mix with hydrothermal fluid, forming a bimodal volcanic gas, no longer solely representing the original magmatic gas.

A general trend can however be observed with on one hand the subduction/arc associated volcanic gas, and on the other hand, gas emitted at intraplate/hotspot or rift volcanoes. Overall, the gas emissions associated with subduction volcanism are particularly rich in water and chlorine (details in Table 1.2). In contrast, CO_2 and SO_2 are more concentrated in volcanic gas from rift or hotspot volcanoes (Sigvaldason and Elísson 1968; Symonds et al. 1994; Gerlach 2004; Oppenheimer et al. 2014; Zelenski et al. 2021).

Table 1.2 Typical major volatile concentrations in subduction and rift/hotspot volcanic gases.

Volcanism	**H_2O**	**CO_2**	**SO_2**	**HCl**
Subduction	> 95 %	< 5 %	< 1 %	> 1 %
Rift/Hotspot	< 90 %	> 20 %	> 5 %	< 1 %

In the last decades, it was uncovered that not only major volatile but also volatile trace elements are emitted at different rates depending on the tectonic settings (Aiuppa 2009; Gauthier et al. 2016; Edmonds and Woods 2018; Mason et al. 2024). Although substantially more arc volcanoes are studied for their gas composition than intraplate or rift volcanoes, Kīlauea extensive monitoring has allowed to compare the emission of different volcanic setting. In their study about metal emission of Kīlauea, Hinkley et al. (1999) presented the difference of emissions between this volcano and the ones of previously studied from arc volcanoes (Etna, Merapi, etc.). The authors found out that the Kīlauea gas emissions contain relatively more Cd and Bi but less Pb, Cu and Zn than arc gases.

Since the beginning of the 21st century, several studies reporting volcanic gas composition were published, expending the available dataset on volcanic gases. Such dataset includes studies on additional intraplate/rift volcanoes, notably Hekla (Moune et al. 2006) and Holuhraun (Gauthier et al. 2016) in Iceland and Erta Ale in the East African Rift (Zelenski et al. 2013). Edmonds et al. (2018) compiled the available literature to characterise the distinction between hotspot/rift and arc volcanic gases in the article “A distinct metal fingerprint in arc volcanic emissions”. In the paper, the authors describe a systematic enrichment in Cd and Te in hotspot and rift gases whereas As, Sn and Tl are particularly enriched in arc gases.

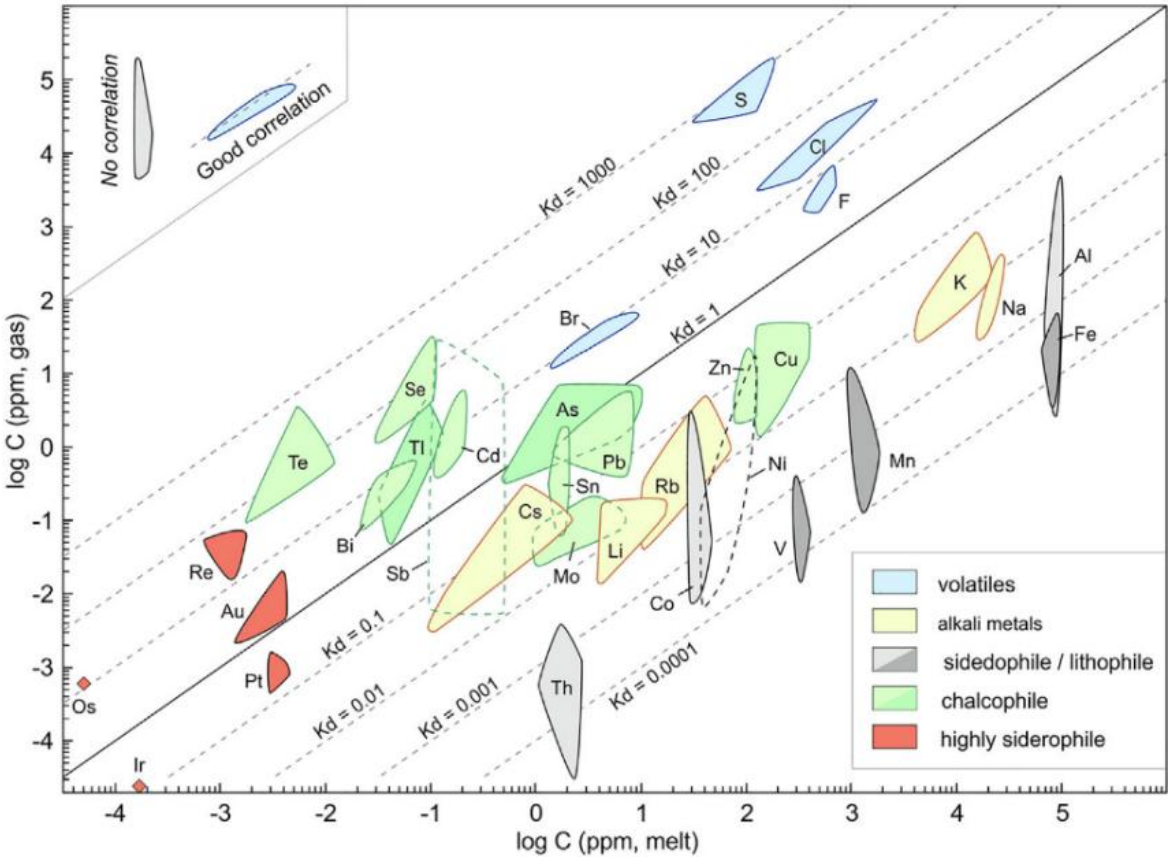

Figure 1.4. Element concentration range in the volcanic gas and silicate melt. *Both element concentrations in the gas and melt along with the partition coefficient (Kd) depends on the tectonic setting. Figure from Zelenski et al. (2021).*

Such difference in volatile trace element gas content depends both on the composition of the magma from which the gas phase formed and the gas/liquid partition coefficient of individual elements (Fig. 1.4). Regarding magma composition, the difference is clear, with diversity within volcanoes of each tectonic setting but strong trend separating the subduction and rift/hotspot. As subduction magmas are generally more evolved than their rift/hotspot counterparts, they are enriched in all incompatible elements, including the volatiles. Gases emitted at arc volcanoes thus tend to be relatively enriched in incompatible volatile elements. Zelenski et al. (2021) investigated the effect of tectonic setting on trace elements volatility in the different tectonic setting by calculating their partition coefficients. The authors revealed strong variability of volatility for many trace volatiles such as Te, Cd and Pb more volatile in rift/hotspot magmas, whereas Tl, Cu and Rb are more volatile in subduction magmas.

Though the volatility of trace element is complex and depends on numerous factors, one key parameter identified is the amount of each major volatile. Indeed, many trace elements tend to form volatile species with sulphur, hydrogen, oxygen, chlorine or fluorine. Thermodynamic modelling brought insight into constraining speciation of most volatile elements (Symonds et al. 1992; Wahrenberger 1997; Mandon et al. 2019; Wainman et al. 2024; Mason et al. 2024). Though model results depend on several input (temperature, oxygen fugacity, major gas concentrations, etc.), the diversity of speciation is clear with Cu

and Sb favourably forming chloride, Re oxide, Te sulphide, Mo fluoride and Cd degassing in its elemental form (Fig. 1.5).

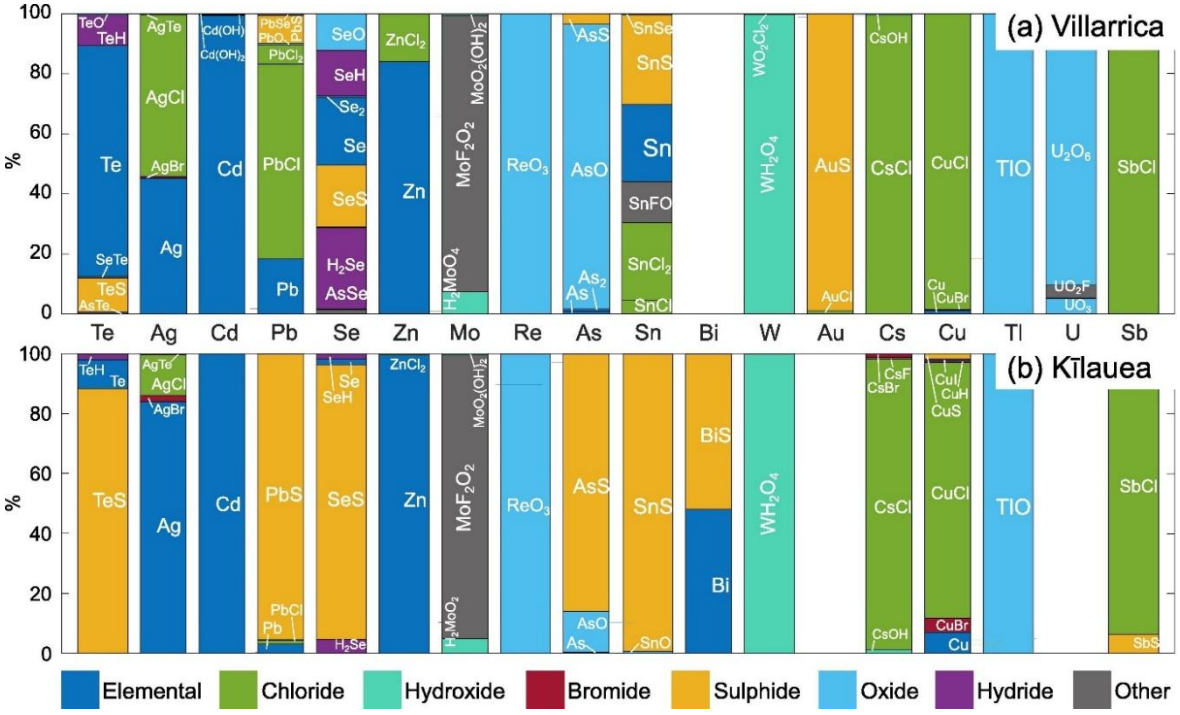

Figure 1.5. Example of volatile trace element speciation model in the gas phase from (a) one HCl-rich subduction volcano (Villarrica) and (b) one S-rich hotspot volcano (Kīlauea). *A few trace elements degas in their elemental form whereas the majority form complex species with sulphur, chlorine, oxygen, water and fluorine. Several elements display distinct speciation in the two volcanic gases, indicative of the effect of variable proportion of major volatiles. Figure from Mason et al. (2024).*

The variable enrichment in volatile in the subduction volcanic gas with respect to hotspot/rift is thus readily explained by the variation in proportion of the main ligands, especially S, Cl and F. However, not only the tectonic context affects the relative proportion of major volatiles. In fact, strong variations of gas composition take place within each eruption. Indeed, if volcanoes emit a generally homogeneous primary gas phase at vent during their eruption, degassing also takes place secondarily, from flowing and crystallising lava along with extinct craters. Such secondary degassing will have distinct composition in terms of major volatiles and thus trace elements.

1.1.5 Secondary degassing

In volcanology, secondary degassing refers to gas emissions from a silicate melt that has already partially degassed, in opposition to primary degassing, where gas escapes from magma considered undegassed. Secondary degassing thus includes emissions from various sources, such as flowing lava, crystallising lava field and extinct craters. A mechanism of fractional degassing takes place in which the most volatile species are released during the primary degassing, leaving a melt depleted in such species. The secondary degassing from

the depleted melt will thus release proportionally less of the most volatile species and more of the less volatile ones.

Differences in gas composition due to fractional degassing were first identified at Kīlauea by Gerlach (1980) and further investigated by Greenland (1984). These authors observed variable amount of CO_2 with respect to H_2O and SO_2 in the gas emitted at Kīlauea. Such changes were attributed to intermittent CO_2 escape from the magma prior to its eruption. This idea was better constrained, conceptualised and quantified and by Terrence Gerlach in 1986 in the so-called article "Exsolution of H_2O, CO_2, and S during eruptive episodes at Kīlauea Volcano, Hawaii" (Gerlach 1986). In their study, Gerlach described two distinct gas emissions, the type I gas being CO_2-rich and type II CO_2-poor. Type I gas is associated with eruption of a magma of deep origin, with no pre-eruptive degassing. In contrast, type II gas originates from a two-stage degassing process in which the magma was stored at shallow depth and lost most of its CO_2 (along with minor amount water and SO_2) before erupting.

A better understanding of such multi-stage degassing process arose from studies of Etna degassing by Gauthier and Le Cloarec (1998) and Aiuppa et al. (2002). Gauthier and Le Cloarec (1998) described the metal emissions from the Etna submit craters and eruptive vents during different activity phases (effusive, strombolian and quiet degassing). The authors identified two distinct gas compositions, one mostly observed at the summit craters and enriched in the very volatile sulphur and polonium, the other at the eruptive vent much poorer in S and Po. Such difference led the authors to classify the first gas type as primary and the latter as secondary, because fed from a volatile-depleted source (i.e., already primarily degassed). Alessandro Aiuppa further characterised the occurring fractional degassing by focussing on the relative abondance of S, Cl and F in Etna gases (Aiuppa et al. 2002; Aiuppa 2009). In these articles, they highlighted the higher relative proportion of S in the gas emitted before and during the initial stage of eruption, whereas late degassing was enriched in halogens and particularly fluorine. Such variability was explained by the progressive depletion in volatile of the magma source. The most volatile elements (in this case S) escape the magma during the early (primary) degassing whereas the least volatile ones (F) become more concentrated and escape later, in the late (secondary) degassing.

Significant variation of syn-eruptive gas composition at a single volcano can thus occur as a result of intermittent pre-eruptive magma degassing, mainly affecting CO_2. Nevertheless, the compositional difference between the syn-eruptive crater gas and the gas released from the flowing lava or post-eruptively could be much larger (Fig. 1.6). Indeed, the extensive degassing occurring at the vent, when magma reach the surface, gives birth to a silicate melt depleted in volatile elements. The secondary degassing from this partially degassed melt could thus be of a very different nature to the primary gas. The first samplings of such secondary gas phase were reported by Olmez et al. (1986) and Crowe et al. (1987), from cooling vents (extinct craters) at Kīlauea. The collected gas was characterised by a F/S and Cl/S increase of almost two orders of magnitude with respect to Kīlauea primary gas. In addition to major gases, Crowe et al. (1987) also collected aerosols both from active and extinct craters. Trace element analyses revealed variable concentration ratios between the cooling vent gas and the primary gas spanning over two orders of magnitude, Cu, Se and Sb being the most enriched in the secondary gas and Ir, As, Zn and Cd the most depleted.

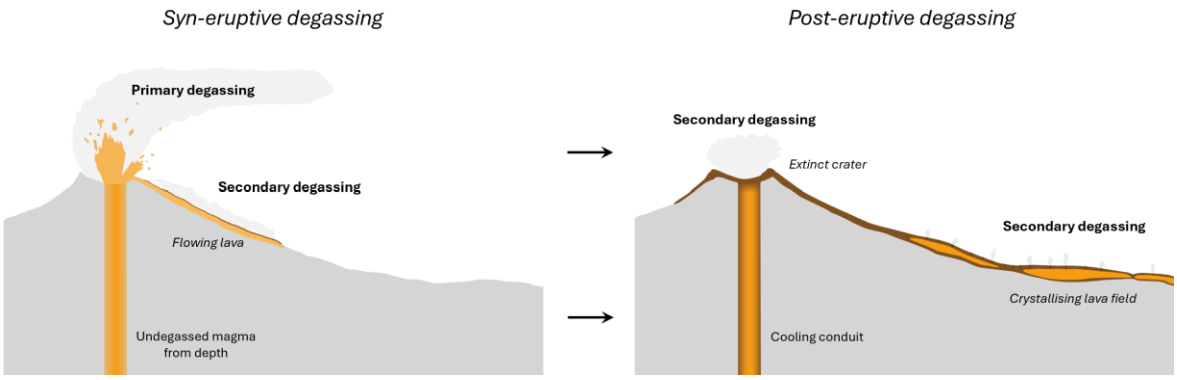

Figure 1.6. Multistage degassing model associated with effusive eruptions. *The primary degassing originates from an assumed non degassed silicate melt, in this case the erupting magma coming from depth. The primary gas is thus made up of the most volatile species and released syn-eruptively at the crater. In contrast, the secondary gas is emitted from a partially degassed silicate melt, having previously gone through the primary degassing. The secondary degassing can originate from different sources: syn-eruptively at the flowing lava and post-eruptively at the extinct crater and at the crystallising lava field.*

Since the 1980's, post-eruptive or lava gas samples were collected and analysed sporadically (Aiuppa et al. 2003; Ilyinskaya et al. 2012; Zelenski et al. 2014), but never were the focus of a study until Sigmarsson et al. (2020). In their paper, these authors reported several post-eruptive gas compositions collected at the cooling crater of Holuhraun, a few weeks after the end of the 2014-2015 eruption. Such analyses revealed a strong change of major volatile proportions, the gas phase shifting from highly sulphur-dominated (mass ratio of S/Cl = 40-52 and S/F = 108-580) to similar concentration of sulphur, chlorine and fluorine (S/Cl = 0.45-1.6 and S/F = 0.62-2.9). As was argued in the case of Etna by Aiuppa et al. (2009), the relative enrichment in halogen in the secondary gas was attributed to Rayleigh distillation. A Reyleigh distillation (or fractionation) describe the evolution of a system with multiple phases in which one phase is continuously removed from the system through fractional distillation. In the case of volcanic degassing, the removed phase is the gas, whose escape deplete the melt of the most volatile species such as sulphur, increasing the proportion of less volatile elements such as the halogens.

The change in relative proportion of major volatiles could be of great importance regarding trace element volatility and thus emissions. Such volatility change should be principally dependent on the availability of the main ligands for these trace elements to form volatile species, which were revealed to be sulphur, halogens and oxygen by thermodynamic modelling (Symonds et al. 1992; Symonds and Reed 1993; Wahrenberger 1997; Taran et al. 2001; Mandon et al. 2019; Mason et al. 2021). Thus, the trace element emissions from secondary degassing, with higher halogens content with respect to sulphur, should be drastically different as suggested by Crowe et al. (1987) data. More recently, secondary gas emissions were investigated at Fagradalsfjall (2021-2023) by Wainman et al. (2024) who compared gas emissions from the flowing lava to those of the eruptive vent. The authors reported at-vent emissions of a gas rich in both S and S-complexing elements, whereas the gas emitted by the flowing lava was richer in Cl and Cl-complexing elements. Wainman et al. (2024) then developed a model in which progressive degassing results in gas composition differentiation, the flowing lava gas being the very first stage of secondary degassing, which continues post-eruptively as the lava crystalise (Fig. 1.7).

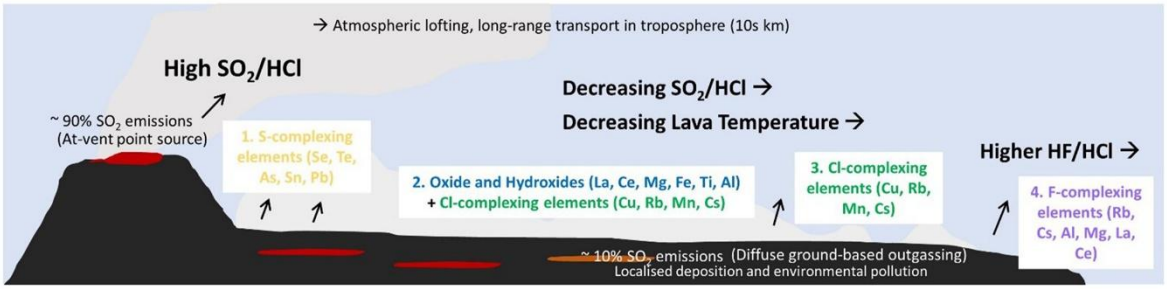

Figure 1.7. Schematic diagram from Wainman et al. (2024) of the "observed and modelled transitions in the gas and trace element composition of lava flow outgassing emissions". *The first stage of secondary degassing is represented by the emissions from the flowing lava, with observed increase in Cl and Cl-complexing elements. The later stage of secondary degassing is represented by the distance lava and during crystallisation, which is hypothesised to have increased F proportion, due to its lower volatility.*

Thus, the crystallising lava degassing is of particular importance because some of the toxic heavy metals are known to form halide and could thus be intensely released during late secondary degassing. While for explosive eruption lava secondary degassing is expected to be limited, effusive eruptions display a significant proportion of gas emitted by the lava flow upon emplacement and cooling (Thordarson et al. 1996, 2001). Thordarson estimated that during Laki and Eldgjá eruptions, around 20 % for H_2O, CO_2 and SO_2 escaped secondarily but over 40 % for Cl and F.

Unlike the primary degassing at the eruptive vent, the origin and the mechanism of the secondary gas release from newly emplaced lava fields remains unclear. Cashman et al. (1994) investigated the vesicle size distribution of the lava and concluded that only minor amount of gas escapes the lava while flowing. Sustained degassing of the lava after emplacement thus requires another mechanism, involving larger scale volatile exsolution and circulation within the solidifying lava. The next section presents the processes was identified in connection with lava internal differentiation by development of segregation structures in emplacing basaltic lava.

1.2 Segregation veins in basaltic lava

Lava bodies (flows, sheet lobes, lakes, etc.) are not homogeneous, the internal structure of the lava often being rather complex with numerous sub-units. The lava is organised vertically as upper crust, lava core and lower (or basal) crust (Self et al. 1996). These layers are characterised by distinct vesicularity, crystallinity and jointing style, originating from their crystallisation history. In terms of thickness, the upper crust makes up to 50 % of the lava whereas the lower/basal crust is typically around a meter thick, the core making the rest (Thordarson 1995; Thordarson and Self 1998; Nikkola et al. 2019). Whitin the core and the lowermost part of the upper crust, darker and vesicle-rich structures called segregations, or segregation veins, are often present.

This section will review the current state of the art regarding the formation of segregation veins and their features, to highlight how it will be used in the PhD thesis. First, I will describe what segregation veins are, outlining their discovery, characterisation and hypothesised formation processes. A summary of the main investigations regarding chemical composition of the segregations and their diversity is then presented, providing a base for interpreting the results from this thesis. Lastly, I will synthetised existing work that have suggested a relationship between the segregation process and lava degassing and presented what is known in terms of segregation volatile content. This section establishes how segregations are worth examining when studying the process of lava differentiation and degassing, which will be done during Chapter 4 of this work.

1.2.1 What is a segregation (vein)?

Segregations were first described and extensively studied by the Japanese geologist Hisashi Kuno in the second part of the 20th century (Kuno et al. 1957; Kuno 1965). Kuno described these structures as “thin vesicular veins, either parallel or perpendicular to the base of the flow” and stated that they were formed by “segregation of residual liquids produced by fractionation of the magmas after their extrusion”. He logically named the structures segregation veins and used them as a tool to characterise the “fractionation trends of basalt magmas in lava flow” (title of the 1965 paper). By studying segregations from several basaltic lava, they identified distinct differentiation trends, depending on both magma composition and oxygen fugacity.

Following Kuno’s papers, increased attention was paid to the segregations and the information they carry. Anderson et al. (1984) attempted to constrain the physical mechanism leading to the formation of the segregations and developed the model of gas-filter pressing. In this model, the residual melt is formed by crystallisation of host lava. The melt can then either accumulate around a bigger vesicle and form a segregation vesicle (Fig. 1.8) or be propelled upwards by the pressure gradient induced by gas effervescence mechanism. The propelled (and thus segregated) residual melt then crystallises and form the segregation veins.

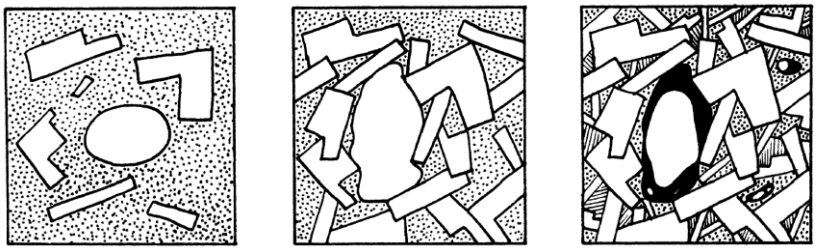

Figure 1.8. Original model of gas-filter pressing and segregation formation proposed by Anderson et al. (1984). *In this model, crystallisation produces an evolved vesicle-rich residual melt. The schematic represents the case of a segregation vesicle formation in which the residual melt (in black) accumulating around a pre-existing vesicle. Occasionally, the exsolved gas would create such a pressure gradient that the melt would be propelled upwards and form the segregation veins.*

Several studies then attempted to constrains the exact conditions leading to segregation (Puffer and Horter 1993; Cashman et al. 1994; Goff 1996; Caroff et al. 2000; Costa et al. 2006; Fowler et al. 2015) and compiled by Nikkola et al. (2019). Though most articles align with Anderson's model, they argue for additional mechanisms such as vesicle coalescence (Puffer and Horter 1993), vapor differentiation (Goff 1996), Rayleigth-Taylor instability (Costa et al. 2006) or mush convection triggered by fluid migration (Fowler et al. 2015).

Segregations veins are ubiquitous in basalt lavas, particularly in thick flows (Thordarson and Self 1998; Martin and Sigmarsson 2007; Kuritani et al. 2010; Nikkola et al. 2019) and even flood basalts (Philpotts et al. 1996), but has also been found in only decimetres thick lobes (Sheth et al. 2017). In addition, drillings in the 100-meters deep Kīlauea Iki lava lake formed in 1959 revealed large amount of segregations (Helz 1980; Helz et al. 1989) of similar nature to those found in lava flows. In terms of lava composition, segregation veins develop essentially in low viscosity melt, with composition ranging from tholeiitic basalt (Martin and Sigmarsson 2007; Nikkola et al. 2019) to alkaline basalts (Goff 1996; Sigmarsson et al. 2009; Kuritani et al. 2010) and basaltic andesite (Anderson et al. 1984; Caroff et al. 2000). Field observation reported in the different papers suggest a highly variable proportion of segregation veins in a basaltic lava, ranging from 0.1-0.2 % in Surtsey lava (Sigmarsson et al. 2009) to several percents in Kīlauea Iki lava lake, Kutsugata lava flow, Hafnarhraun pahoehoe lobe and in the Holyoke Basalt (Helz et al. 1989; Philpotts et al. 1996; Kuritani et al. 2010; Nikkola et al. 2019).

A key feature of the segregations is that they form when a lava crystallises and thus mainly once the lava has stopped moving. For this reason, their formation is closely related to the cooling history of the lava flow/lobe/lake. As lava is a good insulant, cooling and solidification of a lava field is slow and long, the duration being primarily controlled by lava thickness. Based on empirical data, Hon et al. (1994) defined the relationship between crustal thickness and time:

$$C_{800} = 0.0473 * \sqrt{t} - 0.0233 \quad (1.1)$$

where C_{800} is the thickness of crust below 800 °C and t is the cooling time. Taking an average upper crust thickness of one third of the flow, the crystallisation time of a several meters thick lava is on the order of days/weeks and tens of meters thick lava on the order of years to decades. The drillings conducted in the approximately 100-meter-deep 1959 Kīlauea Iki

lava lake revealed melt presence in 1979 which was not found any more in the 1981 core, indicating a crystallisation time of 20-22 years (Helz and Wright 1983; Helz et al. 1989), which is shorter than expected from Hon's equation. This faster crystallisation is readily explained by the integration of additional cooling parameters (not accounted in the equation) such as precipitation and lateral cooling, particularly important in the case of lava lake cooling. The timing of segregation emplacement is the same with new segregations found up to the 1979 core but not in 1981 (Helz and Wright 1983). Goff (1996) attempted to constrain the rising speed of the segregation melt using the cooling history of the lava and found values of in the order of meters per day, the exact value depending on emplacement temperature and the thickness of the flow.

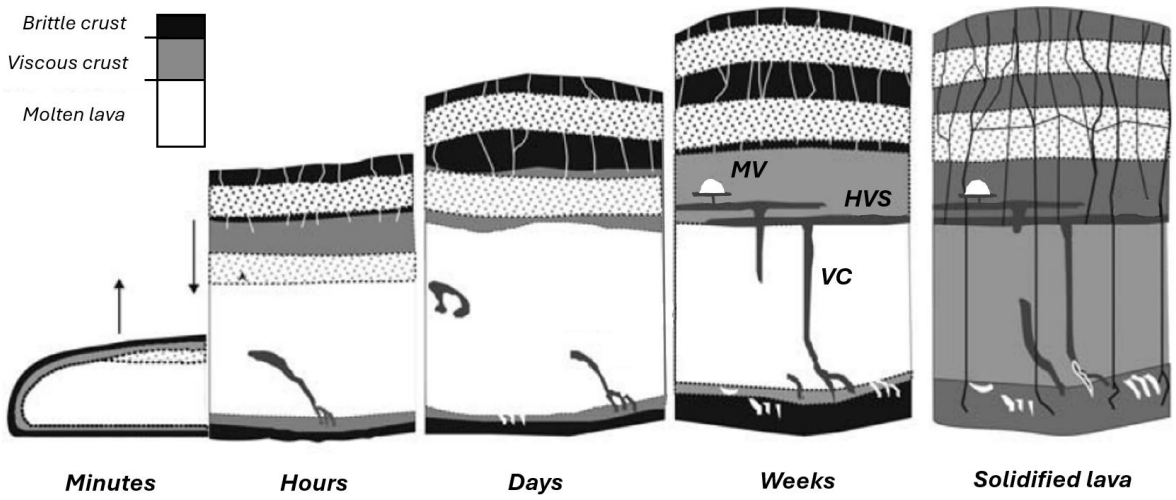

Figure 1.9. Segregation development and resulting structures within the solidified lava. *The lava cross sections show the temporal evolution (from left to right) of a lava lobe and internal differentiation. Figure modified from Thordarson and Self (1998).*

On the field, segregations are easily identifiable due to their darker colour, high vesicularity and higher crystal size. The veins are however not uniform and display diverse features. Kuno already observed segregations both parallel and perpendicular to the base of the flow (Kuno 1965). Given their cylindering shape, the vertical segregation veins were later named vesicles cylinders, or VC, by Goff (1977) whereas the horizontal veins were called vesicle sheet and later horizontal vesicle sheet, or HVS (Thordarson 1995; Goff 1996). Vesicle cylinders are in most cases a few cm wide and decimetres long (occasionally meters). They take root in the lowermost part of the lava, sometimes at the junction of several pipe vesicle (Thordarson 1995), but often with no apparent feeder. Similarly, the top of the VC is sometimes gradually disappearing in the core of the lava flow, whereas occasionally, VC are directly connected to a horizontal vesicle sheet (Goff 1996; Thordarson and Self 1998; Martin and Sigmarsson 2007; Thordarson and Sigmarsson 2009). The HVS have a typical thickness of 1-10 cm and spread horizontally for decimetres to meters. Horizontal vesicle sheets are localised in the lowest part of the upper crust of the lava (Thordarson 1995; Sigmarsson et al. 2009). In addition to the VC and HVS, Thordarson (1995) identified a third segregation type which he named megavesicle, or MV (Fig. 1.9). Such name was given as these segregations are made of a thin (a few cm) pod of segregation melt overlined by a large semi-spherical (dome-shaped) void of dimensions ranging from cm to dm. Megavesicles are generally located in the upper crust, above or at the same level than HVS. In the field, MV are in some cases connected to a VC or HVS and in others not.

The geometrical features of the segregations were used by Goff (1996) and Thordarson (1995) to study their emplacement and development. First, the fact that VC are vertical structures indicate lava had ceased to move at the time they formed (Goff 1996). The segregation process is potentially initiated before the lava flow come to rest, in which case the early forming VC can be deformed and eventually eliminated by the lava motion (Thordarson 1995; Sigmarsson et al. 2009). Bended small VC and pipe vesicles in the basal crust of the lava are evidence for such early segregation process. The abrupt transition from vertical VC to horizontal HVS indicate the presence of a horizontal impermeable boundary for the rising segregation melt. The HVS thus most likely formed at the contact between the lava core and the forming upper crust. The HVS being located at different heights (Helz et al. 1989; Thordarson and Self 1998; Kuritani et al. 2010; Nikkola et al. 2019) in the lava, establishment of HVS occurs over a sustain period of time while the upper crust is propagating downwards. Occasional connections between HVS and MV point out that the latter formed from the former. The size of the void overlying the melt pod of the MV indicates that MV formation is closely associated with gas accumulation. Thordarson (1995) proposed that when the gas accumulation rate and rheological conditions are favourable, part of the HVS segregation melt and gas separate and rise to form a MV, in which the melt is drained down to form the MV pod and the gas accumulate on the top and form the dome-shaped void.

1.2.2 Segregation veins composition

Segregation veins are the product of fractional crystallisation of the lava. Thus, their composition differs from the host lava (HL) and was extensively studied to investigate the differentiation process and constrain the segregation formation. Kuno (1965) already examined the segregation chemical composition with the objective of characterising magma fractionation at surface conditions, previously only approached by the study of shallow intrusions, such as at Skaergaard (Wager 1939) and in Hawaii (Kuno et al. 1957). Their studies included segregations from tholeiites, high alumina basalt and basaltic andesite and largely focused on the SiO_2 and total iron content as well Fe_2O_3/FeO ratio. Using such data, Kuno identified distinct silica and total iron trend in the segregation depending on the oxygen fugacity (indicated by Fe_2O_3/FeO).

Following Kuno´s work, numerous studies attempted to better constrain the differentiation process by analysing more segregations, generally using both major and trace element data. Helz (1987) presented detailed result regarding segregation composition from the Kīlauea Iki lava lake, along with the segregations residual glass composition. Helz identified a clear progressive differentiation trend, starting from the host lava through the different segregation to the residual glass (Fig. 1.10).

Examining segregations and host lava (HL) from alkali basalts, shoshonites and basaltic andesites, Caroff et al. (2000) highlighted the variable differentiation paths, the most evolved products (glass) ranging from rhyolite to phonolite. Martin & Sigmarsson (2005, 2007) used segregation veins and in particular their residual glass to reconstruct the differentiation path of magma through fractional crystallisation at surface condition. Their results allowed to identify that Icelandic silicic rock did not form though such differentiation process but rather by melting of hydrothermally altered basaltic crust. The composition of segregation veins from the Columbia River Basalt Group were studied by Hartley & Thordarson (2009). By comparing the different host rock and segregation vein composition, the authors suggested

that a differentiation process analogue to segregation formation (fractional crystallisation and buoyant rise) could explain the large-scale bimodal composition of the lava. The more evolved lava would thus result from a segregation-like process of the primitive one.

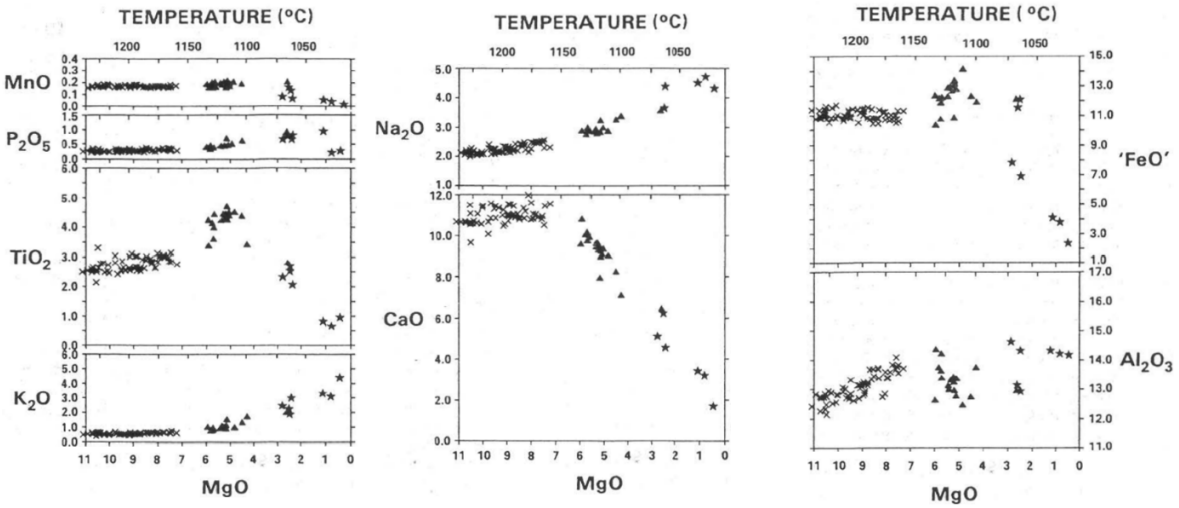

Figure 1.10. Host lava (crosses), segregation (triangles) and residual glass (stars) composition from the Kīlauea Iki lava lake. *All analysed oxides reveal the liquid line of decent with decrease in compatible oxide (MnO and CaO) and increase incompatible oxides (P_2O_5, K_2O and Na_2O), TiO_2 being initially incompatible until crystallisation of oxides at 5 % MgO (segregation concentration). Figure modified from Helz (1987).*

Besides the study of the differentiation, segregation compositions were also used to better constrain the conditions in which they emplaced in the crystallising lava. Using modelling and thermobarometers, emplacement temperature was constrained to 1100 +/- 50 °C (Helz 1980; Goff 1996; Martin and Sigmarsson 2007; Sigmarsson et al. 2009). The same authors also estimated oxygen fugacity using ilmenite-magnetite pairs and consistently found values below QFM buffer for the segregation veins, whereas host lavas had values close to QFM. Such results lead them to state that the segregation melt generally crystallise in an environment isolated from the atmosphere, though one exception was observed for Masaya with much higher oxygen fugacity (Martin and Sigmarsson 2007).

The compositional difference between HL and segregation also brough insight to identify the threshold of fractional crystallisation (FC) that can lead to residual melt segregation. Physically, Philpotts et al. (1996) demonstrated that around 30-35 % of FC, a rigid network of crystal was formed, allowing the residual melt to escape/segregate without mobilising crystals. This lower boundary matches well with the segregation vein composition, which rarely result from less than 30 % FC (Kuritani et al. 2010; Nikkola et al. 2019) but more generally between 30 and 50 % (Caroff et al. 2000; Martin and Sigmarsson 2007; Hartley and Thordarson 2009).

Since segregations are of different nature, a special interest has also been set on investigating the compositional heterogeneity within the segregation veins from the same lava. Caroff et al. (2000) analysed vesicle cylinders, (horizontal) vesicle sheets and segregation vesicles (including both megavesicles and isolated melt pockets next to smaller vesicles) and revealed distinct composition of the different segregations. The authors observed a general trend with VC and HVS being less evolved (FC between 35 and 60 %) than segregation

vesicles, though the latter group displayed high compositional diversity (FC between 35 and 90 %), most likely related to their variable nature. Hartley & Thordarson (2009) reported segregation veins resulting from 30-40 % FC, with HVS slightly more evolved than VC whereas Kuritani et al. (2010) identified variable HVS composition within a single lava, with the lowest most sheet resulting from around 60 % FC, gradually decreasing to 40 for the upper most ones.

Recently, segregation heterogeneous composition was also attributed to other processes than variable extent of FC. To explain the presence of vesicle cylinders with higher MgO than the host lava Kuritani et al. (2010) suggested that during segregation formation, not only the residual melt and gas escaped the forming crystal network but also crystals (plagioclases and olivines). Nikkola et al. (2019) also found segregation veins (both VC and HVS) with similar composition than host lava. The authors however challenged Kuritani's model by pointing out that segregation melt only carrying the dense olivine (and not lighter crystals) in its migration was unlikely. Rather, Nikkola et al. (2019) suggested that during the segregation formation, macrocrysts from the HL were incorporated in the segregation melt (Fig. 1.11). Such HL macrocryst were spotted by Martin and Sigmarsson (2007) in some segregations.

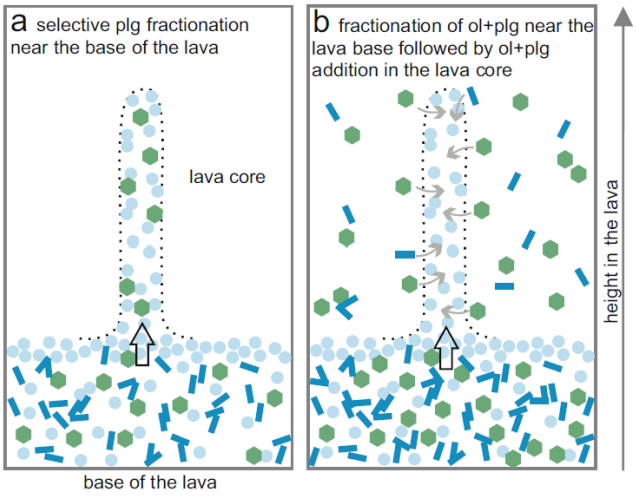

Figure 1.11. Models proposed by Nikkola et al. (2019) to explain the presence of poorly differentiated vesicle cylinder. *Two models are proposed to explain such composition, (a) selective segregation of olivine crystals with the rising melt. This model in considered unlikely given the higher density of olivine with respect to other crystallising minerals. (b) Integration of host lava minerals (mainly olivine) in the rising segregation melt.*

The segregation emplacement is thus a complex process, resulting in formation of variable segregation veins of different composition. The composition of the segregations can mostly be explained by processes involving the liquid and solid phase (FC of different extend, crystal capture or removal). The segregation system can however not be exhaustively studied without considering the gas phase, which play a crucial role in the segregation formation. Such role can be studied by analysing the volatile element concentrations in the segregations and associated HL.

1.2.3 Segregation process, volatiles and lava degassing

The segregation process is initiated by the exsolution of volatiles and the subsequent gas phase pressure on the residual melt. Such process is thus by nature associated with volatile transport in the lava, potentially leading to its escape. This link was often pointed out in papers studying segregation, without further investigation. Puffer and Horter (1993) and Caroff et al. (1997) associated the volatile escape from the lava lobe/flow with propagation of cracks segments or columnar joints. The volatile escape is preceded by massive volatile circulation as stated by Greenough et al. (1999): "vesicle plumes provide a mean of moving exsolved volatile constituents", using volatile concentration in three host lava/segregation pairs from Penghu Islands, Taiwan. Indication of such degassing were presented by Martin and Sigmarsson (2007) with the absence of water in both the minerals and the residual glass from segregations. Sigmarsson et al. (2009) clearly related the lava degassing and melt circulation associated with the segregation process by stating "Liquid displacement as described here may thus be a common process during solidification of lava flows and a driving mechanism for lava degassing". Finally, in their thin (< 1 m) lava lobe, Sheth et al. (2017) observed VC that reach the upper surface of the flow and associated it with profuse degassing at the lava surface during the segregation process (Fig. 1.12).

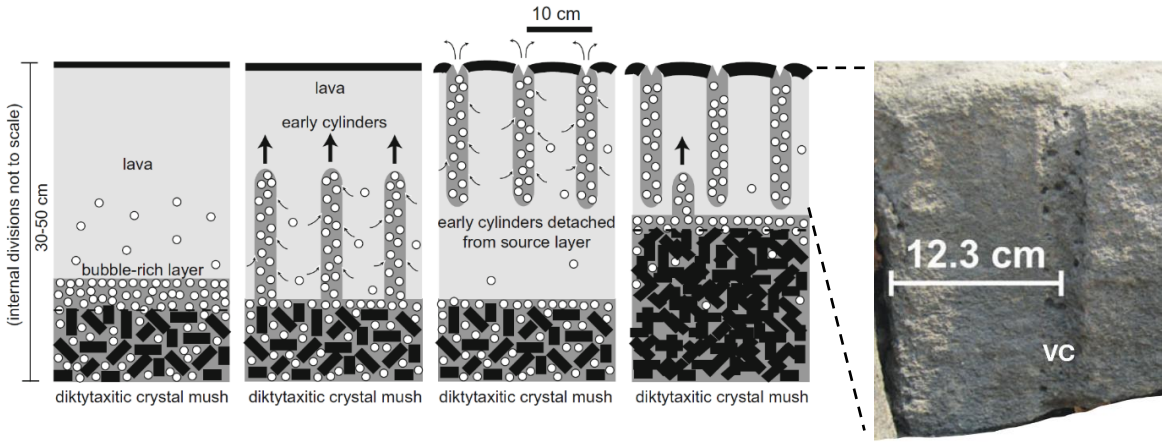

Figure 1.12. Rising cylinders as a degassing mechanism for lava flows. *Figures modified from Sheth et al. (2017).*

If the segregation process does indeed play a large role in lava degassing, crucial information should be revealed by investigating the volatile content in the segregations. Though, to our knowledge, only the study from Greenough et al. (1999) focused on this aspect, several articles presented isolated volatile measurements in segregations and host lavas. The loss on ignition (LOI), assumed to be representative of volatile content, was measured in a few publications dealing with segregations. Kuritani et al. (2010) reported similar LOI in VC and surrounding host lava whereas HVS had slightly lower LOI. Lower loss on ignition in HVS than host lava were also observed by Caroff et al. (1997), though attributed it to alteration process. In their paper, Greenough et al. (1999) reported high LOI values, variable in the host lava (2.6-5.8 %) but not in the segregations (6.0-6.2 %). Variation of LOI within segregation system thus seem erratic, limiting its use to investigate the link between segregation formation and lava degassing.

The structural water (H_2O^+) content in segregations was measured as early as by Kuno (1965). A variable behaviour of water was identified, some segregations having H_2O content

similar to their host lava while others are enriched in the same manner as the incompatible oxide P_2O_5. Goff (1996) also reported H_2O^+ values but without showing any clear trend between host lava and segregations. Water being incompatible in the crystallising minerals in basalts, the lack of enrichment in some segregations most likely translate escape of the excess water through the gas phase.

Sulphur was measured by Philpotts et al. (1996) in the Holyoke Basalt (Hartford Basin, USA) and a few of its segregations (called pegmatitic segregation sheets). The host lava was revealed very heterogeneous in S concentration ranging from 100 to 800 ppm, whereas other elements did not show such variability (TiO_2 from 0.8 to 1.05 wt % and Zr from 68 to 96 wt ppm). The four "segregation sheets" showed S values from 186 to 311 ppm whereas TiO_2 and Zr displayed negligible variability (1.41-1.44 % and 118-122 ppm respectively). Clearly sulphur concentration in both the lava and its segregations is not homogeneous and no obvious trend appear between the host lava and segregations. Sulphur concentrations were also reported by Goff (1996) in two high-alumina tholeiitic basalts but none of the analysed samples (whether host lava or segregation) where found above the detection limit of 10 ppm. Goff however presented results in terms of Cl, which is found clearly enriched in the segregations (particularly HVS), as the incompatible trace elements. One HVS presented Cl concentration of 155 ppm whereas the host lava had 39, when P_2O_5 was 0.57 and 0.20 %, suggesting Cl enrichment somewhat superior to incompatible elements.

The trace volatile elements, including volatile metals (and metalloids), concentrations in segregations were scarcely studied. A few articles included measurements of the slightly volatile Rb and Zn (Puffer and Horter 1993; Goff 1996; Philpotts et al. 1996; Caroff et al. 1997; Stephenson et al. 2000; Martin and Sigmarsson 2007; Hartley and Thordarson 2009; Nikkola et al. 2019). No particular behaviour was observed for these elements, with enrichment in segregation (relative to host lava) similar to other incompatible elements (Th, Zr, P_2O_5, etc.). In addition, Stephenson et al. (2000), Hartley & Thordarson (2009) and Kuritani et al. (2010) presented results regarding the moderately volatile Pb. In these articles, Pb appears to be generally enriched as the incompatible elements, but a few segregations display slightly higher Pb enrichment the most incompatible elements.

To our knowledge, the only detailed investigation regarding the segregation volatile composition and link with degassing was presented by Greenough et al, (1999), who reported concentrations in S, Cl, As, Pb, Zn and Rb. Among these volatile elements, S, Cl and As showed high heterogeneity in the host lava, also visible in the non-volatile Sr, K and Na but unlike most other elements/oxide (MgO, P_2O_5, REE, HFSE, etc.) which are homogeneous (Fig. 1.13). Comparing the three segregations to their adjacent host lava reveals erratic enrichment in segregations for most volatiles (0.6-3 for S, 1-3 for As and 1-2 for Cl, Pb, Zn and Rb), uncorrelated to each other and other elements. The authors thus revealed indication of volatile transport in the lava leading to its heterogeneity but did not identify systematic trends regarding segregations. The limited number of samples and analysed trace volatiles prevented inferences regarding the process related to degassing. It must also be noted that most other studies did not see such host lava variability in Sr, K and Na, suggesting a peculiarity of the Taiwanese basalt flow.

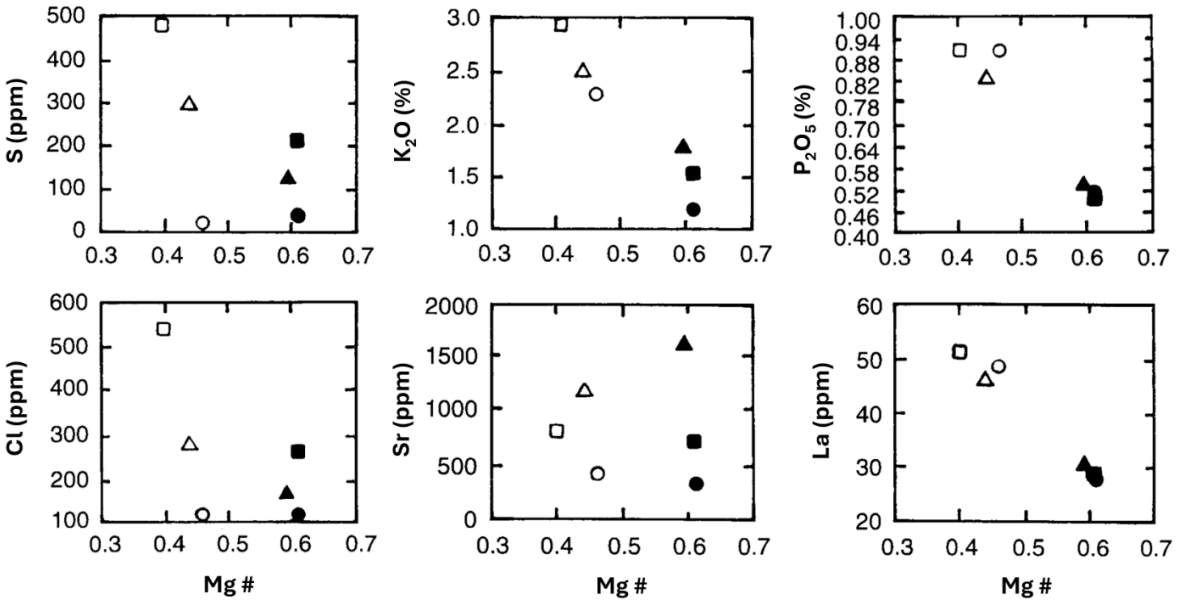

Figure 1.13. Taiwanese host lava (filled) and segregation (empty) volatile (S and Cl) and refractory elements (K_2O, P_2O_5, Sr and La) concentrations. *Figure modified from Greenough et al. (1999).*

Thus, the scarce available data on volatile concentrations do suggest a transport of the volatile elements during the segregation process. The lack of a systematic study of the volatile concentration on an extensive dataset however prevents clear definition of the link between segregation formation and secondary degassing from crystallising lava.

1.3 Icelandic volcanic activity and products

Volcanism around the world is associated with three distinct tectonic contexts: subduction, rifting and hotspot. Subduction volcanism is the result of the subduction of an oceanic tectonic plate under another one, either continental or oceanic. With increased pressure and temperature, water escapes the subducting plate and percolate to the overlying mantle wedge, lowering its melting point and thus favouring magma formation. Rifting also takes place at the boundary between two plates, either offshore as mid oceanic ridges or inland forming continental rift (e.g., East African Rift). In such context, magma is formed by the upwards motion of the mantle, to lower pressure, resulting in partial melting and subsequent magmatic and volcanic activity. Hotspot volcanism is the only type of intraplate volcanism and does not follow the tectonic plate movements, creating series of volcanic islands for oceanic hotspots (e.g., Hawaii, Canary Islands, Réunion, etc.) or volcanic regions for continental hotspots (Eifel, Yellowstone). Hotspots are surface manifestation of mantle plumes, where the mantle convection is upwelling. This upwelling carries heat to lower depth, resulting in partial melting of the mantle, leading to magma genesis and eruption. Iceland represents a one-of-a-kind example of a mid-oceanic ridge crossing a mantle plume.

This section will outline the range of volcanic activity and products, including the lava and gas, in Iceland, providing context for the research and results presented in this PhD thesis. I will thus first describe the different types of volcanism in Iceland, highlighting its wide range of activity. A concise overview of the petrology and geochemistry of Icelandic lavas is then given, which is essential for thorough interpretation of the results presented in Chapter 4 and 5. Following this overview, I will present in further detail the volcanic systems investigated in this work, emphasising their diversities and representativity for Icelandic basaltic volcanism. To finish, I will give a quick introduction to Icelandic volcanic gases, contextualising observation conducted at Fagradalsfjall and described in Chapter 3. Overall, this section should underscore the interest of the Icelandic context when studying basalt lava degassing and provides the necessary background for the correct interpretation of results presented in Chapters 3, 4 and 5.

1.3.1 Volcanism in Iceland

The Icelandic volcanism is set up in a unique tectonic context, being associated both with rifting of the mid-Atlantic ridge and the Icelandic hotspot/plume, located in the centre-East of the island (Fig. 1.14). The peculiar geological setting of Iceland results in quasi unique volcanological features. Due to its dual origin, the Icelandic tectonic setting, plate boundary and volcanic systems are complex. The mid Atlantic ridge rises above sea level as the Reykjanes Volcanic Belt (RVB) in SW Iceland and the North Volcanic Zone (NVZ) to the North. Between these regions the plate boundary is separated between the East Volcanic Zone (EVZ; Fig. 1.14) and the West Volcanic Zone (WVZ) connected by the South Iceland Seismic Zone (SISZ) and the Mid Iceland Belt (MIB). Besides the plate boundaries are two other volcanically active region; the Öræfi Volcanic Belt (ÖVB) and the Snæfellsnes Volcanic Belt (SVB). The mantle plume is approximately located at the junction of the EVZ, MIB and NVZ.

Variable degrees of involvement of the mantle plume and rifting affect the different volcanic systems in the country (Gudmundsson 2000). The contribution of the plume is the greatest

in the northern part of the EVZ, whereas systems located in RVB, WVZ and SVB are virtually only the product of rifting.

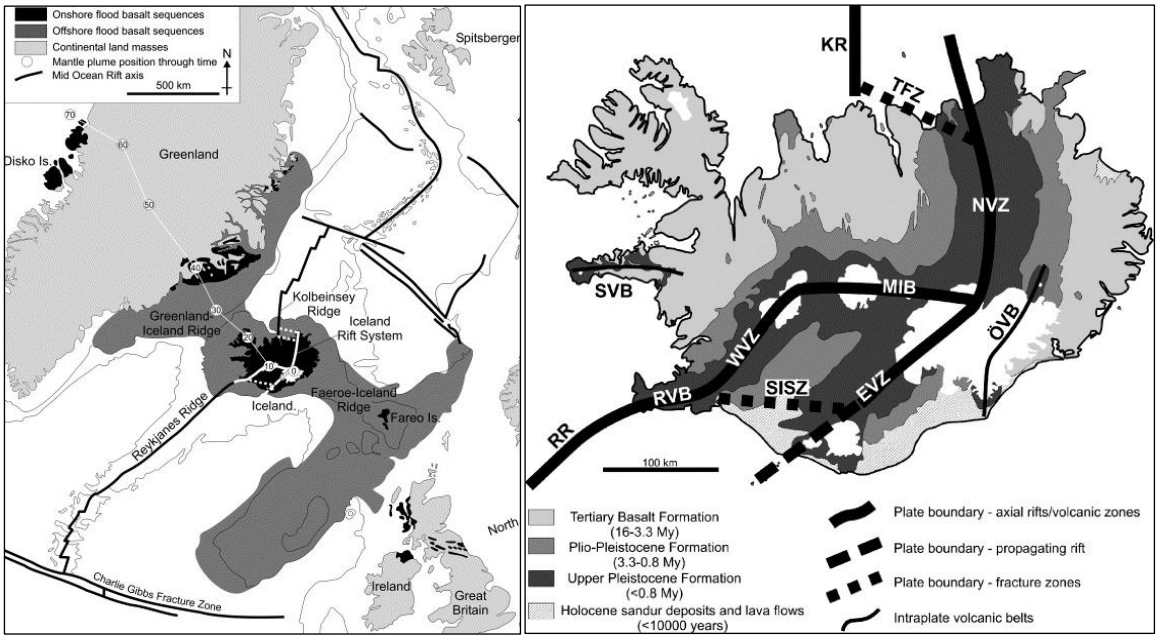

Figure 1.14. Maps of plate boundary and tectonic structures around Iceland. *Left: Icelandic tectonic regional context. Right: Plate boundary and volcanic zones in Iceland. Pictures from Thordarson and Larsen (2007).*

Another major feature affecting Icelandic volcanic activity is the presence of thick ice caps on the volcanically active part of the island (Vatnajökull, Langjökull, Hofsjökull in the central part of the country and Mýrdalsjökull and Eyjafjallajökull to the south). Such predominance of glacier, along with lakes and the sea, leads to frequent magma/water interaction. Subsequently, many eruptions are phreatomagmatic, thus increasing the proportion of explosive eruptions in Iceland. In addition, the evolution of the glacial cover and thickness, in response to climate changes, triggers pressure increase and decrease on underlying volcanoes. This is expected to result in a change of magma productivity at depth and subsequent eruption rate (Maclennan et al. 2002; Pagli and Sigmundsson 2008).

The historical Icelandic volcanic activity (since settlement in ca. 877 AD) was described in details by Thorarinsson & Saemundsson (1979) and more recently by Thordarson & Larsen (2007). These authors established that the majority of Icelandic volcanism is basaltic (around 80 %), which is typical of both rifting (MORBs) and hotspot activity, but a significant amount of andesitic and rhyolitic products also exist. Among the 172 well characterised historical eruptive events (33 other events are poorly known) reported by Thordarson & Larsen (2007), 132 are associated with only four volcanoes of the EVZ: Grímsvötn, Barðabunga, Hekla and Katla, the remaining 25-30 volcanic systems sharing the rest. Thirteen of the historical events are not single eruptions but rather classify as “Fires”, corresponding to a succession of basaltic fissure eruptions in the same system over several years (e.g., Krafla Fires 1975-1984, nine eruptions). The two largest historical events were Fires taking place in the EVZ: namely Eldgjá (ca. 934), associated with the Katla system, and Laki (1783-1784), associated with the Grímsvötn system. These events emitted respectively ca. 20 and 15 cubic kilometres of lava and tephra (Thordarson and Self 1993;

Thordarson et al. 2001; Sigurdardottir et al. 2015) and are the largest recorded historical effusive eruptions worldwide.

Though basaltic activity dominates in Iceland, most eruptions categorise as explosive, whereas mixed and purely effusive eruptions only represent around ten percent of the events each (Thordarson & Larsen, 2007). The rarity of effusive activity originates from the high proportion of phreatomagmatic eruptions such as the sub-marine eruption of Surtsey in 1963-1967 and sub-glacial eruption of Eyjafjallajökull in 2010. The fires distinguish themselves by being mainly effusive (60 %), often taking place on the Reykjanes peninsula (10^{th}-13^{th} century, 2021-ongoing).

1.3.2 Icelandic volcanic rocks composition

Because of its unique tectonic context, Iceland has always been a subject of attention for petrologist and geochemists, the first extensive studies dating back a century ago (Peacock 1925; Tyrrell and Peacock 1927). Though geologists from that period had no access to the modern-days analytical instruments, they already described the wide diversity of the Icelandic petrology, not only because of the significant intermediate and silicic components, but also identifying two distinct series with different alkali content. A renewed interest for Icelandic petrology rose when the plate tectonics model from Alfred Wegener became widely accepted, highlighting the peculiarity of Iceland. Such interest was enhanced by the so-called Surtseyan eruption giving birth to Surtsey Island in 1963 followed a decade later by the Eldfell eruption (1973) on the neighbouring island of Heimaey.

In his paper “Chemistry and distribution pattern of recent basaltic rocks in Iceland”, Jakobsson (1972) explored the existing Icelandic basalt compositions. The author highlighted the diversity and distribution of the basalts, with tholeiitic basalts concentrated in the rift zone whereas alkali-basalts are rather located on the off rift volcanic zone (SVB and ÖVB). Intermediate compositions were also identified, mainly found in the southern part of the EVZ.

The diversity of Iceland rocks composition was early attributed to the presence of several mantle sources, with involvement of the Icelandic plume. Jean-Guy Schilling attempted to relate the variable La/Sm in measured in Reykjanes lavas to different mantle source in Iceland (Schilling 1973). Though such La/Sm variations were later attributed to variable degree of mantle partial melting, the use of isotopic ratios ($^{87}Sr/^{86}Sr$, $^{143}Nd/^{144}Nd$, $^{3}He/^{4}He$, $^{206}Pb/^{204}Pb$, $^{208}Pb/^{204}Pb$), unaffected by partial melting, confirmed the existence of at least two mantellic sources in Iceland (Hart et al. 1973; Sun et al. 1975; O’Nions et al. 1977; Kurz et al. 1985). Simultaneously, oxygen isotope composition in some evolved Icelandic basalts revealed that crustal melting was also involved in magma formation in Iceland (Muehlenbachs et al. 1974). Sigmarsson and Steinthórsson (2007) compiled the data and modern view regarding Icelandic petrology (Fig. 1.15), attributing the composition of Icelandic basalts to the nature of mantle source, the nature of the recycled crust, the proportion of pyroxenite and lherzolite melting, condition of melting (pressure temperature) and contribution of hydrothermally altered crust.

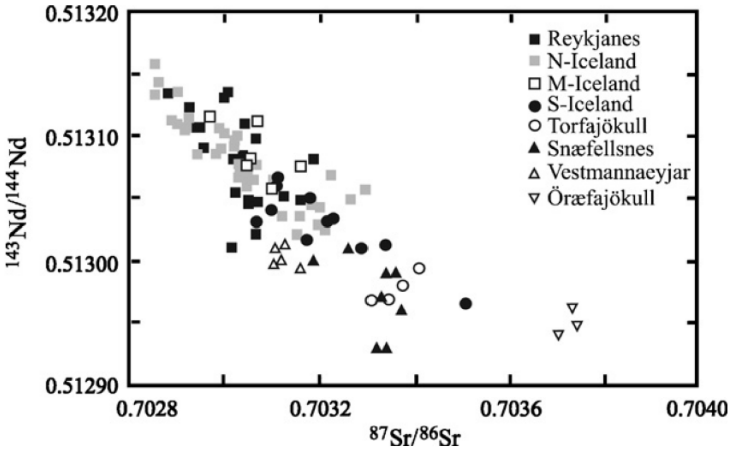

Figure 1.15. Isotopic composition of Icelandic products from diverse volcanic system compiled by Sigmarsson and Steinthórsson (2007). *The spread of both $^{87}Sr/^{86}Sr$ and $^{143}Nd/^{144}Nd$ which do not form a straight line demonstrate that at least three compositional sourced are involved in the formation of Icelandic volcanic products.*

Such complexity and number of parameters affecting the magma eruption, related to the geological history of Iceland and its current tectonic setting, results in wide composition variation, making each volcanic system distinctive (Jakobsson 1979).

1.3.3 Hekla, Eldgjá and Reykjanes

Three volcanic systems/zones are investigated in this thesis: the historical flood basalt of Eldgjá, the fluorine-rich and well-studied Hekla system and the Reykjanes peninsula, where a cycle of eruptive activity that could last centuries started in 2021. Eldgjá and Reykjanes have names directly referring to volcanic activity respectively translating as “fire canyon” and “smoking peninsula” while Hekla can be translated as “hooded” but was in the past thought to be the gateway to hell.

These volcanic systems were selected as study target for two main reasons: the diversity of basaltic volcanic activity they cover and the presence of developed and sampleable segregation structures. Reykjanes was targeted both for volcanic gas at Fagradalsfjall and segregations at Rauðimelur, allowing to investigate the “Fire” activity, which is currently taking place on the peninsula. Furthermore, the products erupted are of tholeiitic composition, which is the dominant component of rift volcanism in Iceland. Eldgjá was selected as it represents the flood lava activity, being the largest historical eruption in Iceland. Segregations were thus collected from the Eldgjá transitional basalt lava field. Finally, segregations from a Holocene lava from Hekla are investigated to represent both minor eruptions of transitional basalts but also particularly lavas richer in F.

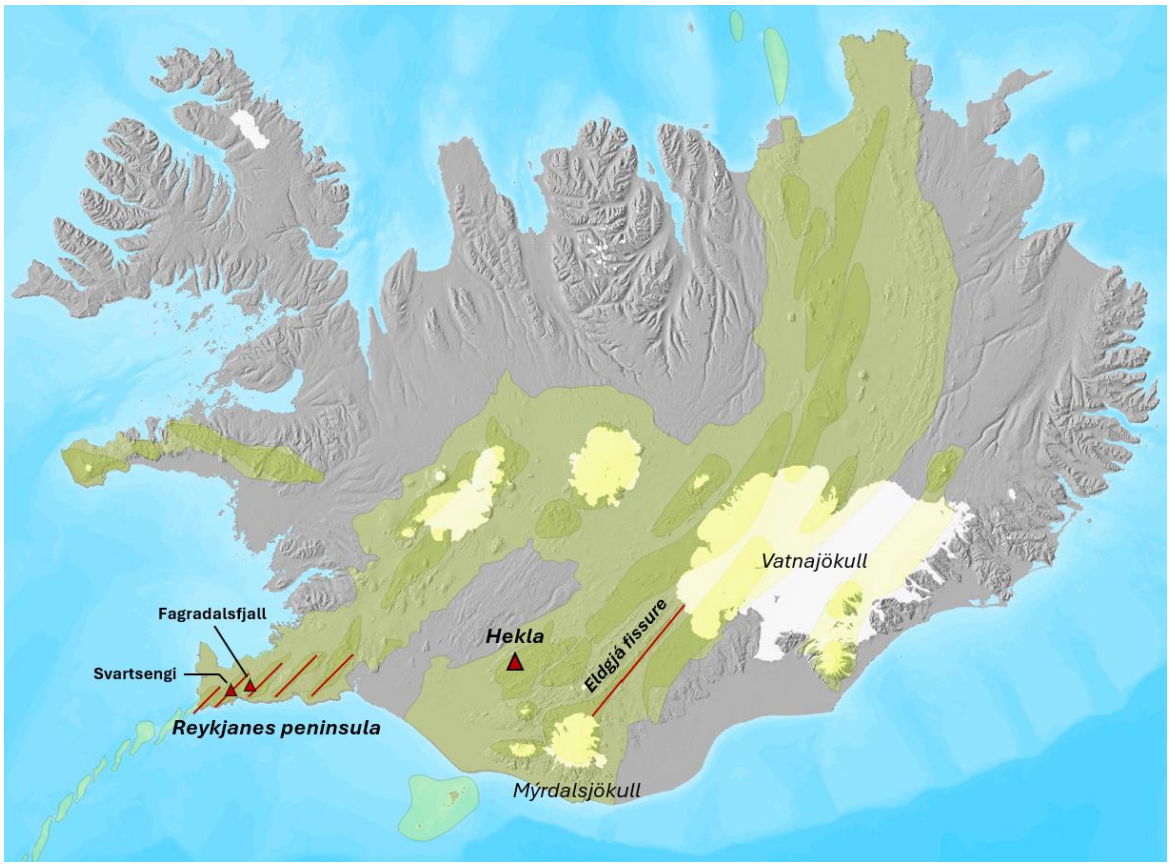

Figure 1.16. Map of Iceland with highlighted the volcanic systems investigated in this thesis: Hekla, Eldgjá and Reykjanes peninsula. *Hekla is a central volcano in South Iceland. Eldgjá is a 75-km long SW-NE fissure spreading between the Mýrdalsjökull and Vatnajökull ice caps. The Reykjanes peninsula is made of five volcanic systems, from West to East: Reykjanes, Svartsengi, Krýsuvík, Brennisteinsfjöll and Hengill, all of which displayed activity in the last eruptive cycles. Since the reawakening of the peninsula on 2020, the Fagradalsfjall complex erupted in 2021, 2022 and 2023 after several millennia of quiescence, followed by Svartsengi from December 2023 onwards.*

Hekla:

Mount Hekla is a stratovolcano located in South Iceland at the junction between the SISZ and the EVZ (Fig. 1.14 and 1.16). Hekla is one of the four most productive volcanoes in Iceland and, unlike the three others, is not subglacial. The central volcano of Hekla (Fig. 1.17) rises almost 1500 meters above sea level whereas its fissure swarm is approximately 60 km long. The first eruption attributed of this stratovolcano goes back to the early Holocene and since settlement 23 eruptions were recorded (the last one in 2000), together emitting over 2 km^3 of tephra dense rock equivalent (DRE) and 10 km^3 of lava (Thordarson and Larsen 2007). Hekla is characterised by its wide range of volcanic activity (from fissure eruptions to Plinian) and products (from basalts to rhyolite; Jakobsson 1979; Larsen et al. 1999). Among these 23 recorded eruptions, 18 took place at Hekla central volcano, generally starting by and explosive phase followed by a sustained effusive phase (Thorarinsson 1967). The remaining five eruptions occurred from craters within the Hekla fissure swarm but away from the central volcano, the last one taking place in 1913.

In terms of composition, all products from Hekla plot in the transitional alkalic series (Jakobsson 1979). The main component of the central volcano is of basaltic andesite composition with SiO_2 content around 55 weight % (Thorarinsson 1967; Sigmarsson et al. 1992). Fissure eruptions in the vicinity emit much more primitive lavas with SiO_2 < 50 % and MgO > 5 %. Regarding volatiles, Hekla products are rather poor in chlorine but particularly rich in fluorine, the recent basaltic andesite having less than 500 ppm of Cl and over 1000 ppm of F (Sigvaldason and Óskarsson 1976, 1986; Moune et al. 2007). Sulphur measured by Moune et al. (2007) in melt inclusions indicate 900 to 2600 ppm of S in the magma source but only 220 to 310 ppm in the residual glass of the lava from the 2000 eruption, translating intense S degassing. Water high content in the melt inclusions (0.5-6 %; Moune et al. 2007; Geist et al. 2021) but low concentration in the residual glass and whole rock (Sigmarsson et al. 1992) indicates that water also outgasses.

Figure 1.17. Pictures of Mount Hekla. *Left: Sketch of the 1845 Hekla eruption drawn by Selsund and reported in the collection of Maurice and Katia Krafft. Right Picture of the modern-day Hekla from Hugi Ólafsson published by Náttúruminjasafn Íslands.*

Eldgjá:

The Eldgjá flood basalt eruption took place in 939 CE (Oppenheimer et al., 2018) and is the largest historical eruption in Iceland producing a lava field of 19.7 km^3 (Thordarson et al. 2001; Sigurdardottir et al. 2015; Morison et al. 2024) and 1.3 km^3 of tephra DRE (Larsen 2000). The Eldgjá vents extend along a SW-NE 75-km long fissure NE of the Mýrdalsjökull ice caps and is part of the larger Katla volcanic system (Fig. 1.16 and 1.18). The eruption occurred a few decades after the settlement of Iceland and there is no known direct description of the eruptions, leaving numerous questions regarding the impact of the eruption on the island. Nevertheless, the *Landnámabók* (book of settlement), the Old Norse mythology book *Vǫluspǫ́* and the observation from a monk reported in *Liber Miraculum* offer indirect accounts of events from the early years of Icelandic settlement. References to the Eldgjá eruption and its dramatic effect were inferred from these documents by Larsen (1979), Thordarson (2010), Glauser et al. (2018) and Morison et al. (2024). The impacts were however not limited to Iceland, the eruption modifying the climate over a wide area (Oppenheimer et al., 2018; Stothers, 1998), reaching as far as China (Fei and Zhou, 2006).

As the other systems of the southern portion of the EVZ, products of Eldgjá eruption are over 99 % of transitional alkali composition, the remaining < 1 % being tholeiites. The transitional component (whether lava or tephra) has relatively homogeneous composition with SiO_2: 46-48 weight %, TiO_2: 4.2-4.8 %, MgO: 4.9-5.4 % and K_2O: 0.64-0.81 % (Kokfelt et al. 2006; Thordarson and Larsen 2007; Óladóttir et al. 2008; Bindeman et al. 2008;

Morison et al. 2024). The tholeiitic component displays higher SiO_2 (~ 50 %) and MgO (up to > 7 %) but less incompatible oxides (K_2O < 0.5 %). The halogen content of Eldgjá products is relatively low with less than 1000 ppm of F and 500 ppm of Cl (Sigvaldason and Óskarsson 1976, 1986; Moune et al. 2007). Sulphur contents were investigated in different Eldgjá products, ranging from around 2000 ppm in the melt inclusion to 500-1000 in tephra and 100 ppm in the "degassed lava", translating progressive sulphur degassing during magma eruption and lava emplacement/cooling (Thordarson et al. 2001).

Figure 1.18. Photo of a portion of the Eldgjá gorge and crater row*, from Ilya Grigorik. The Eldgjá fissure eruption left a tens of kilometre-long line of such canyons and small craters extending from Mýrdalsjökull to Vatnajökull ice caps.*

Reykjanes volcanism:

Volcanism on the Reykjanes peninsula has always attracted particular interest, both because of its geographical location and its tectonic setting. Two thirds of the Icelandic population live on the peninsula or its immediate vicinity which includes the capital Reykjavik and the international airport, Keflavík, located respectively on the East and West of the peninsula. Geologically speaking, the Reykjanes eruptions represent a rare on-shore manifestation of mid oceanic ridge volcanism (along with Krafla in N Iceland; Wright et al. 2012), virtually unaffected by the Icelandic plume (Gudmundsson 2000). Such event thus supplies an opportunity to study a type of volcanism that is normally inaccessible.

The Reykjanes volcanic belt, located in SW Iceland consist of five *en-echelon* SE-NW volcanic systems, from West to East: Reykjanes, Svartsengi, Krýsuvík, Brennisteinsfjöll and Hengill (Fig. 1.16). For the last millennia, the Reykjanes peninsula has exposed a cyclicity in its volcanic activity with series of eruptions (Fires) spanning over a few centuries followed by around 800 years of quiescence. The last eruptive cycle occurred between the 8th and the

13th centuries. Over this period, the activity migrated westwards from Brennisteinsfjöll to Reykjanes systems where the last eruption occurred in 1240 (Sæmundsson et al. 2020). After 770 years without eruption, the activity on the peninsula awoke in 2020 with a series of seismic swarms and ground inflations (Sigmundsson et al. 2022). The eruptive sequence started a year later, in March 2021, with an eruption in Fagradalsfjall, a mountain ridge between Krýsuvík and Svartsengi that had not erupted in the past eruptive cycles. Following the 6-months long 2021 eruption in Geldingadalir, two other eruptions occurred in the Fagradalsfjall volcanic system, Meradalir in August 2022 (Fig. 1.19) and Lítli-Hrútur in July-August 2023. The activity then shifted to the neighbouring Svartsengi system, where a series of short-lived eruptions (< 2 months) started in December 2023.

Figure 1.19. First hours of the Meradalir eruption on August 3rd, 2022. *During this initial period, lava and gas were emitted through a fissure spreading over 200 meters before concentrating on a single vent.*

Volcanism on Reykjanes is characterised by emission of tholeiites, olivine tholeiites and limited amount of picrite (Jakobsson et al. 1978; Peate et al. 2009; Caracciolo et al. 2023). Though all products are basaltic, significant compositional difference exist between the different systems. Svartsengi emits more evolved lavas (MgO = 5-7 %) than the other systems (MgO > 7 %), whereas K_2O/TiO_2 indicates at least two distinct mantle source, the East systems containing more of the enriched mantle components and the West more of the depleted one (Caracciolo et al. 2023). The recent eruptions at Fagradalsfjall and Svartsengi emitted products with variable contributions of the two components within single eruptions, translating heterogeneous magma reservoirs simultaneously feeding eruptions (Halldórsson et al. 2022; Matthews et al. 2024).

Because of the primitive magma composition, the erupted products from Reykjanes have limited volatile content. In Fagradalsfjall lava, melt inclusion water content never exceed 0.3 % whereas less than 0.1 % were found in the glass (Halldórsson et al. 2022). On Reykjanes, sulphur concentrations range from 180 to 450 ppm in the glass but 1000-2000 ppm in the magmatic inclusion (Caracciolo et al. 2024). Halogens were also found in limited amount,

with Cl concentrations ranging from 50 to 150 and fluorine from 50 to 300 ppm, fluorine being slightly more abundant (Sigvaldason and Óskarsson 1976, 1986). Trace volatiles are also found in low amounts in Reykjanes lava (Peate et al. 2009).

1.3.4 Icelandic volcanic gas

This thesis aims to characterise the change of gas composition from primary to secondary degassing at Fagradalsfjall, on the Reykjanes peninsula. Before investigating secondary emissions, it is crucial to have a good understanding of the state of the art about Icelandic gas emissions. Because of its peculiar tectonic setting, volcanic activity and petrology, Icelandic gas emissions are diverse. The gas composition variability was revealed by investigations on degassing associate with the recent eruptions in Iceland.

Due to Iceland geographical features and demographics, most eruption on the island take place in remote areas and/or at high altitude. Volcanic gas sampling is thus often complex in Iceland, which limited the number of studies conducted on degassing from Icelandic volcanoes. Being the only non-glacially covered of the four most active volcanoes in Iceland, Hekla offered the first opportunities to study gas emissions from eruption. Guðmundur Kjartansson investigated such gas emission associated with the 1947-1948 Hekla eruption, characterised by important flux of CO_2 (Kjartanasson 1957). The four-years-long submarine then subaerial Surtsey eruption (1963-1967) allowed the first pristine gas samples to be collected by Sigvaldason and Elísson (1968). Using a tube connected to a cooled condenser and sampling vessel, the authors collected 13 erupting vent gas samples from 1964 to 1967. Though a few samples clearly displayed air contamination, the general gas composition could be assessed from the repeated sampling, revealing water domination (80-90 mol %), variable CO_2 (1-10 %) and SO_2 (2-15 %) and significant HCl (0.4-1.2 %). The proportion of CO_2 in the gas progressively decreased over the eruption, most likely translating continuous depletion of the source in the least soluble volatiles. The Eldfell eruption in 1973 on the neighbouring island of Heimaey allowed Mroz and Zoller (1975) to complete the first aerosol sampling from an erupting volcano in Iceland revealing important emission of some trace metals. During the “Krafla Fire” series of eruptions (Fig. 1.20), the temporal variations of fumarolic gas composition due to magma contribution was studied, thus giving insight on how to investigate gas composition to infer magmatic activity (Óskarsson 1984; Ármannsson et al. 1989).

Figure 1.20. Photo from Michael Ryan (USGS) of the Krafla fissure eruption in 1984, showing extensive degassing through gas plumes over the whole fissure.

Niels Óskarsson investigated the 1970 Hekla gas emissions in the paper "The interaction between volcanic gases and tephra: Fluorine adhering to tephra of the 1970 Hekla eruption" (Óskarsson 1980), highlighting the fluorine-rich nature of Hekla degassing. Óskarsson evidenced that a large quantity of fluorine from the volcanic gas was adsorbed by fine-grained tephra, subsequently causing fluorosis in grass-eating sheep (Sigurdsson and Pálsson, 1957). Such high rate of fluorine emissions was later shown to liberate several heavy metals from the basaltic andesite magma of Hekla in 2000 by Moune et al. (2006) using the trace element composition of snow fallen through the eruption plume and laboratory leaching experiments. The atmospheric loading of S, Cl and F for the same 2000 Hekla eruption was estimated by Moune et al. (2007) using MI from the product of the eruption and more primitive lava from the 1913 eruption. Results of the study revealed the sulphur dominance over halogens but confirmed that high fluorine concentration was released (0.6–3.8 Mt of SO_2, 0.17 Mt of HF and 0.05–0.1 Mt of HCl).

In March 2010, the Eyjafjallajökull eruption started as basaltic lava fountaining in Fimmvöruháls, offering another opportunity to study Icelandic volcanic gas composition. Ilyinskaya et al. (2012) collected several times the gas emitted from this basaltic lava fountaining, revealing a somewhat halogen-rich composition with high temporal variability (SO_2/HCl = 0.1-10). The authors also investigated the aerosol formation and identified that a cold environment favours chloride over sulphide condensation. Following the Eyjafjallajökull eruption, increased attention was set on gas plumes. The 2011 sub-glacial eruption of Grímsvötn was the opportunity to compare the satellite detection and the petrological methods regarding SO_2 discharge (Sigmarsson et al. 2013). The authors obtained much higher values using the petrological method (1.47 ± 0.37 Tg) than satellite measurements (0.31 Tg), attributed to formation of immiscible sulphide phases, adsorption on tephra and dissolution in the lake.

Finally, the basaltic fissure eruption of Holuhraun in 2014-2015 offered a unique opportunity to collect the grounded gas-plume (Fig. 1.21), including the aerosols emitted. Gauthier et al. (2016) conducted such sampling, revealing major volatile composition and trace element pattern similar to rift (Erta Ale) and hotspot (Kīlauea volcano), highlighting the tectonic

control volcanic on gas composition. Environmental impact of this eruption (the largest in Iceland since Laki eruption in 1783) was also assessed by Stefánsson et al. (2017), Ilyinskaya et al. (2017) and Pfeffer et al. (2018) revealing country wide impact on air and water quality. The total sulphur discharge was also estimated using satellite measurements, ground-based measurements and petrological method, all obtaining similar results, of the order of 10 Tg of SO_2 (Gauthier et al. 2016; Pfeffer et al. 2018; Bali et al. 2018). Lack of CO_2 in the primary gas collected there leaned the authors to suggest that carbon dioxide escaped prior to the eruption, potentially around the Barðabunga central volcano (Gauthier et al. 2016; Bali et al. 2018; Sigmarsson et al. 2020).

Figure 1.21. Photos of the Barðabunga eruption and associated degassing, during which extensive monitoring and study of the gas emissions were conducted*. Left: photo from Ilyinskaya et al. (2017) showing the intense gas emissions around the eruptive crater in January 2015. Photo from Pfeffer et al. (2018) illustrating the monitoring conditions at the eruption site.*

Over the past few decades, significant progress has been made in characterising the volcanic degassing in Iceland. However, non-eruptive degassing however remains much less constrained. While inter-eruptive vent degassing is generally negligible in Iceland (with magmatic heat and gas primarily feeding hydrothermal systems), this is not the case of the post-eruptive lava degassing (Thordarson et al. 1996, 2001). Since the composition of gases can differ markedly from those released during eruptions (Sigmarsson et al. 2020), addressing this knowledge gap is crucial. This thesis aims to investigate this subject, examining the current gas emissions on the Reykjanes peninsula along with degassing structures from emplaced lava fields (segregations).

Overall, the research conducted during my PhD and presented in this thesis aim to address the pending questions regarding lava degassing. The main associated research questions, highlighted by the gaps in knowledge described in this chapter, are: How does the gas emitted by the crystallising lava differ from emission at the associated eruptive crater? What explains the main compositional difference between the crystallising lava gas and the primary gas or other secondary gases? How does a stagnant and cooling lava actually degas? What is the role of the gas phase during the segregation process, and can it result in lava degassing? How do the halogens F and Cl affect the liberation of volatile trace elements? How heterogeneous is lava in terms of F and Cl content and is it affected by fractional crystallisation, degassing and/or magma source heterogeneity?

The aim of this thesis is to address these questions and give comprehensive overview of the lava degassing process, from its origin to its potential consequences. In that objective, three

distinct axes were followed, corresponding to the Chapters 3, 4 and 5 of this work. The first one is the investigation of the post-eruptive degassing, focusing on the crystallising lava emissions and its comparison with the degassing taking place at the eruptive crater. The second one is the detailed characterisation of the segregation process and associated structures in several basaltic lavas, with a special emphasis on volatile species behaviour. The last one is the characterisation of Cl and F concentration heterogeneity and its origin within Reykjanes volcanic products, and potential implications. Taken together, these results should help us understanding how important it is to consider the lava differentiation though segregation formation, and subsequent halogen-rich degassing.

2 Fieldwork and methods

Studying the origin, process and the characteristics of lava degassing requires the use of different types of data. To study the system comprehensively, it is essential to sample both volcanic gas and solidified lava flow, along with its internal structure. The composition of these samples in terms of major and trace elements, as well as volatiles, must thus be measured. This chapter provides a detailed description of the sampling sites and the methods used for sample collection, processing, and analysis conducted during the PhD research.

2.1 Sampling sites

2.1.1 Fagradalsfjall eruptions

The volcanic gas sampling campaign was conducted at the Fagradalsfjall volcanic system, where the first eruptive activity on the Reykjanes peninsula was reported since ca. 1240 CE. Unlike the other volcanic systems of the peninsula, Fagradalsfjall was quiescent in the last millennia, with no identified eruption in the last 5 ka (Sæmundsson et al. 2020). In 2021, after a year of ground inflation and seismic swarms (Sigmundsson et al. 2022), a basaltic eruption started on March 19th 2021 in the Geldingadalir valley.

The 2021 eruption and its chronology were described in detail by Pedersen et al. (2022), Barsotti et al. (2023) and Júlíusdóttir et al. (2024) and were reported live on the webpage of the Institute of Earth Sciences of the University of Iceland (https://jardvis.hi.is). The first two weeks of the eruption (Phase I; Fig. 2.1a) were quite constant with emission of around 5 m^3/s of lava from a short fissure (Pedersen et al. 2022). Phase II of the eruption spanned over April and consisted of a series of fissure opening and crater formation with magma extruded alternatively from one vent to the other. The extrusion rate over phase II was similar to phase I. At the end of April, the activity focused on what would become the main crater, thus initiating phase III (Fig. 2.1b). After a few days of sustained activity, a pulsating phase started, with few minutes of quiescent followed by intense fountaining activity (up to over 200 m). Such change in eruption dynamics was associated with increased average extrusion rate (9-13 m^3/s). In late June, the eruption activity changed again, entering phase IV (Fig. 2.1c), which was characterised by much longer cycles of fountaining and pauses (from a few hours to over a day) with similar extrusion rate than phase III. In September 2021, the activity stopped for nine days before reawakening for a week until September 18th, when the last lava emission was reported. The total volume of lava extruded over the entire eruption was measured around 0.15 km^3, covering an area of 4.9 km^2 with a thickness above 100 m around the crater (Júlíusdóttir et al. 2024).

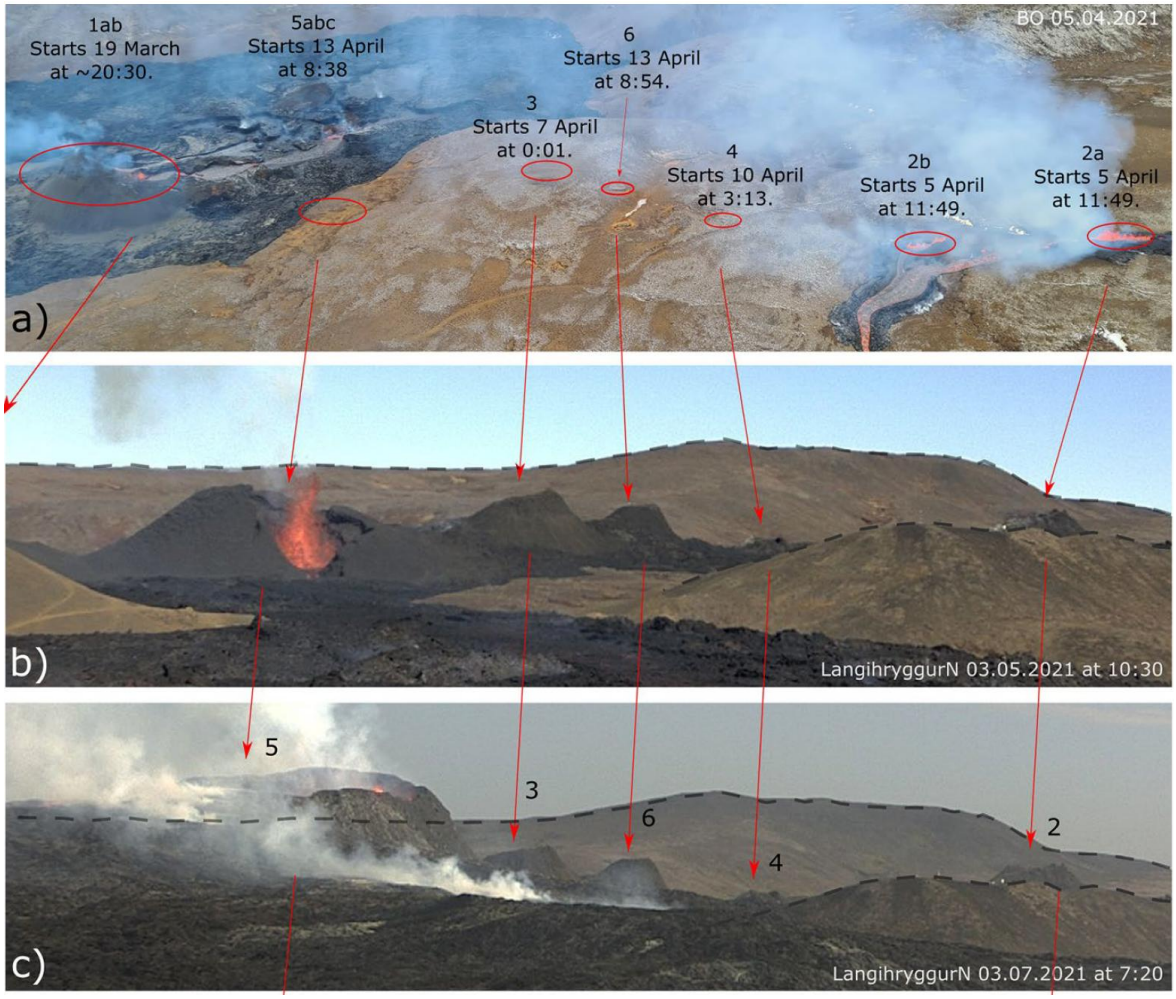

Figure 2.1. First stages of the Geldingadalir eruption and its crater row*. The different panels show the development between (a) April 5th, (b) May 3rd and (c) July 3rd, 2021. Picture modified from Barsotti et al. (2023).*

In late December 2021 a new dyke intrusion occurred beneath Fagradalsfjall, but stopped at shallow depth without erupting (Parks et al. 2023). The system then remained quiescent until the next summer, when a new dyke intrusion started on July 30th, 2022. After three days of intense seismicity, the dyke reached the surface on August 3rd in the Meradalir valley (one km NE of Geldingadalir), resulting in a fissure eruption (Fig 1.19). The first day of eruption was quite intense with extrusion rate of over 30 m^3/s erupted from a several hundred meters long fissure (Parks et al. 2023). The activity then exponentially decreased until the end of the eruption on 21 August. Eleven months with no eruptive activity followed the Meradalir eruption, until a new dyke propagated in early July 2023. The dyke erupted on July 11th, forming a 800 m long fissure about 2 km NE of the previous eruption, besides the Litli Hrútur hill (Júlíusdóttir et al. 2024). As what happened in 2022, this eruption started by an intense phase with over 50 m^3/s of effusion rate before gradually decreasing and concentrating on a single vent. By the beginning of August, the effusion rate had dropped below 1 m^3/s and the eruption stopped a couple of days later on August 5th. As of August 2025, no detected dyke intrusion occurred in the Fagradalsfjall system since the Litli Hrútur eruption.

As the eruptions were ongoing, a large and locally very thick lava field formed. The average lava thickness was measured 30 meters for the 2021 Geldingadalir eruption and ca. 10 meters

for the 2022 and 2023 eruptions (Júlíusdóttir et al. 2024). Locally, thicker lava emplaced, reaching over 100 meters in the Geldingadalur former valley (Pedersen et al. 2022), as shown on figure 2.2. Such lava accumulation slowly cools down and crystallises, initiating a post-eruptive degassing. The crystallising lava gas emissions lasts for a duration that directly depends on the lava thickness (Hon et al. 1994), which can go on for decades when lava thickness is of several tens of meters.

Figure 2.2. Geldingadalir former valley filled with a thick and degassing lava field and the 2021 main eruptive vent. *Photo from March 2022.*

2.1.2 Fagradalsfjall gas sampling

The sampling campaign of syn-eruptive and post-eruptive volcanic gas from Fagradalsfjall spanned from 2021 to 2023, with variable success. Two types of volatiles (Cf. section 1.1.1) were the target of this sampling campaign: the major reactive species (S, Cl and F) present in significant amount in the gas (generally > 0.1 %) and the aerosols/particulate matter made of elements generally present in trace amount (ppts to ppms weight). To collect the reactive species, paper (cellulose) filters impregnated with a base were used. The paper filters used were either Whatman® 47 mm or Millipore® 37 mm diameter. Before going on the field, these filters were put for a minute in a base solution (either $NaHCO_3$ or NaOH) containing 10 % glycerol. The based used was $NaHCO_3$ during the 2021 and 2022 sampling which was replaced for practical reasons by NaOH in 2023 with no visible effect on the results. Aerosols were collected on PTFE membrane filters. The PTFE filters used were Sterlitech® (laminated, 1 µm pore size and unlaminated, 0.2 µm pore size) and Millipore® (unlaminated; 1 µm pore size) 47-mm diameter filters.

Different sampling setups were employed over the sampling campaign (Fig. 2.3), combining an 83 L/min Dustbuster® pump and a SKC® 11 L/min pump. Initially, 47 mm diameter filter packs were used with a series of two or three paper filters set up in a row followed or not by a PTFE filter connected to the Dustbuster® pump. Analyses of the paper filters

revealed similar S, Cl and F concentrations in the three filters, though saturation was not reached (relatively low concentrations). Such results were related to potentially too high pumping rate, and thus PTFE and paper filters were separated to use different pumps. Consequently, different concentrations were obtained in the three filters, decreasing from first to last. While aerosols were still sampled at 83 L/min, reactive major gases were collected simultaneously but separately, connected to the SKC® 11 L/min pump and using the Millipore® 37 mm filters. Typical sampling time was 30 minutes, resulting in collection of 2.5 m^3 of gas/air mixture (0.33 m^3 when the 11 L/min pump was used).

Figure 2.3. Photos of post-eruptive lava gas sampling showing the two set ups used. *(a) One filter pack made of both PTFE laminated filters for aerosol collection and base impregnated filters, connected to the 83 L/min Dustbuster® pump. The photo corresponds to the sample GD-2, collected on a lava channel, 1 km SSW of the main 2021 eruptive vent. (b) Two separated filter packs touching each other and connected by tape to collect very similar gas. The laminated filter is connected to the 83 L/min Dustbuster® pump whereas the base impregnated filters are connected to the SKC® 11 L/min pump. The photo corresponds to the sample MD-8, collected on the Meradalir lava field, 100 m N of the main 2022 eruptive vent.*

The sampling campaign started seven weeks after the end of the Geldingadalur eruption, in November 2021 (Fig. 2.4, Table 3.1). On November 11, we collected the reactive gas emitted from the former lava lake west of the crater (GD-1; Fig. 2.5a) and from a lava channel south of the same crater (GD-2, Fig. 2.5b). Gas was sampled from the same lava channel a week later (GD-3), which then included particulate matter collection. On November 24, two additional gas samples were collected, on the rim of the extinct crater (GD-4, Fig. 2.5d) and at its foot (GD-5; only reactive volatiles; Fig. 2.5c). The next year, on March 1, gas was sampled again from the lava channel (GD-6) and the crater foot (GD-7). In July, new sampling of the extinct crater gas emissions (GD-9) and the lava degassing at its foot (GD-8) were conducted.

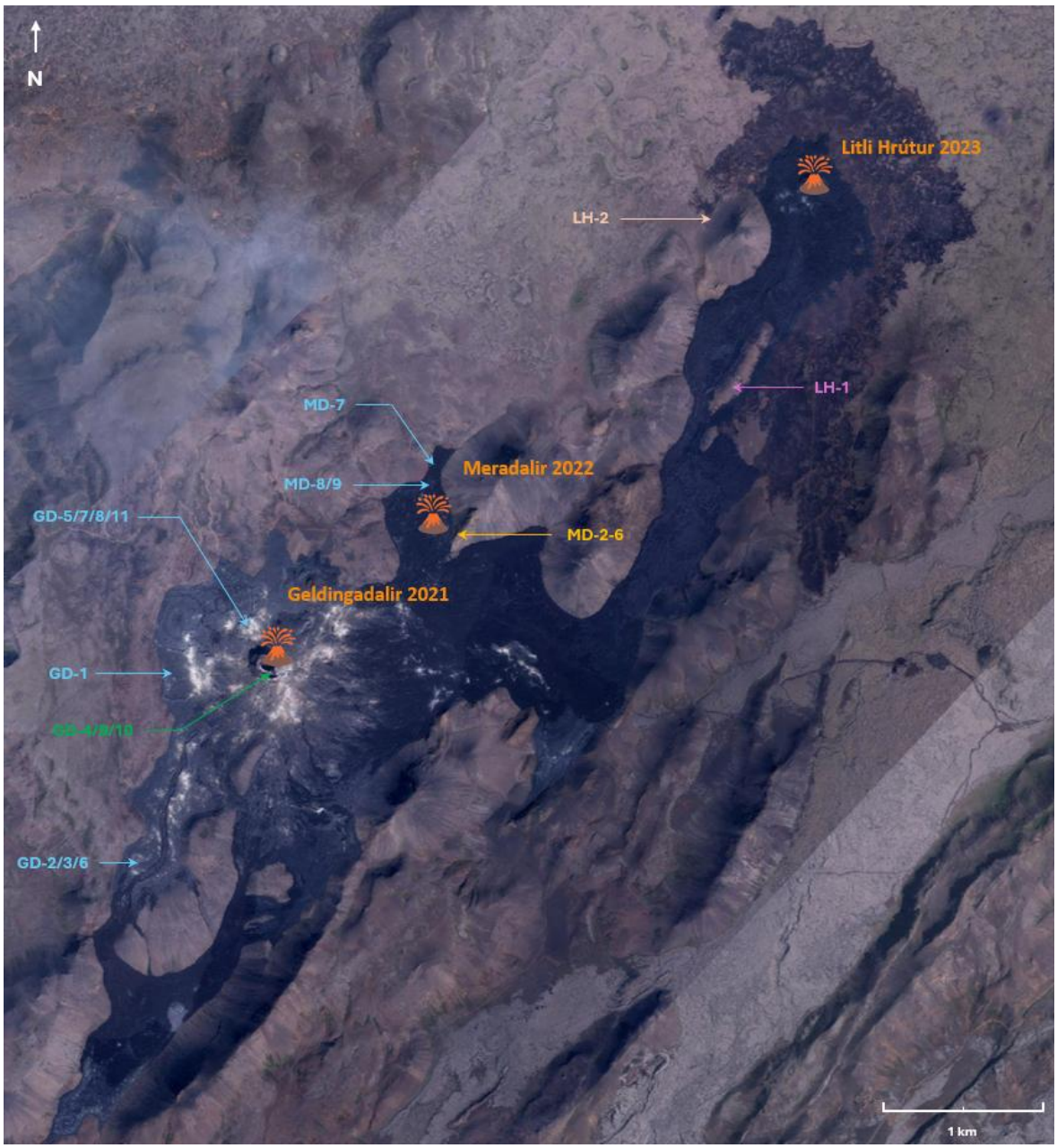

Figure 2.4. Gas sampling locations on a satellite photo of the Fagradalsfjall lava field. *In blue are indicated the post-eruptive lava sample locations, in green the post-eruptive crater one, in yellow the syn-eruptive crater one, pink syn-eruptive lava and beige burning moss.*

The Meradalir eruption in August 2022 offered a great opportunity to sample the syn-eruptive gas from the crater. The crater being located in a valley, its gas emissions were often blown on the surrounding hills, allowing optimal gas collection. Five samples (MD-2 to MD-6; Fig. 2.5e) were thus collected there while the eruption was ongoing. One and two months later, on September and October 2022, gas was sampled from the crystallising lava, roughly 100 m from the Meradalir crater (MD-7 and MD-8; Fig. 2.5f). In March 2023, three post-eruptive gas samples were collected: one from the Meradalir lava at the same location as MD-8 (MD-9), one at the cooling Geldingadalir crater (GD-10) and one at its foot (GD-11).

Figure 2.5. Photos of the Geldingadalir (2021) and Meradalir (2022) sampling sites where syn- and post-eruptive gas was collected. *(a) correspond to where GD-1 was collected, (b) GD-2 and 3, (c) GD-5, GD-7, GD-8 and GD-11, (d) GD-4, GD-9 and GD-10, (e) MD-2 to MD-6, (f) MD-7 to MD-9.*

In summer 2023, the Litli Hrútur eruption revealed itself more complex for gas sampling because of the flatness of the area (apart from the Litli Hrútur hill itself) and unfavourable wind direction. One flowing lava (syn-eruptive lava) gas sampled was however collected (LH-1) along with the smoke from the extensive moss fire (LH-2). Analyses from both Litli Hrútur samples were however not used in this thesis. The syn-eruptive lava LH-1 displayed concentrations close to blank for the vast majority of volatiles, preventing characterisation of the gas composition. LH-2 on the other hand displayed significant concentrations in many

elements, but most of them are not volatile whereas volatile elements were present in low concentration.

Over the whole sampling period (2021-2023), three background air samples were collected on the Reykjanes Peninsula, five kilometres east of the eruption sites while no eruption was ongoing. The sampled background air was collected in altitude (> 100 m, just like the volcanic gas) resulting in minimal sea aerosol influence, on an old lava field to have similar potential dust component as the real gas samples.

2.1.3 Lava and segregation sampling

In 2021 and 2022, solidified lava fields and segregations from Reykjanes, Eldgjá, Hekla, Laki and Þjórsá were sampled. The studied material was extracted from outcrops or boulders using a hammer and a chisel. The host lava was collected in the vicinity of a segregation but not directly adjacent to avoid potential local compositional gradient.

In September 2021, a sampling campaign was conducted at Laki and Þjórsá to look for segregations. At Þjórsá, a few segregations and associated lava were collected on a cliff along the bank of the Þjórsá river (63°55'53"N 20°39'11"W, Fig. 2.6). No exploitable sample could however be analysed, as the segregations were small, weathered and often mixed with host lava. Laki segregations were sampled around the fissure (64°01'53"N 18°18'57"W) and at the distal flow, 20 km SE of the crater row (63°53'55"N 17°44'10"W). Only one segregation sample from Laki was found analysable but measurements displayed inconsistent composition and were not further considered.

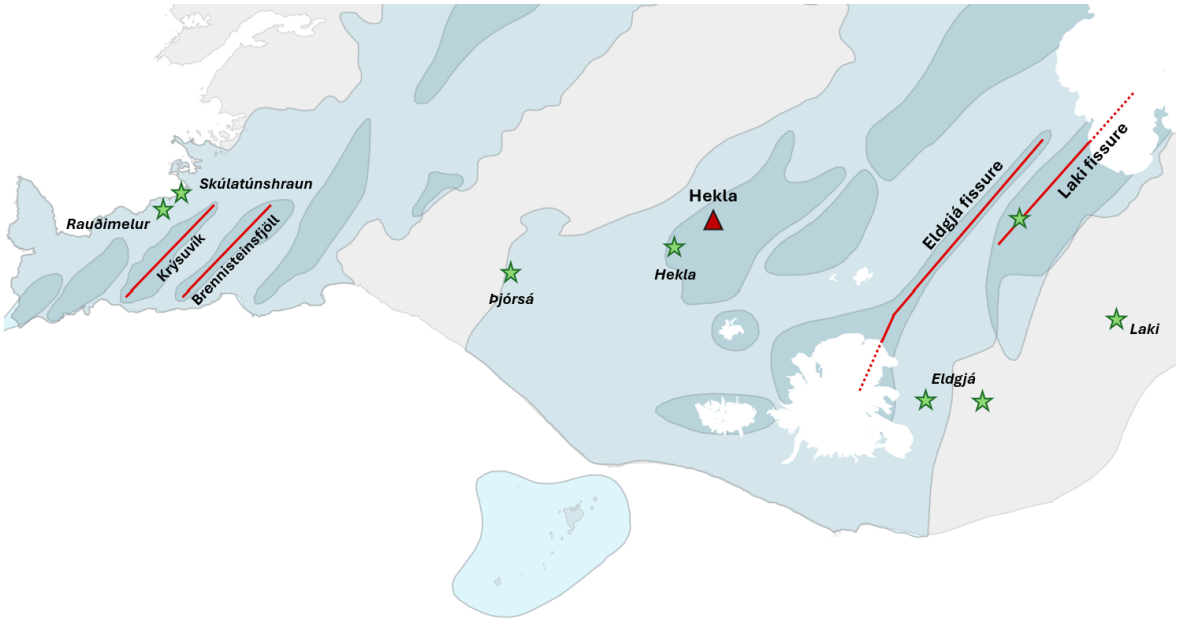

Figure 2.6. Lava and segregation sampling sites (green stars) and associated volcanic system/eruption (red line/triangle).

To collect better quality samples, the site of the Rauðimelur quarry, on the Reykjanes peninsula, was selected since it is known to host numerous segregations in an olivine tholeiitic lava (64°2'2"N, 22°3'53"W; Martin and Sigmarsson, 2005). This lava field originates from the 5-6 ka old Hrútagjá shield volcano associated with the Krýsuvík system

(https://www.visitreykjanes.is; https://ferlir.is). From a four to six meters high outcrop were extracted in September 2021 and June 2022 numerous segregations of different nature along with the host lava. Most segregations were directly extracted from the outcrop (Fig. 2.7), whereas a few came from boulders on the ground. These rock samples, complemented by two others collected by Martin and Sigmarsson (2005), are examined in this thesis.

The neighbouring Skúlatúnshraun lava field was also examined for segregation material in June 2022. Located a few km East of Rauðimelur (64°3'19"N, 22°0'9"), Skúlatúnshraun is 2.5 ka old and originated from the Brennisteinsfjöll volcanic system (Sigurgeirsson and Þorbergsson, 2021). Two segregations and their host lava were collected along a cycling path, from a three meters high outcrop.

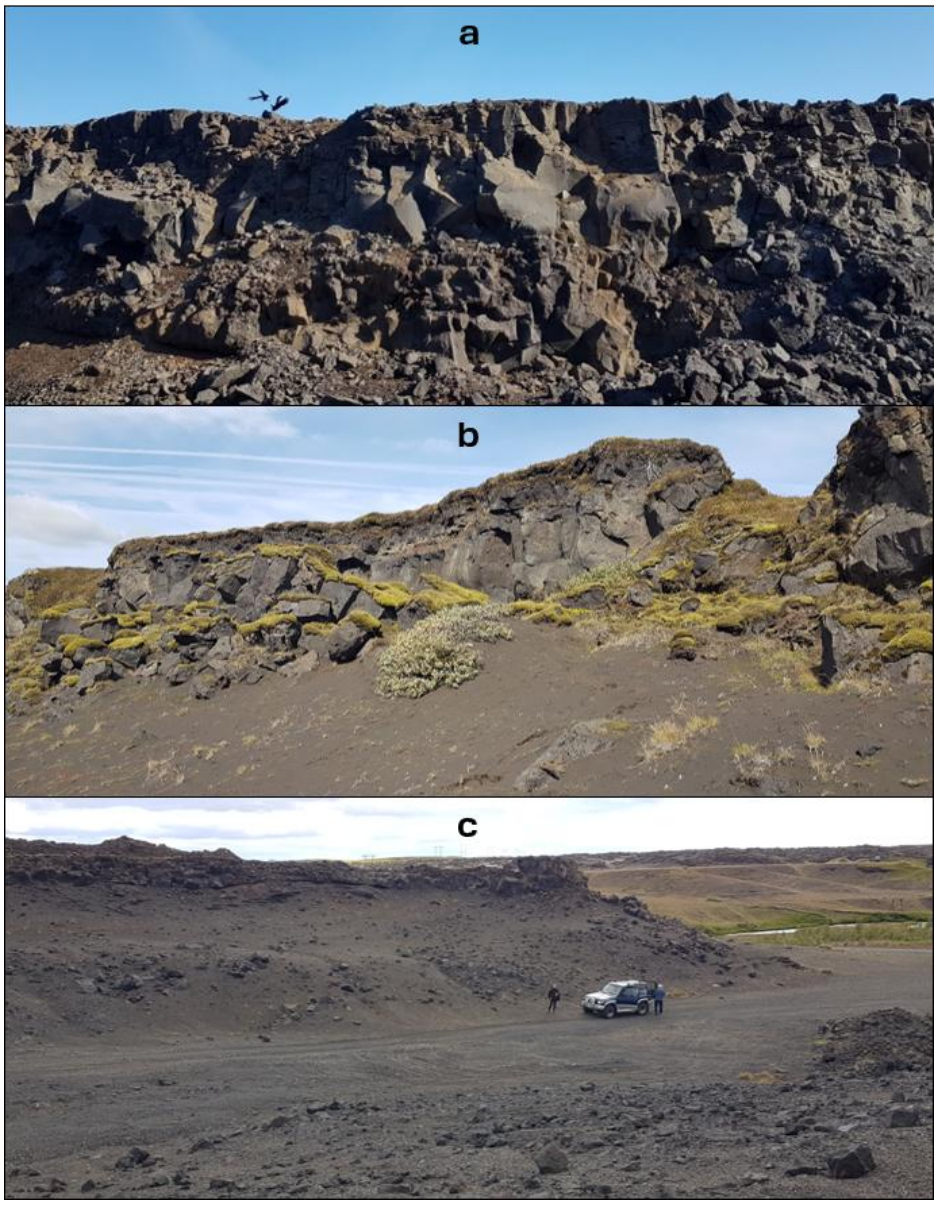

Figure 2.7. Main outcrop hosting the segregations sampled and studies in this thesis. *(a) outcrop in the Rauðimelur quarry (b) outcrop of the Eldgjá lava, next to the Hólmsá river (c) outcrop of an early Holocene Hekla basalt lava.*

In addition to the tholeiitic-dominated Reykjanes peninsula, material was collected from volcanic systems of the Eastern Volcanic Zone, emitting basalt of transitional alkali composition (Jakobsson 1979). In this volcanic region, host lava and segregation sampling was conducted from the 844 km^2 historical Eldgjá (939 AD) lava field (Sigurdardottir et al. 2015). The lava field is made of two main branches, the eastern one being partly buried under the more recent Laki lava (1783-1784 AD). In August 2022, Segregation and host lava were collected from two locations from the southwestern branch of Eldgjá. At the first site, the Kriki formation a few km NE of Kötlujökull, one vesicle cylinders and its surrounding host lava were collected from a boulder (63°38'43"N 18°43'39"W). The other Eldgjá segregations and associated host lava were extracted from a several meters thick outcrop close to the Hólmsá river, 20 km East of Mýrdalsjökull (63°37'54"N, 18°29'38"W).

Finally, an early Holocene basalt lava of Hekla volcanic system was examined. In August 2022, segregations and host lava were collected from a quarry roughly 15 km SW of Hekla central volcano (63°57'27"N, 20°0'57"W), where a small lava field is well exposed. This Holocene lava (4 – 12 ka; Jakobsson 1979) does not originates from the Hekla ridge itself but rather from a small basaltic crater, also belonging to the Hekla system. In this quarry, numerous boulders with abundant and clear segregations are present. Thus, all segregations from Hekla except the horizontal vesicle sheet (H-HVS) were extracted from boulders.

2.2 Analytical methods for gas samples

2.2.1 Major reactive volatiles

After volcanic gas collection, filter packs were set in a clean plastic bag until returning in the laboratory. The proximity of the studied area to the laboratory (Institute of Earth Sciences, IES, University of Iceland, Reykjavik) allowed processing of the filters in the hours following sampling. The paper filters were transversed individually from the filter pack to 120 mL clean Savillex® beakers using Teflon tweezers and approximately 20 mL of Milli-Q water was added. The paper filters were then left at least a day on a vibrating table to allow complete leaching of the collected acidic species (SO_2, HCl and HF) in the water. A couple of hours before the analysis, 1-2 drops of hydrogen peroxide were added to oxidize any sulphide into sulphate and allow simple quantification of sulphur concentration. When a large quantity of gas was collected on the field (generally during syn-eruptive sampling), a 1:10 or 1:20 dilution of the leachate from the first filter was conducted before measurements to avoid having element concentration (especially SO^{4-}) above quantification limit. Additionally, before each run of analysis, leachate of background air and/or blank filters were also prepared.

Before completing Ion Chromatography, 0.7 mL of each leachate (or diluted leachate) were aliquoted into a vial. Along with the samples were prepared vials of in-house standards ranging from 0.025 to 10 ppm F^- and 0.5 to 200 ppm Cl^- and SO^{4-} for calibration, with the 1 ppm F^- / 20 ppm Cl^- and SO^{4-} standard being measured repeatedly and used to monitor instrumental drift. Pure Milli-Q water vials were also analysed to avoid memory effect after high concentration samples measurement and to measure the background noise. The content of all vials was then inserted in the Thermo Dionex® 2000 Ion Chromatography (Fig. 2.8a). As a result of the different retention time of each species, the chromatogram showed

distinctive F^-, Cl^- and SO^{4-} peaks (in this order). No bromine peak could be seen suggesting low Br^- concentration.

Figure 2.8. Instruments used for analyses of the volcanic gas and rock (lava and segregation) samples. *The volcanic gas was analysed by (a) Thermo Dionex® 2000 Ion Chromatography (IES) for the S, Cl and F concentrations and (b) Agilent® 7500 ICP-MS (LMV) for trace element concentrations. The lava and segregation mineralogical composition was analysed in-situ by (c) Electron probe microanalyzer (IES and LMV) for the major elements and (d) LA-ICP-MS for the trace elements (LMV). The whole-rock composition of lava and segregation was measured using (e) an ICP-OES (IES) for the major elements and (b) an Agilent® 7500 (LMV) for trace element concentrations.*

As expected, the leachate from the first filter of each sample generally displayed much higher values than the subsequent filters. In the least concentrated gas samples, the second and third filters displayed concentrations similar to the blank filter leachate. Due to significant air dilution, most post-eruptive gas samples displayed lower volatile concentration than the syn-eruptive gas. Thus, a few samples had all three filter leachates displaying F^-, Cl^- and/or SO^{4-} undistinguishable from blank, translating very low volatile concentrations. Such results are particularly true in the case of sulphur, often not significantly present in the post-eruptive gas. Additionally, because of glycerol interference, fluorine measurements had higher

quantification limit. Thus, a few gas samples have detectable fluorine concentration but too low to be quantified.

When filter leachate concentration was significantly above the corresponding blank filter, the concentration of sulphur, chlorine and fluorine was obtained by subtracting the concentration measured in the blank filter from that of the gas filters. Gas concentration was retrieved by adding together the concentrations of the three filters. Leachate concentration was converted into absolute leachate content, and the air concentration was then calculated using the sampled volume.

2.2.2 Trace elements

After sampling, the PTFE filters were set up in a clean Teflon beaker and left in a hood. They were then transported to a cleanroom at the Laboatory Magmas and Volcanoes (LMV) where they would be prepared and analysed. Once in the clean laboratory, approximately five or ten grams of diluted acid mixture (0.4 M HNO_3 and 0.05 M HF) were put on the filter. The closed beaker was then left for several weeks on a hot plate at warm temperature (80-90 °C) to extract the trace elements from the filter.

An aliquot of each solution was then analysed by a quadrupole Inductively Coupled Plasma Mass Spectrometry (ICP-MS), either the Agilent 7500 or Agilent 8900 (Fig. 2.8b). Sixty-one elements were analysed: Li, Be, B, Sc, Ti, V, Cr, Mn, Fe, Ni, Co, Ni, Cu, Zn, Ga, Ge, As, Se, Rb, Sr, Y, Zr, Nb, Mo, Ru, Rh, Pd, Ag, Cd, In, Sn, Sb, Te, Cs, Ba, La, Ce, Pr, Nd, Sm, Eu, Tb, Gd, Dy, Ho, Er, Tm, Yb, Lu, Hf, Ta, W, Re, Ir, Pt, Au, Tl, Pb, Bi, Th, U. The reaction cell in Helium mode was used to reduce interferences for elements having atomic masses ranging from Sc to As. Instrument calibration was done using two synthetic standards containing 1 and 10 ppb of all analysed trace elements, except Ru, Rh, Pd, Te, Re, Ir, Pt and Au, about four times less concentrated.

Reproducibility and signal ratios were calculated for each set of analyses. For each element, the measurement precision was inferred from the relative standard deviation (RSD) obtained from repeated measurement of the same sample (reproducibility). For the November 2022 analyses (session during which to largest set of leachates were analysed), the reproducibility on the 1 ppm standard is found better 10 % for all elements apart from B and Ti whereas on the blank solution higher variability are found but always below 30 % except for Ga (36 %) and Mo (62 %). Signal ratio between the 10 and 1 ppb standards allows to check measurement quality. Most elements show ratios close to 10 (± 0.5), whereas V, Cr, Fe, Zr, Pd, Pt, Au has ratios between 7 and 9.5 or 10.5 and 13. In contrast, Li, B, Ti, Mn, Sr and Ba had signal ratio far from 10 (< 7 or > 13), translating poor quantification.

The quality of the measurement and calibration was also verified by converting the signal measured in rock standards (BHVO-2, BEN and BIR-1) to element concentration using the artificial standards. Comparing the obtained BHVO-2 composition with the known values reveal good quantification for most elements. The only elements that are poorly quantified in BHVO-2 are B, Ge, Ag, Te, Re, Pt and Tl (measured concentrations 2-10 times the literature values) and Ru, Pd, Rh, Ir and Au (measured concentrations over 10 times the literature values). The vast majority of these elements have measured signal in BHVO-2 similar to blank, explaining their poor accuracy.

2.3 Analytical method for rock samples

2.3.1 Sample preparation

The segregations and host lavas directly extracted from the outcrops were put in clean plastic bags. Boulders containing segregations were brought back to the IES (Fig. 2.9). When needed, a saw was used to expose the segregation material and facilitate its extraction (Fig. 2.9c). The segregation material was carefully examined, and grains were handpicked making sure to exclude host lava and contaminated material. Once the selection was done, the samples were cleaned three times for ten minutes in distilled water in an ultrasonic bath. The clean samples were then powdered using agate grinding mill or an agate mortar (when less than 10 grams were available). Agate was used to avoid trace metal contamination of the powders. The mortar/grinding mill were pre-contaminated with the sample before powdering to minimise potential cross contamination, and the material was carefully cleaned between each sample. In addition to powder, thin section or epoxy mounts were also made for several samples.

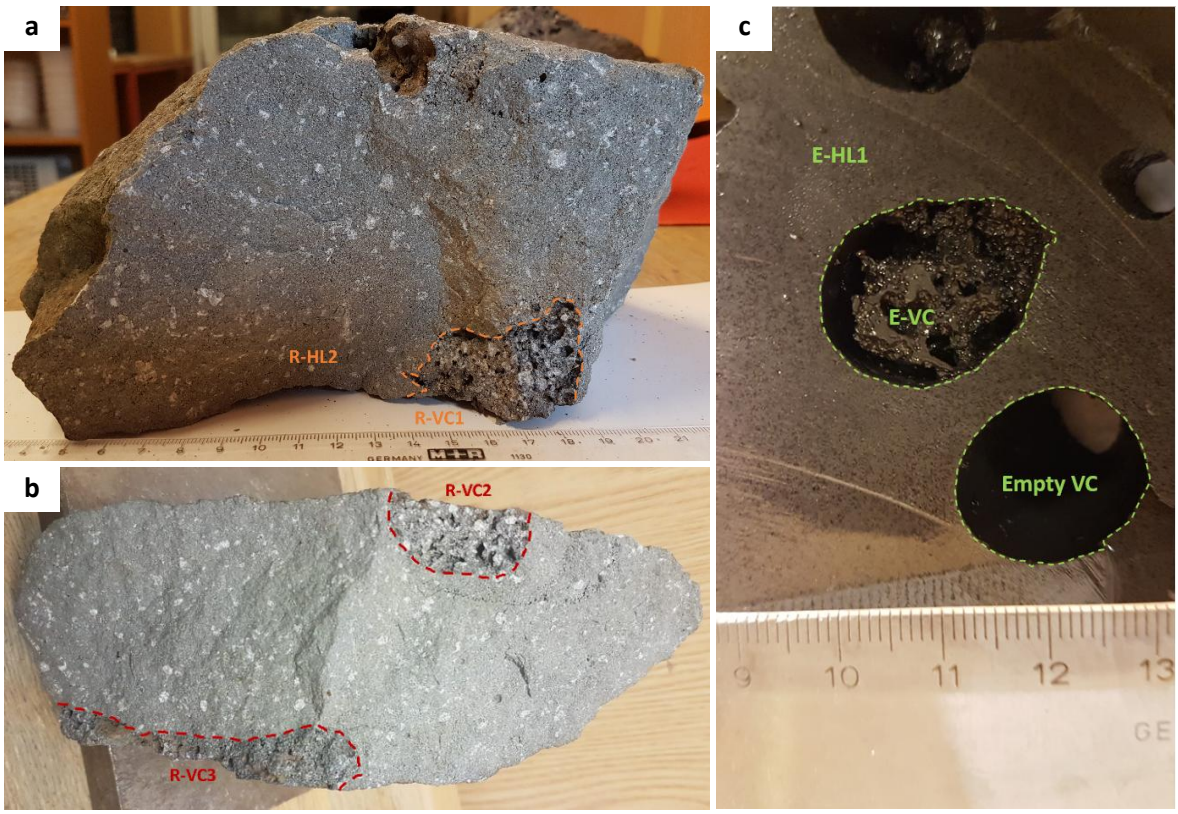

Figure 2.9. Photos of boulders from Rauðimelur (a and b) and Eldgjá (c) presenting several vesicle cylinders (sometimes empty) surrounded by host lava. *The diameters of the VC are typically a couple of cm. The segregation material from these VC was collected using a small chisel before handpicking the grains.*

2.3.2 Mineralogical analyses

The petrology of five samples from Rauðimelur (R-HL2, R-VC1, R-VC2, R-VC3 and R-MV1) and one Eldgjá sample (E-VC) were analysed in detail. Thin sections were made with the samples R-HL2, R-VC2, R-VC3 whereas grains from R-VC1, R-MV1 and E-VC were set up on epoxy mounts. The thin sections/epoxy mounts were first examined by optical microscopy and then secondary electron microscope (SEM; Fig. 2.8c). Numerous pictures were taken, allowing to characterise the petrography of each sample (size and shape of minerals, phase proportion and vesicularity).

The phase composition of the epoxy mount samples was then analysed in January 2022 by electron probe microanalyzer (EPMA) at the LMV whereas the thin sections were analysed at the IES in June 2022. In both cases, an accelerating voltage of 15 kV and a current of 15 nA were used. Beam width varied between five and ten µm. Generally, a larger beam was used to measure the micrographic texture composition since such texture presented heterogeneous small-scale features. Acquisition time varied depending on mineral and program used but was always of the order of minutes. To calibrate the microprobe, three standards were used, either natural minerals of similar composition (at IES) or synthetic crystals (at LMV). Each mineral was analysed using a different program (defining which oxides concentrations are measured) and calibration standards. The raw data were corrected by the ZAF procedure (accounting for the effect of atomic number, absorption and fluorescence excitation; Armstrong 1991).

The segregations R-VC1, R-MV1 and E-VC were also examined for trace element concentrations in the different phases. This was done by laser ablation (LA-ICP-MS; Fig. 2.8d) at the LMV during which the concentration in 23 elements was measured: Li, Al, Ca, Sc, V, Cr, Fe, Ni, Cu, Zn, As, Se, Rb, Sr, Y, Zr, Cd, Sn, Ba, Ce, Pb, Bi and Th. All elements appeared above detection limit at least once. The beam of the laser ranged from 40 to 60 µm in width, limiting the analyses to the largest phase. To quantify the element concentrations, an internal standard was used: Ca for the plagioclases, clinopyroxenes and micrographic texture and Fe for olivines and oxides. The calibration was made based on the concentration in these elements measured in each phase by EPMA analysis. Because the micrographic texture presented the most heterogeneous composition, including in Ca (and Fe), there is significant uncertainty on the conversion factor of the order of 50 % (< 10 % for the other phases).

2.3.3 Whole-rock analyses

Rock samples (segregations and host lavas) were analysed for major, trace and volatile element concentrations. The method described below corresponds to the analyses I conducted for the segregations and lavas. The same analyses of major and trace elements concentrations were conducted on Fagradalsfjall lavas at the same laboratories, but by other members of the ISE. The segregations and host lavas major element concentrations were measured by Inductively Coupled Plasma Optical Emission Spectroscopy (ICP-OES) at the IES. In a carbon crucible, 100 mg of the sample and standard powder were put and mixed with 250 mg of lithium borate ($LiBO_2$). The mixture was then set in a furnace at 1000 °C for a couple of hours to dissolve the sample powder. After allowing the molten mixture to cool, it was transferred into 50 mL of a diluted nitric solution (5 % HNO_3, 1.33 % HCl and 1.33

% $C_2H_2O_4$). The solution was then analysed by the ICP-OES ThermoFisher® iCAP 7400 Duo (Fig. 2.8e).

Measurement reproducibility for three international basalt standards (BHVO-1, BIR-1 and W-2), of similar composition to our samples were used to estimate analytical precision. To calibrate the instrument accuracy, three Icelandic rock standards were used B-THO, A-THO and B-ALK. Lithium concentrations were used as an inner standard for each sample. The analysed oxides were SiO_2, TiO_2, Al_2O_3, FeO, MnO, MgO, CaO, Na_2O, K_2O and P_2O_5. Iron was analysed as a whole without distinguishing FeO and Fe_2O_3. The analyses giving a sum inferior to 97 % were assumed wrong and the samples were rerun.

The trace element concentrations of the rock samples were measured in solution using an ICP-MS Agilent 7500. In a clean room, 200 mg of ammonium bifluoride (NH_4HF_2) were weighted and put in a Savillexs® beaker, together with 50 to 60 mg of sample and standard powders. The mixtures were put in a furnace set up at 220 °C to allow full dissolution of the powder. After 24 hours, the furnace was cooled down to 20 °C allowing the sample to cool down before adding 1 mL of concentrated nitric acid (HNO_3 14 N) in the beaker, which was then closed and left for a day on a hot plate (80 °C). Following this, the beakers were opened and the plate set at 70 °C to allow total evaporation. A cycle of ricing and evaporation was then repeated three times to eliminate the fluorides. This was made by inserting 0.5 ml of HNO_3 14 M in the beaker, which was put on the plate at 70 °C for a few hours before opening the beaker and leaving it to evaporate at 100 °C.

Once the cycles completed, the beakers were cooled down and half-filled with HNO_3 7M and rinsed at 60 °C before transferring the solution into a vial. Such rinsing and transfer were performed three times. The beakers were then filled with deionised (DI) water, rinsed for a couple of hours and dried on the hot plate. From each vial of stock solution was taken 1.2 g (for samples) or 7 g (for standards) of rock equivalent with a 1 mL pipette and transferred to the previously dried beakers and once again put on the hot plate to allow complete evaporation. A last cycle of addition of diluted HF-HNO_3 solution (HNO_3 0.4 M/HF 0.05M), rinsing at 90 °C and transfer a new vial (dilute solution vial) was repeated three times. Diluted acid was then added to the diluted solution to obtain a dilution factor of 5000.

Aliquot of these diluted solutions were then made and run on the ICP-MS. The instrument calibration was done using the standard BHVO-2 whereas BIR-1 and BEN were used for analytical quality check (measurement accuracy). The measurement precision was calculated based on the reproducibility (the relative standard deviation) on BHVO-2.

During the November 2022 run (also the session with the most rock solutions analysed) B, Ru and Te had BHVO-2 concentration below detection limit whereas Li, Se, Re had concentration below quantification limit. In the standards BIR-1 and BEN, many element concentrations were below detection or quantification limit (B, Se, Mo, Ru, Rh, Te, Cs, Re, Ir, Au and Tl in Bir-1; B, Ru, Te and Re in BEN) while BEN has no reference concentration for Se, Ru, Rh, Pd, Ag, Te, Re, Ir, Pt, Au and Bi. Elements below quantification limits and/or with no reference values for both standards thus have unknown accuracies (B, Se, Ru, Rh, Te, Re, Ir and Au). All other elements have values within 30 % of what is recommended, except for Pd, Ag, Sb, W and Pt. In this thesis however, we are mostly interested in comparing the samples to each other, making the precision/reproducibility more critical than accuracy. In BHVO-2 and BEN, all elements above quantification limits have relative

standard deviation (RSD) below 10 %, whereas in BIR-1 As has RSD of 12 %, W 17 % and U 18 %.

2.3.4 Whole-rock volatile element measurements

Water and sulphur measurement

The major volatiles other than halogens of the rock samples were analysed by CHNS/S multielement analyser at the LMV. This instrument permits simultaneous measurements of carbon, hydrogen, nitrogen and sulphur in the rock samples. To do that, twenty to forty mg of dried powders were mixed with five to ten mg of vanadium oxide (V_2O_5) serving as a catalyst. The mixture was then combusted at very high temperature (1800 °C) under high purity oxygen. Through combustion, all volatiles were oxidised, carbon forming CO_2, hydrogen H_2O, sulphur SO_2 and nitrogen diverse oxides. The gas mixture (combustion products) was then transported by helium flow out of the combustion chamber and various absorbents were present to trap the undesirable species (such as hydrogen chloride and fluoride). The remaining gas then went through a gas chromatography column to separate the different species, before flowing to the thermal conductivity detector, where element concentration is quantified.

The instrument was calibrated with an organic analytical standard: 2,5-Bis (5-tertbutyl-benzoxazol-2-yl) thiophene of composition $C_{26}H_{26}N_2O_2S$. The measurement quality and eventual drift was assessed using repeated measurements of a reference soil material (BBOT standard, 72.5 % C, 7.4 % S and O, 6.5 % N and 6.1 % H) and acetic acid ($C_6H_8O_6$). Incoherent results were observed for carbon and nitrogen, showing either erratic or constant values, most likely related to air contamination. Only S and H concentrations are thus discussed in this thesis.

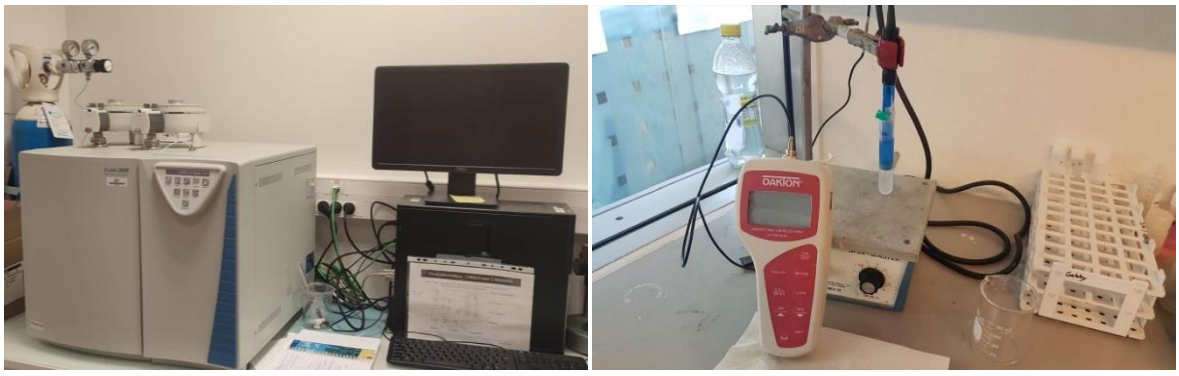

Figure 2.10. Instruments used for volatile concentration analyses in the rock samples. *(a) CHNS/S multielement analyser at the LMV to measure hydrogen and sulphur concentrations and. (b) Ion selective electrodes at the IES to measure the fluorine and chlorine concentrations.*

The precision of element concentration in the different powders was assessed by analysing each sample several times. Depending on the constancy of the results, each sample was analysed between two and six times to obtain the statistical error on element concentrations. The RSD was variable from one sample to another, primarily dependent on their volatile element concentration. Thus, the sample with the lowest S concentration had RSD (2σ) up to 67 % but lower than 5% for the most concentrated ones. Hydrogen, which is present in

larger concentration than sulphur had RSD ranging from 0 to 15 %. Carbon concentrations constantly display very high RSD (generally > 50 %), translating poor precision measurement and potential contamination.

Halogen extraction from rock powders

The fluoride and chloride whole rock measurements were conducted using Cole-Parmer® Ion Selective Electrodes (ISE). This technique was applied both on the segregations and host lava but also on numerous volcanic products from the new cycle of eruption on Reykjanes (samples from Matthews et al. 2024). The exact procedure was however different for the two datasets, the segregation/host lava analyses only yielding interpretable results for Fluorine whereas the method was affined to obtain satisfying measurements also for Cl for the new Reykjanes products. The Chapter 5 of this thesis is dedicated to the presentation of the tests regarding the ISE measurements conducted during the PhD and their main results to assess its reliability and precision of such measurement procedure. The procedure detailed below correspond to the one used initially, before the revisions described in Chapter 5.

The use of an ISE is based on the exchange of ions between the solution of interest and the reference solution through the electrode membrane. The electrode response is dependent on the ion exchange rate and thus on the ion concentration in the analysed solution. Before using the ISE, the halogens must be extracted of from the rock powders. Such extraction is based on the analytical preparation described in Stecher (1998) for F analysis. The sample preparation was made in two platinum crucibles, and samples were thus prepared by pairs. In each crucible, 0.5 g of rock powders were mixed with 3 g of 5:1 Na_2CO_3-ZnO mixture. One gram of Na_2CO_3-ZnO was then added to cover the crucible content. Since chlorine is generally a minor component of Na_2CO_3 such fondant needed to be as pure as possible. Both Na_2CO_3 and ZnO and were dried before being used. Once the mixture was covered, the platinum crucibles were then set in a furnace heated gradually (100°C every 20-30 mins) up to 950°C for 30-40 min and then cooled at room temperature.

To leach the cake (cooled sample-fondant mixture), 30 mL of DI water were added to the crucibles. A couple of clean ethanol drops were also added to avoid extracting chemicals affecting the leachate colour, which complicate the subsequent titration process. The crucibles are then left in the oven overnight at 80 °C for complete leaching. Following that, the crucibles were left to cool at room temperature and their content was filtered through a Whatman® filter into a polyethylene bottle. The residue was rinsed repeatedly with DI water and filtered in the bottle. The solution was then slowly acidified to pH 5 using concentrated HNO_3 in order to eliminate the CO_2. The use of a pH electrode revealed strong Cl contamination originating from the storing solution of the electrode (even if it is well cleaned) and thus avoided. The use of bromocresol green was thus favoured. Finally, DI water was added to make the solution 30, 50 or 100 mL.

Halogen measurements by Ion Selective Electrode

An Ion Selective Electrode is a sensor made of an indicator electrode and a reference electrode. The indicator electrode contains an ion selective membrane, through which only the targeted ion diffuses. This results in an ion concentration gradient across the membrane generating an electrochemical potential in the indicator electrode. Thus, once both electrodes are immerged into a solution, the potential difference between the two electrodes can be measured. This measured potential E obeys to the Nerst equation:

$$E = E_0 + \frac{2.303*R*T}{n*Fa} * log\ (a) \quad (2.1)$$

Where E_0 is the standard electrode potential (constant at a give temperature), R is the gas constant (8.314 J/K/mol), T the temperature (K), n is the charge of the ion measured, Fa is the Faraday constant (96480 C/mol) and a is the ion activity.

For chlorine selective electrode measurements, a small aliquot (~ 9 mL) of the sample leachate was taken. A series of standard (also 9 mL) with concentrations ranging from 0.1 to 1000 ppm were made in parallel. The Cole-Parmer® electrode was filled with a reference solution of 10 % KOH and then immerged in the Cl standards, agitated by a stirrer. The leachates were then analysed by the electrode, paying attention to clean the electrode between each measurement to avoid memory effects. Because of the sensitivity of the electrode, efforts were made to keep the same reading condition (steering speed, electrode placement, volume of solution analysed, etc.). The sample leachate revealed variable electrode potential, ranging from values similar to the 10 ppm standard up to significantly more than pure DI water. This matter is discussed in detail in the Chapter 5 of this thesis, where results of diverse tests are presented.

Before using the fluorine electrode, it was necessary to add a Total Ionic Strength Adjustment Buffer (TISAB) to decomplex fluorine and maintain a constant ionic strength in the measured solutions. The TISAB used was made of 57 mL glacial acetic acid, 58 g sodium chloride 12 g trisodium citrate dehydrate dissolved in 1 L of DI water adjusted to pH 5.5 by adding sodium hydroxide (NaOH). TISAB was added to both the sample leachate and a series of standards with composition ranging from 0.3 to 20 ppm. Each solution to analyse in an aliquot of 9 mL, 1:1 mixing between the F^- standard/sample leachate and TISAB. A minimum of two hours was necessary for the reaction with TISAB to operate before measuring the solutions.

Measurements were conducted is the same way as for chlorine but with a Cole-Parmer® fluorine selective electrode filled with diluted potassium chlorine. Once both the standard solution and the sample leachates were measured, the fluorine concentration by calibration method was obtain by converting the electrode potential to F concentration using the calibration curve built by the standards. This curve was linear ($R^2 > 0.99$) down to 0.3 ppm F, translating very good sensitivity for the range of fluorine investigated.

Because of the presence of fluorine complexes (even after adding TISAB), it was found that the calibration method underestimates the real fluorine concentration. A correction by the standard addition method was thus required, which tends to overestimate the F concentration by the same amount. A more concentrated fluorine solution (from 100 to 1000 ppm, mixed 1:1 with TISAB) was thus added to each leachate, aiming to increase the electrode potential by 30 mV (equivalent to tripling the F concentration). The solution was then left to rest for two additional hours before remeasuring them. From the measured potential can be calculated the so-called standard addition method concentration using this equation:

$$C_x = C_s * \frac{V_s}{V_X+V_s} * (10^{\frac{\Delta E}{S}} - \frac{V_s}{V_s+V_s})^{-1} \quad (2.2)$$

where C_x is the concentration of the analysed leachate and V_x its volume, C_s is the concentration of the added standard, V_s is its volume, ΔE is the difference in electrode potential between the solution before and after adding concentrated solution and S is the

slope of the calibration curve in mV per ten-fold increase in fluoride concentration. The real F concentration in each leachate was obtained by averaging the concentrations obtained by the calibration and standard addition methods (Stecher 1983, 1998).

3 Chapter 3

Post-eruptive outgassing of heavy metals at Fagradalsfjall, Iceland

Nicolas Levillayer, Céline Mandon, Olgeir Sigmarsson

About this chapter

This chapter was submitted to Bulletin of Volcanology and is currently under revision. In it we investigate the gas compositional variability during the different degassing phases associated with the Fagradalsfjall eruptions and we characterise the post-eruptive metal emissions from the crystallising lava field

Author contribution

Conceptualisation: NL and OS; Methodology: NL, OS and CM; Formal analysis and investigation: NL, CM and OS; Visualisation: NL; Writing – original draft preparation: NL, CM and OS; Writing review and editing: NL, CM and OS; Funding acquisition: OS

Keywords

Volcanic gas; Lava outgassing; Toxic metal release; Volatile element behaviour; Basaltic eruptions.

3.1 Abstract

Eruptions of basalt are known to emit a gas phase composed of H_2O, CO_2, SO_2, H_2S, HCl and HF but also trace elements, including toxic heavy metals. While the gas composition released during an eruption has been well studied, the post-eruptive gas emission remains poorly characterised, and its environmental impact is largely unknown. During the 2021 and 2022 Fagradalsfjall eruptions, gas was collected from an active crater and the post-eruptive gas from actively degassing but extinct crater and from the crystallising lava field. A compositional shift is observed from a sulphur dominated syn-eruptive gas phase (mass ratios S/Cl ~ 20, S/F ~ 50) to a halogen-dominated gas phase from the crystallising lava (S/Cl ~ 0.01, S/F ~ 0.1), the extinct crater gas having an intermediate but fluorine-rich composition (S/Cl ~ 0.8, S/F ~ 0.7). The shift in major volatile composition affects the trace element volatility, resulting in a depletion of elements emitted as sulphide or in their elemental form such as Te and Cd. The solidifying lava emits gas rich in chloride-forming species (Sb, Pb and Zn) whereas the gas from the extinct crater is rich in elements forming fluoride species such as Mo and Ru. Estimation of the trace metal emissions reveals significant liberation of a few toxic metals from the crystallising lava, up to 100 tons of Zn over the duration of the lava solidification. Syn- and post-eruptive metal emissions are markedly different and crystallising lava degassing may result in local hazards over extended time.

3.2 Introduction

Volcanoes release gas before, during and after an eruption, with each gas phase having markedly distinct composition. The main constituents of the volcanic gases are H_2O, CO_2, SO_2, H_2S, HCl and HF. Their proportions in the gas phase are principally controlled by their relative solubility that not only depends on the magma degassing pressure but also the magma composition and tectonic settings (e.g. Greenland et al. 1985; Gerlach 1986; Allard et al. 1991; Symonds et al. 1994; Aiuppa 2009). Gas released syn-eruptively at the vent is often referred to as primary gas, highly enriched in water, carbon dioxide and sulphur dioxide. In contrast, the post-eruptive gas, with larger proportions of halides (Olmez et al. 1986; Sigmarsson et al. 2020), is issued from a source already partially degassed and thus referred to as secondary. Secondary gas, however, can be emitted from a range of sources, including extinct craters, active lava flows or crystallising lava fields, and thus may vary in composition.

Volcanic gas is not only composed of major reactive volatiles, but also of volatile trace elements. In a magma, these trace elements partition between the silicate melt and the gas phase to an extent governed by their volatility, described by their gas/melt partition coefficient (Oppenheimer et al. 2014; Zelenski et al. 2021). The element volatility has been investigated and characterised for several volcanoes (Kīlauea; Mather et al. 2012; Mason et al. 2021, Holuhraun; Gauthier et al. 2016, Erta Ale; Zelenski et al. 2013), including Fagradalsfjall (Wainman et al. 2024), highlighting partition coefficient range of many orders of magnitude. Once the gas is released into the cold atmosphere, the trace elements in gaseous form (either free gases or complexes) rapidly form aerosols through condensation or adsorption on already present particulate matter such as ash (Symonds et al. 1992; Witham et al. 2005; Scholtysik and Canil 2021). Among the trace volatile elements are toxic metals (As, Cd, Pb, Zn, etc.; World Health Organisation, 2007), which degassing has been

associated with increased health issues around volcanoes (Vigneri et al. 2017; Stewart et al. 2022).

The gas composition has been studied either by sampling gas plumes from active vents or from passively outgassing volcanoes, revealing distinct composition of volatile emissions from hotspot and rift-related volcanism compared to that from subduction-zone volcanoes (Symonds et al. 1994; Aiuppa 2009; Gauthier et al. 2016; Edmonds et al. 2018). The gas released from hotspot and rift volcanoes is sulphur-rich, whereas volcanism at subduction zones discharges proportionally more water and Cl-rich gas. Moreover, major differences in volatile metal and metalloid volatilities have been identified between the S-rich hotspot volcanic gas and Cl-rich emissions at subduction zones (Hinkley et al. 1999; Edmonds et al. 2018; Zelenski et al. 2021). The variating metal volatility may be explained by their speciation behaviour, forming preferentially sulphide, halide or other gaseous compounds upon their release during magma outgassing (Symonds et al. 1992; Mandon et al. 2019; Renggli and Klemme 2020; Mason et al. 2021, 2024; Wainman et al. 2024). Consequently, variable metal emissions depend on, in addition to magma composition, the relative sulphur and halogens proportions in the gas phase.

During effusive basalt fissure eruptions at hotspot and rift-related settings, a significant proportion of the gas emitted can be of secondary nature. It originates from the cooling and crystallising lava and may form part of the well-known volcanic haze which can have dramatic consequences, such as during the Laki eruption (Thorarinsson 1969; Pétursson et al. 1984; Óskarsson 1984; Thordarson et al. 1996). Due to the distinct proportions of S, Cl and F emitted primarily and secondarily (Aiuppa et al. 2002; Sigmarsson et al. 2020), the volatility of metals and metalloids may vary significantly. The effect of changing S/Cl on element emissions at Piton de la Fournaise volcano, Reunion Island, resulted in substantial emissions of elements forming halide complexes (Toutain et al. 1990). A similar process was described at Fagradalsfjall, Iceland (2021-2023) by Wainman et al. (2024), who collected both primary gas from the eruptive crater and secondary gas from the flowing lava. They reported at-vent emissions of a gas rich both in S and S-complexing element, whereas the gas emitted by the flowing lava was richer in Cl and Cl-complexing elements. The gas from the flowing lava represents the very first stage of the secondary degassing, and the emitted gas composition may continue to evolve as the lava stagnates and cools down. Similarly, gas emissions from extinct craters are known to be depleted in sulphur with respect to syn-eruptive crater gas (Olmez et al. 1986; Sigmarsson et al. 2020), but little is known in terms of the trace element released.

Here we present the results of a syn- and post-eruptive gas sampling campaign during the Fagradalsfjall volcanic activity. We demonstrate a three orders-of-magnitude decrease in sulphur-halogen ratio from the primary gas (sampled syn-eruptively from the active crater) to the secondary gas (sampled post-eruptively at the extinct crater and at the crystallising lava), largely exceeding observations over the flowing lava by Wainman et al. (2024). Such changes in the S-Cl-F ratios of the emitted gas are then shown to severely affect the liberation of metals and metalloids from the basaltic melt, with post-eruptive crater releasing a gas rich in F and fluoride forming elements (Mo) and the post-eruptive lava rich in Cl and elements forming chlorides (Pb, Sb, Zn). The similarity between gas composition above the flowing lava (Wainman et al. 2024) and that of crystallising highlights the continuity of the secondary degassing mechanism. Notable differences are however observed. A few elements are depleted in the post-eruptive lava gas (Cu, Tl, Cs), while other elements are enriched (Zn and Sn), readily explained by their tendency to form chloride or fluoride volatile species at

lower temperature. Finally, we estimate the order of magnitude of volatile metals emitted during the post-eruptive lava degassing. Metal release is shown to markedly vary as the lava cools and age, which may thus have distinctive impacts on the surrounding environment.

3.3 Geological setting

At the Reykjanes peninsula the Mid-Atlantic ridge rises above the sea-level. The associated volcanic activity is characterised by emission of tholeiite, olivine tholeiite and limited amount of picrite (Jakobsson et al. 1978; Peate et al. 2009; Caracciolo et al. 2023). The magmatic activity on the peninsula reawakened in 2020, after approximately eight centuries of quiescence, with a series of seismic swarms and ground deformation (Sigmundsson et al. 2022), followed by an eruption of mantle-derived magma starting in March 2021 (Halldórsson et al. 2022; Marshall et al. 2024) in the Geldingadalir valley (Fig. 3.1). Two eruptions followed: Meradalir in 2022 and Litli Hrútur in 2023, both located a few kilometres to the NE of the 2021 vent.

The erupted lava has low water content (< 0.1 wt % in matrix glass; Halldórsson et al. 2022), halogens (50 to 300 ppm of Cl and F; Sigvaldason and Óskarsson, 1986) and volatile metals (Peate et al. 2009). Sulphur concentrations range from 180 to 450 ppm in the groundmass glass but reach 1000-2000 ppm in melt inclusions (Caracciolo et al. 2024). Over the 2021-2023 eruptive sequence, the emitted olivine tholeiite lava displayed significant compositional variations in the first weeks of the 2021 eruption, shifting from low to elevated K_2O/TiO_2 (Halldórsson et al. 2022). After the initial shift, relative compositional stability was established for the rest of the eruptive sequence (Marshall et al. 2024; Matthews et al. 2024). Analyses of the primary syn-eruptive gas composition by Fourier-transform infrared spectroscopy (FTIR) early in the 2021 Fagradalsfjall eruption revealed CO_2/S variations characteristic of the mantle-derived melt composition (Halldórsson et al. 2022). The variable C-isotope ratios during the 2021 eruption (Moussallam et al. 2024) support the source compositional heterogeneity. In contrast, a simple open-system degassing (Rayleigh distillation) fully explains the large decrease in $\delta^{13}C$ of the four months old secondary gas at the 2023 Litli-Hrútur eruption site compared to its syn-eruptive vent gas (Fischer et al. 2024).

The SO_2 emissions from the 2021 eruption were measured by Pfeffer et al. (2024), showing average rate of 64 ± 34 kg/s, which results in a total emission of 970 ± 540 kt over the entire eruption. The SO_2 flux however showed important temporal variations, associated with the different eruptive phases described in Pedersen et al. (2022) and Barsotti et al. (2023). Scott et al. (2023) characterised the small-scale temporal variation of the emitted gas composition during the periodic lava fountaining at Fagradalsfjall, in May 2021 (Phase III; Barsotti et al. 2023). The authors observed higher proportions of CO_2 and SO_2 relative to H_2O, HCl and HF during the fountaining activity, interpreted as release of foam accumulation exsolved from a fresh undegassed magma, richer in CO_2 and SO_2. Wainman et al. (2024) reported major and trace element content of the gas released during the 2021, 2022 and 2023 eruptions, revealing limited compositional variation, the largest variation being observed in the gas collected at the beginning of the 2021 eruption, when a magma of distinct composition was emitted. All three eruption sites are located on the eastern side of Fagradalsfjall hyaloclastite complex, far from any geo- or hydrothermal activity.

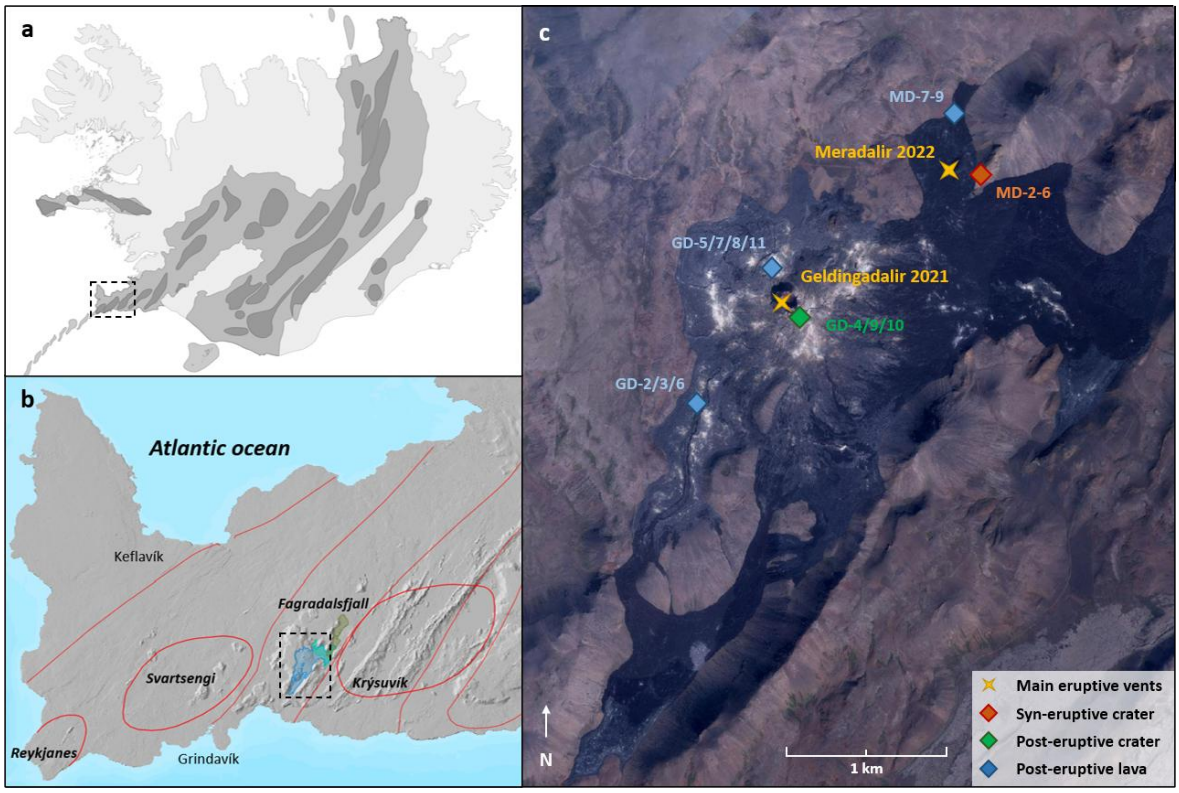

Figure 3.1. Sampling site geological context. *(a) Map of Iceland with Pleistocene/Holocene volcanic rocks in light grey and the active volcanic systems in dark grey. (b) The Reykjanes peninsula and four of its volcanic systems with the recent lava fields from Fagradalsfjall (2021-2023). (c) A satellite image showing the lava field east of the Fagradalsfjall hyaloclastite mountain range, with the different gas sampling sites indicated. Maps were made using data from the National Land Survey of Iceland (https://www.lmi.is/is/landupplysingar/gagnagrunnar/nidurhal, 20/10/2024).*

Over the three Fagradalsfjall eruptions, approximately 0.18 km^3 of magma was erupted, creating a lava field covering over 7 km^2 (Pedersen et al. 2022; Barsotti et al. 2023; Júlíusdóttir et al. 2024). The average lava thickness was measured 30 meters for the 2021 eruption and approximately 10 meters for the 2022 and 2023 eruptions. Locally however, lava can be much thicker, over 100 m around Geldingadalir main crater (Pedersen et al. 2022). The lava cooling and crystallising rate, which depends on the lava thickness, could thus locally last for decades (Hon et al. 1994), resulting in sustained post-eruptive gas emissions.

3.4 Methods

Over the gas sampling campaign, a total of 16 gas samples were collected at the crater/lava field from the 2021 and 2022 eruptions, together with three background air (Table 3.1; Online Resource 1). The syn-eruptive samples (MD-2 to MD-6) were collected from a ridge overlooking the 2022 crater at a distance < 170 m from the source (Fig. 3.2a). The 2022 Fagradalsfjall eruption provided exceptional conditions for ground-sampling due to the topography of the area and the prevailing wind during the eruption. The high topography of the hyaloclastite hills surrounding the valley where the fissure opened allowed the buoyant

plume to be accessible from the sampling ridge, while the contribution from lava degassing was mainly lying low in the valley or was blown lower down along the base of the ridge (Supplementary Fig. 3.1). Post-eruptive samples were collected from actively degassing areas where a blueish plume and precipitates around fractures were observed, to target high-temperature degassing from the crystallising magma. We avoided areas with white dense plumes lacking precipitates, mainly originating from evaporation of meteoric water in contact with the hot rocks. Several samples were collected at the same locations at different time (Fig. 3.1): GD-7, GD-8 and GD-11 from the lava field 50 m north of the 2021 main crater in Geldingadalir (Fig. 3.2b) and GD-4, GD-9 and GD-10 on the rim of that same crater after the eruption had stopped (Fig. 3.2c). The post-eruptive gas samples were collected several weeks up to two years after the eruption had ceased (Table 3.1).

Table 3.1. Gas sample description.

Eruption	Sample name	Sampling date	Sample type
-	Blank-1	01/03/2022	Background air
	Blank-2	27/03/2023	Background air
	Blank-3	10/06/2023	Background air
Geldingadalir eruption (19/03/2021-18/09/2021)	GD-3	17/11/2021	Post-eruptive lava
	GD-4	24/11/2021	Post-eruptive crater
	GD-6	06/03/2022	Post-eruptive lava
	GD-7	06/03/2022	Post-eruptive lava
	GD-8	20/07/2022	Post-eruptive lava
	GD-9	20/07/2022	Post-eruptive crater
	GD-10	16/03/2023	Post-eruptive crater
	GD-11	16/03/2023	Post-eruptive lava
Meradalir eruption (03/08/2022-21/08/2022)	MD-2	10/08/2022	Syn-eruptive crater
	MD-3	10/08/2022	Syn-eruptive crater
	MD-4	10/08/2022	Syn-eruptive crater
	MD-5	12/08/2022	Syn-eruptive crater
	MD-6	16/08/2022	Syn-eruptive crater
	MD-7	23/09/2022	Post-eruptive lava
	MD-8	18/10/2022	Post-eruptive lava
	MD-9	16/03/2023	Post-eruptive lava

We collected the particulate matter (aerosols), using 47-mm diameter Sterlitech® Polytetrafluoroethylene (PTFE) membrane filters, either laminated (1-µm pore size) or unlaminated (0.2-µm pore size). Reactive major gases were sampled using three cellulose filters loaded in a series of stages (Whatman®, 47 mm or Millipore®, 37 mm) and impregnated with a solution of 10 % base and 10 % glycerol. The based used was $NaHCO_3$ during the 2021 and 2022 sampling, replaced by NaOH in 2023 with no noticeable effect on the results. Two distinct setups were used during the campaign. In most cases, PTFE and impregnated filters were set up separately (Fig. 3.2a), allowing the use of a pump with higher flow rates for aerosol (83 L/min) collection than for the major gases (11 L/min). For a few samples, gas was pumped through filter packs (PTFE and impregnated filers stacked up in series) at a rate of 83 L/min (Fig. 3.2b and 3.2c).

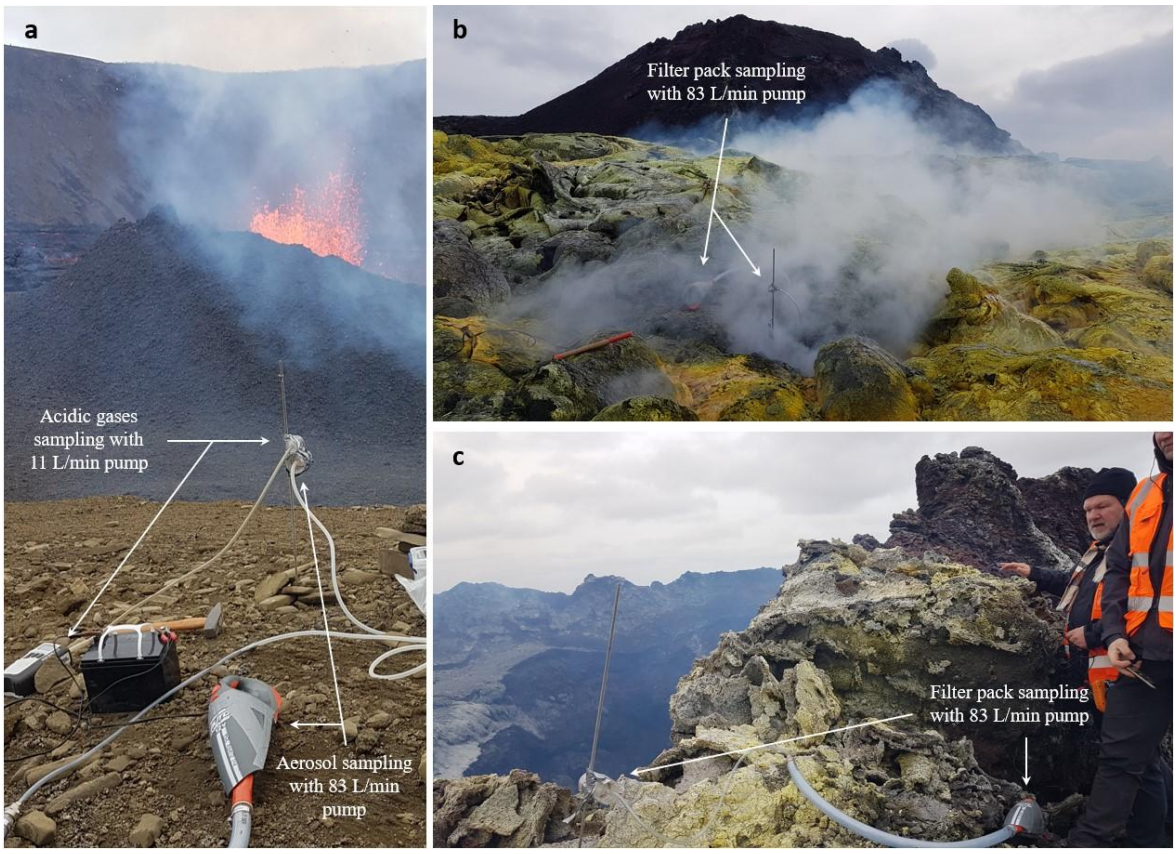

Figure 3.2. Syn- and post-eruptive gas sampling conditions *at: (a) the 2022 (Meradalir) eruptive crater, (b) the post-eruptive lava collected at the foot of the 2021 main crater (Geldingadalir) and (c) on the rim of the post-eruptive 2021 crater. In (a) is shown set-up for simultaneous but separated aerosol and reactive/acidic gas sampling with different pumps whereas panel (b) and (c) show gas collection with PTFE and impregnated filters packed together using a single pump (83 L/min) was used. When reactive gases were collected separately, the 11 L/min pump was used.*

After sampling, the impregnated filters were leached in 20 mL of Milli-Q® water for one to five days at ambient temperature. Two drops of H_2O_2 were added before analyses to convert all sulphur species to SO_4^{2-}. The leachates were consequently analysed by ion-chromatography at the Institute of Earth Sciences, Reykjavik, Iceland. In-house standards of different concentrations were used for the instrument calibration. Reproducibility is typically better than 3 % but closer to 5 % for the less concentrated samples. Results less than 1.5 times the concentration measured from the blank filters were discarded.

The PTFE filters were leached in a diluted acid mixture (0.4 M HNO_3 and 0.05 M HF) for several weeks on a hot plate at 80-100 °C. The leachate was analysed with an Agilent® 7500 or Agilent® 8900 ICP-MS at the Laboratoire Magmas et Volcans (LMV) in Clermont-Ferrand, France. Concentrations of 61 elements, ranging from Li to U were measured. The reaction cell (in He mode) was used to reduce interferences on masses ranging from Sc to As. Synthetic standards (with concentration of 1 and 10 ppb) were used for external calibration. The 2σ reproducibility on these standards is generally better than 5 % (Supplementary Table 3.2). Measurement quality was also checked by calculating the ratio obtained for the 10 ppb and 1 ppb standards. A ratio of 10 ± 0.5 was found for all volatile trace elements except for Pt (8.6) and Au (7.7).

Three blank PTFE filters were analysed to investigate the effect of different contribution from filter types and analytical instrument on the blank composition (Supplementary Table 3.3). Additionally, multiple (three or more) instrumental blanks (lab blank) of leaching solution with no filter were analysed during each measurement session. Gas sample concentrations were corrected for the corresponding blank filter (same filter analysed on the same instrument) and all concentrations that did not exceed 1.5 times those of the blank were discarded.

3.5 Results

3.5.1 Major volatiles

The concentrations of major volatiles are presented in Table 3.2, and more details are given in supplementary Table 3.4. The highest values are obtained in the syn-eruptive crater gas whereas, due to significant air-dilution, several post-eruptive gas samples have concentrations close to that of the blank. In the syn-eruptive gas, sulphur is the most abundant volatile, with concentrations up to 19 mg/m^3, while Cl and F reach 1.3 and 0.37 mg/m^3 respectively. Despite variable air dilution, this gas is of relatively homogeneous composition (similar S/Cl, S/F and Cl/F). In the post-eruptive lava gas, Cl is dominating, reaching concentration of 2.9 mg/m^3, whereas F and S never exceed 1 and 0.1 mg/m^3 respectively. Significant variability is observed in this gas phase regarding the Cl/F and S/F values. Finally, the post-eruptive crater gas displays similar concentrations of S, Cl and F (for example sample GD-4 has approximately 1.7 mg/m^3 for the three volatiles), and the lowest Cl/F.

Table 3.2. Major volatile concentrations (in mg/m^3) in the syn-eruptive crater, post-eruptive lava and post-eruptive crater Fagradalsfjall gas

		S	Cl	F	S/Cl	Cl/F	S/F
Syn-eruptive crater	*MD-2*	3.2	0.18	0.067	18	2.7	48
	MD-3	19	1.3	0.37	14	3.6	51
	MD-4	14	0.60	0.20	24	3.0	71
	MD-5	10.0	0.60	0.20	17	3.1	51
	MD-6	1.37	0.089	0.048	15	1.9	28
	Average	*9.6*	*0.56*	*0.18*	*18*	*2.8*	*50*
Post-eruptive lava	*GD-8*	0.027	2.2	0.52	0.012	4.3	0.051
	MD-8	0.018	1.6	0.65	0.011	2.4	0.027
	MD-9	0.036	1.9	0.14	0.019	14	0.26
	Average	*0.027*	*1.9*	*0.44*	*0.014*	*6.8*	*0.11*
Post-eruptive crater	*GD-4*	1.7	1.7	1.7	0.99	1.0	1.0
	GD-9	1.5	2.9	3.7	0.54	0.79	0.42
	Average	*1.6*	*2.3*	*2.7*	*0.77*	*0.92*	*0.73*

3.5.2 Trace elements concentrations in the gas

All analysed trace elements are listed in the supplementary Table 3.3, where the mass of trace element in each gas and blank sample (filter) is given. The trace elements of use to discuss the different gas phase compositions are: Cu, Zn, Ge, As, Se, Rb, Mo, Ru, Ag, Cd, In, Sn, Sb, Te, Cs, W, Re, Ir, Pt, Au, Tl, Pb and Bi. The blank corrected element concentrations are presented in Table 3.3. The syn-eruptive crater gas displays the highest concentration of most elements. Within that group, gas samples MD-4 and MD-5 have similar trace element abundances, whereas MD-6 displays values half an order of magnitude lower, confirming its more diluted nature. In the syn-eruptive crater gas, the most concentrated elements are Cu, Se, Cd and Te (≥ 100 ng/m^3 in MD-4 and MD-5) followed by Pb, Sn, Ge, As, Rb, Tl and Bi (≥ 10 ng/m^3). Iridium, Pt and Au are the least concentrated of the selected elements, with concentration below 1 ng/m^3.

Table 3.3. Trace element concentrations (in ng/m^3) of the different Fagradalsfjall gas phases. *Concentrations lower than 1.5 times the blank are not considered*

	Syn-eruptive crater gas			***Post-eruptive lava gas***								***Post-eruptive crater gas***		
	MD-4	*MD-5*	*MD-6*	*GD-3*	*GD-6*	*GD-7*	*GD-8*	*GD-11*	*MD-7*	*MD-8*	*MD-9*	*GD-4*	*GD-9*	*GD-10*
Cu	1214	2533	322	1.35	6.35	8.32	2.26	1.62	3.51	43.1	17.1	205	11.9	4.54
Zn	--	253	--	--	26.4	403	--	46.1	--	--	1709	21.2	12.0	48.7
Ge	21.9	21.7	5.36	0.00	0.17	--	--	--	0.08	0.06	0.19	0.02	--	0.04
As	20.7	23.9	7.79	0.27	2.41	--	--	--	0.11	1.23	2.07	12.8	3.38	0.27
Se	394	728	115	1.96	1.57	1.01	7.54	1.35	4.30	133	152	144	104	51.2
Rb	19.6	40.3	8.22	--	0.58	0.50	--	0.09	0.58	0.48	0.53	9.61	1.08	0.29
Mo	1.48	4.39	1.10	--	1.29	--	0.81	0.05	0.16	9.96	0.65	74.3	164	5.82
Ru	--	--	--	--	--	--	--	--	--	--	--	0.003	0.014	0.004
Ag	4.11	8.71	2.82	--	0.06	0.42	0.48	--	--	0.51	9.06	204	1.18	--
Cd	101	123	39.8	0.03	0.08	0.08	0.10	0.08	0.44	0.43	0.66	--	0.32	0.04
In	4.47	5.15	1.18	--	0.11	0.01	0.01	0.00	0.00	0.01	0.26	--	0.07	0.01
Sn	35.4	33.4	15.9	--	1.00	0.84	2.61	0.43	1.60	1.64	12.4	0.17	23.1	1.18
Sb	2.55	1.35	0.70	--	0.27	0.18	--	0.15	0.41	--	2.00	--	0.03	0.38
Te	107	121	35.4	0.08	0.06	0.02	0.09	--	0.07	0.89	0.04	15.2	6.52	0.09
Cs	0.66	1.31	0.24	0.00	0.02	--	--	--	0.01	0.03	0.17	0.28	0.06	--
W	0.77	3.10	7.02	0.25	--	0.24	1.19	0.29	--	0.83	0.09	2.91	3.87	1.37
Re	4.03	6.33	1.02	0.044	0.005	0.004	0.005	0.003	0.071	0.90	0.062	1.23	0.25	0.07
Ir	0.09	0.09	0.02	--	0.0004	0.0007	--	0.0006	0.0007	--	--	0.004	0.007	0.001
Pt	0.11	0.09	0.03	0.001	--	--	--	--	0.005	0.004	0.004	0.13	0.02	--
Au	0.74	0.68	0.29	--	--	--	--	--	--	0.04	0.16	1.71	0.97	0.04
Tl	15.2	31.5	5.66	0.24	0.10	0.07	1.51	0.00	0.02	8.71	0.08	22.9	27.6	0.18
Pb	58.7	83.7	22.8	--	5.82	1.98	0.14	0.21	0.88	0.90	11.1	5.79	0.76	0.23
Bi	13.3	16.7	4.01	0.028	0.134	0.018	--	--	0.037	0.176	0.376	0.405	0.024	0.015

The secondary/post-eruptive gas generally has lower trace element concentrations than the primary gas. The post-eruptive lava gas shows significant variability with Zn being the most abundant (1709 ng/m^3 in MD-9), followed by Se, Cu, Sn, Pb (≥ 10 ng/m^3), As and Sb (≥ 1 ng/m^3). Overall, the same relative concentration of trace elements is observed in the different post-eruptive lava gas samples, apart from samples GD-8 and MD-8 displaying Zn concentrations below blank but relatively high amount of Mo, Te and Tl. The post-eruptive crater gas displays higher variability both in terms of absolute concentrations and in terms of relative abundances of individual elements. The most concentrated elements are however the same for the three extinct crater gas samples: Cu, Se, Mo, Tl and Te. In addition, Ru

displays concentrations significantly above the blank in these samples (0.003 to 0.014 ng/m^3), in marked contrast to the other gas phase.

3.5.3 Compositional characteristics of syn- and post-eruptive degassing

The potential contribution of solid particles from the environment (ash, dust, etc…) is assessed using Sc as a purely non-volatile element to calculate the weight ash fraction (WAF; Aiuppa et al. 2003). The WAF is low for the volatile metals and metalloids (generally < 5 %, details in supplementary Table 3.5) and thus can be considered negligible. The measured trace elements concentrations normalised to those of the lava emitted during the 2021 eruption (details in supplementary Table 3.6) are displayed in figure 3.3. The pattern of element enrichment over lava is consistent across the three syn-eruptive crater gas samples. The most enriched major volatile in the gas from the active vent is S, followed by Cl and F, in agreement with their solubility in the silicate melt (e.g., Carroll and Webster 1994). In terms of trace elements, Te, Se and Re are the most enriched followed by Bi, Tl and Cd, whereas Zn, Pt and Mo are the least enriched elements.

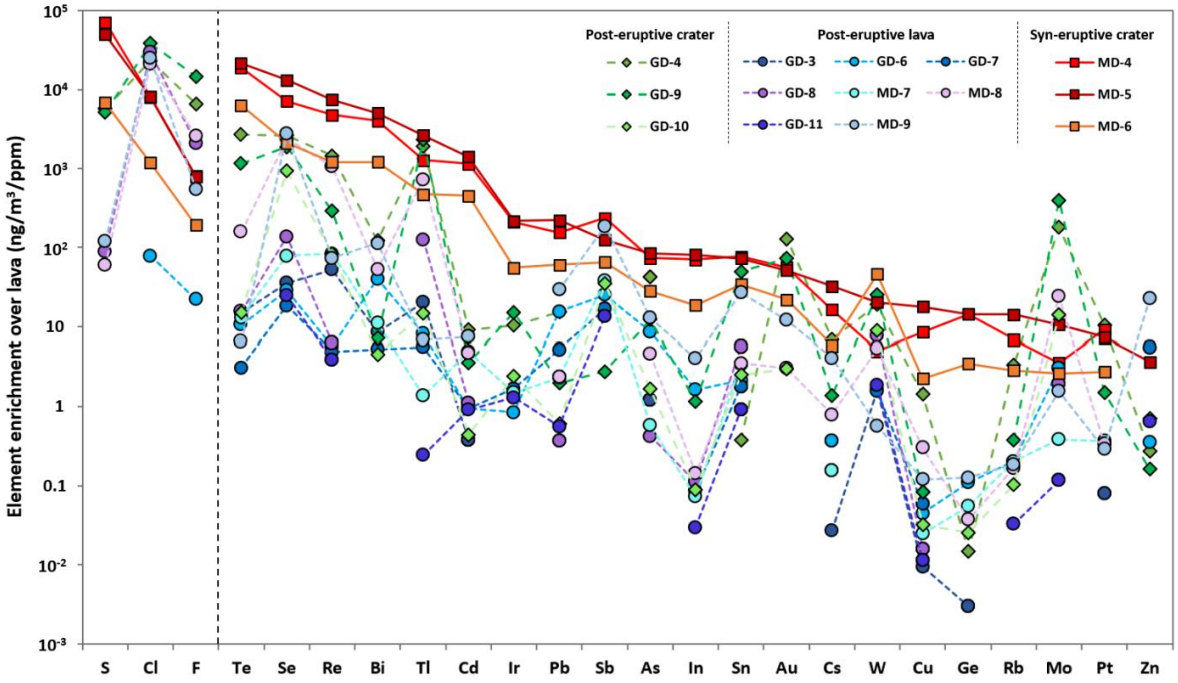

Figure 3.3. Fagradalsfjall gas composition from the syn-eruptive crater, post-eruptive lava and post-eruptive crater normalised to that of the Geldingadalir basalt lava. *The Geldingadalir lava corresponds to quenched lava collected by members of the IES the day after the eruption started. Trace elements concentration measurements were conducted at LMV following the same procedure as described in section 2.3.3. The results are affected both by the gas composition and the proportion of gas collected, explaining the general higher values for the more concentrated syn-eruptive crater gas. Regardless of the absolute values, the element enrichment pattern is similar within each group. Between groups, variable element enrichments are observed, and the most enriched elements are different in each gas phase*

The post-eruptive lava gas displays a wider range of enrichment, most likely originating from variable proportions of gas collected, MD-9 showing the highest concentrations in most elements whereas GD-3 and GD-11 are the most depleted. This secondary gas phase however has common features with Cl being the most enriched major volatile, followed by F and S. Again, Re and Se are the most enriched trace elements, followed by Sb and Bi, whereas, in contrast to the primary gas, Te and Cd are of lower concentration. The samples GD-8 and MD-8 have features distinct from the other post-eruptive lava gas with higher F, Mo, W and Tl but lower Ge, Zn and Pb.

The composition of the post-eruptive crater gas GD-4 and GD-9 is alike (except for Sn), whereas GD-10 displays similar pattern but lower concentrations. That gas phase is characterised by higher enrichment of F and Cl compared to S. The most enriched elements are Tl, Te and Se (to a similar extent), followed by Re and Mo whereas Ge, Cu, Rb and Zn are the least enriched elements. Overall, similarities are observed between extinct crater gas and GD-8 and MD-8 composition, which thus plot between the post-eruptive crater and post-eruptive lava gas endmembers (Fig. 3.3).

Therefore, a few trace elements such as Re and Se (the two elements having very similar behaviour) are highly enriched in all gas phases despite drastically different major volatile composition. Conversely, the three gas phases display distinct enrichment in numerous elements such as Te, Tl, Sb, Cd and Mo. In their recent study of the gas emitted during the 2021-2023 eruptions at Fagradalsfjall, Wainman et al. (2024) observed similar trace element behaviour with decreasing S/Cl that can be discussed after elimination of the different air dilution during sampling.

3.6 Discussion

The main characteristics of volcanic gas from divergent tectonic settings and hotspots are known to be the high concentrations of sulphur relative to that of chlorine (Symonds et al. 1994; Aiuppa 2009; Gauthier et al. 2016; Edmonds et al. 2018). Basalt fissure eruptions in Iceland demonstrate the dominance of sulphur over halogens in the primary gas phase (Gauthier et al. 2016; Stefánsson et al. 2017; Ilyinskaya et al. 2017; Scott et al. 2023; Wainman et al. 2024). The relative proportion of major volatiles in the volcanic gas evolves from the primary to the secondary outgassing stage (Aiuppa 2009; Sigmarsson et al. 2020), affecting the trace element behaviour (i.e., volatility; Johnson and Canil 2011; Scholtysik and Canil 2020; Renggli and Klemme 2020). The syn-eruptive crater gas from the Fagradalsfjall basalt eruptions corresponds to the primary outgassing of the magma, with an emission temperature of ~1180°C (Wainman et al. 2024). Other gas phases (syn-eruptive lava; post-eruptive crater and post-eruptive lava) are emitted from a magma already partially degassed and are therefore classified here as secondary gas. The emission temperature of the secondary gases in this study could not be measured as it was neither possible to reach the bottom of the fractures nor that of the crater with a thermocouple. However, temperatures > 500°C were measured at one meter depth within a deep degassing fracture, evidencing the high-temperature emission of these secondary gases. The main process differentiating primary and secondary outgassing is fractional degassing, or the Rayleigh distillation, leading to higher proportion of less volatile/more soluble elements in the later outgassing stages (Aiuppa 2009; Sigmarsson et al. 2020). To investigate the entire volcanic emissions (including release of heavy metals) to the environment, the secondary outgassing must be

accounted for. This is particularly important for effusive lava-forming eruptions, which release a significant proportion of the gas secondarily (Thordarson et al. 1996; Wainman et al. 2024).

3.6.1 Major volatiles gas concentration shift

The sulphur-rich primary gas phase emitted syn-eruptively at Fagradalsfjall, with mass ratios of S/Cl and S/F > 10 and Cl/F close to 3 (Fig. 3.4), concurs with published FTIR measurements (Scott et al. 2023; Wainman et al. 2024). The most significant variability is observed between the gas emitted immediately after the beginning of the Geldingadalir eruption, richer in S (S/Cl > 60) and gas collected three weeks later onwards, either during the 2021, 2022 or 2023 eruptions (S/Cl < 25). Such initial temporal variation, followed by stability, reflects the early contribution of deep source volatile (richer in less soluble elements). Overall, the Fagradalsfjall syn-eruptive crater gas emitted after the initial composition shift has almost identical major volatile composition to that of Erta Ale, Ethiopia (Zelenski et al. 2013) and similar to those of Kīlauea (Edmonds and Gerlach 2007; Edmonds et al. 2009; Mather et al. 2012) and Holuhraun (Gauthier et al. 2016; Stefánsson et al. 2017; Ilyinskaya et al. 2017; Sigmarsson et al. 2020). The dominance of sulphur over halogens in the primary gas is readily explained by its lower solubility in basaltic melt (Carroll and Webster 1994; Fischer 2008; Wallace et al. 2015; Zelenski et al. 2021).

Sampling of the gas emitted by the syn-eruptive lava by Wainman et al. (2024) revealed decreasing sulphur over halogen ratios with respect to the eruptive vent (Fig. 3.4). Such observation was interpreted by the authors as the initiation of a Rayleigh distillation process, decreasing the relative proportion of the most volatile elements such as sulphur. It is important to note that the S/Cl and S/F presented by Wainman et al. (2024) corresponds to FTIR measurements pointing at flowing lava but conducted during the very beginning of the 2021 eruption and relatively close to the eruptive vent (< 300 m). The measured values thus most likely represent the very early secondary degassing of the initial phase of the eruption, richer in sulphur. Ion chromatography of base impregnated filters conducted by Wainman et al. (2024) suggest lower S/Cl in the syn-eruptive lava gas (1.4-5.2, collected at distances ranging from 150-1400 m), arguing for a progressive fractional degassing.

The gas collected in this study from the extinct crater (post-eruptive crater) and the crystallising lava (post-eruptive lava) confirms this trend, with more extensive depletion of sulphur relative to halogens: S/Cl and S/F of 0.8 and 0.7 respectively. That gas composition is close to that of Holuhraun (Sigmarsson et al. 2020) and Kīlauea (Olmez et al. 1986) post-eruptive crater gas (Fig. 3.4). Thus, the shift in gas composition from the eruptive vent to extinct crater of Holuhraun, Kīlauea and Fagradalsfjall is similar, with decreasing S/Cl and S/F ratio of 1.5 to 2 orders of magnitude respectively (Fig. 3.4).

As shown for the Holuhraun 2014-2015 gas (Sigmarsson et al. 2020), the gas/melt partition coefficients for the halogens at Fagradalsfjall can be estimated from the Rayleigh distillation law:

$$C = C_0 \times f^{(D^{\frac{l}{g}} - 1)} \quad (3.1)$$

where C stands for the measured concentration of a given gas species, C_0 its initial gas concentration, f the fraction of gas remaining in the magma and D the concentration in liquid divided by that of the gas. The vapour/melt partition coefficient ($D^{V/M}$) is simply the

reciprocal of $D^{l/g}$, which yields $D^{V/M}$ of 19 and 3.5 for Cl and F in the primary gas, respectively, in agreement with the average partition coefficient at hotspot/rift volcanoes calculated by Zelenski et al. (2021). The calculated $D^{V/M}$ of Cl and F are 1.4 and 1.8, respectively, in the post eruptive crater gas of Fagradalsfjall, similar to those determined at Holuhraun (2.2 and 1.9 for Cl and F respectively).

The post-eruptive lava gas is further enriched in halogens relative to sulphur, particularly chlorine with S/Cl < 0.05 and Cl/F > 2. Such chlorine enrichment over sulphur is even higher than observed in the lava-seawater (laze) plume at Kīlauea lava (S/Cl of 0.09; Mason et al. 2021; Fig. 3.4).

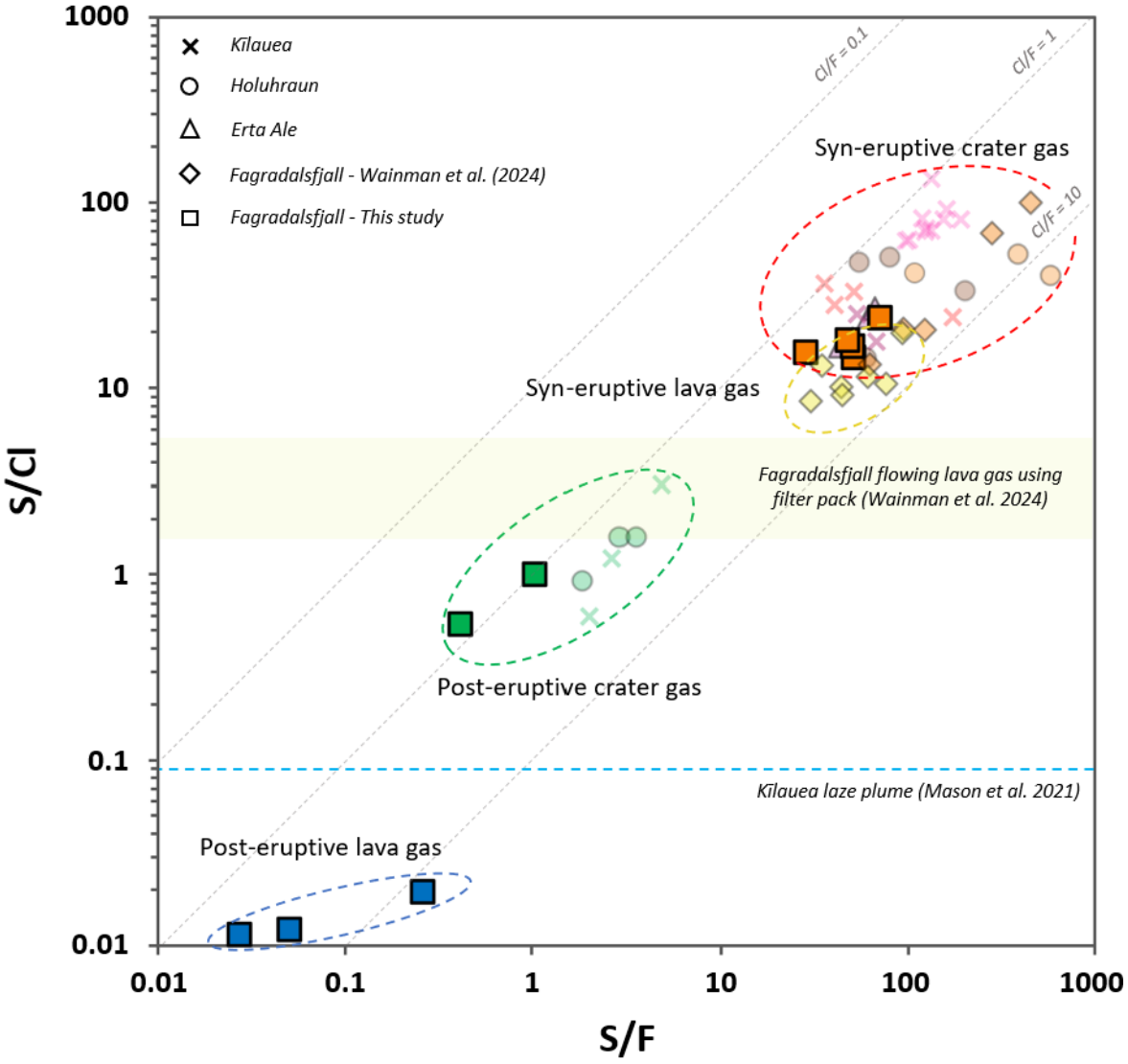

Figure 3.4. Mass ratio of S/Cl as a function of S/F for the Fagradalsfjall syn-eruptive crater (orange), post-eruptive crater (green) and post-eruptive lava (blue) gas compared to published values for Kīlauea, Holuhraun and Erta Alea *(Edmonds and Gerlach 2007; Edmonds et al. 2009; Mather et al. 2012; Zelenski et al. 2013; Gauthier et al. 2016; Stefánsson et al. 2017; Ilyinskaya et al. 2017; Sigmarsson et al. 2020). The FTIR results from Wainman et al. (2024) (syn-eruptive crater gas in orange and syn-eruptive lava in yellow) are also plotted, together with the yellow horizontal band representing the range of S/Cl obtained by the filter pack method. The Fagradalsfjall primary gas plots in the cluster*

formed by the hotspot/rift gas of Holuhraun, Kīlauea and Erta Ale. The post-eruptive crater gas from Fagradalsfjall is enriched in halogen concentrations relative to that of sulphur and plots close to the secondary gas of Holuhraun (Sigmarsson et al. 2020) and Kīlauea (Olmez et al. 1986). Finally, the Fagradalsfjall post-eruptive lava gas plots on the S-poor end of the graph, with the lowest S/F and S/Cl values

As precipitates are ubiquitous in secondary degassing sampling locations, loss of major volatiles to minerals cannot be entirely discarded. Sublimates studies from high temperature fumarolic gases, indicate that sulphates, sulphides and chloride minerals may form at temperatures > 400°C (e.g. Wahrenberger 1997; Africano et al. 2002). However, Mandon et al. (2025) showed the importance of kinetics in preventing efficient precipitation during rapid cooling and expansion of fumarolic gases, with only a small portion by mass lost to sublimates. The yellow sulphur deposit around the degassing fissure (Fig. 3.2b) most likely reflects the admixture of atmosphere causing oxidation of the gas and cooling below 115 °C, resulting in the precipitation of sulphur crystals. Therefore, while loss to precipitating minerals cannot be ruled out, it is unlikely that the orders of magnitude shift in S/halogen ratios observed is solely related to such process.

The composition of the different gas phases appears best explained by the progressive Rayleigh distillation of the magmatic volatiles in the Fagradalsfjall basalt melt. The intense degassing at the crater releases sulphur and proportionally less halogens. The secondary degassing then starts with the release of syn-eruptive lava gas, whose limited S-depletion (Fig. 3.4) indicates that a significant amount of sulphur remains in the molten lava during displacement. Continuous degassing from the flowing and emplacing lava progressively depletes sulphur in the silicate melt. A depletion that results in the final emission of a sulphur-poor gas from the emplaced lava field, as represented by our post-eruptive lava gas. The observed progressive and intense sulphur loss leads to the very low concentrations measured in lavas on Reykjanes compared to those of melt inclusions (Caracciolo et al. 2024). The intermediate S-depletion in the post-eruptive crater gas suggests contribution, in addition to the crystallising lava, of a less degassed source, namely the cooling conduit and possibly residual magma at depth.

3.6.2 Fagradalsfjall primary gas trace element content

Analyses of Fagradalsfjall gas from the 2021, 2022 and 2023 eruptions by Wainman et al. (2024) revealed minor compositional variation. The largest difference in composition was observed for the gas collected during the first days of the 2021 eruption (SFP4; Wainman et al. 2024), whereas the other gas samples had similar composition (Online resource 8). The trace element composition of the 2022 primary gas of this study is of similar composition. Discrepancies such as higher Cu and Sb but lower Pt concentration in the gas from this study can however be observed (Fig. 3.5). Given that both data set are quite constant in their difference, this latter is more likely associated with sampling and/or analysis bias than actual gas composition variation. Regardless, taken together, the Fagradalsfjall gas has a trace element composition alike those of both divergent zone volcanism such as that of Erta Ale, and hotspot volcanism represented by Kīlauea volcano (Mather et al. 2012; Zelenski et al. 2013; Mason et al. 2021).

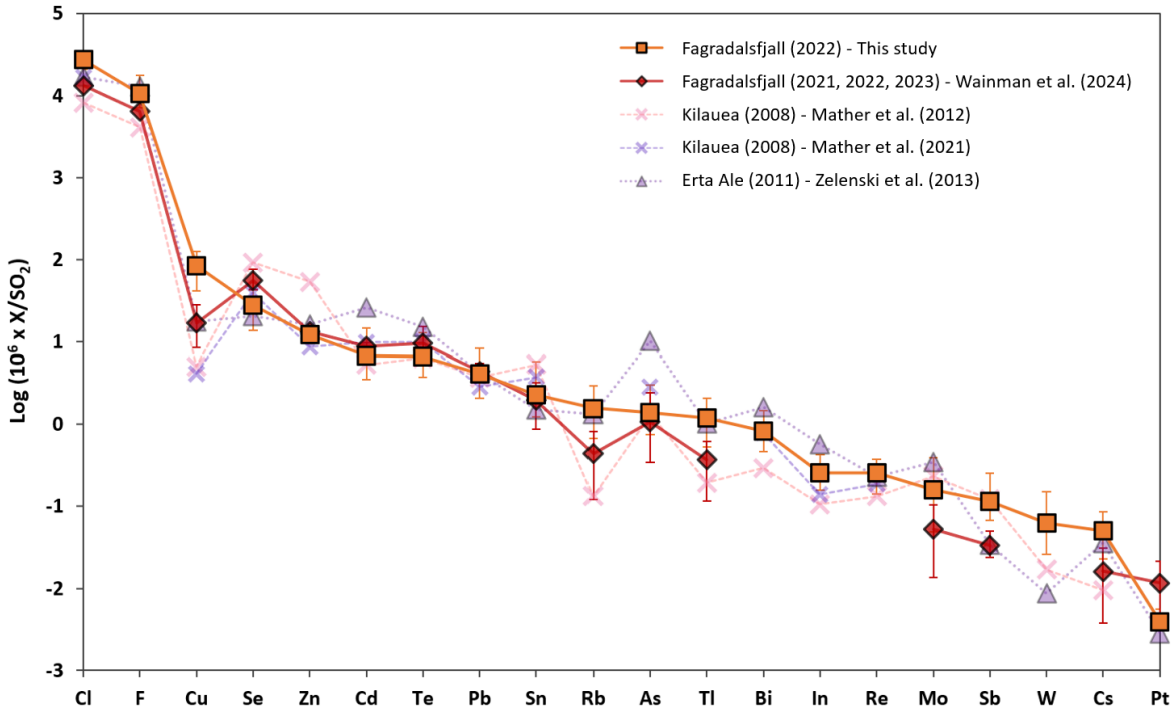

Figure 3.5. SO_2-normalised primary gas composition from Fagradalsfjall (this study and Wainman et al. 2024) compared to gas from Kīlauea and Erta Ale volcanoes*, ordered by decreasing X/SO_2 in the Fagradalsfjall syn-eruptive crater gas (of this study). Values for Fagradalsfjall from Wainman et al. (2024) correspond to the average of five samples collected during the 2021, 2022 and 2023 eruptions (SFP4, SFP12, LW1, LW2 and FP8), with the error bar showing the variability. The X/SO_2 (X representing different trace elements) is the average composition from the 2008 (Mather et al. 2012) and 2018 (Mason et al. 2021) Kīlauea eruptions whereas the Erta Ale gas composition is taken from Zelenski et al. (2013). The Fagradalsfjall gas composition is similar to those of Erta Ale or Kīlauea, emphasising similar gas composition emitted from hotspot/rift volcanism*

3.6.3 Syn- to post-eruptive gas evolution

The changes of trace element volatility from syn-eruptive to post-eruptive gas emissions can be evaluated by calculating the relative enrichment factors (EF) over a given element. Copper is an element of choice for normalisation because its concentration is well above the analytical detection limit and blank concentration in all gas samples and with a low ash contribution (details in supplementary Table 3.5). The enrichment factor is calculated as:

$$EF = (X_{gas}/X_{lava})/(Cu_{gas}/Cu_{lava}) \quad (3.2)$$

where X is the element of interest. The average EF for each gas phase is shown in Fig. 3.6 illustrating the level of enrichment/depletion of each element in all gas phases relative to that of Cu.

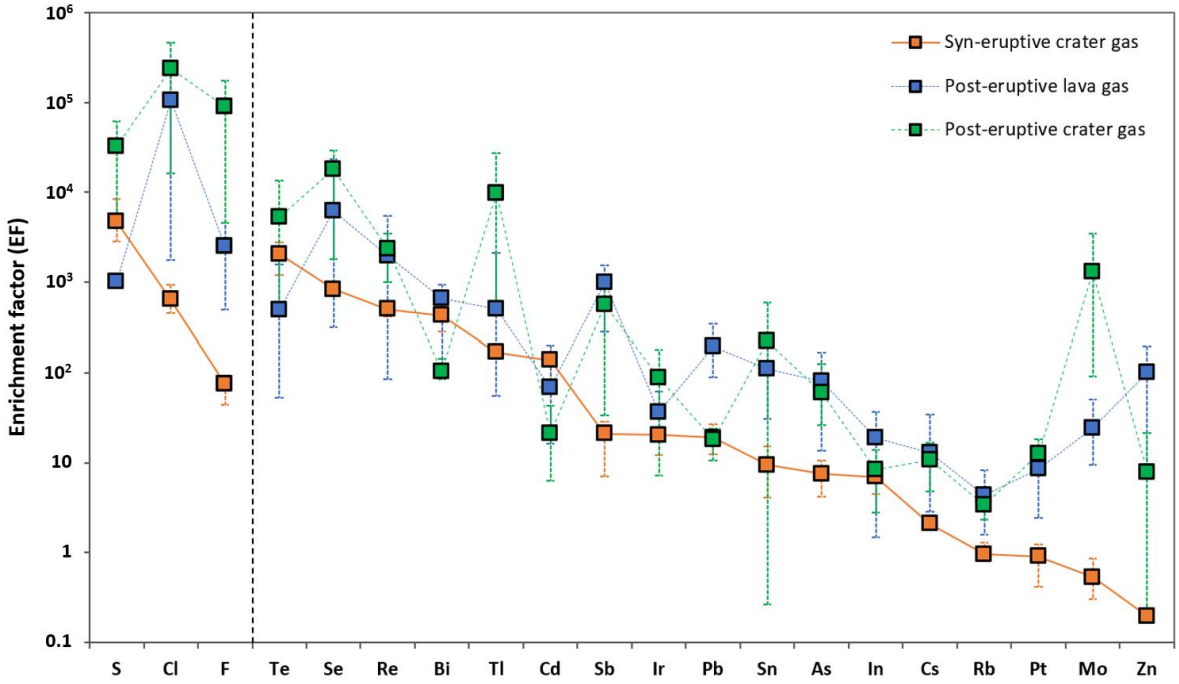

Figure 3.6. Average enrichment factors (EF) relative to Cu for the three gas phases sampled at Fagradalsfjall *(gas from the syn-eruptive crater, post-eruptive lava and post-eruptive crater). Elements are ordered by decreasing EF in syn-eruptive gas, with the major volatiles (S, Cl an F) separated for clarity. The range of EF for each gas group is indicated by the bars through the average values. Larger ranges are observed for the of post-eruptive lava gas (with the outliers GD-8 and MD-8, showing post-eruptive crater gas compositional features, excluded) compared to the syn- and post-eruptive crater gas. Larger enrichment factors in the post-eruptive halogen-rich gas are visible, with the exception of Te, Bi and Cd.*

In the syn-eruptive crater gas, the most enriched element is Te (EF ~ 2000; Fig. 3.6), followed by Se, Re, Bi, Tl and Cd (1000 > EF > 400). The least volatile elements in the primary gas are Zn, Mo, Pt and Rb, being less enriched than Cu (EF < 1). These EF factors are comparable to what Edmonds et al. (2018) calculated for Kīlauea and Holuhraun using data from Gauthier et al. (2016) and Mather et al. (2012). The slightly lower EF found for most elements in Fagradalsfjall is readily associated with the higher Cu concentration observed in this study (Fig. 3.5). Overall, the calculated EF correlate with the emanation coefficient calculated by Wainman et al. (2024), although Sb is found significantly more enriched in the primary gas presented here and As more depleted.

In the post-eruptive lava gas, all selected elements are more enriched than Cu, the most enriched being Se (EF ~ 6000), Re (EF ~ 2000) and Sb (EF ~ 1000). In the post-eruptive crater gas, Se, Tl and Te are the most volatile elements (EF > 5000), followed by Re and Mo (EF > 1000). There are thus important changes of enrichment between the syn-eruptive and post-eruptive gas emissions. Changes in element EF in the secondary gases can be related to element exhaustion in the silicate melt or volatility changes associated with distinct major gas proportions and temperature as previously observed by Wainman et al. (2024).

With respect to the primary gas, the post-eruptive lava gas is particularly depleted in Te and Cd. Such depletion is consistent with their speciation either as free elements or sulphide species (Wainman et al. 2024; Mason et al. 2024; Mandon et al. 2025), leading to reduced volatility in the cooler, S-poor crystallising lava gas. Note that as Te is extremely volatile,

its depletion could be accentuated by reduced melt concentration following significant primary degassing of Te. In contrast, Zn, Mo, Sb and Pb display the largest increase in the post-eruptive lava gas. This concurs with higher proportions of halogens, favouring volatilisation of these halide-forming elements (Wainman et al. 2024; Mason et al. 2024; Mandon et al. 2025). In the extinct crater gas, Mo is the most enriched element compared to the primary gas (EF increase of over 1000 times) followed by Tl and Zn (EF increase of over 100 times). Such enrichment may be explained by higher halogen concentrations, notably that of fluorine, as speciation models predict that Mo form fluoride and Tl and Zn chloride gaseous species (Zelenski et al. 2021; Mason et al. 2021; Mason et al. 2024).

3.6.4 Comparison between the post-eruptive gas and that of the syn-eruptive lava

The gas sampled over the flowing lava (syn-eruptive lava) by Wainman et al. (2024) is taken here to represent the initial stage of the secondary degassing process, whereas the post-eruptive lava gas represents the final stage of the Rayleigh distillation. In figure 3.7 are presented the average X/Cu ratios for our three gas phases, along with the gas phases from the syn-eruptive crater and the syn-eruptive lava reported in Wainman et al. (2024). The difference between the syn-eruptive gas of both studies mostly originate from distinct Cu concentration in the two gases (Fig. 3.5). Most elements have higher X/Cu in the post-eruptive lava gas compared to the primary gas of this study, which results from the relatively low Cu concentration in the post-eruptive lava gas.

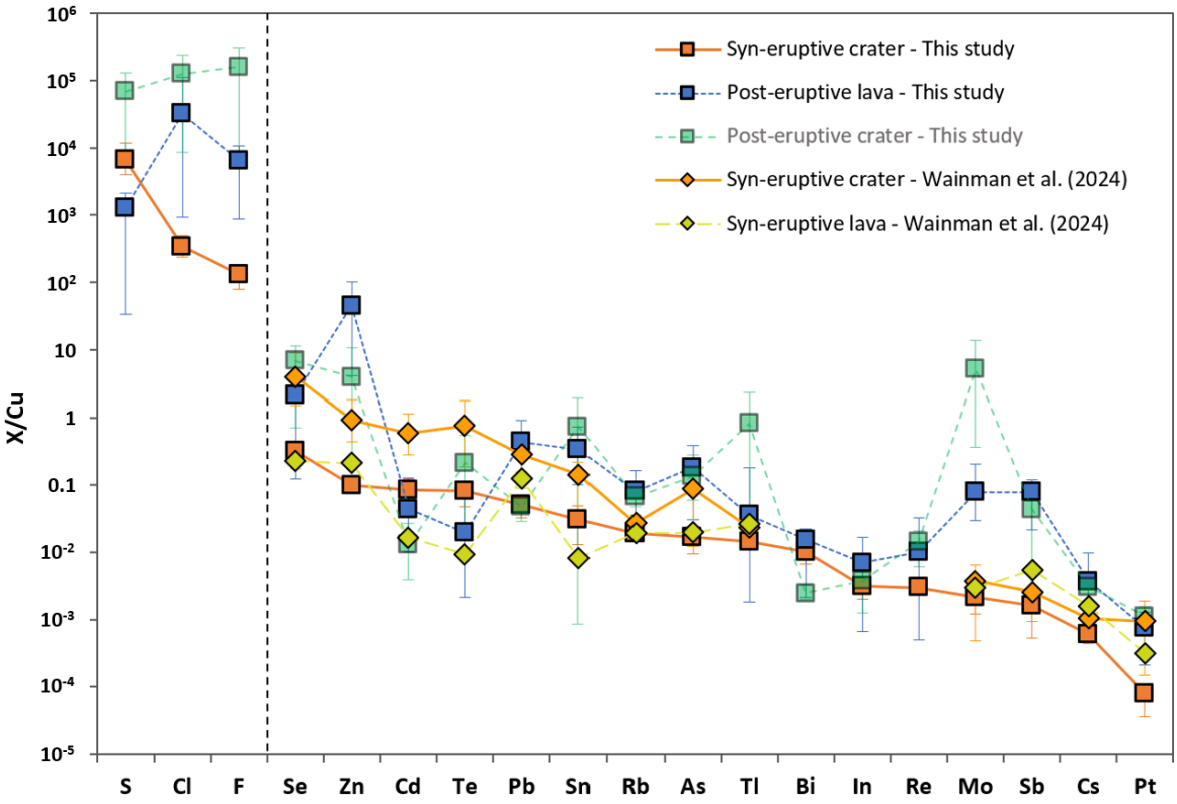

Figure 3.7. The average X/Cu in primary and secondary gas at Fagradalsfjall*, ordered by decreasing X/Cu in the syn-eruptive crater gas of this study. The syn-eruptive crater data from Wainman et al. (2024) correspond to the average of the vent samples collected in 2021, 2022 and 2023 with the error bars indicating the variability. The syn-eruptive lava data*

from Wainman et al. (2024) correspond to the average of the distal lava gas samples (LHFP3 and LHFP4 collected in 2023, 1 and 1.4 km from the eruptive vent) with the error bars indicating the variability (generally hidden by the symbol). The syn-eruptive lava gas of Wainman et al. (2024) has lower (Se, Zn, Cd, Te, Sn)/Cu compared to their primary gas composition whereas other elements over Cu are within error in their two gases. In contrast, the differences of primary and secondary gas composition of this study, with generally higher X/Cu in the secondary gas (only exception being lower Te/Cu in the final post-eruptive lava gas) most likely reflects most likely reflects lower Cu concentrations.

Despite large differences in S/Cl (Fig. 3.4), compositional difference between the primary and secondary gas from Wainman et al. (2024) and this study is comparable for numerous elements. The evolution from primary to secondary degassing at the syn-eruptive lava and the post-eruptive lava are compared in figure 3.8. The ratio of Cu-normalised element concentration of the syn- and post-eruptive lava gases to their respective primary gas composition correlates well, Te and Cd being relatively depleted while Mo and Sb are amongst the most enriched in both lava gas. In contrast, a few elements display different behaviour, with Tl and Cs particularly enriched in the gas released by the syn-eruptive lava while Sn and Zn are substantially more enriched in the post-eruptive lava gas.

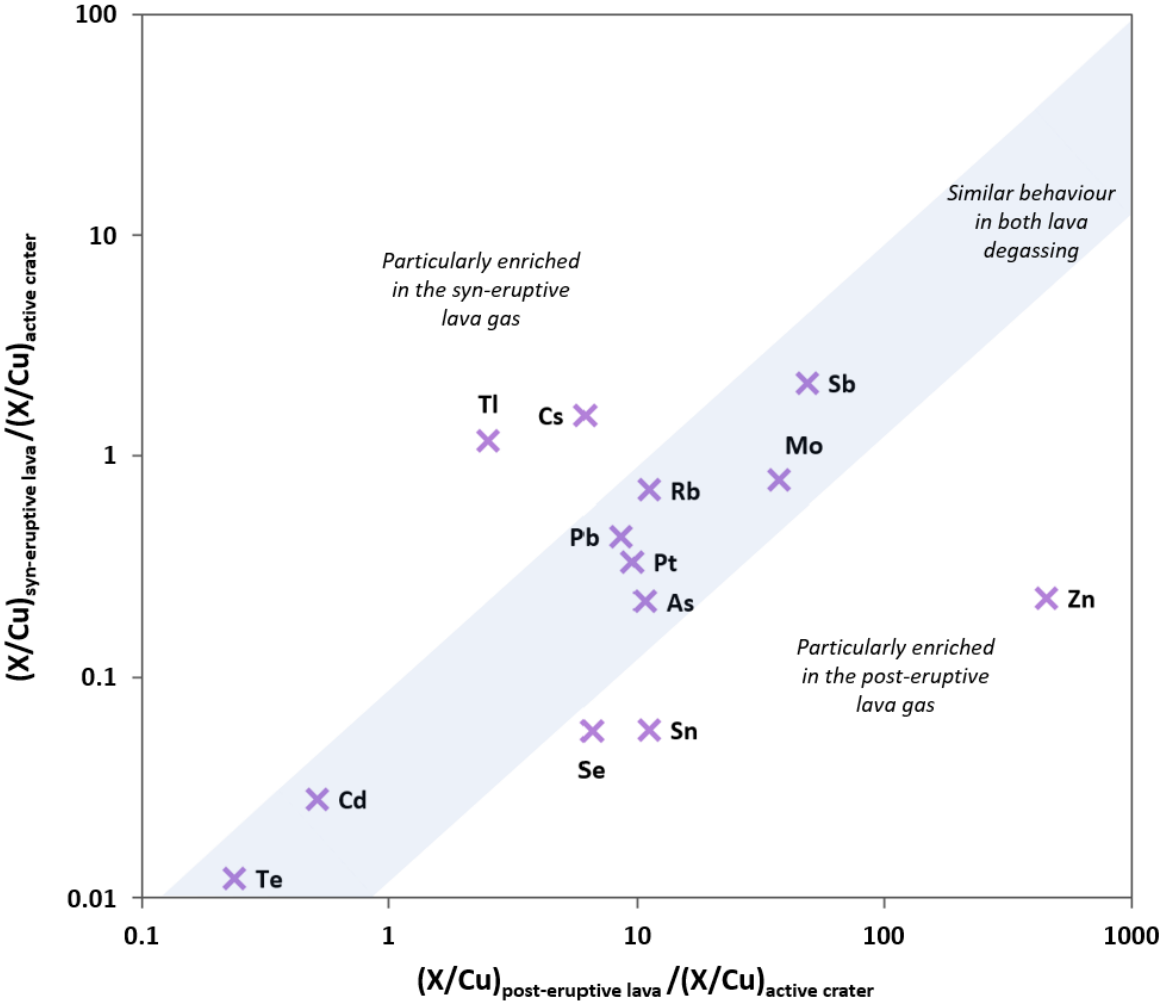

Figure 3.8. Changes of Cu-normalised element gas concentration between the primary and syn-eruptive lava degassing (y-axis; Wainman et al. 2024) as a function of the shift between primary and post-eruptive lava gas degassing (x-axis; this study). *Most elements*

have a similar enrichment trend in both lava degassing whereas a few are more significantly enriched in the syn-eruptive lava gas (Tl and Cs) or in the post-eruptive lava gas (Se, Sn and Zn).

Several reasons could explain the higher element concentration in the syn-eruptive lava gas. The first would be the depletion and exhaustion of these elements in the lava leaving little to release post-eruptively (as is the case for S). However, given the moderate volatility of these elements (Tl, Cs; Fig. 3.6), an alternative hypothesis would be a drop in their volatility at the post-eruptive conditions, due to lower temperature. Finally, it is also possible that a few elements may have been partially lost to incrustations (Óskarsson 1981; Renggli and Klemme 2020). The much larger enrichment in Sn and Zn in the post-eruptive gas most likely reflects increased volatility at lower temperature. Such behaviour is expected for both elements as they are likely to form chlorine species at low temperature according to the thermodynamic models (Wainman et al. 2024; Mason et al. 2024) and would thus favour the Cl-rich cool gas from the solidifying lava. Zinc has indeed been shown to be significantly degassed when lava enters the ocean and liberates a Cl-rich gas (Mason et al. 2021).

3.6.5 Gas differentiation model

A conceptual model for progressive degassing at Fagradalsfjall was presented by Wainman et al. (2024), shown on figure 1.7. In their model and supporting results, the sulphide forming elements are favourably degassed at the eruptive vent, as previously observed in other hot-spot/rift volcanic environment (Mather et al. 2012; Zelenski et al. 2013; Gauthier et al. 2016; Ilyinskaya et al. 2021). Our results fit such a model, the hot and S-rich syn-eruptive crater gas releasing large amount of sulphide forming elements, along with elements degassing freely or as oxides (Te, Se, Bi, Tl, Cd and Re). The gas emitted by the syn-eruptive lava (Wainman et al. 2024) was marked by depletion of Te and Cd, whereas Cl-complexing elements such as Cu, Rb and Cs were particularly enriched. The evolution was explained by decreasing proportion of sulphur over chlorine, favouring the volatility of chloride species. In their conceptual model, Wainman et al. (2024) hypothesised that as degassing goes on as the lava is aging, the emitted gas composition should vary with decreasing temperature and increasing proportion of fluorine.

Our post-eruptive samples permit to test and complete this model (Fig. 3.9). The increase in fluorine relative to chlorine is not observed in the post-eruptive lava gas but is present in our samples from the extinct crater ($Cl/F < 1$). In this gas, the role of fluorine as a main ligand is supported by the marked enrichment in Mo, known to form a gaseous species with F as MoF_2O_2 (Mason et al. 2024; Mandon et al. 2025). The other elements particularly enriched in the extinct crater gas are Tl, known to form oxides (Tl_2O; Mandon et al. 2019; Mason et al. 2021) and Ru, only present in the post-eruptive crater gas (Table 3.3), which is consistent with its volatile behaviour as fluoride (RuF_5; boiling point: 227 °C; Haynes et al. 2016). The extinct crater degassing thus represents gas emissions relatively rich in F, favouring volatility of trace elements forming fluorides.

The crystallising lava gas does not show the same trend regarding fluorine, as it is much richer in chlorine ($Cl/F > 3$, similar to what is observed at the syn-eruptive lava by Wainman et al, 2024, Fig 3.4). This gas can be used to investigate the effect of a Cl-dominated degassing regime ($S/Cl < 0.02$) at lower lava temperature. The Cl-rich post-eruptive lava gas does indeed display particularly high concentrations in chloride forming elements (Zn, Sb, Sn, Fig 3.9). In contrast, the least enriched elements in the final gas emitted from the lava

post-eruptively are those with a strong tendency to degas as sulphide (Te and Bi) or in their elemental form such as Bi and Cd (Zelenski et al. 2021; Mason et al. 2021), consistent with the a cooler and S-depleted nature of the gas. As hypothesised by Wainman et al. (2024), lower lava temperature appears to play a role as the post-eruptive lava gas is particularly enriched in Sn and Zn compared to the syn-eruptive lava gas, elements that are known to degas as chloride species at cooler temperature (Wainman et al. 2024).

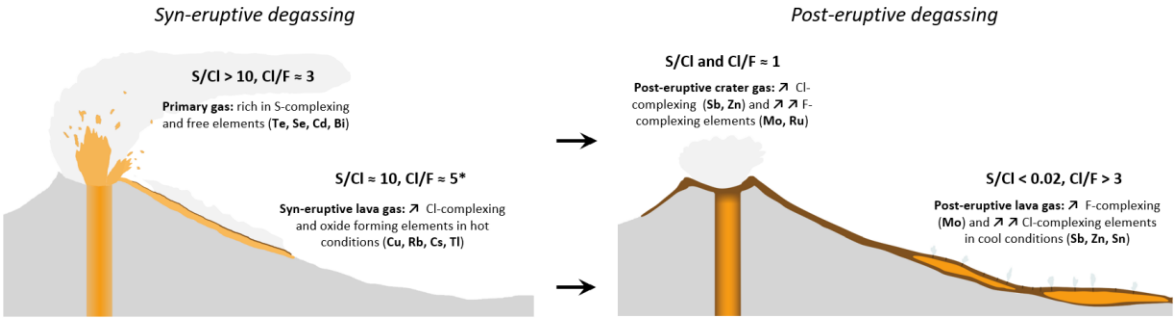

Figure 3.9. Schematic illustration of the different volcanic degassing stages and their compositional features in terms of major and trace elements. *The gas features of each secondary degassing are compared to the primary ones, emitted at the syn-eruptive crater. The moderate sulphur depletion in the syn-eruptive lava gas and its effect on trace element release was evidenced by Wainman et al. (2024). Post-eruptive gas emissions are much poorer in S and S-affine elements, readily explained by advanced fractional degassing. The extinct crater gas sampled at Fagradalsfjall is rich in F (in agreement with observations from Olmez et al. 1986 and Sigmarsson et al. 2020) and F-affine elements. The post-eruptive lava gas sampled is dominated by Cl emissions along with elements forming chloride species at cooler temperature.*

3.6.6 Constraining the post-eruptive trace elements emission.

Attempts to quantify volatile metal emissions are generally based on a known total sulphur discharge from an entire eruption and the measured element over sulphur ratio, taken to represent the composition of the total gas phase (Gauthier and Le Cloarec 1998; Hinkley et al. 1999). As an example, Wainman et al. (2024) estimated, based on comparison of degassed and undegassed lavas, that the syn-eruptive lava emits 10 % of the sulphur liberated during the Fagradalsfjall eruptions. The inaccessibility of sulphur-flux proportion from the post-eruptive lava together with the very low sulphur concentrations at this final degassing stage hampers the traditional way of estimating the flux for the volatile metals. Hence, a different method must be attempted.

In their degassing study of the Laki eruption, Thordarson et al. (1996) estimated from the eruption products the proportion of Cl and F released during different degassing stages (at the eruptive vent, the syn-eruptive lava and the post-eruptive lava). They proposed that the vent degassing released 27 % of Cl and 29 % of F initially present in the undegassed magma, while 11 % of the original chlorine and 17 % of the fluorine were released during the last degassing stage, from the crystallising lava. Although these values are unlikely to be exactly the same at Fagradalsfjall, using them as a first order approximation for our calculation should yield the order of magnitude of trace element emissions. The total mass of element released during a given degassing stage are thus assessed from the ratio of an element over chlorine and fluorine as follows:

$$X_{emitted} = [halogen]_{lava} \times m_{lava} \times F_{hal} \times \frac{X}{halogen} \quad (3.3)$$

In which $X_{emitted}$ is the total mass of an element X released, $[halogen]_{lava}$ is either Cl or F concentration in the undegassed basaltic magma, m_{lava} the mass of lava erupted, F_{hal} the fraction of Cl or F emitted (using estimations from Laki), and $X/halogen$ is the measured concentration ratio of the element X over Cl or F in the investigated gas phase. The equation can be applied on different degassing stages and is used here to calculate the emissions from the eruptive vent and from the post-eruptive lava.

The calculated masses of trace element release differ between the two halogens, with higher values calculated using F compared to Cl (around 3 times for at-vent emissions and 10 times for post-eruptive lava emission; details in Online resource 9). This difference originates from the similar F_{hal} used for Cl and F (as found at Laki), which does not match the measured Cl/F ratio in both the eruptive vent and post-eruptive lava gas (Cl/F = 3-15). The average result using both F and Cl is presented in figure 3.10.

The estimations give total syn-eruptive crater emissions over the three Fagradalsfjall eruptions of over 10 tons of Cu, Se, Zn, Cd and Te and between 1 and 10 tons of Cd, Te, Pb, Sn, As, Tl, Bi and W. These emissions are similar to those calculated for the eruptive vent, using the measured SO_2 flux and X/SO_2 (Wainman et al. 2024). However, significantly higher estimates are obtained for emitted masses of Cu, Rb, Tl, Mo, Sb and Cs, reflecting the difference in the measured gas composition (Fig. 3.5).

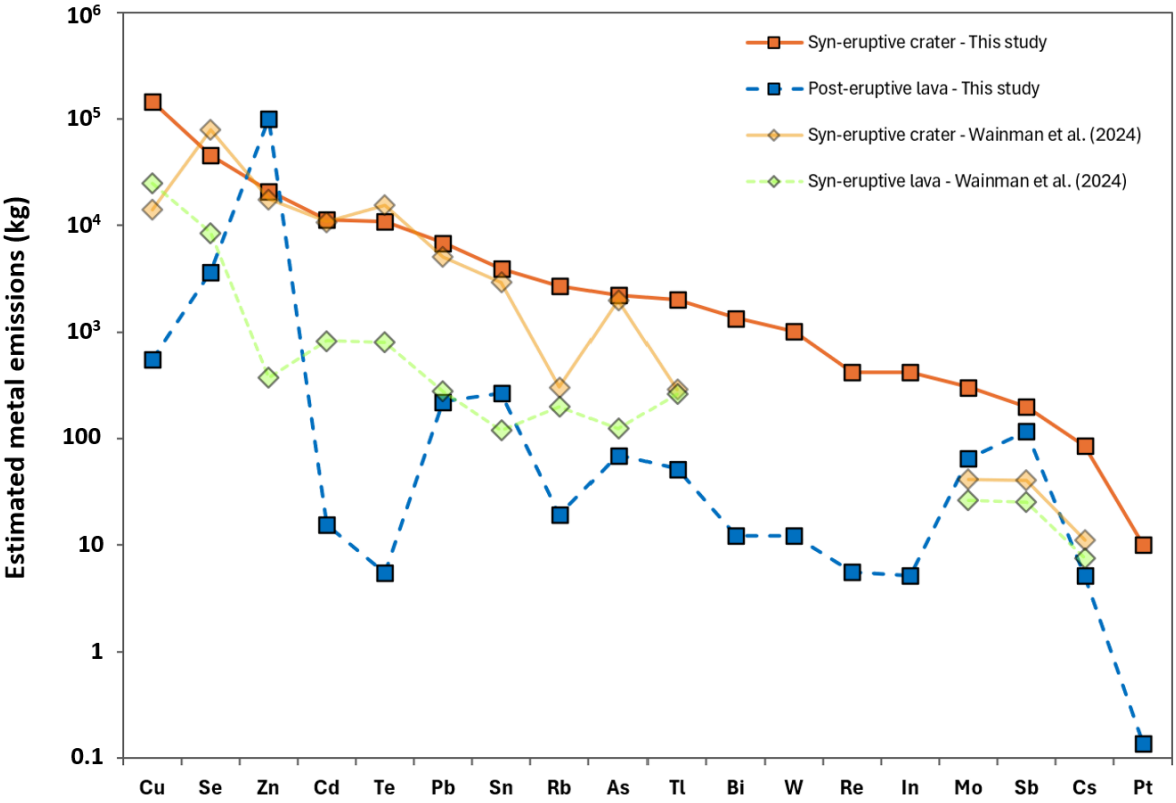

***Figure 3.10. Estimate of total volatile metal emissions from the three Fagradalsfjall eruptions combined**, ordered by decreasing mass emissions in the syn-eruptive crater degassing (of this study). The syn-eruptive crater and post-eruptive lava emissions were estimated from an initial concentration of 160 ppm Cl (Caracciolo et al. 2024) and 200 ppm F (Sigvaldason and Óskarsson 1986) and the mass of lava extruded of 4.6 x 10^{11} kg*

(calculated with a lava density of 2600 kg/m^3 and total volume of 0.18 km^3; Júlíusdóttir et al. 2024). The fraction of halogen used for calculations corresponds to the estimation from Thordarson et al. (1996) at Laki. Syn-eruptive crater and lava emissions reported by Wainman et al. (2024) were recalculated using the total of SO_2 emitted in 2021 (970 kt) reported by Pfeffer et al. (2024) and assuming constant S emission per unit of volume in 2022 and 2023. The syn-eruptive lava emissions correspond to the average of the results classified as "proximal lava" and "distal lava" by Wainman et al. (2024).

The emissions from the post-eruptive lava are the highest for Zn (100 t), followed by Se, Cu, Sn, Pb and Sb (0.1-10 t) before As, Mo and Tl (50-100 kg). The least emitted elements during the post-eruptive lava degassing compared to the syn-eruptive degassing at the vent, are the chalcophile Te and Cd, whereas emissions of chloride or fluoride forming compounds (Zn, Mo, Sb) are comparable to vent emissions. The mass emissions from the syn- and post-eruptive lava are comparable but varies from one element to another. In particular, the mass of Te and Cd liberated post-eruptively is much lower, which highlight their very low volatility because of near exhaustion of sulphur. In contrast, most Cl- and F-affine elements are increasingly released post-eruptively, in particularly Zn.

In addition to the change in the gas composition, it must be noted that the spatiotemporal distribution of post-eruptive lava degassing is distinct from the emissions at the vent. The post-eruptive lava degassing is of much longer duration and locally concentrated. The potentially associated hazards are thus distinct, with the post-eruptive lava degassing being more likely to have longer albeit reduced environmental effects on the immediate vicinity of the crystallising lava field.

3.7 Conclusions

The primary and secondary gases from Fagradalsfjall have distinct compositions, with progressive depletion of sulphur relative to halogens, readily explained by different element solubilities and the fractional degassing process (i.e., Rayleigh distillation). The secondary gas has heterogeneous composition with distinct emissions from the syn-eruptive lava (Wainman et al. 2024), the post-eruptive crater and the post-eruptive lava. The gas composition of the extinct crater is similar to the gas collected the same way at Holuhraun and Kīlauea, whereas the post-eruptive lava gas exposes exceptionally high halogen-sulphur ratios.

The compositional difference between the different gas phases is reflected in the volatile metal and metalloids concentrations that vary by orders of magnitude. The high temperature S-rich primary gas is enriched in elements degassing as sulphide species or in their elemental form, such as Te and Cd, as was previously observed by Wainman et al. (2024). In contrast, chloride-forming elements such as Sb are enriched in the syn- and post-eruptive lava gas whereas fluoride-forming elements (Mo and Ru) tend to degas at the extinct crater. Comparing composition of the gas released from the syn-eruptive lava collected by Wainman et al. (2024) and gas from the crystallising lava reveal a stronger enrichment in Zn and Sn in the latter, elements known to form chloride species at low temperature.

The diversity in emitted gas composition highlights the dynamic outgassing process from an active gas plume at vent to a crystallising basalt lava. The difference of secondary gas emission compared to primary and its enrichment in some heavy metals such as Zn, Mo, Sb,

Sn and Pb emphasise the necessity to account for secondary degassing when investigating effects of volcanic degassing. The distinct emissions from the crystallising lava, in particularly as it ages, along with its specific spatio-temporal distribution, could result in hazard distinct from well-known primary degassing. Investigating the fate of the species emitted from the lava (such as their transport when released in the atmosphere and environmental lifetime) thus appear critical to assess this potential hazard. Along with that, monitoring the effect long-term secondary gas exposure on the flora and grazing animal surrounding the lava field would help constrains the consequences of secondary degassing.

Acknowledgements

We acknowledge the help of Sveinbjörn Steinþórsson during gas collection on the recently extinct and fragile 2021 crater. The assistance of Ríkey Kjartansdóttir and Glúmur Björnsson with the ion chromatography measurements and Krzysztof Suchorski during the trace element analyses was greatly appreciated. The project was funded by the Icelandic Research Fund (Rannís) and the ANR labex programme “ClerVolc”. We thank the anonymous reviewers for their comments which greatly improved the manuscript.

3.8 Supplementary information

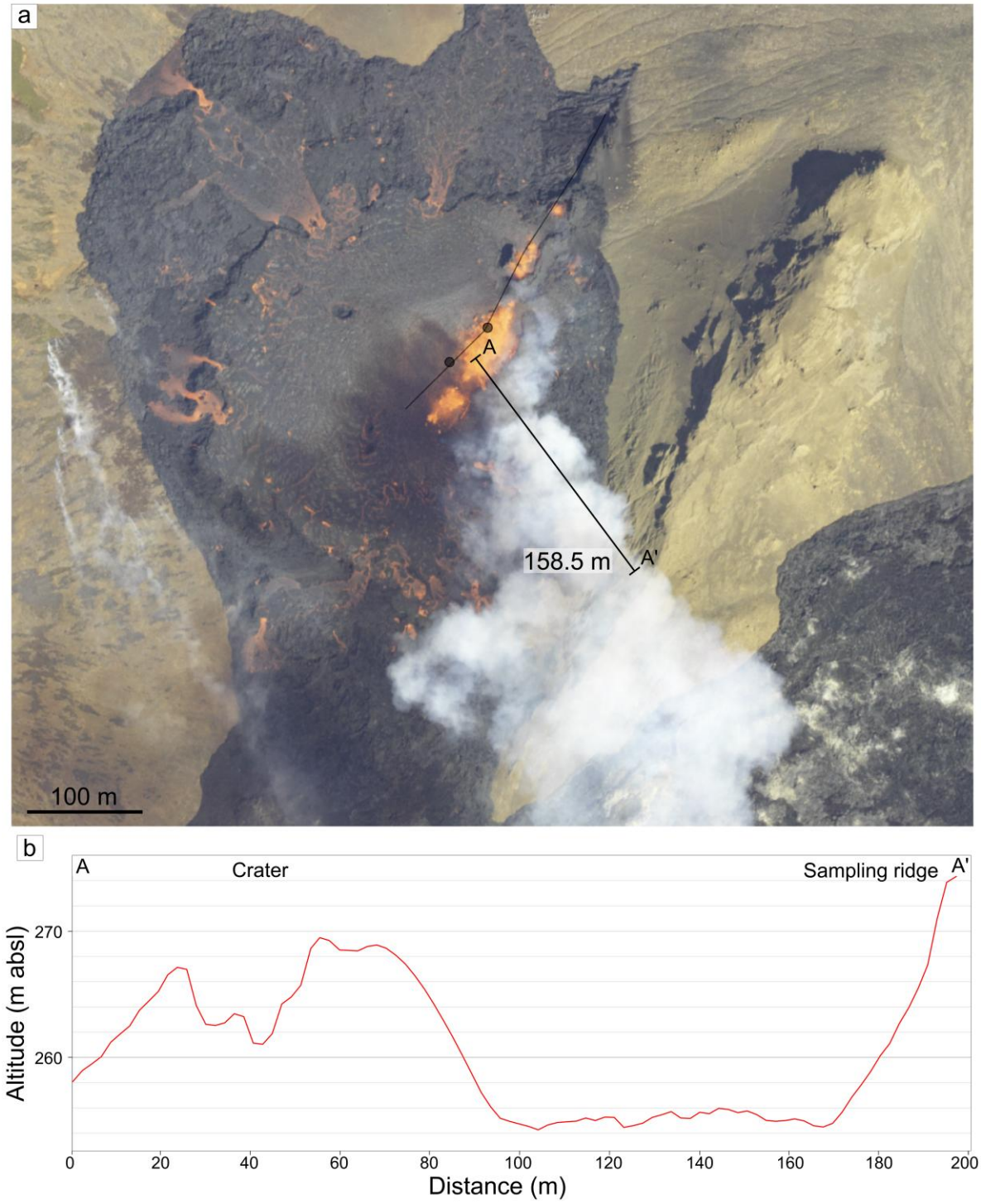

Supplementary Figure 3.1. Sampling location and conditions during the Fagradalsfjall 2022 (Meradalir) eruption. *a) Aerial picture (https://atlas.lmi.is/mapview/?application=umbrotasja) showing the location of the fissure and craters (dark grey segment and circles), the sampling ridge along with the distance between the two. The altitude profile AA' is shown in b). This aerial photo shows the favourable conditions for ground-sampling when the wind was blowing from the northwest, as a drone would have been much closer to the crater to avoid the extreme heat released and plume buoyancy. b) Altitude profile along the segment*

AA' drawn in a) showing how the buoyant crater gases can easily reach the sampling ridge compared to the degassing lava field, which low-lying gases are more likely to be blown lower down the ridge.

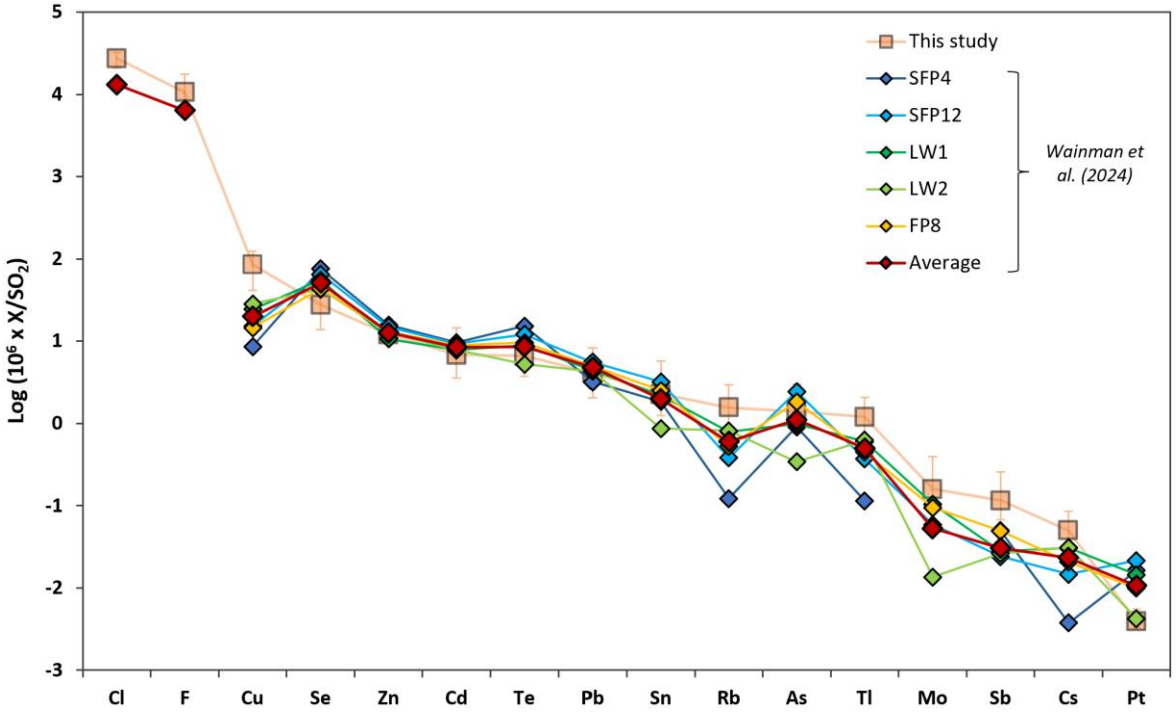

Supplementary Figure 3.2. Comparison between the Fagradalsfjall primary gas composition sampled during the different eruptions. *Data from this study is the average between the three analysed samples from the 2022 Meradalir eruption. The samples from Wainman et al. (2024) were collected during the 2021 (SFP4 and SFP12), 2022 (LW1 and LW2) and 2023 (FP8). The largest difference in composition is between the gas collected during the first days of the 2021 eruption (SFP4) and the other gas samples, the former having significantly lower Tl, Cs and Rb concentrations. Such result suggests an initial change in gas composition at the very beginning of the 2021 eruption, followed by relative compositional stability, as was observed for the lava and major gases (Halldórsson et al. 2022; Marshall et al. 2024; Matthews et al. 2024). Such change in gas and lava composition may be explained by the contribution of an undegassed magma coming from depth in the first week of the eruptions.*

Supplementary Table 3.1. Sampling conditions and sample details.

Sample name	Volume of major volatiles (m^3)	Paper filter	Volume of aerosols (m^3)	PTFE filter	Sampling date	Sample type	GPS Location
Blank-1	2.5	Whatman, 47 mm	2.5	Laminated Sterlitech	01/03/2022	Background air	63°51'36"N, 22°10'32"W
Blank-2	2.5	Whatman, 47 mm	2.5	Laminated Sterlitech	27/03/2023	Background air	63°51'36"N, 22°10'32"W
Blank-3	2.42	Whatman, 47 mm	2.42	Laminated Sterlitech	10/06/2023	Background air	63°51'36"N, 22°10'32"W
GD-3	2.5	Whatman, 47 mm	2.5	Laminated Sterlitech	17/11/2021	Post-eruptive lava	63°52'43"N, 22°17'02"W
GD-4	2.5	Whatman, 47 mm	2.5	Laminated Sterlitech	24/11/2021	Post-eruptive crater	63°53'24"N, 22°16'02"W
GD-6	2.5	Whatman, 47 mm	2.5	Laminated Sterlitech	06/03/2022	Post-eruptive lava	63°52'44"N, 22°16'59"W
GD-7	2.5	Whatman, 47 mm	2.5	Laminated Sterlitech	06/03/2022	Post-eruptive lava	63°53'32"N, 22°16'11"W
GD-8	2.5	Millipore, 37 mm	0.33	Laminated Sterlitech	20/07/2022	Post-eruptive lava	63°53'32"N, 22°16'11"W
GD-9	2.5	Millipore, 37 mm	0.33	Laminated Sterlitech	20/07/2022	Post-eruptive crater	63°53'24"N, 22°16'02"W
GD-10	1.25	Millipore, 37 mm	0.17	Unlaminated Sterlitech	16/03/2023	Post-eruptive crater	63°53'24"N, 22°16'02"W
GD-11	2.5	Millipore, 37 mm	0.33	Unlaminated Sterlitech	16/03/2023	Post-eruptive lava	63°53'32"N, 22°16'11"W
MD-2	2.5	Millipore, 37 mm	0.33	Unlaminated Sterlitech	10/08/2022	Syn-eruptive crater	63°53'54"N, 22°14'46"W
MD-3	2.5	Millipore, 37 mm	-	Unlaminated Sterlitech	10/08/2022	Syn-eruptive crater	63°53'54"N, 22°14'46"W
MD-4	2.5	Millipore, 37 mm	0.33	Unlaminated Sterlitech	10/08/2022	Syn-eruptive crater	63°53'54"N, 22°14'46"W
MD-5	2.5	Millipore, 37 mm	0.33	Unlaminated Sterlitech	12/08/2022	Syn-eruptive crater	63°53'54"N, 22°14'46"W
MD-6	2.5	Millipore, 37 mm	0.33	Unlaminated Sterlitech	16/08/2022	Syn-eruptive crater	63°53'54"N, 22°14'46"W
MD-7	2.5	Millipore, 37 mm	0.33	Unlaminated Sterlitech	23/09/2022	Post-eruptive lava	63°54'07"N, 22°14'58"W
MD-8	2.5	Millipore, 37 mm	0.33	Unlaminated Sterlitech	18/10/2022	Post-eruptive lava	63°54'06"N, 22°14'57"W
MD-9	2.5	Millipore, 37 mm	0.22	Unlaminated Sterlitech	16/03/2023	Post-eruptive lava	63°54'11"N, 22°14'54"W

Supplementary Table 3.2. Raw trace element concentrations (pg/filter) measured in the leachate of the PTFE filters.

Sample name	*Blank-1*	*Blank-2*	*Blank-3*	*GD-3*	*GD-4*	*GD-6*	*GD-7*	*GD-8*	*GD-9*	*MD-2*	*MD-4*	*MD-5*	*MD-6*	*MD-7*	*MD-8*	*GD-10*	*GD-11*	*MD-9*	*Standard deviation (2σ)*
Li	bdl	2.4E+3	177	394	6.2E+3	bdl	bdl	bdl	bdl	3.0E+3	8.9E+3	5.6E+3	1.4E+4	4.9E+4	4.2E+3	894	1.5E+3	715	2.1
Be	11	7.6	bdl	bdl	96	96	15	bdl	17	0	106	194	40	19	23	29	22	58	3.6
B	bdl	2.0E+4	3.2E+3	9.6E+4	1.6E+5	bdl	bdl	bdl	bdl	bdl	bdl	bdl	bdl	bdl	bdl	1.8E+4	5.6E+3	1.9E+6	33
Sc	195	633	144	56	250	925	bdl	293	348	bdl	8.1E+3	1.5E+4	1.7E+3	811	1.1E+3	bdl	bdl	381	7.1
V	1.1E+3	3.1E+3	459	1.4E+3	3.6E+5	6.5E+3	1.2E+3	7.1E+3	2.9E+5	1.0E+3	6.0E+4	1.1E+5	1.6E+4	7.6E+3	4.3E+4	7.9E+3	1.6E+3	4.4E+3	6.5
Cr	6.1E+4	8.7E+3	2.7E+4	6.1E+4	6.6E+4	8.2E+4	7.4E+4	5.0E+4	6.4E+4	6.4E+4	1.2E+5	1.1E+5	3.1E+4	2.3E+4	1.1E+5	6.4E+3	4.4E+3	1.5E+4	5.9
Mn	1.8E+4	1.4E+4	1.2E+3	bdl	2.8E+3	1.9E+5	bdl	9.4E+3	bdl	bdl	2.6E+5	4.8E+5	2.8E+5	1.0E+5	1.4E+5	1.5E+4	9.4E+3	3.0E+4	5.3
Co	5.1E+3	847	56	181	243	2.1E+4	2.7E+4	123	bdl	bdl	9.7E+3	1.5E+4	3.8E+3	1.2E+3	1.2E+3	851	296	761	5.4
Ni	1.1E+4	3.3E+3	478	1.2E+3	2.6E+3	3.4E+4	3.3E+4	bdl	bdl	890	2.7E+4	6.0E+4	3.8E+4	1.9E+4	8.9E+3	3.5E+3	5.9E+3	1.0E+4	4.5
Cu	2.4E+3	1.4E+4	2.1E+3	5.8E+3	5.1E+5	1.8E+4	2.3E+4	8.1E+3	3.2E+4	6.3E+3	1.0E+6	2.1E+6	2.8E+5	2.3E+4	1.2E+5	7.8E+3	6.2E+3	4.5E+4	4.8
Zn	1.9E+4	2.5E+5	1.2E+4	1.1E+4	7.2E+4	8.5E+4	1.0E+6	2.7E+4	4.9E+4	4.4E+4	1.9E+5	4.6E+5	1.3E+5	2.9E+5	4.8E+4	7.3E+4	1.3E+5	4.3E+6	7.3
Ga	bdl	214	24	108	58	1.6E+4	bdl	bdl	bdl	bdl	3.8E+3	6.2E+3	1.1E+3	355	313	315	144	1.1E+3	6.1
Ge	bdl	116	9.2	11	56	422	bdl	bdl	bdl	bdl	1.8E+4	1.8E+4	4.6E+3	324	258	58	bdl	490	4.4
As	171	359	31	834	3.2E+4	6.2E+3	129	195	8.6E+3	173	1.8E+4	2.0E+4	6.8E+3	628	3.4E+3	364	bdl	5.2E+3	5.2
Se	bdl	bdl	142	4.9E+3	3.6E+5	3.9E+3	2.5E+3	1.9E+4	2.6E+5	bdl	3.3E+5	6.0E+5	9.6E+4	1.1E+4	3.3E+5	6.4E+4	3.5E+3	3.8E+5	0.91
Rb	289	254	62	188	2.4E+4	1.7E+3	1.5E+3	bdl	3.0E+3	323	1.7E+4	3.4E+4	7.1E+3	1.7E+3	1.4E+3	430	295	1.4E+3	3.5
Sr	bdl	2.8E+3	1.0E+3	81	2.1E+3	1.8E+4	bdl	bdl	bdl	bdl	8.2E+4	1.5E+5	2.0E+4	5.7E+3	4.7E+3	4.6E+3	2.6E+3	6.0E+4	3.7
Y	187	269	29	bdl	158	1.9E+3	112	143	252	45	3.5E+3	6.5E+3	1.4E+3	529	510	625	166	1.3E+3	3.6
Zr	2.2E+3	3.7E+3	598	1.5E+3	2.3E+3	2.1E+4	1.9E+3	2.8E+3	2.4E+3	669	2.3E+4	4.0E+4	1.3E+4	6.9E+3	6.3E+3	2.5E+3	2.4E+3	1.2E+4	3.2
Nb	bdl	540	53	55	169	1.5E+3	bdl	bdl	bdl	bdl	2.0E+3	4.4E+3	875	bdl	bdl	232	142	1.6E+3	3.7
Mo	931	245	48	265	1.9E+5	4.1E+3	bdl	3.0E+3	4.1E+5	bdl	1.5E+3	3.9E+3	1.2E+3	642	2.5E+4	7.3E+3	169	1.7E+3	3.3
Ru	bdl	bdl	1.0	bdl	7.5	bdl	bdl	bdl	35	bdl	bdl	bdl	bdl	bdl	bdl	6.2	bdl	bdl	4.9
Rh	bdl	0.38	0.44	bdl	0.87	1.1	bdl	bdl	bdl	0.79	7.6	13	2.4	0.47	1.4	1.3	bdl	1.3	3.9
Pd	16	bdl	3.0	bdl	78	41	bdl	bdl	bdl	bdl	193	188	61	12	12	bdl	bdl	22	3.0
Ag	231	954	934	5.2E+4	5.1E+5	373	1.3E+3	1.4E+3	3.2E+3	201	4.4E+3	8.2E+3	3.3E+3	976	2.2E+3	1.2E+3	367	2.4E+4	3.0
Cd	20	150	30	104	2.0E+3	232	229	268	811	353	8.4E+4	1.0E+5	3.3E+4	1.2E+3	1.2E+3	79	231	1.7E+3	3.0
In	9.5	22	1.1	2.1	3.5	273	23	27	195	25	3.7E+3	4.3E+3	1.0E+3	34	45	8.2	5.8	650	3.4
Sn	675	2.6E+3	231	768	1.1E+3	3.2E+3	2.8E+3	7.2E+3	5.8E+4	1.3E+3	3.2E+4	3.0E+4	1.6E+4	6.6E+3	6.7E+3	1.7E+3	1.3E+3	3.1E+4	2.5
Sb	131	903	57	66	170	807	581	89	207	1.8E+3	3.0E+3	2.0E+3	1.5E+3	1.9E+3	752	529	424	5.1E+3	3.2
Te	bdl	43	bdl	210	3.8E+4	151	44	220	1.6E+4	265	8.9E+4	1.0E+5	2.9E+4	228	2.3E+3	106	bdl	93	2.2
Cs	bdl	6.2	5.8	2.7	703	38	bdl	bdl	143	17	554	1.1E+3	203	22	87	6.9	bdl	425	3.0
Ba	1.8E+4	3.8E+3	1.1E+3	5.7E+3	6.3E+3	6.1E+4	bdl	bdl	bdl	2.1E+4	3.7E+4	2.4E+5	3.0E+4	2.7E+4	6.0E+3	2.4E+3	2.1E+3	1.9E+4	2.4
La	bdl	302	35	bdl	100	3.8E+5	bdl	bdl	bdl	bdl	1.7E+3	3.4E+3	640	379	202	332	164	4.5E+3	3.1
Ce	bdl	445	64	bdl	169	7.1E+5	bdl	208	bdl	bdl	4.1E+3	8.2E+3	1.3E+3	449	391	696	323	4.4E+3	3.3
Pr	bdl	55	8.3	bdl	22	2.1E+3	bdl	bdl	bdl	bdl	486	994	164	64	54	90	37	514	2.8
Nd	bdl	228	32	bdl	109	4.3E+3	bdl	bdl	bdl	bdl	2.3E+3	4.6E+3	805	255	238	400	132	1.8E+3	2.6
Sm	bdl	46	6.8	bdl	35	408	bdl	bdl	16	bdl	563	1.1E+3	200	44	72	96	36	336	2.2
Eu	bdl	17	1.6	bdl	8.5	122	bdl	bdl	bdl	bdl	192	387	90	31	20	33	13	95	3.0
Tb	4.4	8.2	0.91	bdl	6.2	142	bdl	bdl	5.8	bdl	109	203	36	15	14	17	4.9	49	2.8
Gd	18	52	7.5	bdl	29	443	bdl	bdl	36	bdl	655	1.2E+3	235	87	90	117	37	306	2.3
Dy	31	51	4.8	bdl	26	369	bdl	bdl	bdl	bdl	669	1.3E+3	219	94	93	107	37	244	1.3
Ho	9.3	10	1.4	bdl	5.0	74	bdl	bdl	11	bdl	144	259	45	20	21	24	7.4	43	2.4
Er	19	30	2.7	bdl	18	224	bdl	12	27	bdl	397	778	139	52	49	67	19	114	2.6
Tm	3.0	4.9	0.43	bdl	1.4	30	bdl	bdl	4.0	1.9	56	111	17	8.8	8.2	9.6	4.9	13	2.5
Yb	24	37	3.2	bdl	11	179	bdl	18	31	bdl	365	698	119	49	46	55	14	97	2.6
Lu	bdl	4.0	0.54	bdl	1.2	29	bdl	bdl	bdl	bdl	55	103	16	9.8	8.3	7.8	1.4	13	2.3
Hf	47	99	17	32	60	404	43	65	58	bdl	511	899	279	148	143	64	63	309	2.0
Ta	bdl	37	6.4	12	6.1	99	bdl	32	bdl	bdl	127	299	69	bdl	54	23	19	174	2.0
W	456	1.1E+3	71	1.1E+3	7.7E+3	543	1.1E+3	3.4E+3	1.0E+4	3.2E+3	1.7E+3	3.6E+3	6.9E+3	1.2E+3	3.1E+3	1.8E+3	785	293	0.23
Re	bdl	0.27	0.100	111	3.1E+3	12	10	13	617	9.1	3.3E+3	5.3E+3	849	178	2.3E+3	88	8.4	156	2.0
Ir	bdl	0.97	0.73	bdl	11	12	1.8	bdl	16	1.2	76	79	21	2.6	bdl	2.0	2.2	0.16	2.5
Pt	bdl	5.1	5.1	2.5	324	12	bdl	bdl	47	bdl	100	81	34	16	16	5.8	6.0	14	2.6
Au	37	46	7.8	4.3	4.3E+3	12	11	28	2.5E+3	45	663	614	287	33	149	58	bdl	407	2.9
Tl	9.4	3.1	bdl	617	5.7E+4	12	179	3.8E+3	6.9E+4	30	1.3E+4	2.6E+4	4.7E+3	44	2.2E+4	222	7.3	206	2.4
Pb	660	1.7E+3	299	482	1.5E+4	12	5.6E+3	1.0E+3	2.6E+3	906	5.0E+4	7.1E+4	2.1E+4	3.9E+3	4.0E+3	589	831	2.8E+4	1.9
Bi	24	60	7.2	95	1.0E+3	12	68	30	84	71	1.1E+4	1.4E+4	3.4E+3	153	500	26	8.8	947	2.3
Th	bdl	29	5.9	bdl	6.8	12	bdl	bdl	bdl	bdl	149	326	55	24	51	34	51	373	2.6
U	4.8	20	2.3	bdl	28	12	bdl	bdl	4.6	bdl	52	109	26	13	13	5.8	8.0	75	2.5

Supplementary Table 3.3. Blank details and volatile metal concentrations (pg/filter).

	Blank-1	Blank-2	Blank-3
Filter type	Laminated Sterlitech	Unaminated Sterlitech	Unaminated Sterlitech
ICP-MS	Agilent 7500	Agilent 7500	Agilent 8900
Cu	2.45E+03	1.33E+04	2.1E+03
Zn	1.89E+04	2.40E+05	1.2E+04
As	bdl	267	31
Se	bdl	606	142
Rb	289	254	62
Mo	931	245	48
Ag	231	954	934
Cd	20	150	30
In	9	22	1
Sn	675	2.6E+03	231
Sb	131	903	57
Te	bdl	43	bdl
Cs	bdl	6	6
W	456	1.1E+03	71
Re	bdl	0.27	0.10
Ir	bdl	0.97	0.73
Pt	bdl	5.1	5.1
Au	37	46	8
Tl	9.4	3.1	bdl
Pb	660	1.7E+03	299
Bi	24	60	7

The comparison of blank-1 and blank-2 reveals the difference between the Sterlitech® laminated and unlaminated filters on the blank composition. With respect to blank-1, blank-2 has higher concentrations of volatile metals (except for Mo and Tl) by up to an order of magnitude. The blank 2 and 3 comparison demonstrates significantly lower instrumental blank contribution from the Agilent® 8900 ICP-MS. The differences in blank composition make it necessary to correct the measured gas composition with a corresponding filter blank.

Supplementary Table 3.4. Major volatile concentrations in the Fagradalsfjall gas (µg.m^{-3}).

	S	Cl	F
GD-3	-	19	-
GD-4	1695	1734	1652
GD-6	-	5.9	5.5
GD-7	-	-	-
GD-8	27	2231	523
GD-9	1545	2883	3672
GD-10	-	-	-
GD-11	-	-	-
MD-2	3208	174	64
MD-3	18995	1316	370
MD-4	14235	600	200
MD-5	10035	605	198
MD-6	1371	89	48
MD-8	18	1581	654
MD-9	36	1871	137

Supplementary Table 3.5. Calculated weight ash fraction (%) using Sc as the nominally refractory element.

		MD-4	MD-5	MD-6	MD-9	GD-6	GD-9
Volatile trace elements	Cu	2.40	2.16	1.34	1.79	**14.9**	1.66
	Zn	--	**11.0**	--	0.01	1.82	0.84
	Ge	1.43	2.70	0.86	1.71	**5.99**	--
	As	0.32	0.52	0.13	0.03	0.09	0.01
	Se	0.00	0.00	0.00	0.00	0.02	0.00
	Rb	2.97	2.71	1.05	1.15	3.24	0.37
	Mo	0.56	0.36	0.11	0.01	0.02	0.00
	Ag	0.52	0.46	0.11	0.00	1.22	0.01
	Cd	0.02	0.03	0.01	0.03	0.69	0.04
	In	0.29	0.48	0.16	0.05	0.40	0.12
	Sn	0.27	0.53	0.09	0.01	0.31	0.00
	Sb	0.09	0.31	0.05	0.00	0.03	0.05
	Te	0.00	0.00	0.00	0.03	0.06	0.00
	Cs	1.26	1.20	0.52	0.05	1.80	0.10
	W	4.09	1.90	0.07	0.37	--	0.01
	Re	0.00	0.01	0.00	0.00	0.12	0.00
	Ir	0.10	0.18	0.05	--	0.78	0.01
	Pt	2.24	**5.21**	1.10	0.74	--	0.09
	Au	0.37	0.75	0.14	0.02	--	0.00
	Tl	0.02	0.01	0.01	0.03	0.08	0.00
	Pb	0.13	0.17	0.05	0.01	0.04	0.07
	Bi	0.01	0.01	0.00	0.00	0.02	0.02
Refractory elements	Sc	**100.0**	**100.0**	**100.0**	**100.0**	**100.0**	**100.0**
	V	**84.4**	**85.4**	**54.7**	**38.8**	**87.6**	0.34
	Mn	**96.0**	**96.2**	**13.0**	**25.9**	**13.7**	--
	Sr	**25.8**	**25.6**	**17.5**	1.10	**11.2**	--
	Y	**106**	**102**	**45.7**	**8.76**	**19.3**	--
	Zr	**44.5**	**45.5**	**13.8**	2.31	4.54	--
	La	**51.6**	**44.4**	**32.6**	0.53	0.02	--
	Ce	**49.8**	**44.2**	**30.8**	1.33	0.03	--
	Sm	**74.4**	**69.9**	**37.0**	3.70	**9.22**	**49.2**
	Gd	**76.9**	**74.2**	**37.6**	4.92	**10.6**	**51.8**
	Yb	**104**	**96.8**	**61.7**	**11.6**	**21.5**	--
	Lu	**102**	**98.2**	**66.0**	**13.3**	**17.7**	--
	Th	**52.0**	**39.2**	**35.0**	0.54	3.22	--

Solid particles often adhere to the filters while sampling the gas phase. The weight ash fraction (WAF, Aiuppa. 2003) was estimated using Sc, an element considered as one of the most refractory. The WAF is just calculated: WAF (%) = $(Sc_g/Sc_r)/(X_g/X_r)$ x 100 and the results are shown in supplementary Table 3.5. Because of the important air dilution and its virtual absence in the background air, Sc is sometimes found below detection limit in the secondary gas. The samples MD-9 and GD-6 allowed however to verify that ash contribution was low for all selected trace elements but significant for Ge (7 %) and Cu (15 %) in GD-6. Among the post eruptive lava gas, only GD-9 showed significant Sc concentration and its WAF shows no significant solid particle contribution for the volatile trace elements. Regarding the syn-eruptive crater gas, solid particle contribution is minimal with WAF below ten percent for all elements, except Zn (11 %) and Pt (5 %) in MD-5. Given the low WAF found overall, it was chosen not to correct for it to keep consistent data processing for al samples. The solid particle contribution to the less volatile elements is high for the syn-eruptive crater gas (generally 40 to 100 %).

Supplementary Table 3.6. Trace elements analysis of the Fagradalsfjall lava and glass used for normalisation of the gas composition (wt ppm). *The glass composition from Wainman et al. (2024) correspond to the average of the four glasses analysed conducted, which displayed no systematic differences. Results from Marshall et al. (2024) correspond to the average of eight glass analyses from March samples and eight glass analyses from August and September 2021.*

	21/03/2021 whole rock (this study)	08/09/2021 whole rock (this study)	Glass composition (Wainman et al. 2024)	March 2021 glass (Marshall et al. 2024)	September 2021 glass (Marshall et al. 2024)
Li	13	3.8	4.6	4.0	4.1
Be	0.33	0.45	0.44	0.32	0.44
B	0.10	0.79			
Sc	43.9	38	47	44	44
V	282	261	346	294	298
Cr	330	597	255	304	460
Mn	1.4E-03	1.3E-03	1.5E-03		
Co	48	58	47	47	49
Ni	125	180	73	113	141
Cu	141	103	147	144	117
Zn	72	72	103	76	75
Ga	15	14	16		
Ge	1.5	1.4	1.7		
As	0.32				
Se	0.055				
Rb	2.8	5.2	8.1	3.0	5.7
Sr	120	159	163	119	162
Y	20	18	20		
Zr	51	61	77	51	62
Nb	6.0	9.6	14	6.4	9.9
Mo	0.41	0.57	0.6		
Ru	6.6E-05	2.6E-05			
Rh	3.2E-04	2.6E-04			
Pd	0.0076	0.00156			
Ag	0.10				
Cd	0.088	0.085	0.10		
In	0.064		0.073		
Sn	0.46	0.79	0.80		
Sb	0.011	0.015	0.033		
Te	0.0057				
Cs	0.041	0.059	0.10	0.035	0.058
Ba	41	67	96	43	74
La	4.4	7.1	10		
Ce	11	17	23	11	18
Pr	1.5	2.2	3	1.6	2.4
Nd	7.4	9.8	13	7.5	11
Sm	2.3	2.5	3.3	2.3	2.7
Eu	0.82	0.91	1.2	0.79	0.98
Tb	0.51	0.51	0.60	0.52	0.56
Gd	2.7	3.0	3.6	2.9	3.2
Dy	3.4	3.3	3.8	3.4	3.5
Ho	0.73	0.69	0.81	0.74	0.75
Er	2.1	1.9	2.3	2.1	2.1
Tm	0.32	0.29	0.33	0.32	0.32
Yb	2.0	1.9	2.3	2.1	2.1
Lu	0.30	0.28	0.33	0.31	0.31
Hf	1.4	1.7	2.1	1.5	1.7
Ta	0.38	0.60	0.8	0.41	0.64
W	0.15		0.15		
Re	8.5E-04	0.0013			
Ir	4.3E-04	3.3E-04			
Pt	0.012	0.0062			
Au	0.013				
Tl	0.012	0.0069	0.010		
Pb	0.38	0.57	0.76	0.34	0.55
Bi	0.0033	0.0041	0.010		
Th	0.36	0.63	0.91	0.36	0.68
U	0.091	0.19	0.29	0.11	0.21

The lava samples analysed in this study were powdered and digested by acid following the procedure described by Zhang et al. (2012), and described in section 2.3.3.

Comparing the analyses of two lavas collected at Fagradalsfjall (in March and September 2021) along with the laser ablation measurements on Fagradalsfjall lava glass reported by Wainman et al. (2024) reveals comparable results (Supplementary Table 3.6). Between the two lavas, most elements display similar concentrations (difference < 20 %), the compatible elements being generally slightly more enriched in the September lava and the incompatible elements slightly enriched in the March one. These results are in very good agreements with the average glass composition reported by Marshall et al. (2024). This similarity is visible for all analysed elements and for both Marsh and September lavas. The results are also comparable to the glass analyses from Wainman et al. (2024), though more significant differences can be observed. A few elements display more substantial concentration differences between the two lavas, with Ir being 13 times more concentrated in the early lava than the late one, Pd 5 times, Ru 2.5 times and Pt 2 times. These elements were not analysed in the glass by Wainman et al. (2024) or Marshall et al. (2024), thus not permitting to know which value is the most trustworthy. The March lava was chosen for normalisation as its analysis recovers all the elements analysed in the gas, unlike the September lava.

Supplementary Table 3.7. Calculation of volatile trace element emissions from the eruptive crater and the post-eruptive lava.

	Measured elements over halogen ratio in the Fagradalsfjall gas types				Calculated volatile trace element emissions			
	Average X/Cl		Average X/F		Emitted mass using Cl		Emitted mass using F	
	Syn-eruptive crater	Post-eruptive lava	Syn-eruptive crater	Post-eruptive lava	Syn-eruptive crater	Post-eruptive lava	Syn-eruptive crater	Post-eruptive lava
Li	5.7E-5	2.8E-7	1.1E-4	1.3E-6	1.1E+3	2.3E+0	3.0E+3	2.1E+1
Be	3.4E-7	8.1E-9	8.5E-7	8.9E-8	6.7E+0	6.5E-2	2.3E+1	1.4E+0
B		4.0E-4		5.4E-3		3.2E+3		8.4E+4
Sc	1.9E-5	6.0E-8	5.3E-5	3.5E-7	3.8E+2	4.8E-1	1.4E+3	5.4E+0
V	1.7E-4	4.0E-6	4.4E-4	1.4E-5	3.3E+3	3.2E+1	1.2E+4	2.1E+2
Cr	2.4E-4	2.5E-5	6.2E-4	6.1E-5	4.8E+3	2.0E+2	1.6E+4	9.5E+2
Mn	1.7E-3	1.9E-5	3.7E-3	8.1E-5	3.3E+4	1.5E+2	9.8E+4	1.3E+3
Fe	1.1E-1	4.8E-4	2.1E-1	3.1E-3	2.2E+6	3.9E+3	5.7E+6	4.8E+4
Co	2.8E-5	1.5E-7	7.1E-5	2.1E-6	5.6E+2	1.2E+0	1.9E+3	3.2E+1
Ni	2.1E-4	1.8E-6	4.5E-4	1.6E-5	4.1E+3	1.4E+1	1.2E+4	2.5E+2
Cu	3.3E-3	1.2E-5	8.5E-3	6.5E-5	6.5E+4	1.0E+2	2.3E+5	1.0E+3
Zn	4.2E-4	9.1E-4	1.3E-3	1.2E-2	8.3E+3	7.4E+3	3.4E+4	1.9E+5
Ga	1.0E-5	2.4E-7	2.7E-5	3.3E-6	2.0E+2	1.9E+0	7.1E+2	5.1E+1
Ge	4.4E-5	6.9E-8	1.1E-4	7.5E-7	8.7E+2	5.6E-1	2.9E+3	1.2E+1
As	5.4E-5	9.4E-7	1.3E-4	8.5E-6	1.1E+3	7.6E+0	3.4E+3	1.3E+2
Se	1.1E-3	5.6E-5	2.7E-3	4.4E-4	2.1E+4	4.5E+2	7.1E+4	6.9E+3
Rb	6.4E-5	2.9E-7	1.6E-4	2.3E-6	1.3E+3	2.4E+0	4.2E+3	3.6E+1
Sr	2.3E-4	6.5E-6	6.1E-4	8.7E-5	4.6E+3	5.3E+1	1.6E+4	1.3E+3
Y	1.1E-5	1.6E-7	2.8E-5	1.9E-6	2.2E+2	1.3E+0	7.6E+2	2.9E+1
Zr	7.9E-5	1.6E-6	1.9E-4	1.8E-5	1.6E+3	1.3E+1	5.0E+3	2.8E+2
Nb	5.0E-6	3.3E-7	1.3E-5	4.5E-6	9.9E+1	2.6E+0	3.6E+2	7.0E+1
Mo	7.4E-6	2.3E-6	1.7E-5	7.2E-6	1.5E+2	1.9E+1	4.6E+2	1.1E+2
Ru	-	-	-	-	-	-	-	-
Rh	2.2E-8	2.2E-10	5.6E-8	1.6E-9	4.4E-1	1.7E-3	1.5E+0	2.4E-2
Pd	5.3E-7	3.5E-9	1.3E-6	3.1E-8	1.0E+1	2.8E-2	3.4E+1	4.8E-1
Ag	1.8E-5	1.8E-6	4.1E-5	2.3E-5	3.5E+2	1.4E+1	1.1E+3	3.5E+2
Cd	2.7E-4	2.2E-7	6.5E-4	1.9E-6	5.4E+3	1.8E+0	1.7E+4	2.9E+1
In	9.8E-6	4.9E-8	2.4E-5	6.4E-7	1.9E+2	4.0E-1	6.5E+2	1.0E+1
Sn	9.7E-5	2.9E-6	2.3E-4	3.3E-5	1.9E+3	2.4E+1	6.0E+3	5.1E+2
Sb	4.8E-6	1.1E-6	1.1E-5	1.5E-5	9.5E+1	8.6E+0	3.0E+2	2.3E+2
Te	2.6E-4	2.1E-7	6.3E-4	6.0E-7	5.1E+3	1.7E+0	1.7E+4	9.3E+0
Cs	2.0E-6	5.5E-8	4.9E-6	6.4E-7	3.9E+1	4.4E-1	1.3E+2	9.9E+0
Ba	3.0E-4	2.2E-6	7.7E-4	2.7E-5	5.9E+3	1.8E+1	2.0E+4	4.2E+2
La	4.6E-6	9.6E-7	1.2E-5	1.3E-5	9.0E+1	7.7E+0	3.2E+2	2.0E+2
Ce	1.2E-5	4.8E-7	3.0E-5	6.4E-6	2.3E+2	3.9E+0	8.1E+2	1.0E+2
Pr	1.4E-6	1.1E-7	3.7E-6	1.5E-6	2.8E+1	8.7E-1	9.8E+1	2.3E+1
Nd	6.9E-6	3.9E-7	1.8E-5	5.3E-6	1.4E+2	3.1E+0	4.7E+2	8.3E+1
Sm	1.7E-6	3.8E-8	4.4E-6	4.9E-7	3.4E+1	3.1E-1	1.2E+2	7.6E+0
Eu	6.9E-7	2.0E-8	1.7E-6	2.7E-7	1.4E+1	1.6E-1	4.5E+1	4.2E+0
Tb	3.2E-7	5.9E-9	8.3E-7	7.3E-8	6.4E+0	4.8E-2	2.2E+1	1.1E+0
Gd	2.0E-6	3.7E-8	5.1E-6	4.5E-7	4.0E+1	3.0E-1	1.4E+2	7.0E+0
Dy	2.0E-6	3.1E-8	5.1E-6	3.6E-7	3.9E+1	2.5E-1	1.4E+2	5.6E+0
Ho	4.1E-7	5.9E-9	1.1E-6	6.5E-8	8.1E+0	4.7E-2	2.8E+1	1.0E+0
Er	1.2E-6	1.4E-8	3.2E-6	1.7E-7	2.4E+1	1.2E-1	8.4E+1	2.6E+0
Tm	1.6E-7	1.8E-9	4.2E-7	2.0E-8	3.2E+0	1.4E-2	1.1E+1	3.1E-1
Yb	1.0E-6	2.0E-8	2.7E-6	2.7E-7	2.0E+1	1.6E-1	7.1E+1	4.2E+0
Lu	1.5E-7	1.9E-9	4.0E-7	1.9E-8	3.0E+0	1.5E-2	1.1E+1	3.0E-1
Hf	1.6E-6	6.2E-8	4.0E-6	8.5E-7	3.2E+1	5.0E-1	1.1E+2	1.3E+1
Ta	3.8E-7	2.1E-8	9.7E-7	2.6E-7	7.4E+0	1.7E-1	2.6E+1	4.0E+0
W	2.8E-5	3.7E-7	5.5E-5	1.4E-6	5.6E+2	3.0E+0	1.5E+3	2.2E+1
Re	9.6E-6	2.0E-7	2.4E-5	6.2E-7	1.9E+2	1.6E+0	6.5E+2	9.6E+0
Ir	1.9E-7	-	4.8E-7	-	3.8E+0	-	1.3E+1	-
Pt	2.4E-7	2.3E-9	5.8E-7	1.6E-8	4.8E+0	1.9E-2	1.5E+1	2.6E-1
Au	1.9E-6	5.6E-8	4.4E-6	6.1E-7	3.7E+1	4.5E-1	1.2E+2	9.6E+0
Tl	4.7E-5	2.1E-6	1.2E-4	5.6E-6	9.3E+2	1.7E+1	3.1E+3	8.7E+1
Pb	1.6E-4	2.2E-6	4.0E-4	2.7E-5	3.2E+3	1.8E+1	1.1E+4	4.3E+2
Bi	3.2E-5	1.6E-7	7.8E-5	1.5E-6	6.3E+2	1.3E+0	2.1E+3	2.3E+1
Th	4.0E-7	4.2E-8	1.1E-6	5.4E-7	7.8E+0	3.4E-1	2.8E+1	8.4E+0
U	1.2E-7	1.6E-8	3.7E-7	2.1E-7	2.4E+0	1.3E-1	9.9E+0	3.3E+0

4 Chapter 4

Role of segregation processes on volatile degassing during basalt lava crystallisation

Nicolas Levillayer, Olgeir Sigmarsson

About this chapter

This chapter was submitted to Journal of Volcanology and Geothermal Research and is currently under revision. This chapter focuses on detail characterisation of the segregations and associated host lava composition to assess the connection between volatile circulation and segregation formation in crystallising lava fields and subsequent lava degassing.

Author contribution

Conceptualisation: NL and OS; Methodology: NL, OS; Formal analysis and investigation: NL and OS; Visualisation: NL; Writing original draft preparation: NL and OS; Writing review and editing: NL and OS; Funding acquisition: OS

Keywords

Volcanic degassing; Lava differentiation; Toxic metal emission; Segregation veins; Volatile elements behaviour; Basaltic eruptions.

4.1 Abstract

Atmospheric loading of volatile metals from crystallising basalt lava and consequent environmental impacts are largely unknown. During basaltic lava eruption, most degassing occurs at the eruptive crater, but non-negligible post-eruptive degassing takes place during the lava emplacement and solidification. Moreover, such secondary degassing is known to be enriched in halogens and volatile metals forming halide species. One mechanism that may trigger gas liberation from a solidifying lava is the gas-filter pressing process and formation of segregation structures. The composition of such segregations may reveal the functionning of the post-eruptive lava degassing. Here are presented the segregation configurations in three basalt lava, one Holocene olivine-tholeiite lava from Reykjanes Peninsula and two FeTi-rich transitional lava from Hekla and Eldgjá, south Iceland. Textural and mineralogical constraints along with whole-rock compositions reveal different maturity stages of the segregations. Moderately evolved vesicle cylinders occupy the lava core, leading to formation of horizontal vesicle sheets at the core-upper crust boundary that develop into megavesicles (MV), containing the most evolved segregation product. In most cases the volatile metals behave as highly incompatible elements such as Th, but MVs are occasionally over-enriched in volatile metal. A few tholeiitic MVs are for instance enriched in Mo, Pb and Sb, whereas MVs with high concentrations in numerous volatile metal (Pb, As, Cd, In, Sn, Sb and Mo) are present in the FeTi-rich basalts. The enrichments could be explained by occasional condensation of the gas phase in the MVs, whereas the gas phase most likely escaped the nonenriched MVs leading to the atmospheric loading of toxic metals. The volatile metals over-enrichments suggest condensation of a gas phase rich in Sn, Pb and Mo but poor in Cd, similar to the post eruptive lava gas.

4.2 Introduction

During large effusive eruptions, a significant proportion (> 10 %) of the volcanic gas is emitted secondarily, from the cooling and crystallising lava (Óskarsson et al. 1984; Thordarson et al. 1996, 2001). Such secondary degassing is of particular importance for more soluble volatiles such as halogens (Aiuppa et al. 2002; Sigmarsson et al. 2020) and metals forming halide volatile species (Wainman et al. 2024; Chapter 3). However, the mechanism by which lava degasses during solidification remains poorly constrained (Anderson et al. 1984; Wilmoth and Walker 1993; Cashman et al. 1994; Fowler et al. 2015).

Coarse-grained and vesicle-rich structures within basaltic lava flows or lava lakes are most likely caused by internal magma differentiation and gas-filter pressing during the solidification (Helz 1980, 1987; Anderson et al. 1984). Although the exact physical mechanisms are still debated (Goff 1996; Costa et al. 2006; Fowler et al. 2015), the genesis of the segregation melt and associated structures has been shown to result from the crystallisation of anhydrous minerals, giving rise to a volatile-rich residual melt (Kuno 1965; Anderson et al. 1984; Goff 1996; Caroff et al. 2000; Martin and Sigmarsson 2007; Sigmarsson et al. 2009; Kuritani et al. 2010; Sheth et al. 2017; Nikkola et al. 2019). The residual melt is enriched in incompatible volatile elements that may reach saturation, exsolve, and form a gas phase. The pressure increase caused by the enhanced volume needed for the gas phase eventually leads to gas-filter pressing of the volatile-rich segregation melt through the crystallising magma towards a lower pressure region of the lava flow (vesicles, fissures, etc.; Anderson et al. 1984).

Little attention has however been paid to the behaviour of the volatile elements during the segregation processes, elements that may improve our understanding of lava outgassing and the potential environmental impacts associated with toxic metal release. To test the hypothesis that lava outgassing may be associated with the segregation formation, segregations from three basalt lavas in Iceland are examined in this work. The three lavas were selected to cover the range of basaltic volcanic activity taking place on the island (small eruptions, eruptive "Fires", and flood basalt eruptions). Additionally, sampled lava have distinct composition, ranging from tholeiitic to transitional basalts. We show that the liquid lava degassing is synchronous with the internal differentiation and segregation formation during which, gas, liquid and solid separation occurs before the complete lava solidification. The gas phase may either escape the lava through fractures to the surface, precipitate within the segregation system or condensate within the last drop of melt leading to high concentrations of volatile metals and metalloids.

4.3 Geological setting and sample description

Fissure eruptions are frequent in Iceland, producing basaltic lava fields of variable size and thickness. The internal structure of the lava is often rather complex with sub-units of upper crust, lava core and lower crust (i.e., Thordarson and Self 1998). Segregation features are often visible in lava lobes. When such features are observed, the host lava has a diktytaxitic texture (i.e., angular voids between interlocking crystals; Anderson et al. 1984) together with various types of segregations (solidified segregation melt, Table 4.1). The segregations can be classified as vesicle cylinder (VC), horizontal vesicle sheets (HVS) and megavesicles (MV; Goff 1996; Thordarson and Self 1998). They are generally organised as follows: VC take root in the core or lower crust of the lava flow and extend up to the upper crust where they spread horizontally forming the HVS, within which MV may eventually develop.

Table 4.1. Term definitions and abbreviations.

	Abbreviation	*Definition*
Segregation melt	-	Residual silicate melt produced by lava flow crystallisation and pushed upwards by the gas-filter pressing process
Segregation	-	Any type of solidified segregation melt (VC, HVS, MV)
Host lava	**HL**	Lava body hosting the segregation process and resulting products
Vesicle cylinder	**VC**	Few centimetres wide segregation extending vertically. Generally, the VC are located lower than other segregations, in the core of the lava body
Horizontal vesicle sheet	**HVS**	Segregation spreading horizontally for decimetres to meters but only a few centimetres thick
Megavesicle	**MV**	Large vesicles found in the upper part of the lava core and the upper crust, often connected with the HVS. The vesicles can have flat segregation material underlying a large void
Enrichment factor	**EF**	Element concentration ratio between a segregation and its host lava

Multiple samples of host lava (HL) and segregations were collected from a Holocene olivine-tholeiite lava field associated with Hrútagjá shield volcano on the Reykjanes peninsula,

historical lava field of Eldgjá (at Kriki and Hólmsá) and from an early Holocene basalt lava south of Hekla (Fig. 4.1). Taken together, these three sampled lavas recover well the range of basaltic activity taking place in Iceland. The lava from Hrútagjá represents the "Fire" activity and emissions of products of tholeiitic basalts. The eruptive cycle initiated on the Reykjanes peninsula in 2021 is one example of such Fires. Eldgjá is a good study case for the flood basalts, which are the largest effusive events taking place in Iceland. The Eldgjá lava field further represent an example of more evolved lava than tholeiite: transitional basalt. Finally, the Hekla lava, which is also of transitional nature, illustrate the case of smaller (but more common) eruptions.

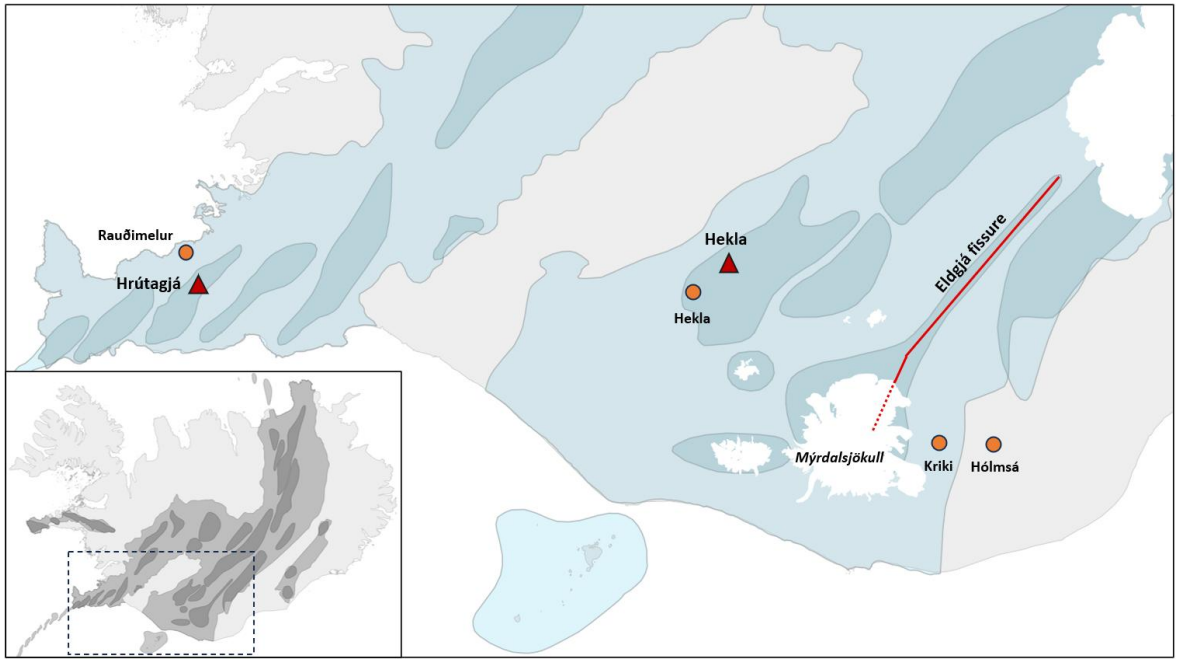

Figure 4.1. Map of SW Iceland indicating the sampling sites on the Reykjanes peninsula, at Hekla and at Eldgjá. *The orange circles represent the sampling sites whereas the red triangles are the associated volcanic system/eruptive fissure. Some sampling sites are out of volcanic areas because lava flowed over large distance. The Eldgjá lava was sampled at two locations: Kriki and Hólmsá. In the inset is a map of Iceland with Pleistocene/Holocene volcanic rocks in light grey and the volcanic systems in dark grey.*

4.3.1 Hrútagjá – Rauðimelur:

The Hrútagjá shield volcano, on the Reykjanes peninsula, produced lava of olivine tholeiite composition (Martin and Sigmarsson 2005). In the Rauðimelur quarry (Fig. 4.1 and 4.2a), the lava core exposes numerous vesicle cylinders of different widths (cm-dm). Horizontal vesicle sheets appear in the upper part of the core, often together with large voids presenting dark material at their base: megavesicles (Fig. 4.2b). The VC can be observed to be connected to the MV-HVS system. All these segregations are made of a highly vesicular material, darker in colour than the host lava.

One host lava (HRG2) and one horizontal vesicle sheet (HRG4) were collected by Martin and Sigmarsson (2007). For consistency, these samples will be called respectively R-HL1 and R-HVS1 in this study. In addition, we sampled one HL (R-HL3), one HVS (R-HVS2)

and two MV (R-MV1 and R-MV2, Fig. 4.2b) from the outcrop together with one HL (R-HL2) and three VC (R-VC1 to R-VC3, Fig. 4.2c and 4.2d) from loose blocks in the quarry.

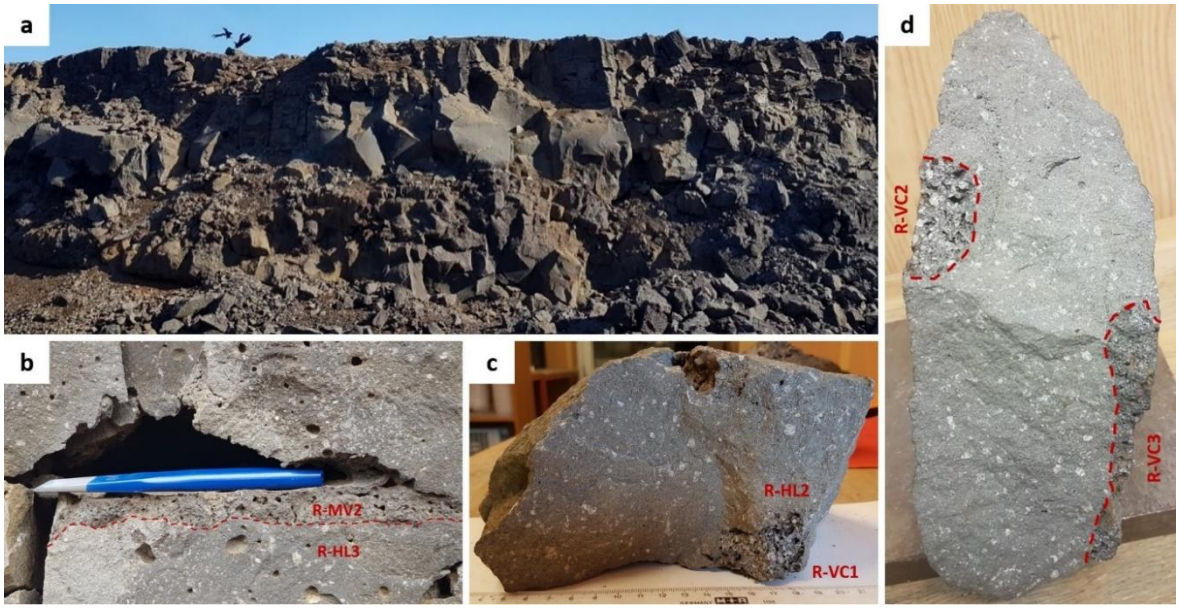

Figure 4.2. Photos of the Rauðimelur quarry and sampled boulders. *(a) Approximately 6 m high outcrop of the Rauðimelur quarry. (b) Megavesicle (sample R-MV2) made up of a large void overlying flat-topped segregation: R-MV2. Length of the wedge is 20 cm. (c) Lava block from which the vesicle cylinder R-VC1 was extracted. (d) Sixty cm long block of host lava with the cylinders R-VC2 and R-VC3.*

4.3.2 Eldgjá

The Eldgjá eruption took place in 939 CE (Oppenheimer et al. 2018) and is the largest historical eruption in Iceland producing a lava field of 20 km^3 (Sigurdardottir et al. 2015). The Eldgjá fissure extends 75 km NE of the Mýrdalsjökull ice caps (Fig. 4.1). The climatic impacts of this eruption were large, reaching as far as China (Stothers 1998; Oppenheimer et al. 2018; Fei and Zhou 2006). Though most of the sulphur was degassed at the vents, a significant part (around 20 %) has been proposed as emitted secondarily, from the flowing and crystallising lava (Thordarson et al. 2001).

The Eldgjá lava was sampled at two distinct locations (Fig. 4.1). One host lava (E-HL1) and one vesicle cylinder (E-VC) were collected at the Kriki formation, E of Mýrdalsjökull. The second set of samples, one host lava (E-HL2) and five segregations (2 HVS and 3 MV) were taken 20 km East of Mýrdalsjökull, close to the Hólmsá river, from a 4-5 meters thick outcrop (Supplementary Fig. 4.1).

4.3.3 Hekla

A wide range of magmas are produced in the Hekla volcanic system. The most evolved products erupt from the Hekla ridge itself, whereas basaltic lava flowed from craters in the vicinity. A quarry in the Bæjarhraun (#109, Jakobsson 1979) lava approximately 15 km SW (Fig. 4.1) of Mount Hekla ridge exposes abundant segregations (Supplementary Fig. 4.2).

One host lava (H-HL) and five distinct segregations were collected: one VC, two HVS and two MV.

4.4 Analytical methods

All samples were cleaned three times in distilled water in an ultrasonic bath. Efforts were made to minimise contamination from the host lava when collecting the segregation material. Polished thin sections and epoxy mounts were made for mineralogical analyses for one host lava (R-HL2), three VC (R-VC1 to R-VC3) and one MV (R-MV1). For whole rock analyses, samples were powdered using an agate grinding mill to minimise any trace metal contamination.

4.4.1 Mineralogical analyses:

The petrological and mineralogical features were examined by optical microscopy and secondary electron microscope (SEM). Size and shape of minerals, phase proportion and vesicularity were estimated visually using multiple SEM pictures for each sample. The different phases were analysed by electron probe microanalyzer (EPMA) at the Institute of Earth Sciences (IES; Reykjavik, Iceland) and at the Laboratoire Magmas et Volcans (LMV; Clermont Ferrand, France). An accelerating voltage of 15 kV and a current of 15 nA were used for mineral analyses. The beam width was 5 µm for mineral analysis and 10 µm for micrographic texture (quartz-feldspar intergrowth). Natural and synthetic standards were used to calibrate the microprobe, and the raw data were corrected by the ZAF procedure.

In the segregations R-VC1 and R-MV1, the different phases were also analysed for 23 element concentrations including some volatile metals and metalloids (As, Bi, Cd, Pb, Se, Sn and Zn) by LA-ICP-MS at the LMV. The sample beam of the laser was 40 to 60 µm wide. Calcium (for plagioclases, clinopyroxenes and micrographic patches) and iron (for olivines and oxides) were used as internal standards. Analyses displaying a sudden shift in signal during the analysis (lasting 60 s), indicating that more than one phases was measured, were excluded.

4.4.2 Whole-rock major and trace element analyses:

For major element concentration measurements at the IES, 100 mg of sample (or standard) rock powder were mixed with 200 mg of lithium borate ($LiBO_2$). The sample mixture was fused at 1000 °C, cooled down and transferred into 5 % HNO_3, 1.33 % HCl and 1.33 % $C_2H_2O_4$. The resulting solutions were analysed on an ICP-OES (ThermoFisher iCAP 7400 Duo) together with standards. The standards used for calibration B-THO (alias BIR-1), A-THO and B-ALK (Icelandic rock standards) and the precision was estimated through duplicate measurements on the international standards BHVO-1, BIR-1 and W-2. Four samples were measured under similar conditions at the LMV.

Trace and ultra-trace element concentration measurements were conducted at the LMV. The sample (and standard) powders were first dissolved using ammonium bifluoride (NH_4HF_2) and left for a day in a furnace at 220 °C for the reaction to operate. Repeated cycles of nitric acid (HNO_3 14N then 7N) addition, rinsing and evaporation were then realised to remove fluorides (SiF_4). The samples and standards were consequently diluted by a factor 5000 in a

diluted HF-HNO_3 solution. The analyses were performed on an inductivity coupled plasma mass spectrometry (ICP-MS) (Agilent 7500). Concentrations of 60 elements, ranging from Li to U were measured. The reaction cell (in He mode) was used to reduce interferences on masses ranging from Sc to As. Three international standards were used: BHVO-2 for instrumental calibration and precision calculation (and BIR-1 and BEN for analytical quality check. Several elements, including a few volatile metals, showed poor measurement accuracy (i.e., large difference from recommended values in the standard) such as B, Tl, Te, W. The precision of our measurements was controlled by repeated measurements on BHVO-2 (and calculation of the relative standard deviation) and is better than 10 % for all elements except Te, Re (< 20 %) and B (31 %).

4.4.3 Volatile element analyses:

The whole rock sulphur and hydrogen concentrations were measured with a Thermo Fisher CHNS/O analyser at LMV. Twenty to 40 mg of dried sample powder were mixed with 5 to 10 mg of vanadium oxide and combusted under oxygen and helium flow at 1800°C before gas chromatography measurements. Each sample was analysed two to six times. The instrument was calibrated with an organic analytical standard: 2,5-Bis (5-tertbutyl-benzoxazol-2-yl) thiophene and accuracy was assessed from repeated measurements a reference soil material calibrated against the Acetanilide 141d standard.

Fluorine concentration was measured using an ion-selective electrode. The sample preparation and the leaching method is based on that of Stecher (1998). In a platinum crucible, 0.5 grams of powder were mixed with 3 g of fondant (5:1 mixture of Na_2CO_3 and ZnO) and covered by 1 g of the fondant. The crucible was then heated in a furnace progressively from 500 to 950 °C (100 °C every 20 minutes) and left 30 minutes at the final temperature. After cooling, 30-35 mL of deionised water was added to the crucibles to leach the halogens out of the fused powder/fondant mixture. A couple of clean ethanol drops was also added to avoid extracting chemicals affecting the leachate colour, which complicate the subsequent titration process. The crucible is then left in the oven overnight (~ 18 hours) at 80 °C for complete leaching. After that, the leachate is filtered, and nitric acid is added to reduce the pH to around 5, expelling CO_2. The resulting solution is diluted with H_2O to 50 mL.

A set of standards ranging from 0.25 to 10 ppm F were prepared from concentrated F^- solution (1000 ppm) and diluted by deionised. Before using the fluorine electrode, the leachates and standards are mixed 1:1 with a Total Ionic Strength Adjustment Buffer (TISAB) to maintain a constant ionic strength and to decomplex fluorine (Stecher 1998). Due to matrix effect, this method tends to underestimate the actual F concentration. This was corrected by using the standard addition method described in Stecher (1983). A calibration curve is based on our standard and the samples electrode potential measurements are converted into F concentrations. This method was first applied and calibrated on known rock standards (JR-2, B-ALK, A-THO, B-THO) before using it on our samples. Several leachates were prepared for each sample to allow repeated measurements and estimate the analytical error.

4.5 Results

4.5.1 Mineralogy

The Rauðimelur lava and segregation mineralogy was analysed in detail, both regarding the phase modal proportions and the mineralogical composition in terms of major and trace elements.

Petrography

The phases observed and their proportion in Rauðimelur lava/segregations are reported in Table 4.2. A detailed description of each sample with SEM pictures is given in the supplementary figures 4.3 to 4.5.

Table 4.2. Visually estimated phase proportions in the Rauðimelur host lava and segregations.

	R-HL2	*R-VC1*	*R-VC2/VC3*	*R-HVS1**	*R-MV1*
Vesicularity	5%	> 5 %**	~ 20 %	20%	> 5 %**
Macrocrysts	~ 10 %	~ 30 %	~ 25 %	0%	0%
	90 % Pl 10 % Ol	90 % Pl 10 % Ol	90 % Pl 10 % Ol	-	-
Groundmass microcrysts	~ 80 %	~ 60 %	~ 40 %	78%	~ 70 %
	45 % Pl 40 % Cpx 10 % Ox 5 % Ol	45 % Cpx 40 % Pl 10 % Ox 5 % Ol	50 % Cpx 35 % Pl 10-15 % Ox < 5 % Ol	47 % Pl 40 % Cpx 9 % Ox 3 % Ol	50 % Cpx 30 % Pl 20 % Ox
Micrographic patches	< 5 %	5%	~ 15 %	?	25%

*Estimated volume percentage, Cpx standing for clinopyroxene, Pl for plagioclase, Ox for iron- and titanium oxide and Ol for olivine. R-VC2 and R-VC3 are shown together as the two cylinders display identical features. *R-HVS1 results are taken from Martin and Sigmarsson (2007) (HRG4). **Vesicularity estimated from epoxy mounts is given as a minimum as the largest vesicles disappeared during the mounting and the void above the segregation material is not included.*

The Rauðimelur host lava (R-HL2) was examined on several thin sections, revealing homogeneous texture, and observations matching those of Martin and Sigmarsson (2007) on R-HL1 (their HRG2). Plagioclase (90 %) and olivine (10 %) macrocrysts (crystals > 500 μm) are observed in both the host lava and the vesicle cylinders in the megavesicle segregation (R-MV1). The greater part of each sample is made of microcrysts of plagioclase, clinopyroxene, oxides, and olivine (absent in the R-MV1). The microcrysts are larger in the segregations than in the HL, around 300 μm and 100 μm respectively. Small micrographic patches (micrographic texture + accessory microcrystals) are present in all samples, but to a larger extent in the segregations (up to 25 % in R-MV1) than in the HL (< 5 %). The proportion of such patches seems highly variables in the vesicle cylinders, representing only 5 % in R-VC1 but 15 % in R-VC2 and R-VC3. The patches are microcrystalline (< 50 μm), composed of oxide, clinopyroxene, feldspar and tiny apatite, surrounded by a micrographic texture most likely of intergrown feldspar and quartz too small to be analysed by the EMPA.

Vesicles are ubiquitous, more abundant and larger in the segregations (> 15 vol %, up to 10 mm) than in the host lava (< 5 vol %, < 0.5 mm).

Mineral major element composition

Major element composition of all identified phases larger than 5 μm were analysed by the electron microprobe. The detailed results are listed in the supplementary Tables 4.1 to 4.5.

The core of the plagioclase macrocryst observed in the host lava and the vesicle cylinders have similar composition of $An_{85}Ab_{15}Or_{0}$. Groundmass microcrysts have cores ranging from An_{57} to An_{68}, with decreasing An content from the host lava (HL) through VC and HVS to MV. The accessory plagioclases in the micrographic patches are the most evolved, having an average composition up to $An_{26}Ab_{67}Or_{7}$ in R-MV1. These results are well within the range ($An_{88}Ab_{12}Or_{0}$-$An_{5}Ab_{54}Or_{41}$) observed by Martin and Sigmarsson (2007). The clinopyroxene (cpx) microcrysts have average core composition from $Wo_{41}En_{46}Fs_{13}$ in R-HL2 to $Wo_{35}En_{35}Fs_{30}$ in R-MV1, confirming that the MV has more evolved mineral composition. The most Fe-rich cpx are observed in the micrographic patches, around $Wo_{26}En_{17}Fs_{57}$. As for the feldspar, the clinopyroxene has composition within the published range.

Olivine is present in host lava and vesicle cylinders from Rauðimelur as macrocrysts and zoned microcrysts in the groundmass. The VC macrocrysts are of primitive and homogeneous composition (Fo_{82}-Fo_{84}), similar to the those reported by Martin and Sigmarsson (2007) in the host lava (Fo_{84}). The groundmass olivine cores are less magnesian, spanning from Fo_{75} to Fo_{55}, those of the VC being systematically more evolved than HL ones. Iron oxides are present in all samples, both in the groundmass and micrographic patches, with a great majority of titanomagnetite and scarce ilmenite.

The micrographic texture found in the patches was analysed using a wider beam (10 μm) avoiding the accessory crystals. Several analyses of the texture in multiple patches were undertaken for each sample. The measured composition is similar in all our samples, with high SiO_2 (75-80 wt %) and Na_2O content (4-6 %), low CaO (0.7 to 2.1 %) and variable K_2O (0 to 6.7 %). This composition matches those of Martin and Sigmarsson (2007).

Mineral trace element concentrations

The different mineral phases of the Rauðimelur segregations R-VC1 and R-MV1 were further analysed by LA-ICP-MS. The phases analysed in R-VC1 are plagioclase macrocrysts, all the groundmass microcrysts (plagioclase, pyroxene, olivine and titanomagnetite) and the micrographic patches. In R-MV1 are the microcrysts of plagioclase and pyroxene along with the micrographic patches were analysed. In table 4.3 are presented the trace element concentrations in all phases analysed (concentration range and standard error are available in the supplementary Table 4.6).

The most abundant elements in the plagioclases are Sr and Ba with highest values in R-MV1, lower in R-VC1 microcrysts and even less in R-VC1 macrocrysts, following the lower albite component (Table 4.3). The same order is visible for the less concentrated elements (< 10 ppm), apart from Ni, Cr, Cu and V. Low concentrations (< 0.1 ppm) are obtained for all the volatile metals (and metalloids). The clinopyroxenes of the segregations display significant concentration in many trace elements with over 10 ppm of Sr, Zr, Y, Cu, Zn, Sc, Ni, V, and Cr (Table 4.3). Several volatile metals (As, Sn, Cd and Pb) have concentrations higher than 0.1 ppm. Compared to the R-VC1, the cpx from R-MV1 are enriched in all incompatible elements but depleted in the most compatible Cr and Ni. One olivine from R-VC1 was

analysed and contains over 100 ppm of Cr, Zn and Ni and over 10 ppm Sc, Cu and V. The volatile metal concentrations are all close or below detection limit. One titanomagnetite from R-VC1 was successfully analysed and displays a wide range of element concentration with V > 0.5 wt % and Cu, Ni, Zr and Zn over 100 ppm but most incompatible element concentration below 1 ppm.

Table 4.3. Average trace element concentrations (ppm) in Rauðimelur segregation (R-VC1 and R-MV1) mineral phases (plagioclase, clinopyroxene, olivine, oxide and micrographic patches), *together with the detection limit (DL).*

	Micrographic patches			Plagioclases				Clinopyroxenes			Olivines		Oxides	
	R-VC1	R-MV1	DL	R-VC1*	R-VC1	R-MV1	DL	R-VC1	R-MV1	DL	R-VC1	DL	R-VC1	DL
Sc	3.5	3.9	0.03	0.5	0.45	0.52	0.05	117	127	0.02	11	0.03	24	0.02
V	1.4	2.6	0.02	3.7	6.1	2.7	0.04	556	659	0.02	31	0.02	4875	0.02
Cr	2.0	1	0.5	6.2	3.7	3.1	1.0	587	7.7	0.5	99	0.5	21	0.5
Ni	2.3	1.4	0.15	0.5	0.5	0.5	0.29	153	69	0.13	1086	0.15	248	0.14
Cu	306	142	0.06	1.1	1.8	1.0	0.11	60	128	0.05	22	0.06	162	0.05
Zn	35	79	0.19	4.4	10.9	17.5	0.35	61	155	0.16	357	0.18	741	0.17
As	1.4	0.6	0.04	0.12	0.13	0.09	0.08	0.09	0.13	0.04	0.11	0.06	0.19	0.03
Se	1.6	1.4	0.17	b.d.l	b.d.l	b.d.l	0.33	b.d.l	b.d.l	0.15	b.d.l	0.18	0.24	0.16
Rb	19	4.6	0.01	b.d.l	0.18	0.42	0.03	b.d.l	b.d.l	0.01	b.d.l	0.01	0.09	0.01
Sr	132	115	0.01	264	339	464	0.02	10.3	11.7	0.01	b.d.l	0.01	8.3	0.01
Y	96	68	0.002	0.15	0.18	0.24	0.004	13.9	31.2	0.002	0.28	0.002	3.5	0.002
Zr	662	266	0.03	b.d.l	0.10	0.23	0.05	10.5	27.4	0.02	b.d.l	0.03	250	0.03
Cd	0.08	0.10	0.04	0.07	0.08	b.d.l	0.06	0.17	0.32	0.03	0.06	0.04	0.04	0.03
Sn	3.9	1.4	0.01	b.d.l	0.05	0.05	0.02	0.09	0.20	0.01	0.04	0.01	4.0	0.01
Ba	589	128	0.01	8.0	26	89	0.03	0.11	0.80	0.01	b.d.l	0.01	1.5	0.01
Ce	83.1	57.7	0.00	0.6	0.8	1.6	0.00	1.9	4.5	0.00	b.d.l	0.00	3.2	0.00
Pb	3.5	2.0	0.003	0.04	0.13	0.45	0.006	0.017	0.54	0.002	0.01	0.003	0.13	0.002
Bi	0.023	0.016	0.003	0.011	0.012	b.d.l	0.006	0.005	b.d.l	0.003	b.d.l	0.005	b.d.l	0.002
Th	3.0	1.8	0.0003	b.d.l	b.d.l	0.002	0.0005	0.003	0.013	0.0004	b.d.l	0.0003	0.03	0.0003
Nb of analyses	4	10	-	1	3	5	-	4	7	-	1	-	1	-

Due to the compositional variability of the micrographic patches (in terms of Ca content), there is uncertainty regarding its conversion factor and thus the exact trace-element concentrations, but all elements are affected to the same extent. R-VC1 corresponds to the plagioclase macrocryst analysed in the R-VC1. Details regarding measured concentration range and associated standard deviation in supplementary Table 4.6.*

In the micrographic patches of R-VC1 and R-MV1, the most concentrated elements are Zr, Ba and Cu (Table 4.3). The incompatible elements display higher concentration than in all other phases, demonstrating that the micrographic patches reflect the composition of the last drops of melt. Comparing element concentrations in the minerals and micrographic patches gives indications on their partition. In agreement with the literature values (Bougault and Hekinian 1974; Bindeman et al. 1998; Bindeman and Davis 2000; Adam and Green 2006), we find that Sc partitions in Cpx, V in Ox and Cpx, Cr in Cpx, Ni in Ol and Sr in plagioclases whereas Th partition in no mineral. In terms of volatile metals, Se, As and Rb seem to remain almost exclusively in the melt while Zn significantly partition in Ox and Ol and Cd enters Cpx as previously pointed out by Adam and Green (2006).

4.5.2 Whole rock

Major elements composition

All sampled segregations and host lava (HL) were analysed for whole rock major element concentrations (Table 4.4). The Rauðimelur lava is of rather homogeneous composition and classifies as olivine tholeiite with 8% MgO, similar to published results for the Reykjanes peninsula (Jakobsson et al. 1978; Peate et al. 2009). In contrast, the Eldgjá and Hekla lavas are of FeTi-rich transitional basalt composition, close to those reported by Wood et al. (1979) and Jakobsson (1979) respectively.

Table 4.4. Major element composition of host lava and segregations.

Lava flow	Sample name	SiO_2	TiO_2	Al_2O_3	FeO^t	MnO	MgO	CaO	Na_2O	K_2O	P_2O_5	Raw Total
Rauðimelur	R-HL1	48.2	1.34	15.4	11.8	0.17	8.13	12.9	1.98	0.15	0.13	100.2
	R-HL2	48.9	1.30	15.8	10.7	0.18	7.96	12.9	2.01	0.15	0.12	99.9
	R-HL3	49.5	1.33	15.6	10.5	0.17	8.07	12.7	1.95	0.15	0.13	99.7
	R-VC	48.7	1.61	17.6	11.2	0.19	5.79	12.5	2.16	0.18	0.14	97.4
	R-HVS1	48.7	2.20	12.6	15.5	0.22	6.36	11.5	2.46	0.26	0.21	100.0
	R-HVS2	49.1	2.58	12.5	16.0	0.27	5.59	11.0	2.45	0.28	0.24	99.3
	R-MV1	48.7	3.06	11.6	17.9	0.30	5.04	10.3	2.40	0.32	0.29	99.5
	R-MV2	48.6	3.41	11.2	19.0	0.31	4.43	9.85	2.50	0.38	0.35	98.9
Eldgjá	E-HL1	47.3	4.59	12.7	14.9	0.23	5.46	10.3	3.02	0.81	0.59	99.4
	E-HL2	46.8	4.42	13.0	15.5	0.22	5.50	10.6	2.80	0.67	0.46	99.7
	E-VC	49.5	4.33	10.9	17.6	0.27	3.81	8.25	3.10	1.22	1.07	99.8
	E-HVS1	49.0	4.17	11.3	17.8	0.28	3.44	8.45	3.28	1.28	1.00	98.7
	E-HVS2	49.2	3.97	11.2	18.2	0.29	3.25	8.18	3.37	1.38	1.08	99.0
	E-MV1	49.2	4.07	11.2	18.1	0.29	3.30	8.15	3.31	1.39	1.07	98.3
	E-MV2	49.2	4.17	11.4	17.6	0.29	3.43	8.43	3.27	1.33	1.03	99.2
	E-MV3	49.5	3.78	11.1	17.9	0.28	3.23	8.25	3.41	1.41	1.09	98.3
Hekla	H-HL	46.3	3.70	14.3	16.0	0.25	5.92	9.58	2.89	0.57	0.44	97.7
	H-VC	46.4	4.44	12.8	17.2	0.27	4.97	9.80	2.87	0.68	0.55	100.3
	H-HVS1	45.9	5.30	11.2	18.5	0.29	4.68	9.93	2.80	0.76	0.60	98.5
	H-HVS2	48.2	4.80	10.7	18.0	0.31	3.65	9.26	3.16	1.05	0.88	99.2
	H-MV1	48.5	4.46	10.8	18.2	0.32	3.46	9.30	3.02	1.07	0.92	97.7
	H-MV2	48.8	4.33	10.9	18.0	0.32	3.36	8.94	3.27	1.12	0.96	98.4
Standard deviation	(2σ)	0.54	0.02	0.14	0.10	0.00	0.01	0.06	0.04	0.01	0.02	

The standard deviation Is based on repeated analyses on the rock standards BIR-1, BHVO-2 and W-2. Each analysis is normalised to 100 % but the raw total is indicated.

The Rauðimelur segregations have composition distinct from the host lava, with MgO content ranging from 4.5 to 6.4 weight % (Table 4.4, Fig. 4.3). Apart from R-VC1, they are also all significantly enriched in incompatible oxides (K_2O, TiO_2 and P_2O_5) by a factor up to 3 (P_2O_5 in R-MV2). Conversely, the most compatible oxides (MgO, CaO…) are systematically depleted. This evolved nature is typical of segregations found worldwide (Helz 1987; Martin and Sigmarsson 2007; Sigmarsson et al. 2009; Hartley and Thordarson 2009), with a few notable exceptions (Kuritani et al. 2010; Nikkola et al. 2019). The enrichment in compatible elements and depletion in MgO in the segregations is shown in figure 4.3. Whereas the three host lava from Rauðimelur are of a similar composition, the segregations display different stages of evolution, R-HVS1 being the least evolved, followed by R-HVS2, R-MV1 and R-MV2. The variable evolution stages of the segregations form a differentiation trend (i.e., liquid line of descent), on which R-VC1 falls off.

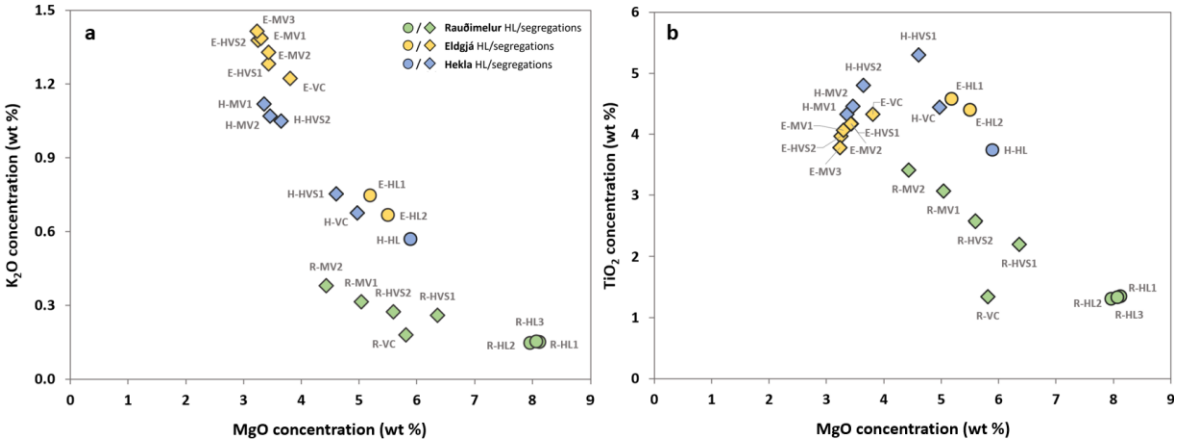

Figure 4.3. Host lava and segregation incompatible oxide concentrations compared to that of MgO. *(a) MgO vs K_2O and (b) MgO vs TiO_2 in the host lava (circles) and segregations (diamonds) from Rauðimelur (green), Eldgjá (yellow) and Hekla (blue). Obvious differentiation trends appear for each HL-segregation system with increasing K_2O as MgO decrease and TiO_2 reaching a maximum around 5.5 % before decreasing together with MgO (when oxides initiate crystallisation).*

Overall, segregations from Eldgjá and Hekla display differentiation trends similar to those of Rauðimelur from their respective HL (albeit steeper K_2O vs MgO; Fig. 4.3a). A notable difference is the evolution of TiO_2 concentrations that reach a maximum around MgO of 4.5 % (TiO_2 ~ 5 %). Similarly to Rauðimelur, Hekla segregations represent different stages of differentiation (H-VC being the least evolved and H-MV2 the most), whereas the segregations from Eldgjá are rather homogeneous in composition.

Trace elements composition.

The host lavas and segregations were analysed for trace element composition, including volatile metals (i.e., As, Bi, Cd, In, Pb, Re, Sb, Se, Sn, Te and Zn), with detailed results presented in Table 4.5. Within Rauðimelur host lava, Pt, Mo, Se and Sb show moderate degree of variability (15 % > SD 2σ > 30 %), unlike other trace elements. In contrast, the two Eldgjá host lava (collected at very distant locations) only have distinct concentrations of Ir, suggesting homogeneous composition, including in terms of volatile metals. Overall, the trace elements composition of the analysed host lavas are in good agreement with the previously published values for Reykjanes (Peate et al. 2009), Eldgjá (Kokfelt et al. 2006) and Hekla (Chekol et al. 2011), as shown in the supplementary figure 4.6. However, to our knowledge, no study reported any segregation composition from these lavas.

Table 4.5. Trace element concentrations (in ppm) in the different host lava and segregations.

	STD (2σ)	Detection limit	R-HL1	R-HL2	R-HL3	R-VC1	R-HVS1	R-HVS2	R-MV1	R-MV2
Sc	4.86	0.49	44.6	42.3	42.3	35.2	58.5	49.9	47.8	45.1
V	3.77	0.47	323	320	319	373	554	513	586	532
Cr	3.08	1.30	316.2	296.2	291.9	67.7	28.9	11.9	5.1	4.0
Co	2.82	0.11	77.68	49.65	49.66	42.98	77.63	53.95	55.01	53.76
Ni	2.50	1.76	122	116	117	89	60	40	31	24
Cu	2.41	0.87	155	138	108	177	261	173	233	330
Zn	3.15	4.12	86	87	83	93	127	143	164	179
Ga	4.35	1.08	17.1	16.6	16.2	18.0	21.1	21.0	21.4	22.6
Ge	4.80	0.04	1.47	1.40	1.42	1.42	2.06	2.06	2.20	2.42
As	2.19	0.03	0.24	0.24	0.21	0.28	0.38	0.38	0.50	0.55
Se	4.04	0.07	0.09	0.08	0.07	0.09	0.16	0.16	0.18	0.22
Rb	2.87	0.15	2.42	2.42	2.36	3.05	4.27	4.97	5.85	7.18
Sr	2.78	2.22	164	160	157	177	177	166	165	167
Y	2.67	0.05	21.4	21.6	21.0	25.2	36.8	40.5	46.8	54.4
Zr	2.69	0.80	58	60	60	72	110	125	152	180
Nb	2.42	0.16	6.73	6.87	6.56	8.44	11.91	13.99	16.89	20.17
Mo	2.10	0.12	0.38	0.31	0.41	0.41	0.59	0.84	0.87	1.62
Ru	6.74	0.0001	0.0002	b.d.l	b.d.l	b.d.l	0.0002	b.d.l	b.d.l	b.d.l
Rh	6.30	0.0002	0.0003	0.0003	0.0003	0.0003	0.0004	0.0003	0.0003	0.0003
Pd	4.19	0.0001	0.002	0.002	0.002	0.002	0.003	0.003	0.003	0.004
Ag	5.02	0.002	0.036	0.039	0.040	0.046	0.063	0.077	0.089	0.107
Cd	5.68	0.02	0.10	0.08	0.11	0.09	0.15	0.16	0.16	0.18
In	2.13	0.004	0.08	0.09	0.10	0.09	0.14	0.15	0.17	0.18
Sn	2.14	0.04	0.66	0.64	0.62	0.80	1.16	1.26	1.54	1.89
Sb	3.83	0.01	0.015	b.d.l	0.013	0.013	0.027	0.027	0.066	0.035
Te	10.61	0.02	b.d.l	b.d.l	b.d.l	b.d.l	b.d.l	0.018	b.d.l	b.d.l
Cs	1.49	0.02	0.028	0.028	0.028	0.031	0.050	0.059	0.065	0.085
Ba	2.15	1.61	40.04	40.05	37.81	48.12	65.16	73.31	86.08	100.63
La	2.24	0.13	5.09	5.11	4.90	6.20	8.68	10.13	12.05	14.63
Ce	1.89	0.24	12.48	12.84	12.32	15.51	21.61	25.38	30.22	36.55
Pr	1.88	0.03	1.85	1.90	1.84	2.29	3.14	3.73	4.39	5.28
Nd	1.73	0.12	8.93	9.09	8.88	10.92	15.08	17.61	20.87	24.86
Sm	1.28	0.03	2.58	2.66	2.58	3.16	4.37	5.02	5.91	6.98
Eu	1.92	0.01	1.00	1.01	1.00	1.17	1.60	1.77	2.04	2.34
Tb	2.04	0.004	0.56	0.58	0.57	0.68	0.93	1.09	1.26	1.48
Gd	1.78	0.02	3.32	3.43	3.37	4.07	5.54	6.44	7.47	8.76
Dy	1.59	0.02	3.71	3.80	3.70	4.43	6.14	7.01	8.14	9.41
Ho	1.77	0.004	0.78	0.81	0.78	0.94	1.30	1.49	1.73	2.01
Er	2.47	0.01	2.20	2.26	2.25	2.66	3.70	4.29	4.94	5.68
Tm	1.59	0.003	0.32	0.33	0.33	0.40	0.55	0.63	0.73	0.85
Yb	2.45	0.02	2.07	2.17	2.13	2.56	3.52	4.16	4.72	5.56
Lu	1.70	0.003	0.31	0.33	0.32	0.39	0.52	0.60	0.72	0.81
Hf	2.03	0.02	1.69	1.78	1.75	2.16	2.90	3.47	4.14	4.87
Ta	2.49	0.01	0.59	0.43	0.41	0.53	0.85	0.87	1.05	1.24
W	2.04	0.02	308.20	0.07	0.07	0.23	281.94	0.14	0.94	0.21
Re	14.32	0.0005	0.0020	0.0009	b.d.l	0.0016	0.0019	0.0027	0.0074	0.0023
Ir	5.09	1.9×10^{-5}	b.d.l	2.1×10^{-5}	3.5×10^{-5}	b.d.l	2.1×10^{-5}	5.3×10^{-5}	3.6×10^{-5}	5.3×10^{-5}
Pt	6.35	0.0023	0.0050	0.0044	0.0037	0.0085	0.0058	0.0072	0.0075	0.0108
Au	1.71	0.0008	0.0019	0.0010	0.0012	0.0016	0.0028	0.0019	0.0030	0.0033
Tl	3.26	0.01	0.03	b.d.l	b.d.l	0.04	0.04	b.d.l	0.04	0.01
Pb	3.11	0.06	0.49	0.40	0.45	0.45	1.92	1.14	3.31	1.34
Bi	2.00	0.004	0.446	b.d.l	0.025	b.d.l	0.009	0.008	0.011	0.010
Th	3.80	0.02	0.32	0.33	0.31	0.41	0.53	0.65	0.80	0.96
U	3.92	0.01	0.10	0.10	0.09	0.12	0.17	0.21	0.25	0.29

Table 4.5. *continued (Eldgjá)*

	STD (2σ)	Detection limit	E-HL1	E-HL2	E-VC	E-HVS1	E-HVS2	E-MV1	E-MV2	E-MV3
Sc	4.86	0.49	32.9	34.1	25.2	29.6	27.7	27.0	28.4	28.5
V	3.77	0.47	481.7	494.0	355.9	373.2	334.0	339.9	286.6	340.9
Cr	3.08	1.30	12.70	33.78	2.78	b.d.l	b.d.l	b.d.l	b.d.l	b.d.l
Co	2.82	0.11	52.6	55.7	45.6	45.0	43.2	44.4	43.3	40.5
Ni	2.50	1.76	35.4	51.8	15.0	6.8	5.2	6.1	7.3	5.0
Cu	2.41	0.87	86	139	148	100	94	128	132	73
Zn	3.15	4.12	155	146	212	222	229	224	213	225
Ga	4.35	1.08	25.8	24.9	30.9	33.1	33.7	33.3	32.0	34.1
Ge	4.80	0.04	2.21	2.19	2.67	2.97	3.03	2.96	2.89	3.05
As	2.19	0.03	1.04	0.85	1.54	1.83	1.83	1.82	1.79	2.06
Se	4.04	0.07	0.29	0.23	0.47	0.48	0.50	0.50	0.48	0.49
Rb	2.87	0.15	15.2	13.5	27.5	29.5	32.1	31.1	30.1	32.7
Sr	2.78	2.22	437	416	405	423	416	411	423	414
Y	2.67	0.05	39.0	34.6	66.8	68.7	72.1	71.9	69.1	72.7
Zr	2.69	0.80	247	222	405	446	467	461	451	478
Nb	2.42	0.16	35.90	31.00	56.60	61.95	64.40	63.90	62.77	65.49
Mo	2.10	0.12	1.85	1.95	3.27	4.32	4.66	4.75	4.53	5.09
Ru	6.74	0.0001	0.0002	b.d.l	b.d.l	b.d.l	b.d.l	b.d.l	b.d.l	b.d.l
Rh	6.30	0.0002	0.0008	0.0007	0.0007	0.0007	0.0008	0.0007	0.0007	0.0007
Pd	4.19	0.0001	0.004	0.003	0.005	0.005	0.005	0.005	0.005	0.005
Ag	5.02	0.002	0.125	0.110	0.201	0.209	0.221	0.218	0.218	0.235
Cd	5.68	0.02	0.22	0.20	0.32	0.35	0.34	0.36	0.37	0.36
In	2.13	0.004	0.16	0.14	0.19	0.21	0.20	0.20	0.22	0.23
Sn	2.14	0.04	2.33	2.13	4.24	4.57	4.81	4.63	4.37	6.47
Sb	3.83	0.01	0.084	0.079	0.134	0.150	0.149	0.152	0.143	0.171
Te	10.61	0.02	b.d.l	b.d.l	b.d.l	0.063	0.029	0.035	0.025	0.036
Cs	1.49	0.02	0.194	0.164	0.346	0.362	0.399	0.379	0.364	0.401
Ba	2.15	1.61	185.07	164.32	287.48	316.81	332.49	327.52	321.09	342.49
La	2.24	0.13	26.70	23.63	47.70	50.45	53.52	53.39	51.66	52.34
Ce	1.89	0.24	66.10	55.40	116.77	117.62	124.19	124.42	121.03	123.83
Pr	1.88	0.03	8.44	7.58	14.90	15.78	16.62	16.57	16.16	16.58
Nd	1.73	0.12	37.80	33.47	65.40	69.25	72.83	72.86	70.70	72.68
Sm	1.28	0.03	9.13	8.00	15.20	16.06	16.88	16.81	16.33	16.97
Eu	1.92	0.01	2.99	2.69	4.64	5.04	5.22	5.18	5.08	5.31
Tb	2.04	0.004	1.37	1.24	2.28	2.44	2.52	2.54	2.46	2.55
Gd	1.78	0.02	9.20	8.24	15.30	16.19	16.89	16.96	16.53	17.12
Dy	1.59	0.02	7.76	6.98	12.70	13.65	14.21	14.09	13.67	14.34
Ho	1.77	0.004	1.44	1.31	2.37	2.55	2.67	2.66	2.59	2.69
Er	2.47	0.01	3.73	3.38	6.13	6.60	6.88	6.84	6.74	6.93
Tm	1.59	0.003	0.49	0.44	0.81	0.86	0.91	0.91	0.86	0.92
Yb	2.45	0.02	2.99	2.72	4.85	5.30	5.48	5.55	5.41	5.57
Lu	1.70	0.003	0.42	0.37	0.69	0.72	0.77	0.75	0.73	0.76
Hf	2.03	0.02	6.14	5.57	10.10	10.90	11.35	11.45	11.16	11.70
Ta	2.49	0.01	2.28	1.99	3.47	3.75	3.91	3.93	3.79	3.96
W	2.04	0.02	1.53	0.39	1.14	0.87	0.91	0.93	0.86	0.99
Re	14.32	0.0005	0.0010	0.0012	0.0050	0.0015	0.0013	0.0038	0.0106	0.0023
Ir	5.09	1.9×10^{-5}	3.2×10^{-5}	8.1×10^{-5}	6.0×10^{-5}	1.7×10^{-4}	1.8×10^{-4}	1.6×10^{-4}	1.7×10^{-4}	1.8×10^{-4}
Pt	6.35	0.0023	0.0119	0.0109	0.0175	0.0187	0.0189	0.0214	0.0203	0.0214
Au	1.71	0.0008	0.0055	0.0039	0.0077	0.0072	0.0078	0.0078	0.0071	0.0073
Tl	3.26	0.01	0.02	0.02	b.d.l	0.09	0.06	0.05	0.06	0.07
Pb	3.11	0.06	1.57	1.54	2.94	3.51	3.38	3.29	3.08	3.93
Bi	2.00	0.004	0.019	0.017	0.022	0.048	0.017	0.017	0.020	0.016
Th	3.80	0.02	2.35	2.12	4.37	4.60	4.87	4.91	4.71	4.99
U	3.92	0.01	0.70	0.63	1.29	1.38	1.45	1.48	1.42	1.51

Table 4.5. *continued (Hekla)*

	STD (2σ)	Detection limit	H-HL	H-VC	H-HVS1	H-HVS2	H-MV1	H-MV2
Sc	4.86	0.49	34.2	42.6	48.7	42.1	41.3	36.6
V	3.77	0.47	474.3	508.7	592.8	328.2	318.1	252.6
Cr	3.08	1.30	23.95	18.04	14.46	b.d.l	3.20	4.49
Co	2.82	0.11	59.4	54.1	51.7	42.2	41.8	40.8
Ni	2.50	1.76	59.1	46.6	22.5	11.2	10.7	8.6
Cu	2.41	0.87	162	178	218	295	295	307
Zn	3.15	4.12	155	175	189	203	208	220
Ga	4.35	1.08	25.4	27.2	28.3	30.7	31.4	31.8
Ge	4.80	0.04	2.25	2.53	2.63	2.77	2.88	2.91
As	2.19	0.03	0.70	0.91	1.04	1.39	1.62	1.53
Se	4.04	0.07	0.24	0.29	0.35	0.47	0.46	0.49
Rb	2.87	0.15	11.0	14.0	16.0	22.6	23.6	24.3
Sr	2.78	2.22	355	332	304	315	319	327
Y	2.67	0.05	38.2	48.9	57.0	76.5	78.5	81.8
Zr	2.69	0.80	221	283	327	435	451	466
Nb	2.42	0.16	31.57	40.78	47.37	63.08	65.01	67.38
Mo	2.10	0.12	1.79	2.32	2.66	3.72	4.03	4.04
Ru	6.74	0.0001	b.d.l	b.d.l	b.d.l	b.d.l	b.d.l	b.d.l
Rh	6.30	0.0002	0.0006	0.0005	0.0005	0.0005	0.0006	0.0006
Pd	4.19	0.0001	0.003	0.004	0.004	0.005	0.006	0.006
Ag	5.02	0.002	0.114	0.146	0.164	0.224	0.226	0.228
Cd	5.68	0.02	0.18	0.21	0.26	0.31	0.38	0.33
In	2.13	0.004	0.15	0.18	0.21	0.22	0.30	0.22
Sn	2.14	0.04	1.98	2.56	3.38	4.10	5.01	4.50
Sb	3.83	0.01	0.050	0.067	0.070	0.087	0.105	0.102
Te	10.61	0.02	b.d.l	0.031	b.d.l	0.122	0.061	0.025
Cs	1.49	0.02	0.135	0.177	0.206	0.282	0.306	0.303
Ba	2.15	1.61	158.24	192.51	215.10	287.70	295.43	307.77
La	2.24	0.13	22.58	28.77	32.95	46.02	48.10	50.16
Ce	1.89	0.24	52.81	67.76	78.50	108.82	113.99	118.27
Pr	1.88	0.03	7.19	9.21	10.60	14.56	15.07	15.73
Nd	1.73	0.12	31.60	40.60	46.91	63.98	66.25	69.12
Sm	1.28	0.03	7.60	9.67	11.20	15.08	15.47	16.18
Eu	1.92	0.01	2.60	3.18	3.61	4.70	4.84	5.00
Tb	2.04	0.004	1.24	1.60	1.82	2.43	2.49	2.58
Gd	1.78	0.02	8.10	10.28	11.86	15.82	16.16	16.82
Dy	1.59	0.02	7.29	9.36	10.78	14.27	14.59	15.32
Ho	1.77	0.004	1.44	1.84	2.13	2.82	2.85	2.99
Er	2.47	0.01	3.82	4.91	5.62	7.39	7.67	7.97
Tm	1.59	0.003	0.53	0.68	0.79	1.05	1.08	1.11
Yb	2.45	0.02	3.29	4.24	4.89	6.42	6.65	6.86
Lu	1.70	0.003	0.48	0.62	0.71	0.92	0.95	1.00
Hf	2.03	0.02	5.53	7.10	8.26	10.86	10.99	11.47
Ta	2.49	0.01	1.92	2.52	2.89	3.83	3.88	4.04
W	2.04	0.02	0.33	0.42	0.49	0.69	0.74	0.74
Re	14.32	0.0005	0.0006	0.0006	0.0007	0.0010	0.0010	b.d.l
Ir	5.09	1.9×10^{-5}	9.0×10^{-5}	1.1×10^{-4}	1.4×10^{-4}	1.8×10^{-4}	1.9×10^{-4}	2.0×10^{-4}
Pt	6.35	0.0023	0.0098	0.0127	0.0151	0.0188	0.0184	0.0188
Au	1.71	0.0008	0.0042	0.0050	0.0063	0.0080	0.0082	0.0084
Tl	3.26	0.01	0.02	0.04	0.04	0.05	0.08	0.04
Pb	3.11	0.06	1.41	1.82	2.12	2.95	4.18	3.20
Bi	2.00	0.004	0.008	0.009	0.011	0.012	0.103	0.012
Th	3.80	0.02	1.80	2.34	2.69	3.77	3.94	4.11
U	3.92	0.01	0.52	0.69	0.80	1.13	1.19	1.23

To investigate the segregation process and the behaviour of trace elements, an enrichment factors (EF) is calculated:

$$EF = \frac{[X]_{segregation}}{[X]_{host\ lava}} \quad (4.1)$$

In Rauðimelur segregations, all incompatible lithophile elements (LILE, REE and HFSE) are enriched to a similar extent (i.e., similar EF, Fig. 4.4a). Their EF varies between the five segregations: from 1.2-1.3 in R-VC1 to 2.5-3 in R-MV2, reflecting decreasing MgO. The compatible elements Cr and Ni are strongly depleted in the segregations (especially in the megavesicles), whereas moderately compatible elements in plagioclase (Sr) and clinopyroxene (Sc) have EF close to unity as expected from their known partition coefficients. Most volatile metals behave like the incompatible lithophile elements, whereas Cd, In and Zn are only moderately enriched in the segregations. Remarkably, three elements have higher EF than nominally incompatible elements (U, Th or Zr), namely Mo, Sb and Pb. Molybdenum is over-enriched in R-MV2 (EF_{Mo} = 3.9) and Sb and Pb in R-MV1 and R-HVS1 (EF_{Pb} = 8.3 in R-MV1).

Eldgjá segregations exhibit the same trends of enrichment/depletion, E-VC being less differentiated than other segregations (Fig. 4.4b). Again In, Zn and Cd are only moderately enriched in the segregations whereas other volatile metals have enrichment close to that of Th. E-MV3 however differs from the other segregations, having higher concentrations of many volatile metals, particularly Sb, As, Pb, Sn and Mo. The Hekla segregations are more heterogeneous with EF of incompatible elements reaching only 1.2-1.3 for H-VC but 1.9-2.3 for H-MV2 (Fig. 4.4c), whereas V is enriched in the former but depleted in the latter. Most volatile metals have EF in the same range as the incompatible lithophile elements with, again, one segregation (H-MV1) displaying significantly higher enrichment in many volatile metals: In, Cd, Sb, As, Pb and Sn.

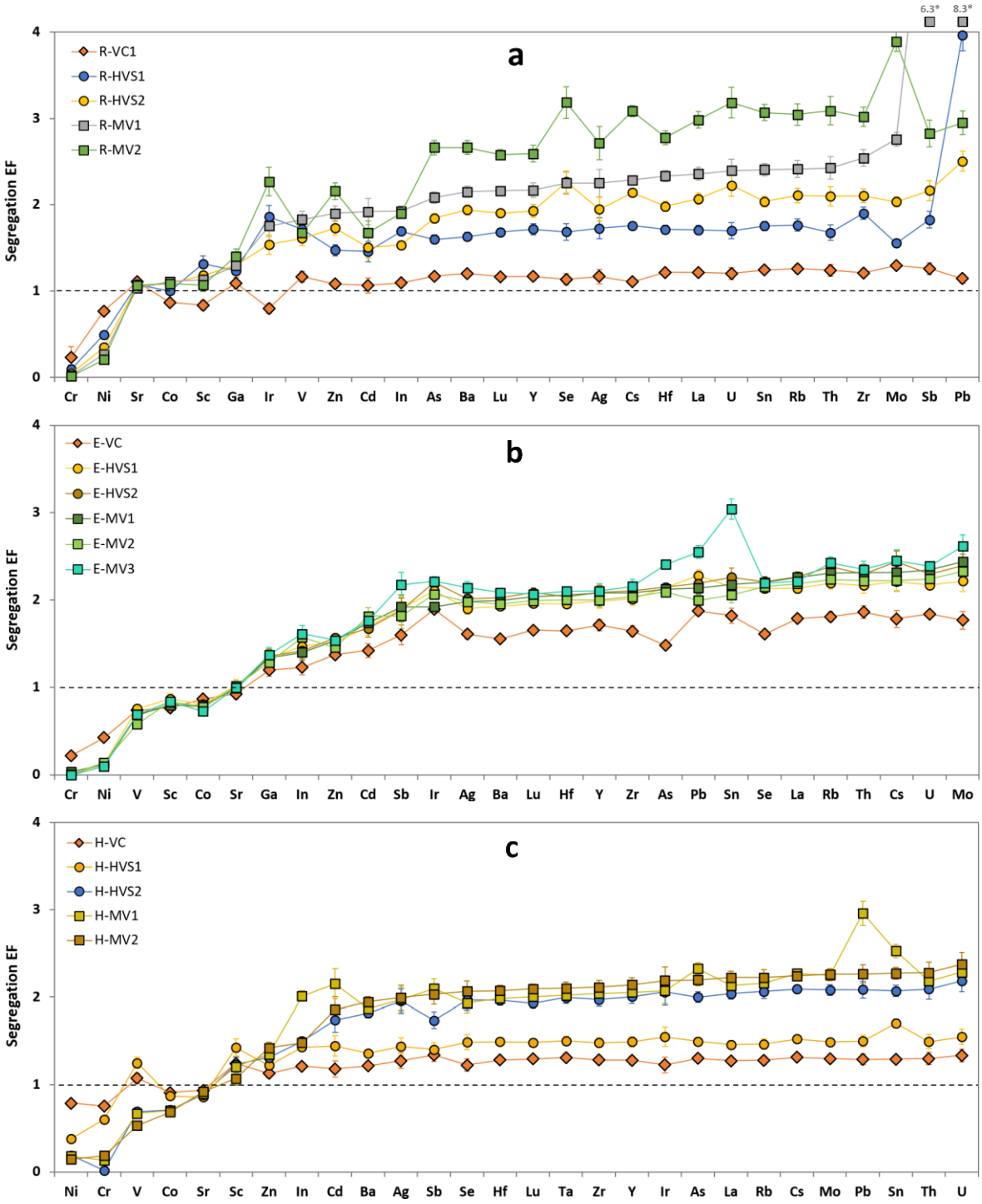

Figure 4.4. Trace element enrichment factors in the segregations with respect to their host lava *at Rauðimelur (a), Eldgjá (b) and Hekla (c). Element order on the x-axis reflects increasing EF for R-MV1, E-MV1 and H-MV2. The bars indicate the analytical error (2σ). The EF were calculated based on the concentration of the host lava collected next to the segregation. *The Sb and Pb enrichment factor in R-MV1 plot off the scale.*

Volatile elements

The measured concentrations of the major volatile elements, sulphur, hydrogen and fluorine in the host lavas and segregations are given in Table 4.6.

Table 4.6. Major volatile concentrations (ppm) measured in the host lava and segregations.

	Hydrogen		Sulphur		Fluorine	
	Average	2σ	Average	2σ	Average	2σ
R-HL1	116	18	10	6	117	14
R-HL2	105	14	9	5	126	12
R-HL3	175	12	13	6	161	8
R-VC1	-	-	13	4	152	7
R-HVS1	122	10	13	6	112	17
R-HVS2	201	13	46	7	145	28
R-MV1	171	14	47	8	255	36
R-MV2	238	8	162	30	309	19
E-HL1	324	24	145	34	488	12
E-HL2	263	14	109	7	350	45
E-VC	429	9	293	44	865	75
E-HVS1	218	23	250	35	837	66
E-HVS2	266	14	283	6	893	46
E-MV1	217	14	365	1	912	55
E-MV2	266	0	302	8	919	64
E-MV3	470	20	271	0	989	5
H-HL	262	30	88	11	316	38
H-VC	235	18	84	8	494	18
H-HVS1	306	13	109	5	582	25
H-HVS2	280	37	206	31	734	65
H-MV1	240	14	212	5	821	39
H-MV2	368	12	228	12	856	169

Sulphur and hydrogen were measured by multielement analyser and fluorine by ion selective electrode. The standard deviation was calculated from replicate measurement of the same sample. The low S concentration in the Rauðimelur lava results in low measurement precision (RSD 2σ ~ 50 %)

The measured hydrogen concentrations are largely above detection limit and have relative standard deviation better than 15 % at the 2σ limit. The host lava R-HL1 and R-HL2 from Rauðimelur have similar H concentration (105 - 116 ppm), in contrast to R-HL3 (175 ppm). Eldgjá lavas contain 263 to 324 ppm H, similar to the measured concentration in Hekla host lava: 262 ppm. The horizontal vesicle sheets from Rauðimelur (R-HVS1 and R-HVS2) have H concentration similar to that of the host lava ($EF_H \sim 1$; Fig. 4.5), whereas the megavesicle R-MV1 has $EF_H \sim 1.5$. The vesicle cylinder E-VC collected at Kriki (Eldgjá) is also enriched in hydrogen, but to a limited extent ($EF_H \sim 1.3$). The other segregations from Eldgjá (collected at Hólmsá) and those of Hekla have roughly the same H content as the HL (260 ± 50 ppm in both formations). In both cases, an exception is observed, with significant enrichment in E-MV3 (470 ppm ± 20 ppm) and in H-MV1 (368 ± 12 ppm).

Sulphur concentration of host lava ranges from around 10 ppm in Rauðimelur to around 90 ppm in Hekla and over 100 ppm in Eldgjá lava (Table 4.6). The sulphur enrichment factor (EF_S) of Rauðimelur segregations is variable, with R-HVS1 and R-VC1 showing no clear enrichment with respect to the host lava ($EF_S \sim 1$) whereas R-HVS2, R-MV1 and R-MV2 are highly enriched in S, exceeding that of the nominally incompatible elements (e.g., R-MV2 has $EF_S > 10$ whereas $EF_{Th} \sim 3$). Segregations from Eldgjá and Hekla generally have EF_S similar to EF_{Th} (Fig. 4.5) but one segregation from Eldgjá have EF_S slightly higher than

EF_{Th} (E-MV1), whereas the most primitive ones at Hekla (H-VC and H-HVS1) show negligible S enrichment.

A relative homogeneity of F concentrations is observed in the host lava of Rauðimelur (Table 4.6), whereas the Eldgjá HL displays variable F concentration. Of all the lavas, Rauðimelur has the lowest fluorine concentration (106-123 ppm) and Eldgjá the highest (> 350 ppm F). The results of this study concur with data reported in the literature, the Rauðimelur lava results being within the range obtained from Reykjanes samples, whereas Eldgjá HL has marginally lower F than published values (Sigvaldason and Óskarsson 1986; Stecher 1998). In most segregations, fluorine enrichment is similar to that of Th ($EF_F \sim EF_{Th}$), though lower enrichments are observed in Rauðimelur.

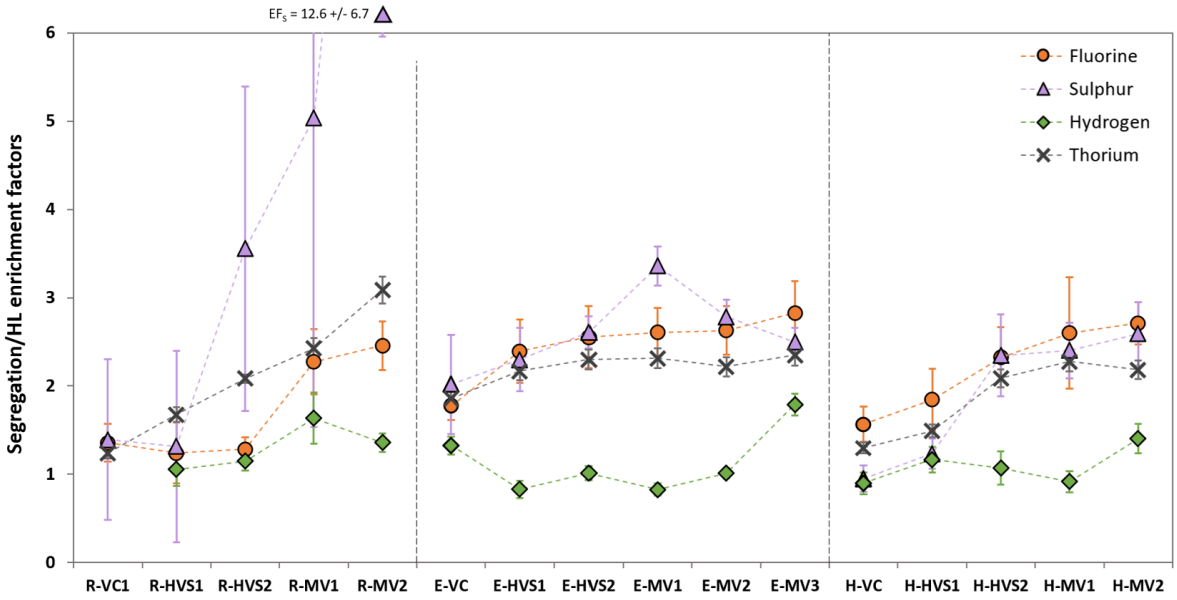

Figure 4.5. Major volatiles (S, H and F) and Th enrichment factors (EF) in the segregations of Rauðimelur, Eldgjá and Hekla. *R-MV2 sulphur EF plots off the graph as indicated above the diagram.*

4.6 Discussion

The segregation mechanism is a well-known process leading to internal differentiation and gas-rich melt displacement in a basalt lava (e.g., Anderson et al. 1984; Goff 1996; Martin and Sigmarsson 2007; Sigmarsson et al. 2009; Hartley and Thordarson 2009; Kuritani et al. 2010; Sheth et al. 2017; Nikkola et al. 2019). The role of the gas phase, not only in the gas-filter pressing mechanism, but also in the displacement and the outgassing of volatile elements, allows the use of segregations to discuss the final lava degassing and assess its potential environmental impacts. The observation of "K_2O-poor" and "K_2O-rich" glass in the Rauðimelur lava (Martin and Sigmarsson 2005) as well as the extreme Na_2O concentration in glass patches of segregations from Surtsey Island (14 wt %; Sigmarsson et al. 2009) also highlight that fractional crystallisation alone cannot explain segregation composition.

The over-enrichment ($EF_X > EF_{Th}$) of volatile metals in many of the segregations strongly suggest a gas-phase condensation in the final segregation melt or gas phase precipitation.

After discussion of the complete segregation process, we will attempt a characterisation of the gas phase composition leaving the lava by comparing over-enriched segregations to non-enriched ones. Finally, an estimation of the total trace element release from the Eldgjá lava field is calculated and the results compared to Fagradalsfjall lava emissions (Chapter 3).

4.6.1 Segregation formation

The crystallisation of the segregation melt and its mobility within the lava give rise to a variety of segregation structures. Their mineralogy and whole-rock composition reveal the hierarchical structural relationship between the different segregations. The higher proportions of early crystallising phases (olivine and plagioclase) in Rauðimelur host lava, and of later forming minerals (clinopyroxene and oxide) in the segregations concur with fractional crystallisation as the magma differentiation mechanism. Further evidence comes from the rather primitive mineral composition (An-rich plagioclases, Fo-rich olivines and Fe-poor clinopyroxenes) of HL whereas the segregation minerals are of a more evolved composition, particularly in the megavesicle segregations.

Despite the different whole rock composition of the three basaltic lavas, segregations from Rauðimelur, Eldgjá and Hekla display similar characteristics. The segregations form clear trends resulting from FC of the host lava (Fig. 4.3) and the trace element compositions reveal enrichment in incompatible elements and depletion in compatible elements, such as Cr and Ni. As previously done by Caroff et al. (2000), Martin and Sigmarsson (2007), Sigmarsson et al. (2009) and Hartley and Thordarson (2009), the degree of fractional crystallisation of each segregation can be estimated from the Rayleigh distillation law:

$$C = C_0 F^{D-1} \quad (4.2)$$

Using an incompatible element with a partition coefficient close to nil (D ~ 0) such as Th, the degree of crystallisation (1-F) is given as follow:

$$1 - F = 1 - \frac{C_0}{C} \quad (4.3)$$

Where C is the Th concentration measured in a segregation and C_0 that of the HL. Applying Eq. (4.3) to Rauðimelur and Hekla segregations give a fractional crystallisation of 24 to 67 % and 25 to 58 % respectively. Eldgjá segregations are more homogeneous, with FC of 47 % for the VC and ranging from 54 to 58 for the HVS and MV. These percentages are similar to literature values (30-70 %; Caroff et al. 2000; Sigmarsson et al. 2009; Hartley and Thordarson 2009). The lower values for some vesicle cylinders such as H-VC (25 %) and R-VC1 (24 %) suggest that, during the rise of the VC through the lava core, macrocrysts from the HL can be incorporated and/or that the buoyant gas phase may drive residual melt out of the VC. Such VC will thus plot off the evolution trend (Fig. 4.3) as in the case of R-VC1 from Rauðimelur. The variable evolution stages can be explained by continuous crystallisation taking place within the segregation system after the initial melt escape. Indeed, the VC are the lowest most component of the segregation system, being in the lava core, and could thus represent the initial segregation melt escaping from the interlocked-crystalline-lattice without further evolution. The melt that formed HVS, which are higher up in the lava, is likely to have experienced further FC during its migration upwards, resulting in a more evolved segregation melt, the final stage being the formation of the MV from the HVS.

To further investigate the segregation emplacement conditions, the segregation compositions were compared to crystallisation models using Comagmat 5.5 (detailed input and results shown in the supplementary data 4.7). The segregation compositions are best explained by pure fractional crystallisation (no equilibrium crystallisation) of a melt of host lava composition. Though models do not reproduce perfectly the composition of the segregations (e.g., TiO_2 content), they confirm that FC of 40-65 % fit best the segregation composition. The crystallising phases are first plagioclase quickly followed by olivine (in reverse order for Hekla), whereas clinopyroxenes and iron oxides (ilmenite and magnetite) crystalise later. Such results match the observed mineral phases and their modal proportions in the Rauðimelur segregations.

The modelled mineral compositions correspond relatively well with the measured composition in Rauðimelur host lava and segregations. Both plagioclase and olivine macrocrysts are slightly more primitive (An-rich and Fo-rich) than what the model predicts as the first crystallising mineral (Fo81 and An82). Such results support the fact that the macrocrysts formed before host lava crystallisation. The host lava plagioclase, olivine and clinopyroxene microcryst core compositions fit with the modelled mineral compositions crystallising in the first 40 % FC. The mineral cores analysed in R-MV1 have compositions that are associated with a crystallisation of 60-65 % FC, fitting the results from whole-rock analysis. According to the models, the Rauðimelur host lava started to crystalise at over 1200 °C, while its most evolved segregations emplaced at around 1100 °C. Eldgjá and Hekla host lava both started crystallising at temperatures around 1150 °C while their segregations crystallised down to 1070 °C.

The detailed observations of the internal structures from the three lava thus bring additional constrain to the gas-filter pressing model (Anderson et al. 1984). Due to its low density and pressure increase, the residual melt-gas mixture starts to migrate out of the crystal lattice and upwards in the lava. While rising in the vesicle cylinder, the segregation melt may incorporate already formed macrocrysts and experience late residual melt escape (Fig. 4.6). Simultaneously, the segregation melt undergoes further crystallisation, resulting in progressively more evolved melt composition. When the melt reaches the solidifying upper crust of the lava flow, it spreads out laterally leading to the formation of horizontal vesicle sheets and eventually forming megavesicles with horizontal segregation base (Thordarson and Self 1998; Walker et al. 1999). The segregations in the lower part of the MV, having the lowest MgO (Fig. 4.3), were therefore formed by melt that had experienced the highest degree of fractional crystallisation (≥ 50 %), and the upper part (the void) was formed by the exsolved gas accumulation. The residual gas is released if the lava crust cracks, intersects the segregations and liberates the final gas phase to the atmosphere.

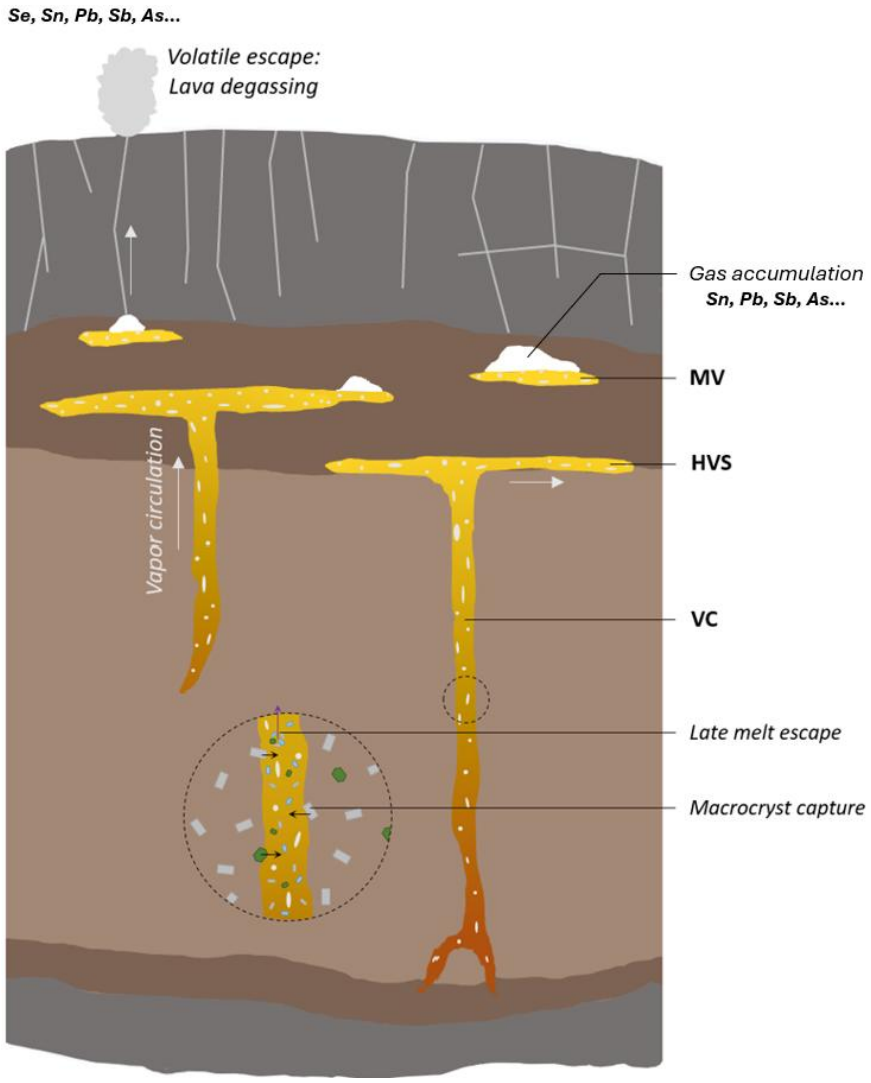

Figure 4.6 Conceptual model describing the segregation process and the resulting internal lava structure. *The cartoon shows a cross-section through a lava flow. In grey is represented the frozen upper and lower crust, dark brown the crystallising lava and light brown the molten lava. The different segregation types (VC: vesicle cylinder, HVS: horizontal vesicle sheet, MV: megavesicle) are shown and the degree of differentiation by fractional crystallisation is indicated by the colour change (brown being more primitive and yellow evolved). Additional processes shown are macrocryst (olivine and plagioclase) capture, late melt loss and volatile circulation. The gas exsolved during fractional crystallisation of the host lava is represented by the white circles. The gas occasionally merge, forming the void of the MV.*

4.6.2 Volatile behaviour during the segregation process

The segregation formation is therefore the consequence of gas-filter process operating within the basaltic lava. The residual gas phase can then either escape the lava flow through the segregation system, precipitate or condensate within the megavesicles with the last drop of melt. In the latter cases, the volatile elements present in the gas phase should appear in excess compared to refractory incompatible elements such as Th in the segregations. Since no precipitate phase was observed in the investigated segregation, condensation is considered

more likely. Such process would also explain the large Pb enrichment in the different phases of R-MV2

Major volatiles

Water (measured as H) is systematically less enriched than Th in the segregations and often of similar concentration as measured the host lava (Fig. 4.5). Since only anhydrous mineral phases are present, crystallisation results in H_2O enrichment in the derived melt forming the segregation. Water being the most volatile element of this study, it is most likely the first to reach saturation and exsolve, forming a gas phase. Consequently, the absence of water enrichment in the segregations most likely translate water escape from the segregation system to the atmosphere. However, a few segregations, such as E-MV3, display significant water enrichment with respect to the host lava, possibly representing a segregation melt in which water vapour partially condensed.

Sulphur behaves differently with EF generally similar to that of Th, suggesting a behaviour mainly controlled by fractional crystallisation. However, S is occasionally significantly more enriched than Th ($EF_S > EF_{Th}$), which may be termed over-enrichments. It is clear in the case of the Rauðimelur megavesicles (particularly R-MV2), where the S over-enrichment may reflect gas phase condensation together with the solidification of the last melt. In most cases fluorine has an enrichment factor in the segregations close that of Th (Fig. 4.6) suggesting that F remained mostly soluble in the segregating melt, increasing in concentration through simple fractional crystallisation.

Volatile trace elements

Due to variable partitioning between crystal, melt and gas phase, the volatile metals can be variably enriched in the segregations. With respect to the whole rock, significantly higher concentrations in Zn are observed in FeTi-Oxide and Olivines, Cd in Clinopyroxene and Sn in Oxide. Therefore, these elements are expected to be less enriched in the segregation melt compared to Th, which is indeed observed as Cd and Zn are the least enriched volatile metals in the segregations (Fig. 4.4), together with In, previously identified as compatible in clinopyroxene (Greaney et al. 2017).

In contrast, the volatile metals Mo, Sb and Pb display over-enrichment in Rauðimelur megavesicles ($EF_{Pb}/EF_{Th} \sim 3$ and $EF_{Sb}/EF_{Th} \sim 2.5$ in R-MV1 and $EF_{Mo}/EF_{Th} \sim 1.45$ in R-MV2, Fig. 4.7a and 4.7b). This over-enrichment is associated with high S-enrichment (Fig. 4.5, supplementary Fig. 4.8). These elements being known to form volatile species, their over-enrichment can be explained by their partition in the gas phase, followed by their condensation along with sulphur. These elements are however known to rather form volatile species with halogens (Cl and F) rather than sulphur (c.f., Chapter 3). One way to explain these observations would be that only the portion of halogens complexed with these volatile metals would have condensed, whereas the large majority would have escaped (unlike sulphur), leaving no resolvable halogen enrichment.

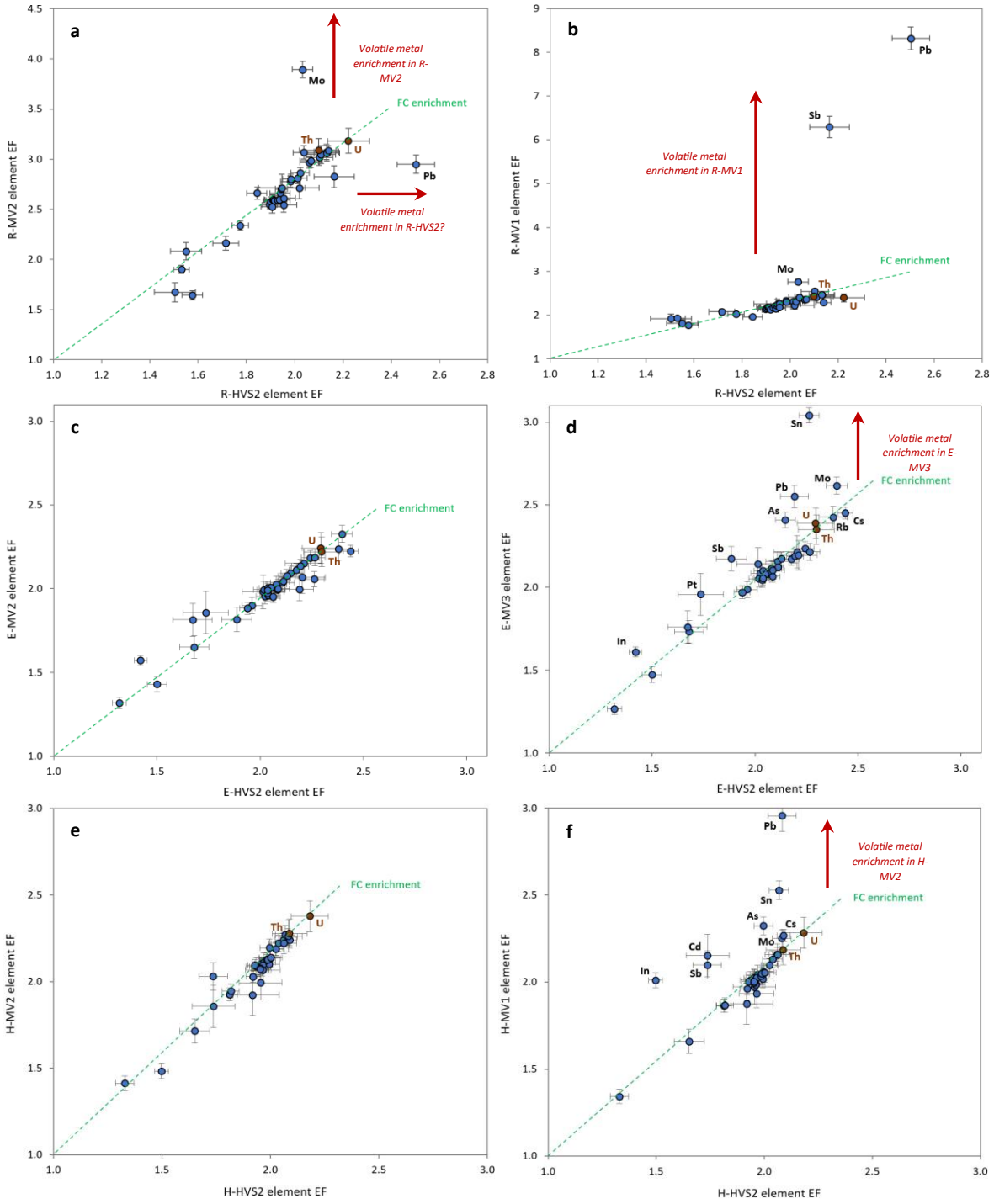

Figure 4.7. Comparison of the element enrichment factors in different segregations. *Enrichment factors of: (a) Two Rauðimelur segregations indicating over-enrichment in a couple of volatile metals (R-MV2 and R-HVS2). (b) R-MV1 over-enriched in Sb and Pb as a function of R-HVS2. (c) Two non-enriched evolved segregations from Eldgjá (E-HVS2 and E-MV2). (d) An over-enriched segregation (E-MV3) compared to E-HVS2. (e) Two non-enriched evolved segregations from Hekla (H-HVS2 and H-MV2). (f) An over-enriched segregation (H-MV1) compared to H-HVS2. Uranium and Th are indicated in brown and should represent the most incompatible refractory elements.*

In both Hekla and Eldgjá, a single megavesicle segregation shows volatile metal over-enrichment (E-MV3 and H-MV2) whereas other segregations have composition reflecting enrichment by liquid-solid separation during simple fractional crystallisation. Figure 4.7c and 7e compare the EF of two non-enriched segregations from Eldgjá and Hekla respectively. Both comparisons reveal alignment of all elements, with incompatible elements U and Th being among the most enriched. Such alignment translates similar behaviour of all elements in the two Eldgjá and Hekla segregations, with enrichments (or depletions) fully explained by fractional crystallisation. The comparison between the over-enriched segregation E-MV3 and E-HVS2 (Fig. 4.7d) also reveals alignment of the refractory (i.e., non-volatile) elements. In marked contrast, most volatile metals do not fall on this line and are significantly enriched in E-MV3. The segregation from Hekla H-MV1 displays features similar to that of E-MV3 when plotted against another segregation of similar maturity (H-HVS2, Fig. 4.7d). Both these over-enriched segregations also have significantly higher H_2O concentrations than the other segregations, which have values like that of the host lava (Fig. 4.5, supplementary Fig. 4.8). Other major volatiles (S and F) display normal incompatible element enrichment ($EF_{S,F} \sim EF_{Th}$).

The composition of two types of segregation (over-enriched and non-enriched) could be explained by variable behaviour of the volatiles during the segregation formation. When all volatiles remain in the gas and escape the segregation system (feeding the lava/secondary degassing), it leaves behind a segregation melt without over-enrichment in volatile metals and low water content. Occasionally the gas phase would undergo such condition that many volatile metals would condensate together with the segregation melt, leading to the formation of volatile metal over-enriched segregations with higher water content. The fact that enrichment in H_2O remains significantly less than that of Th ($EF_H < EF_{Th}$) in these segregations suggests that part of the gas still escaped the segregation melt, likely carrying off some highly volatile elements such as Se.

The role of gas circulation within a crystallising lava thus appears critical. The gas phase formed by host lava crystallisation and causing segregation formation displaces major and trace volatile elements, which are either degassed from the lava flow or condensate with the final segregation melt.

4.6.3 Implications for lava/secondary degassing

To investigate the potential environmental hazard induced by lava degassing fed by segregation process, we evaluate to what extent the volatile metals were liberated from the large lava field of Eldgjá Fires 939 CE. To estimate the mass of volatile metals emitted by the segregation process and subsequent degassing, the proportion of segregations in the lava field must be estimated. Mass proportions of the order of 1 % appears reasonable (Helz, 1987; Nikkola et al., 2019; Sigmarsson et al., 2009). Since most of our segregations are degassed (without volatile metal over-enrichment), this value is taken as equivalent to the proportions of degassed segregation melt.

To quantify the atmospheric loading for each element from Eldgjá lava, we use the comparison between the segregation that supposedly retained the gas (E-MV3) and a similar segregation but that has lost its gas enrichment (E-HVS2). The volatile metals found significantly enriched in E-MV3 (> 1.05 E-HVS2 concentration) are As, Mo, Ag, Cd, In, Sn, Sb and Pb (Fig. 4.4e). For these elements we can calculate the difference between E-MV3

and E-HVS2 (the so-called excess in the undegassed segregations) and multiply this excess by the approximate mass of degassed melt to estimate the atmospheric loading:

$$X_{emitted} = m_{lava} \times f_{deg} \times [X]_{excess} \quad (4.4)$$

$X_{emitted}$ is the mass of an element X released from the lava, m_{lava} is the mass of erupted lava, f_{deg} is the mass fraction of degassed segregations in the lava field and $[X]_{excess}$ the over-enrichment in X in E-MV3. Assuming a mass fraction of 1 % of the entire lava being degassed segregations, we calculate a degassing of several tons for all the identified volatile metals, up to 215 t of Mo, 278 t of Pb and 835 t of Sn (Table 4.7). Because of the necessary assumptions used for this calculation, such result should not be considered as precise values, but rather a first order estimation of the mass emissions. Nevertheless, it remains of interest to confront these results with other data regarding secondary lava gas emissions.

Table 4.7. Estimated volatile metal emissions from the cooling Eldgjá lava field.

	As	Mo	Cd	In	Sn	Sb	Pb
Excess in Eldgjá undegassed segregations (µg.g^{-1})	0.22	0.43	0.02	0.03	1.66	0.02	0.55
Estimated volatile emissions (t)	112 x 10^3	215 x 10^3	9.19 x 10^3	13.5 x 10^3	835 x 10^3	11.4 x 10^3	278 x 10^3
Volatile metal emissions (kg) in Fagradalsfjall (Chapter 3)	70	65	15.6	5.2	266	118	222

The obtained mass released can thus be compared with the estimations from the gas composition sampled at the crystallising lava of Fagradalsfjall (Chapter 3). The calculated values for Eldgjá are about three orders of magnitude higher than the Fagradalsfjall estimations (Fig. 4.8). Such difference is readily explained by the two orders of magnitude higher volume of the Eldgjá eruption with respect to Fagradalsfjall together the five-fold enrichment in most trace element concentration in the Eldgjá lava. Additionally, the particular enrichment of the halide forming elements (Mo, Pb, Sn) observed in the crystallising lava gas is also visible in the over-enriched segregations. In contrast, our results show limited Cd emissions, which is in line with its tendency to rather degas at the eruptive vent than from the crystallising lava.

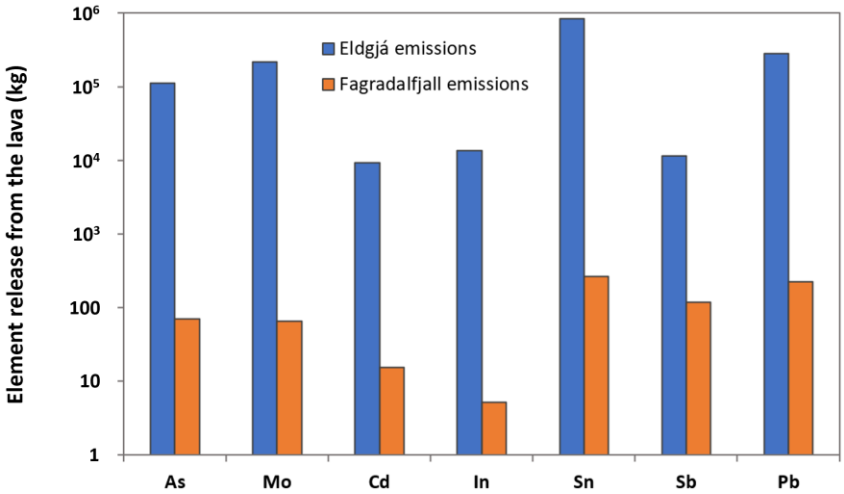

Figure 4.8. Comparison between volatile metal release from Eldgjá and Fagradalsfjall lava fields. *The estimations are based on the segregation compositions for Eldgjá and the*

one based on gas sampled over the crystallising lava for Fagradalsfjall (Chapter 3). The three order of magnitude difference is readily explained by the largest volume of the Eldgjá eruption and the volatile metal enrichment in the transitional Eldgjá magma with respect to the one of Fagradalsfjall.

Estimating the amount of volatile metal release using undegassed and degassed segregations thus appear promising. Though obtaining exact numbers would require better constrain on several parameters (volatile metals enrichment, proportion of segregation being over-enriched, proportion of segregation in the lava field), the estimations presented here suggest significant release of some toxic metals, particularly those forming halide species (as directly observed in the crystallising lava gas; Wainman et al. 2024; Chapter 3). The liberations of over 100 t of Mo, Pb and Sn from the cooling Eldgjá lava has strong implications in terms of local environmental hazard, in the years following lava emplacement. It is worth pointed out that Eldgjá size eruptions, and associated metal emissions, are rare (Laki being the only other historical example in Iceland) whereas Fagradalsfjall size eruptions are much more frequent.

4.7 Conclusions

The petrological, mineralogical and compositional study of segregations and host lava from Reykjanes, Hekla and Eldgjá brings new insights on the emplacement and diversity of the segregations. Segregation results from the three lavas are readily explained by the gas-filter pressing model and highlight a maturity gradient from vesicle cylinder to megavesicles, formed by 35 to 60 % fractional crystallisation of magma with the composition of the host lava. Crystal capture from the host lava occasionally take place, resulting in vesicle cylinder of rather primitive composition. The trace element analyses revealed specific behaviour of the volatile metals, resulting in variable enrichment factors in the segregations. Most segregations displayed enrichment in volatile metal readily explained by simple fractional crystallisation, whereas a few displayed higher enrichments that cannot be explained by fractional crystallisation alone. In a nutshell, the key conclusions are interpretations drawn from the presented results:

- Fractional crystallisation and resulting gas-filter pressing are confirmed as the main process leading to the segregation formation.

- The residual melt undergoes continuous evolution, forming first the vesicle cylinders, then the horizontal vesicle sheets and finally the most evolved megavesicles.

- Occasional volatile metal condensation from the gas phase results in their over-enrichment in some megavesicles.

- The volatile metal excess in the over-enriched segregation indicates gas composition with similar features as the secondary gas from solidifying lava at Fagradalsfjall, supporting the role of segregation process in lava degassing.

Acknowledgements

We thank all the technicians whose expertise greatly helped us obtain the results. First, we want to thank Jóhann Gunnarsson Robin for his precious help on developing/adapting the method to be able to measure F from our samples using Ion selective electrodes. We acknowledge Jean-Luc Devidal for his support in running the EPMA and LA-ICP-MS at the Laboratoire Magmas Volcans and Guðmundur Heiðar Guðfinnsson for his help with the EPMA at Institute Earth Sciences. We would like to thank Krzysztof Suchorski who guided the trace element analyses at LMV. Finally, we want to acknowledge Claire Fonquernie for running the multielement (CHNS/O) analyser. This work was supported by the Icelandic Research Found (Rannís).

4.8 Supplementary information

4.8.1 Sampling site pictures

Supplementary Figure 4.1. Eldgjá sampling site pictures. *(a) Eldgjá 4 m high outcrop close to Hólmsá river. Numerous small megavesicles are present, from which were extracted E-HL2 and several segregations. (b) Example of sampled horizontal vesicle sheet (E-HVS1) and (c) megavesicle (E-MV1).*

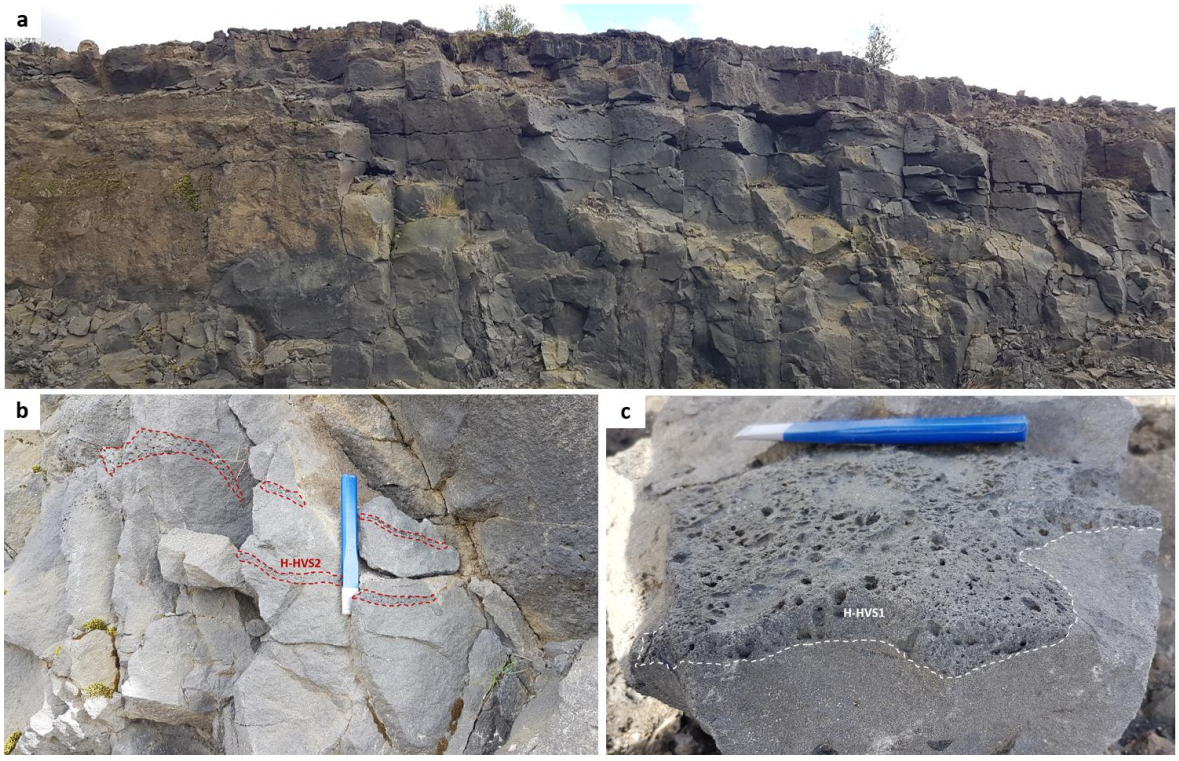

Supplementary Figure 4.2. Hekla sampling site pictures. *(a) Holocene 7 m high lava flow outcrop, from which H-HVS2 (b) was extracted. (c) One of the boulders from which segregations were collected (H-HVS1)*

4.8.2 Detailed petrographic observations

Host lava:

The Rauðimelur host lava (R-HL2) was examined using both a thin section with only HL (Supplementary Fig. 4.3a) and thin sections showing a segregation surrounded by host lava (Supplementary Fig. 4.3b). Similar features were found in all these locations, translating homogeneous petrology of the HL. R-HL2 is composed of macrocrysts, microcrysts and micrographic patches finely crystallised (micrographic texture) together with small vesicles (< 0.5 mm) of erratic shapes representing 5 % of the sample (Table 2). The macrocrysts range from 0.5 to 5 mm. Most of them are plagioclase, displaying dark cores on SEM back scattered electron (BSE) images and even darker rims (i.e., composed of lighter elements). Rare large olivines (around 0.5 mm) are also present. Both minerals are cracked and zoned. They make up 5-10 % of the sample, with a great majority being plagioclase (Supplementary Fig. 4.3a), which is in agreement with observations from Martin and Sigmarsson, (2007).

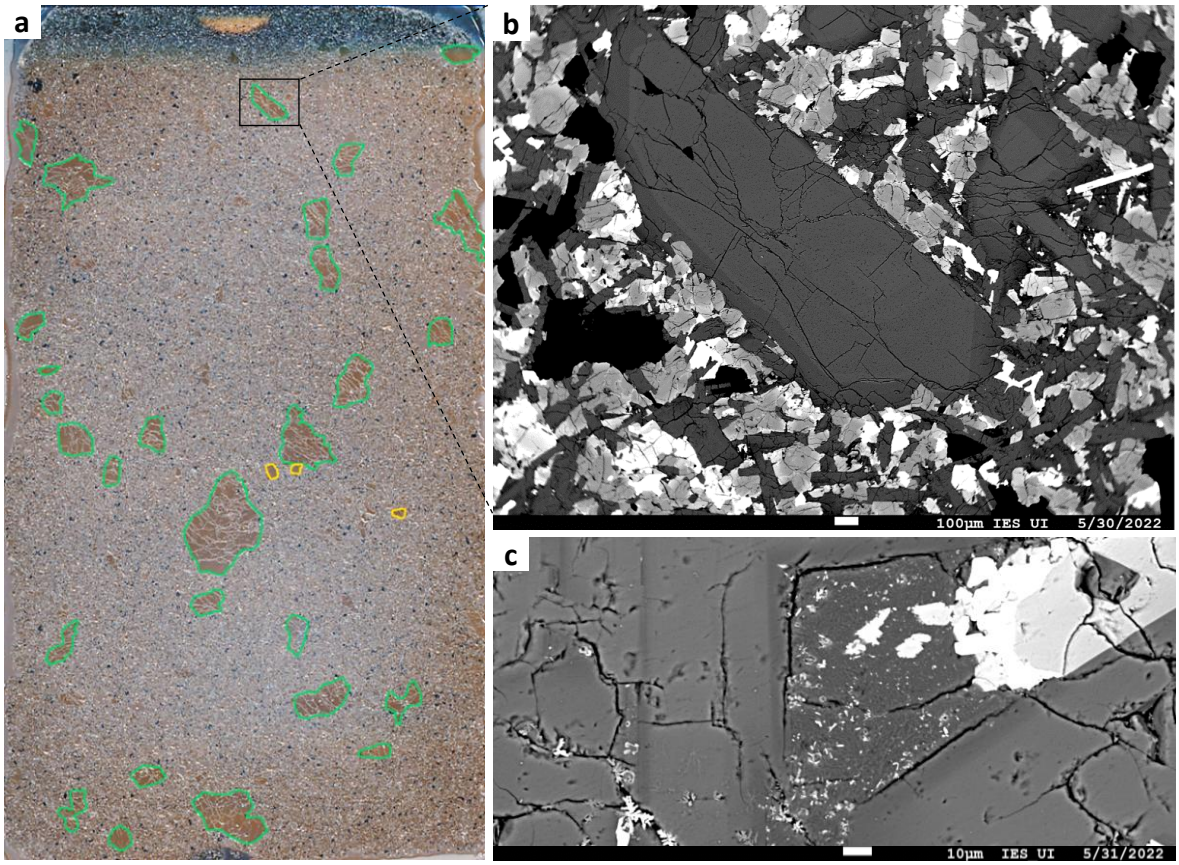

Supplementary Figure 4.3. Rauðimelur host lava (R-HL2) thin section pictures. *(a) Photo of the thin section with encircled the largest macrocrysts of plagioclase (green) and olivine (yellow). (b) The same thin section observed under back scattered electron (BSE). All the components of our sample appear here: Macrocryst, groundmass microcrysts, micrographic patches and vesicles. (c) Zoom in on one micrographic patch displaying a few accessory crystals surrounded by micrographic texture.*

The groundmass represents approximately 80 % of the volume and is made of microcrysts smaller than 0.4 mm (typically 100 µm). Plagioclase and clinopyroxene are the principal phases, both representing approximately 40 %. Most plagioclase crystals are elongated and of euhedral to subhedral shape. They are cracked and display small darker rims in the SEM back scattered images (i.e., lighter meaning less Ca). The pyroxene crystals vary in shape from euhedral to anhedral. They are also cracked and show in many cases clear rims, which are brighter (i.e., denser because of higher Fe content) than the core. Oxides make up approximately 10 %, present as crystals of variable size and shape. The final microcryst is olivine, representing 5 to 10 %. The olivine is less cracked but display obvious zonation with much brighter rim than core.

The micrographic patches (< 5 %, Supplementary Fig. 4.3c) are present between larger microcrysts (often elongated plagioclase). They are made of small accessory minerals (< 20 µm) in a micrographic texture (quartz-feldspar intergrowth), which represent the last liquid to crystalise. The proportion of micrographic crystals in the patches varies spatially, with accessory phases of oxides (often skeleton shaped), pyroxenes and occasionally with angular shaped feldspar larger than in the micrographic texture.

Vesicle cylinders:

Two thin sections made from vesicle cylinders (R-VC2 and R-VC3) display similar features, with only slightly distinct macrocryst and vesicle content. The phases observed are like those in the host lava but of different proportion and features (Supplementary Fig. 4.4a). The VC have much larger vesicles (up to 10 mm) representing a larger volume (10 to 30 %, spatially variable). Macrocrysts are abundant, making 25 % of the thin sections with sizes up to 6 mm, also visible with the naked eye (Fig. 4.2c). The great majority of them is zoned and cracked plagioclase, showing similar features to HL macrocrysts. A few large olivine crystals (> 1 mm) are also visible (Supplementary Fig. 4.4b) and display strong zonations.

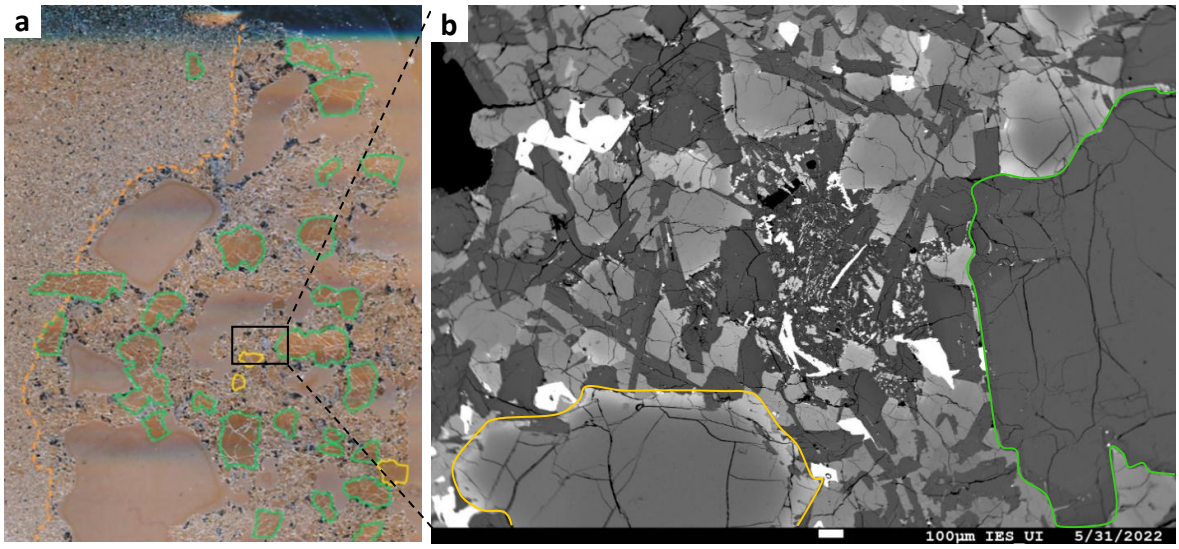

Supplementary Figure 4.4. Rauðimelur vesicle cylinder (R-VC2) thin section pictures. *(a) Photo of the thin section with encircled the largest macrocrysts of plagioclase and olivine. (b) Electron microprobe BSE (back-scattered electron) image showing a plagioclase and olivine macrocrysts and the ubiquitous groundmass patch with micrographic texture.*

The groundmass microcrystals are larger than in the HL, around 300 µm. Half of these crystals is clinopyroxene (cpx), unzoned apart from the largest. Elongated plagioclases are 30 % of the groundmass, often zoned. The oxides are of diverse size and shape and represent roughly 15 %. The remaining 5 % of the microcrysts is made of small zoned olivines.

Finally, patches with micrographic texture (found as large as 1 mm wide) make up the last 15 % of the VC, three-times higher than in the HL. The phases present in these patches are again, in diminishing proportions, oxides, cpx and finally feldspar (olivine is absent). Rare small and elongated apatite were also observed. In general, these patches are made of around 50 % accessory minerals and 50 % micrographic texture (Supplementary Fig. 4.4b).

The cylinder R-VC1 has the same phases as the other samples but with considerably lower proportions of micrographic patches (Table 4.2). The epoxy plug reduces the visible vesicle volume (only 5 %), but naked eye observation suggests similar vesicularity than in the other VC (Fig. 4.2).

Megavesicle (R-MV1):

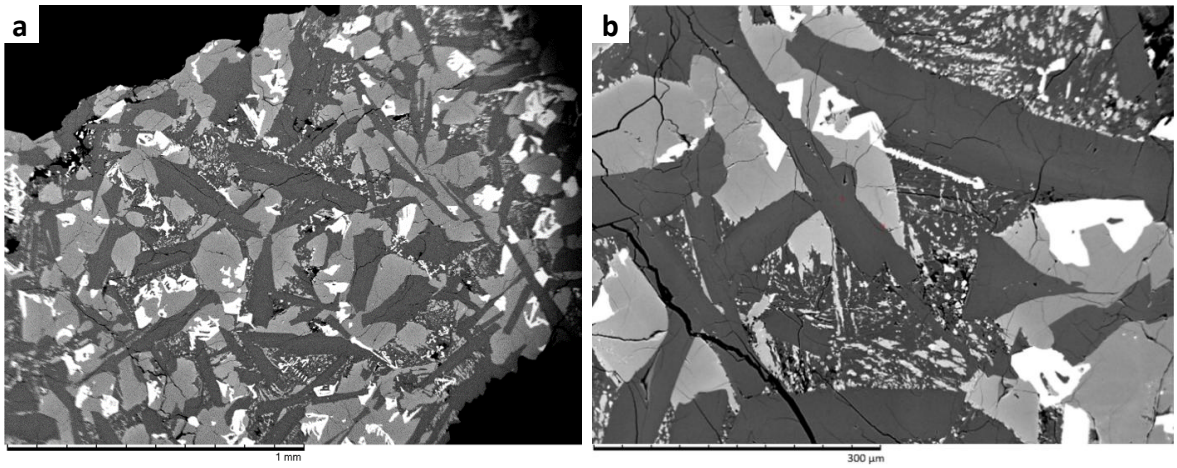

Supplementary Figure 4.5. Back-scattered electron images of the Rauðimelur megavesicle R-MV1 set up as a grain in epoxy. *(a) One R-MV1 grain displaying microcrysts and micrographic patches. (b) Zoom in on the patches composed of numerous small crystals within a micrographic texture.*

The megavesicle R-MV1 displays many similarities with the VC but also important differences. The megavesicle shows only two distinct mineralogical types (Supplementary Fig. 4.5a), the groundmass made of hundreds-µm-size microcrysts (about 75 % of the sample) and micrographic patches (around 20 %, supplementary Fig. 4.5b), in addition to a few small vesicles. Importantly, plagioclase (and olivine) macrocrysts observed in the VC and HL are absent in R-MV1.

The groundmass crystals are cpx (45-55 %), plagioclase (30-40 %) and oxides (15-20 %). Therefore, more cpx and oxides but less plagioclase are present compared to the VC and HL, and no olivine (in marked contrast to the HVS (HRG4/R-HVS1) of Martin and Sigmarsson (2007).

The micrographic patches are composed of small, elongated crystals of cpx and skeleton shaped oxides together with plagioclase and small elongated apatite. All these microcrysts are immerged in the micrographic texture.

Comparison samples

Comparison of the different samples reveal clear trends. Overall, we observe a trend in the mineralogic mode from R-HL through R-VC (and HRG4/R-HVS1) to R-MV1. The proportion of pyroxene and oxides increases from HL to MV, whereas the proportion of olivine decline and become absent in MV. The quantity of micrographic patches rises from below 5 % in HL to 15 % in R-VC2/R-VC3, and 20 % in R-MV1.

Vesicularity is much higher for the segregations than in the HL (around 20 % and 5 % respectively). The difference is striking for the size of these vesicles, which reach up to 10 mm in the VC but is only 0.5 mm in the HL (Supplementary Fig. 4.3 and supplementary Fig. 4.4). Similar observations were reported by Martin and Sigmarsson (2007) between their segregation (HRG4/R-HVS1) and their HL (HRG2/R-HL1). It is also worth noting that crystal size is much larger in the segregations compared to HL, around 300 and 100 µm respectively.

A different trend appears regarding macrocrysts: They are moderately present (~ 10 %) in the HL (in agreement with Martin and Sigmarsson (2007), more abundant (~ 25 %) in the different VC but absent in the MV and HVS.

Within the different vesicle cylinder samples, one main difference is observed for R-VC1 relative to R-VC2 and R-VC3 (Table 4.2), namely distinct amount of micrographic patches within the cylinders (5 % in R-VC1 and 15 % in R-VC2/3).

4.8.3 Trace element composition of the studied lava

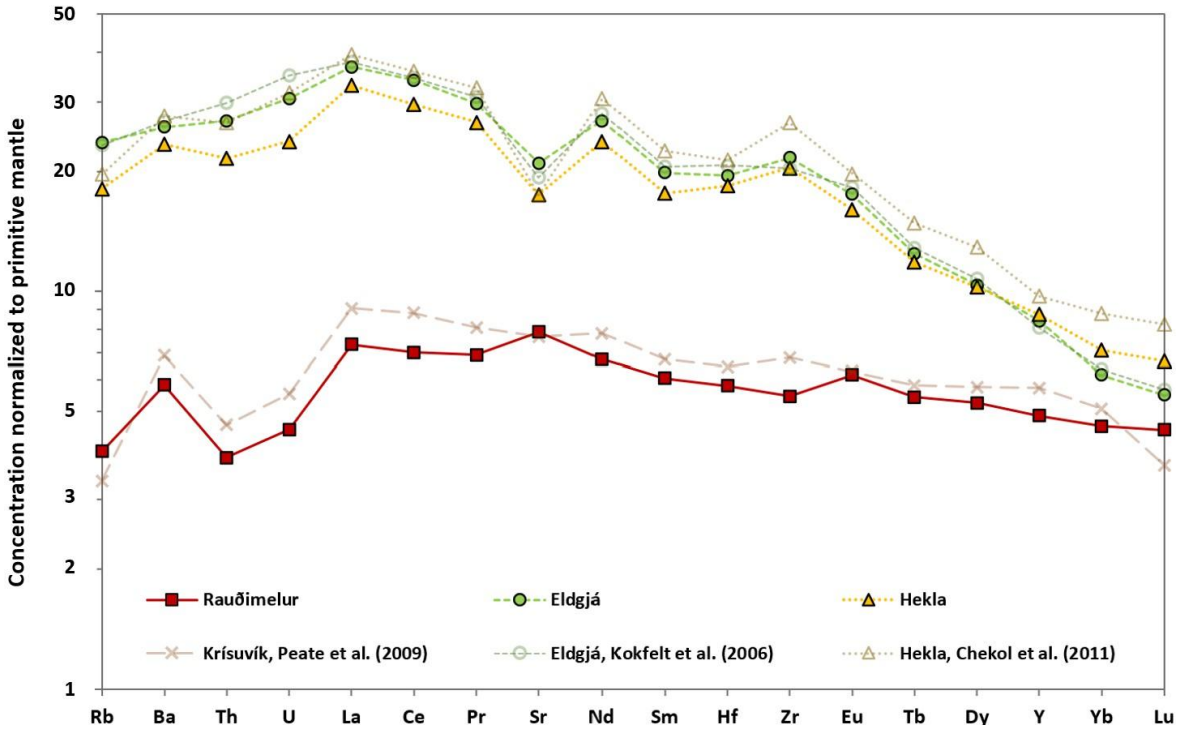

Supplementary Figure 4.6. Primitive mantle-normalised composition of Rauðimelur, Eldgjá and Hekla lava. *The element order is taken from Halldórsson et al. (2022). The host lava trace element concentrations are normalised by those of the primitive mantle (Palme and O'Neill, 2003) and compared with published results on basalt lava from the same volcanic systems (Peate et al., 2009; Kokfelt et al., 2006; Chekol et al., 2011).*

4.8.4 Major element mineralogical composition of Rauðimelur products

Supplementary Table 4.1. Detailed composition of the different feldspars found in the Rauðimelur HL and segregations.

		SiO_2	TiO_2	Al_2O_3	FeO	MnO	MgO	CaO	Na_2O	K_2O	Total
Macrocryst core	R-HL2 (9)	46.7	0.03	33.9	0.53	0.01	0.19	16.9	1.69	0.04	100.0
	min	45.3	0.006	33.2	0.48	0.00	0.12	16.3	1.41	0.01	99.0
	max	47.5	0.05	34.4	0.58	0.03	0.23	17.3	2.09	0.15	100.9
	R-VC1 (5)	45.9	0.03	34.3	0.45	0.01	0.21	17.0	1.49	0.02	99.4
	min	45.5	0.00	34.2	0.44	0.00	0.20	16.9	1.41	0.01	99.1
	max	46.2	0.05	34.5	0.48	0.02	0.23	17.1	1.56	0.03	99.7
	R-VC2/3 (5)	46.8	0.02	34.0	0.52	0.02	0.18	17.0	1.59	0.02	100.2
	min	46.0	0.01	33.3	0.44	0.01	0.17	16.6	1.27	0.01	99.6
	max	47.1	0.04	34.6	0.59	0.03	0.19	17.5	1.84	0.02	100.8
Macrocryst rim	R-HL2 (7)	52.8	0.07	29.4	0.78	0.01	0.15	12.1	4.42	0.22	99.9
	min	48.8	0.04	25.6	0.64	0.00	0.04	7.41	2.89	0.05	97.9
	max	58.9	0.13	32.3	1.1	0.03	0.26	15.0	7.03	0.64	101.2
	R-VC2/3 (5)	53.4	0.10	29.1	0.85	0.01	0.13	11.9	4.47	0.12	100.1
	min	52.5	0.09	28.4	0.78	0.00	0.10	11.2	4.14	0.10	99.2
	max	54.8	0.10	29.6	0.94	0.02	0.14	12.4	4.96	0.16	100.6
Microcryst core	R-HL2 (7)	50.1	0.06	31.2	0.83	0.01	0.15	14.3	3.17	0.08	99.9
	min	48.9	0.04	30.6	0.72	0.00	0.09	13.4	2.93	0.06	98.6
	max	51.7	0.07	32.0	0.99	0.03	0.23	14.6	3.62	0.12	100.7
	R-VC1 (4)	51.5	0.11	30.3	1.0	0.02	0.14	12.8	3.79	0.10	99.8
	min	51.0	0.06	30.0	0.82	0.01	0.11	12.7	3.64	0.07	99.1
	max	51.8	0.19	30.6	1.4	0.02	0.17	13.0	3.87	0.11	100.5
	R-VC2/3 (11)	53.1	0.09	29.4	0.89	0.02	0.15	12.2	4.33	0.10	100.3
	min	50.1	0.06	27.7	0.80	0.00	0.11	10.5	3.01	0.07	98.9
	max	54.4	0.11	31.9	1.0	0.05	0.18	14.5	5.11	0.16	101.1
Microcryst rim	R-MV1 (10)	56.3	0.10	26.7	0.97	0.12	0.02	10.5	5.38	0.17	100.3
	min	54.9	0.07	25.8	0.73	0.08	0	9.43	4.81	0.13	100.0
	max	57.8	0.15	27.7	1.2	0.19	0.05	11.5	6.00	0.22	101.0
	R-HL2 (10)	51.8	0.08	30.5	0.90	0.01	0.13	13.2	3.71	0.10	100.4
	min	50.1	0.06	28.0	0.79	0.002	0.08	10.3	3.13	0.06	99.5
	max	55.8	0.11	31.6	1.0	0.03	0.21	14.0	5.44	0.19	102.5
	R-VC1 (5)	57.5	0.13	26.7	0.95	0.01	0.06	8.47	5.81	0.28	99.9
	min	56.2	0.08	25.6	0.65	0.00	0.05	7.01	5.15	0.21	99.6
	max	60.5	0.32	27.2	1.6	0.03	0.07	9.29	6.36	0.34	100.8
	R-MV1 (4)	60.1	0.05	24.4	0.93	0.04	0.02	7.72	6.77	0.31	100.3
	min	59.0	0.04	23.7	0.70	0.01	0	7.04	6.45	0.24	100.0
	max	61.2	0.08	25.0	1.2	0.06	0.03	8.41	7.16	0.46	100.7
Patch crystals	R-HL2 (3)	59.1	0.10	24.9	0.70	0.003	0.04	7.38	6.80	0.40	99.4
	min	55.9	0.09	22.2	0.61	0.00	0.03	5.37	5.55	0.24	97.9
	max	61.5	0.11	27.6	0.82	0.01	0.07	9.97	7.60	0.54	100.3
	R-VC1 (2)	61.6	0.09	24.5	0.80	0.002	0.01	5.37	6.58	0.71	99.7
	min	61.5	0.09	24.3	0.70	0.000	0.01	5.28	5.97	0.67	99.6
	max	61.8	0.10	24.7	0.90	0.004	0.01	5.46	7.19	0.75	99.8
	R-VC2/3 (18)	61.9	0.07	23.8	0.80	0.02	0.02	5.46	7.46	0.97	100.5
	min	58.1	0.03	20.6	0.51	0	0	1.92	6.42	0.26	99.4
	max	67.0	0.11	26.1	1.3	0.04	0.06	8.25	8.01	3.36	101.9
	R-MV1 (2)	65.7	0.58	18.6	2.1	0.04	0.01	2.63	4.86	5.93	100.4
	min	65.0	0.16	16.5	1.2	0.03	0.01	0.49	2.86	1.11	99.6
	max	66.3	0.99	20.7	2.9	0.05	0.02	4.77	6.87	10.8	101.2

Supplementary Table 4.2. Detailed composition of the different clinopyroxenes found in the Rauðimelur HL and segregations.

		SiO_2	TiO_2	Al_2O_3	FeO	MnO	MgO	CaO	Na_2O	Cr_2O_3	Total
Microcryst core	R-HL2 (5)	52.7	0.57	2.24	7.89	0.21	16.4	19.8	0.21	0.26	100.3
	min	52.4	0.50	1.90	7.45	0.20	15.8	19.4	0.19	0.18	99.8
	max	53.1	0.90	4.06	8.35	0.22	17.2	20.4	0.23	0.35	101.2
	R-VC1 (4)	50.1	1.0	2.60	11.8	0.28	14.4	18.6	0.27	0.04	99.2
	min	49.5	0.92	2.11	10.0	0.24	13.7	17.3	0.26	0.02	98.9
	max	50.6	1.2	3.16	14.3	0.33	14.8	19.8	0.28	0.08	99.4
	R-VC2/3 (7)	51.1	0.92	1.95	14.4	0.37	14.5	16.4	0.23	0.007	99.8
	min	49.6	0.66	1.14	11.9	0.29	12.1	12.9	0.19	0	99.3
	max	52.4	1.3	3.29	18.4	0.50	16.2	18.4	0.28	0.01	100.4
	R-MV1 (4)	49.3	1.39	2.78	17.3	0.44	12.4	16.2	0.22	0.03	99.0
	min	49.0	0.99	1.51	14.8	0.37	9.87	14.7	0.22	0	100.3
	max	49.6	1.7	3.49	18.9	0.51	13.9	18.3	0.23	0.07	100.6
Microcryst rim	R-HL2 (4)	51.3	0.77	1.08	21.2	0.52	15.5	9.71	0.15	0.009	100.3
	min	50.6	0.50	0.83	18.2	0.46	12.7	4.64	0.09	0	100.0
	max	52.0	1.0	1.45	23.6	0.59	18.5	15.3	0.25	0.02	100.8
	R-VC1 (3)	49.0	0.74	0.86	28.2	0.64	10.8	9.16	0.14	0.01	99.5
	min	47.6	0.56	0.66	22.7	0.50	8.39	5.53	0.08	0	99.4
	max	49.9	0.95	1.08	35.7	0.84	14.0	14.7	0.22	0.03	99.7
	R-VC2/3 (4)	49.9	0.73	0.90	24.9	0.65	10.6	12.1	0.16	0	99.9
	min	49.0	0.66	0.71	24.0	0.65	9.11	10.3	0.14	0	99.5
	max	49.7	0.94	1.13	27.6	0.73	10.6	13.1	0.17	0	99.8
	R-MV1 (2)	48.6	0.81	1.43	22.2	0.59	8.52	17.0	0.22	0.04	100.1
	min	48.2	0.70	1.38	19.9	0.53	7.92	16.3	0.20	0	99.8
	max	49.1	0.93	1.48	24.5	0.65	9.12	17.8	0.24	0.07	100.3
Patch crystals	R-VC1 (3)	47.2	1.1	1.24	29.9	0.77	5.13	13.2	0.27	0.005	98.7
	min	46.9	1.0	1.06	25.5	0.64	4.22	10.9	0.27	0.005	98.7
	max	47.6	1.2	1.35	33.0	0.86	6.92	15.6	0.27	0.005	98.7
	R-VC2/3 (7)	48.0	0.95	1.04	33.1	0.87	5.79	10.4	0.14	0.005	100.3
	min	47.4	0.51	0.76	30.1	0.76	3.56	6.36	0.09	0	99.5
	max	49.2	1.3	1.29	35.8	0.94	7.40	13.6	0.19	0.02	100.9
	R-MV1 (5)	47.5	1.0	1.21	32.1	0.94	5.48	11.8	0.16	0.04	101.1
	min	46.5	0.87	1.00	26.5	0.76	3.27	7.80	0.10	0	100.4
	max	48.4	1.2	1.53	39.0	1.2	7.41	16.0	0.23	0.09	101.9

Supplementary Table 4.3. Detailed composition of the different olivines found in the Rauðimelur HL and segregations.

		SiO_2	TiO_2	Al_2O_3	FeO	MnO	MgO	CaO	Na_2O	NiO	Total
Macrocryst core	R-VC2/3 (4)	37.7	0.01	0.10	16.4	0.28	44.0	0.33	0.02	0.19	99.0
	min	35.0	0	0.06	15.6	0.24	40.6	0.32	0.01	0.18	96.7
	max	39.9	0.02	0.14	18.3	0.31	46.0	0.34	0.03	0.21	102.6
Macrocryst rim	R-VC2/3 (4)	35.2	0.04	0.07	38.6	0.57	23.9	0.33	0.0003	0.05	98.8
	min	33.6	0.02	0.03	31.9	0.41	20.0	0.31	0	0.02	97.8
	max	36.1	0.05	0.12	45.1	0.75	30.6	0.35	0.001	0.10	99.9
Microcryst core	R-HL2 (6)	36.6	0.02	0.05	29.2	0.45	32.8	0.33	0.02	0.10	99.5
	min	35.8	0	0.02	25.8	0.36	29.0	0.29	0	0.07	99.2
	max	37.1	0.04	0.07	33.6	0.54	36.4	0.36	0.04	0.15	100.2
	R-VC1 (3)	35.9	0.01	0.02	34.8	0.49	28.0	0.31	0.01	0.07	99.6
	min	35.4	0.01	0.02	32.9	0.46	26.0	0.29	0	0.06	99.5
	max	36.2	0.02	0.03	37.1	0.53	29.6	0.36	0.01	0.08	99.8
Microcryst rim	R-VC2/3 (1)	38.2	0.005	0.11	21.9	0.29	36.0	0.33	0.03	0.15	97.0
	R-HL2 (8)	34.2	0.02	0.18	39.1	0.56	24.8	0.32	0.007	0.07	99.2
	min	31.9	0.01	0.02	37.2	0.40	21.1	0.29	0	0.05	97.4
	max	35.6	0.03	0.83	40.6	0.66	26.8	0.36	0.02	0.09	100.3
	R-VC1 (2)	34.2	0.05	0.01	44.8	0.63	20.1	0.29	0.003	0.07	100.1
	min	33.7	0.04	0.01	42.9	0.62	18.8	0.29	0	0.06	100.0
	max	34.6	0.06	0.01	46.7	0.63	21.4	0.30	0.006	0.07	100.2
	R-VC2/3 (1)	35.7	0.05	0.12	39.8	0.59	21.3	0.31	0	0.03	97.8

Supplementary Table 4.4. Detailed composition of the different iron oxides found in the Rauðimelur HL and segregations.

		SiO_2	TiO_2	Al_2O_3	FeOt	MnO	MgO	Cr_2O_3	NiO	V_2O_3	Total
Ilmenite	R-HL2 (7)	0.11	50.1	0.23	46.3	0.45	1.46	0.02	0.01	0.31	99.0
	min	0.07	48.1	0.13	45.3	0.40	0.87	0	0	0.22	98.5
	max	0.18	51.1	0.34	48.3	0.49	1.95	0.05	0.03	0.42	99.4
	R-VC1 (2)	0.25	48.7	0.08	47.0	0.48	0.58	0.008	0	0.39	97.5
	min	0.08	48.6	0.08	47.0	0.47	0.49	0.002	0	0.38	97.3
	max	0.41	48.7	0.08	47.0	0.49	0.67	0.01	0	0.41	97.7
	R-VC2/3 (3)	0.11	46.6	0.38	49.3	0.49	1.10	0.01	0.01	0.40	98.4
	min	0.08	44.1	0.26	46.2	0.47	0.99	0	0.004	0.35	97.8
	max	0.16	50.7	0.53	51.5	0.53	1.20	0.01	0.02	0.46	99.1
Titanomagnetite	R-HL2 (10)	0.14	23.5	1.86	69.4	0.42	1.05	0.03	0.04	0.79	97.2
	min	0.10	21.4	1.59	68.2	0.37	0.75	0.001	0.007	0.67	96.2
	max	0.20	24.7	2.19	70.4	0.49	1.33	0.07	0.06	0.94	97.9
	R-VC1 (9)	0.12	24.4	1.58	68.6	0.47	0.82	0.02	0.03	0.76	96.8
	min	0.08	21.5	1.29	65.7	0.43	0.43	0	0	0.29	95.2
	max	0.27	26.4	2.14	72.0	0.57	1.20	0.05	0.04	1.2	98.0
	R-VC2/3 (11)	0.18	22.7	1.65	69.6	0.44	0.50	0.03	0.02	0.61	95.8
	min	0.11	21.3	0.79	66.1	0.40	0.18	0	0	0.12	93.3
	max	0.35	25.2	2.41	72.9	0.67	0.80	0.06	0.05	1.1	97.8
	R-MV1 (9)	0.19	22.5	1.80	70.4	0.38	0.55	0.07			96.0
	min	0.12	17.5	1.29	65.5	0.06	0.49	0			93.1
	max	0.29	24.9	2.50	75.3	0.62	0.62	0.12			97.7
Titanomagnetite patches	R-VC1 (8)	0.33	19.3	1.34	71.8	0.54	0.32	0.01	0.02	0.14	93.8
	min	0.20	17.6	1.25	70.5	0.46	0.26	0	0	0.12	93.1
	max	0.74	20.9	1.46	73.3	0.62	0.44	0.01	0.02	0.16	94.5
	R-VC2/3 (11)	0.36	19.4	1.01	73.0	0.51	0.17	0.01	0.01	0.09	94.6
	min	0.22	17.4	0.90	69.3	0.50	0.10	0	0	0.06	92.3
	max	1.08	21.3	1.13	75.2	0.68	0.22	0.04	0.03	0.13	95.4
Embayment	R-VC1 (1)	0.15	25.4	1.44	66.9	0.40	0.94	0.02	0.02	0.89	96.1

Supplementary Table 4.5. Detailed composition of the micrographic texture found in the Rauðimelur HL and segregations.

	SiO_2	TiO_2	Al_2O_3	FeOt	MnO	MgO	CaO	Na_2O	K_2O	P_2O_5	SO_3	Cl	Total
R-HL2 (12)	77.7	0.37	12.2	1.05	0.01	0.02	1.42	4.90	1.83	0.14	0.01	0.10	99.7
min	73.9	0.16	11.4	0.47	0	0	0.71	3.39	0.55	0.00	0.00	0.01	98.7
max	80.1	0.68	13.0	2.07	0.04	0.07	2.10	5.45	6.71	0.54	0.02	0.64	100.4
R-VC1 (12)	78.8	0.43	12.4	1.83	0.03	0.04	1.99	5.15	0.76	0.10			101.5
min	76.3	0.16	9.3	0.66	0.003	0	0.94	3.74	0.40	0.003			100.7
max	81.7	0.88	14.1	4.22	0.13	0.27	2.62	6.75	1.83	0.45			102.0
R-VC2/3 (28)	77.7	0.26	12.5	0.85	0.02	0.01	1.76	4.99	1.38	0.12	0.01	0.03	99.6
min	75.0	0.13	10.0	0.48	0	0	0.85	3.75	0.36	0.00	0.00	0.01	98.0
max	83.3	0.40	13.6	1.36	0.04	0.03	3.97	5.80	4.89	1.31	0.04	0.07	101.2
R-MV1 (11)	79.1	0.15	12.0	1.17	0.02	0.04	2.45	4.38	0.83				100.2
min	70.7	0	4.9	0.68	0	0	1.67	1.35	0.32				98.7
max	85.8	0.35	15.9	3.12	0.13	0.18	5.11	5.49	1.31				101.4

4.8.5 Average mineral trace element composition

Supplementary Table 4.6. Trace element concentration range and average in the micrographic patches, plagioclase, clinopyroxene, olivine and iron oxide.

	Micrographic patches				Plagioclase				
Element	**VC1**	**MV1**	**SD (2σ)**	**DL**	**VC1**	**MV1**	**Macrocryst**	**SD (2σ)**	**DL**
Li	1.7 (0.2 - 4.3)	0.2 (0 - 0.5)	0.09	0.11	3.9 (3.1 -4.4)	1.6 (0.3 - 3.8)	3.4	0.19	0.20
Sc	3.5 (1.8 - 6.3)	3.9 (2.5 - 5.3)	0.12	0.03	0.45 (0.44 - 0.47)	0.52 (0.49 - 0.57)	0.35	0.03	0.05
V	1.4 (0.3 - 3.3)	2.6 (0.6 - 6.4)	0.05	0.02	6.1 (5.6 - 7)	2.7 (1.4 - 4.4)	3.7	0.20	0.04
Cr	2.0 (1.0 - 3.4)	1 (1 - 1)	0.21	0.5	3.7 (2.3 - 4.7)	3.1 (2.4 - 3.5)	4.7	0.45	1.0
Ni	2.3 (0.7 - 5.0)	1.4 (0.7 - 2.2)	0.10	0.15	0.5 (0.4 - 0.9)	0.5 (0.3 - 0.6)	0.5	0.12	0.3
Cu	306 (105 - 601)	142 (32 - 368)	13	0.06	1.8 (0.6 - 4.0)	1.0 (0.3 - 2.3)	1.1	0.10	0.11
Zn	35 (16 - 57)	79 (47 - 132)	1.5	0.19	10.9 (9.9 - 11.4)	17.5 (13.4 - 23.6)	4.4	0.49	0.35
As	1.4 (0.8 - 2.6)	0.6 (0.4 - 0.9)	0.08	0.04	0.13 (0.09 -0.16)	0.09 (0.05 - 0.12)	0.09	0.04	0.08
Se	1.6 (1.3 - 1.9)	1.4 (0.8 - 2.1)	0.10	0.17	b.d.l	b.d.l	b.d.l	0.14	0.33
Rb	19 (1 - 54)	4.6 (0.6 - 25)	0.64	0.01	0.18 (0.13 - 0.22)	0.42 (0.27 - 0.53)	b.d.l	0.01	0.03
Sr	132 (95 - 151)	115 (69 -185)	4.2	0.01	339 (302 - 361)	464 (350 - 558)	264	10.8	0.02
Y	96 (87 - 113)	68 (48 - 87)	3.1	0.002	0.18 (0.17 - 0.18)	0.24 (0.18 - 0.34)	0.15	0.007	0.004
Zr	662 (270 - 1222)	266 (139 -462)	21	0.03	0.10 (0 - 0.14)	0.23 (0 - 0.47)	b.d.l	0.02	0.05
Cd	0.08 (0 - 0.011)	0.10 (0.06 - 0.13)	0.01	0.04	0.08 (0.07 - 0.08)	b.d.l	0.07	0.03	0.06
Sn	3.9 (0.8 - 9.7)	1.4 (0.5 - 3.8)	0.13	0.01	0.05 (0.04 -0.05)	0.05 (0.03 - 0.07)	b.d.l	0.01	0.02
Ba	589 (113 - 1199)	128 (98 - 218)	19	0.01	26 (20 -30)	89 (52 -147)	8.0	0.87	0.03
Ce	83 (74 - 90)	58 (39 - 83)	2.7	0.002	0.81 (0.68 - 0.87)	1.6 (1 - 2.2)	0.63	0.03	0.003
Pb	3.5 (0.8 - 7.7)	2.0 (0.7 - 3.9)	0.12	0.003	0.13 (0.1 - 0.18)	0.45 (0.20 - 0.68)	0.04	0.008	0.006
Bi	0.023 (0.007 - 0.050)	0.016 (0.004 - 0.033)	0.002	0.003	0.01 (0.009 - 0.015)	b.d.l	0.01	0.003	0.006
Th	3.0 (1.9 - 3.9)	1.8 (1.1 - 2.9)	0.11	0.0003	b.d.l	0.002 (0.001 - 0.004)	b.d.l	0.0002	0.0005
Nb of analyses	3	10	-	-	3	5	1	-	-

Supplementary Table 4.6. continued

	Clinopyroxene				Olivine			Oxide		
Element (ppm)	**VC1**	**MV1**	**SD (2σ)**	**DL**	**VC1**	**SD (2σ)**	**DL**	**VC1**	**SD (2σ)**	**DL**
Li	7.6 (5.7 - 8.8)	6.4 (2.6 - 14)	0.33	0.09	3.0	0.11	0.11	3.0	0.13	0.10
Sc	117 (98 - 142)	127 (106 - 141)	3.8	0.02	11	0.34	0.03	24	0.73	0.02
V	556 (416 - 701)	659 (219 - 1092)	18	0.02	31	0.95	0.02	4875	150	0.02
Cr	587 (131 - 989)	7.7 (2.6 - 16)	19	0.46	99	3.1	0.53	21	0.77	0.50
Ni	153 (137 - 171)	69 (30 - 105)	5.1	0.13	1086	34	0.15	248	7.8	0.14
Cu	60 (24 -114)	128 (3 - 519)	2.5	0.05	22	0.86	0.06	162	7.0	0.05
Zn	61 (55 -74)	155 (104 - 220)	2.6	0.16	357	13	0.18	741	26	0.17
As	0.09 (0.08 - 0.11)	0.13 (0.10 - 0.18)	0.015	0.04	0.11	0.02	0.06	0.19	0.03	0.03
Se	b.d.l	b.d.l	0.06	0.15	b.d.l	0.06	0.18	0.24	0.12	0.16
Rb	b.d.l	b.d.l	0.004	0.01	b.d.l	0.01	0.01	0.09	0.01	0.01
Sr	10 (9 -12)	12 (8 - 15)	0.33	0.01	b.d.l	0.004	0.01	8.3	0.26	0.01
Y	14 (10 - 17)	31 (26 - 50)	0.44	0.002	0.28	0.009	0.002	3.5	0.11	0.002
Zr	10 (6 -18)	27 (13 - 35)	0.33	0.02	b.d.l	0.010	0.03	250	7.7	0.03
Cd	0.17 (0.14 - 0.21)	0.32 (0.24 - 0.47)	0.01	0.03	0.06	0.02	0.04	0.04	0.03	0.03
Sn	0.09 (0.06 -0.15)	0.20 (0.09 - 0.40)	0.01	0.01	0.04	0.01	0.01	4.0	0.13	0.01
Ba	0.11 (0.03 -0.31)	0.80 (0 - 4.0)	0.01	0.01	b.d.l	0.005	0.01	1.5	0.07	0.01
Ce	1.9 (1.2 - 2.6)	4.5 (2.7 - 6.7)	0.06	0.001	b.d.l	0.001	0.002	3.2	0.10	0.002
Pb	0.017 (0.009 - 0.025)	0.54 (0.04 - 2.3)	0.001	0.002	0.01	0.001	0.003	0.13	0.009	0.002
Bi	0.01 (0.003 - 0.007)	b.d.l	0.001	0.003	b.d.l	0.002	0.005	b.d.l	0.002	0.002
Th	0.003 (0.001 - 0.005)	0.013 (0.003 - 0.04)	0.0003	0.0004	b.d.l	0.0001	0.0003	0.03	0.004	0.0003
Nb of analyses	4	7	-	-	1	-	-	1	-	-

4.8.6 Crystallisation model and results

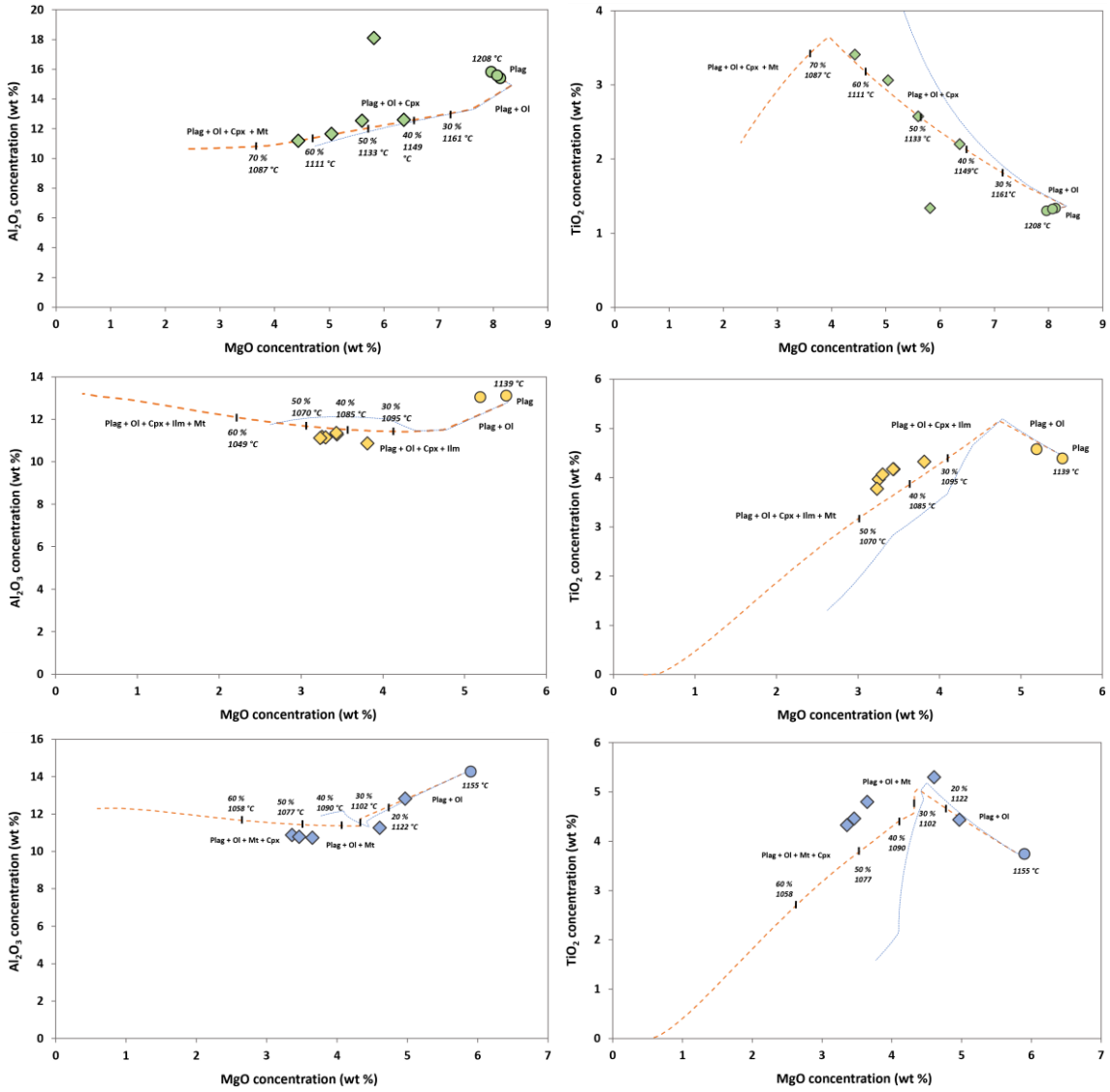

Supplementary Figure 4.7. Rauðimelur, Eldgjá and Hekla host lava crystallisation model results. *The initial composition for the models corresponds to the host lava composition (R-HL2, E-HL2 and H-HL for Rauðimelur, Eldgjá and Hekla respectively. All models were run with a step of 0.5 wt %, at an oxygen fugacity equivalent to QFM buffer and at atmospheric pressure. Model results correspond to pure fractional crystallisation (orange) and pure equilibrium crystallisation (blue). The liquid line of decent was modelled with a step of 0.5 wt % at an oxygen fugacity equivalent to QFM buffer.*

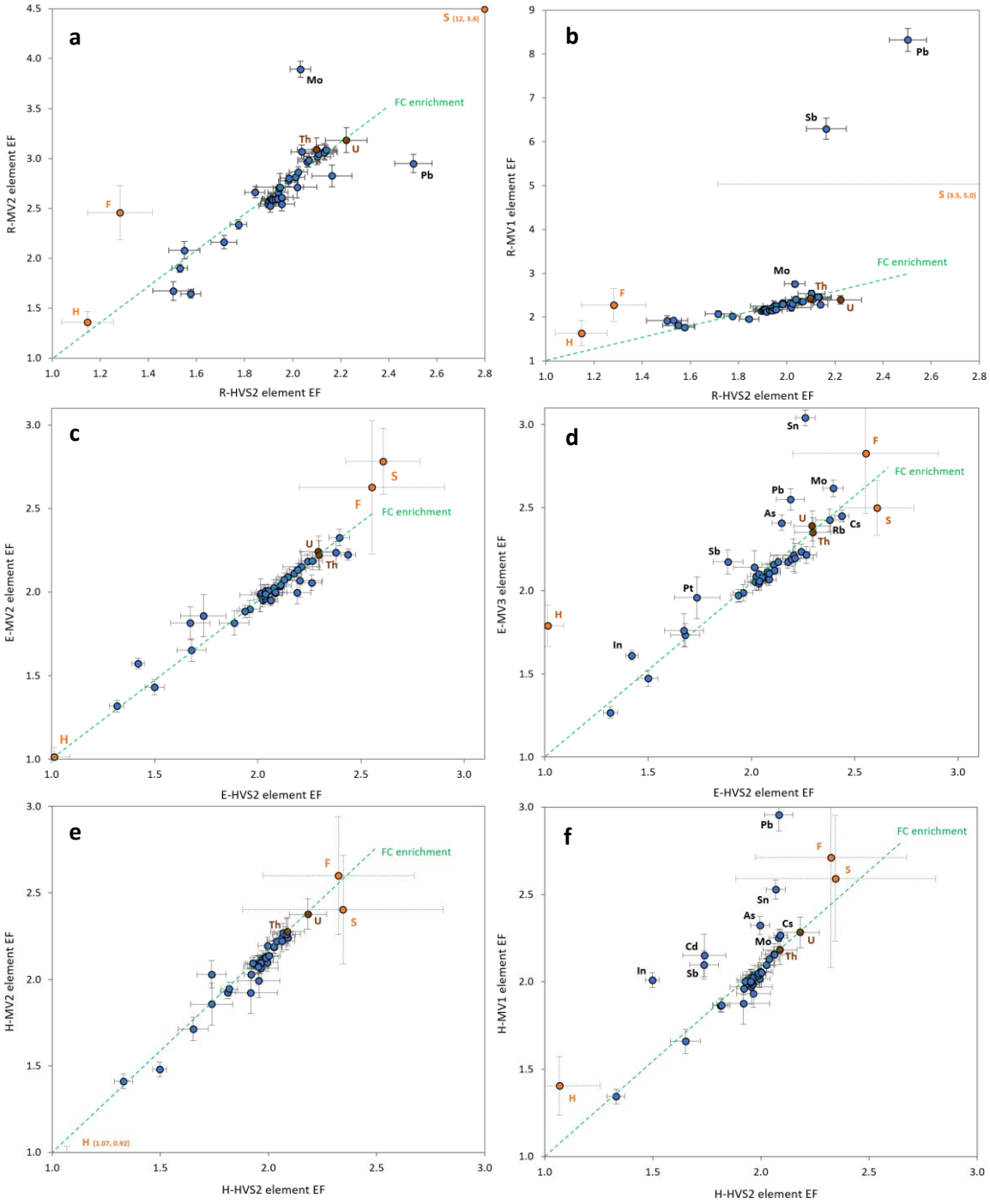

Supplementary Figure 4.8. Major volatile and trace element enrichment factors comparison in segregations from Rauðimelur Eldgjá and Hekla.

5 Chapter 5

Investigating Cl and F concentration in Reykjanes lava using Ion Selective Electrodes

Nicolas Levillayer, Olgeir Sigmarsson

About this chapter

This chapter is in preparation for submission. In this chapter, after assessing the potentials and limitations of Cl and F ion selective electrodes, we characterise the halogen concentration heterogeneity in the newly erupted Reykjanes magma and investigate the origins of Cl and F concentration variations.

Author contribution

Conceptualisation: NL and OS; Methodology: NL; Formal analysis and investigation: NL and OS; Visualisation: NL; Writing original draft preparation: NL and OS; Writing review and editing: NL and OS; Funding acquisition: OS

Keywords

Ion selective electrodes, Halogens in basaltic magmas; Reykjanes eruptions; Magma mixing and degassing

5.1 Abstract

The halogens chlorine and fluorine are elements of interest in volcanological studies due to their intermediate volatility and variable abondance in magmas and volcanic gases. Within the magma, many parameters can affect halogen concentration, such as fractional crystallisation, degassing, magma source heterogeneity and hydrothermal contamination. All of these processes have been suggested to affect the Cl and F concentration of Icelandic volcanics. The halogen concentrations from 2021-2024 Reykjanes eruptive products were investigated using ion selective electrode. The reliability of fluorine and chlorine selective electrodes to resolve small F and Cl concentration change is assessed using rock standards of known halogen concentration. Though the methods allow quantification of both halogens, more accurate and precise measurements are obtained for F than Cl. The analyses of Reykjanes products reveal large variation of both Cl and F concentrations. Fractional crystallisation is shown to affect the halogen abundance but cannot explain the whole variability. No halogen loss through lava degassing could be identified from comparison of their tephra and lava concentrations. To fully explain the Cl and F concentration variation, mixing of magma from three sources of distinct composition is required. The lack of correlation between Cl and F concentrations indicates that the magma involved have variable Cl over F ratios.

5.2 Introduction

Halogens are amongst the most abundant volatiles present in the Earth mantle and crust (Wedepohl 1995; Saal et al. 2002; Salters and Stracke 2004; Pyle and Mather 2009) and magma derived thereof (Oppenheimer et al. 2014). Subsequently, halogens are important component of the volcanic gas (Giggenbach 1996; Oppenheimer et al. 2003; Aiuppa et al. 2009), with chlorine and fluorine being released in amounts orders of magnitude larger than bromide and iodine (Pyle and Mather 2009). However, unlike other volatile species (H_2O, CO_2, SO_2, etc.), halogens are known to degas only at very shallow depth (Edmonds et al. 2009). Such limited degassing at depth result in increased proportion of halogens in secondary degassing (Aiuppa et al. 2002; Sigmarsson et al. 2020; Wainman et al. 2024, Chapter 3). Halogen content in the magma and associated gas phase thus may reflect composition of the magma source as well as subaerial degassing. However, the higher solubility of fluorine relative to chlorine in basaltic melt (e.g. Caroll and Webster 1994) is likely to affect their final relative concentrations in the erupted lava and tephra.

The ratio of halogens over an incompatible element such as K in basalt not only allows discussion about magma degassing processes but also petrogenetic processes such as crustal contamination, seawater integration and the magma sources at their origin. Basaltic lavas from Iceland and the surrounding mid Atlantic ridge were investigated to study the role of shallow degassing and mantle plume contribution on magma halogen concentration by Schilling and collaborators. Such investigation revealed lower Cl and Br concentration than expected in Icelandic products, suggesting that both Cl and Br were significantly degassing at shallow depth and subaerially (Unni and Schilling 1978) whereas no significant F loss could be detected (Rowe and Schilling 1979). However, analyses of Icelandic products from different volcanic systems by Sigvaldason and Óskarsson (1976) indicated that limited

chlorine loss was taking place, and that chlorine concentration variation was better explained by fractional crystallisation. Additionally, source heterogeneity was highlighted by the variable Cl concentration in the melt inclusion from the Barðabunga eruption (Bali et al. 2018). Similarly, no sign of significant fluorine loss through degassing could be identified in Icelandic products, the variation of F being associated with variable implication of F-rich minerals (apatite) in the magma as well as fractional crystallisation (Sigvaldason and Óskarsson 1986; Stecher 1998). The effect of pre-, syn- and post-eruptive degassing was investigated by Óskarsson et al. (1984) and Thordarson et al. (1996) at Laki, by comparing halogen concentration in melt inclusion, tephra, glass and lava.

To investigate the variability of halogen concentration in the products of a single eruption, a method resolving small Cl and F concentration difference in the volcanic material is needed. Among the technique used to analyse Cl and F, Ion Selective Electrodes (ISE) offers the advantage of simplicity, limited costs and relative quickness. The use of ISE for fluorine concentration measurement in rock powders has been developed in the 1970's, giving results in line with other techniques for international standards (Ingram 1970; Bodkin 1977; Troll et al. 1977; Stecher 1983). Though other techniques are now available, determination of fluorine concentration in rocks by ISE remains regularly used (Langenauer et al. 1992; Stecher 1998; Mazziotti-Tagliani et al. 2012; De Rita et al. 2012; Delmelle et al. 2021; Regenspurg et al. 2022). Determination of chlorine by ISE is possible but less common because of the lower sensitivity of the chlorine selective electrode and the existence of more precise techniques (Potts 1987). Nevertheless, several studies conducted Cl measurements by this technique, obtaining variable success (Haynes and Clark 1972; Olade 1976; Aruscavage and Campbell 1983; Elsheimer 1987; Zreda et al. 1991).

The objective of this study is double. First, we try to develop an extraction and measurement procedure using ISE that allows F and Cl quantification from the same leachate and assess its potential and limitations. Since F concentration measurement using ISE is much more established that Cl measurement, the objective is to assess how well Cl can be measured in parallel to F, using the same leachate. Second, we apply the developed method to investigate the halogen concentrations in the newly erupted (2021-2024) Reykjanes volcanics. To do that we conducted halogen extraction from rock powders through fusion and leaching in deionised water. Such process was first performed on international and Icelandic rock standards to adjust the method and estimate its reliability. Following this, the technique was applied on multiple lava and tephra from the recent Fagradalsfjall and Svartsengi eruptions. The measured F and Cl concentrations are then compared to incompatible minor element concentrations and isotope ratios to investigate the parameters affecting the halogen concentrations, especially compositionally heterogeneous magma mixing, potential interaction with the geothermal system beneath Svartsengi and the halogen loss through degassing.

5.3 Geological setting and sampling campaign

The material examined in this study is volcanic products from the recent volcanic activity on the Reykjanes Peninsula, SW Iceland. The petrology of the region has been documented, with lava ranging from picrite to tholeiite in composition, Holocene products being predominantly tholeiites (Jakobsson et al. 1978). However, there are compositional variations between the systems, with Svartsengi emitting more evolved basalts (MgO < 7

%) than the other systems (MgO > 7 %; Peate et al. 2009). Additionally, the observed variable K_2O/TiO_2 ratios (Caracciolo et al. 2023) in products of every single volcanic system on Reykjanes reflects the multiplicity of magma sources feeding the eruptions.

After 800 years of quiescence, the Reykjanes peninsula entered in a new cycle of activity in 2020 marked by a series of seismic swarms and ground inflations which lead to the first eruption in March 2021. From 2021 to 2023, the volcanic activity took place in the Fagradalsfjall mountain complex, which had not witnessed an eruption for over 5000 years (Sæmundsson et al. 2020). The first eruption occurred in the Geldingadalir valley and lasted about six months (Pedersen et al. 2022; Barsotti et al. 2023). A year later, another dyke broke into the surface, triggering an 18-days long eruption in the Meradalir valley. The third and last eruption at Fagradalsfjall occurred the following summer, lasting a bit less than a month. The activity then shifted west, towards the Svartsengi volcanic system where a series of eight (as of May 2025) eruptions started in December 2023 at the Sundhnúksgígar crater row. These eruptions were of variable duration, ranging from less than a day (08/02/24-09/02/24; 01/04/25) to almost two months (16/03/24-08/05/24; Júlíusdóttir et al. 2024). With the exception of the 2021 event, all eruptions started with a phase of intense activity which then exponentially decreased until the end of the eruption.

During and soon after the eruptions at Fagradalsfjall and Sundhnúksgígar volcanic system tephra and lava were extensively sampled, and their petrology and geochemistry investigated. Halldórsson et al. (2022) and Marshall et al. (2024) revealed heterogeneous K_2O/TiO_2 and radiogenic isotopic ratios in the material erupted in 2021, translating multiple magma sources of variable contribution on the scale of days to weeks. Such variation was then observed in the products of most Sundhnúksgígar eruptions, with lava of distinct composition emitted virtually at the same time, suggesting simultaneous contribution of more than one magma source (Matthews et al. 2024).

The samples investigated in this study come from the studies cited above and spans the three Fagradalsfjall eruptions and the first three eruptions at Sundhnúksgígar volcanic system. We selected 34 (17 for each volcanic system) samples of variable composition, both in terms of major elements, K_2O/TiO_2 and Sr-Nd isotopic ratios. Additionally, volcanic products of different nature were analysed, lava (whether quenched or naturally cooled), glassy surface and tephra.

5.4 Analytical method

Ion selective electrodes (ISE) are sensors measuring the potential difference between a reference electrode and an indicator electrode. The indicator electrode has an ion selective membrane that is permissive to only one ion, Cl^- for the chlorine selective electrode and F^- for the fluorine selective electrode. Once the electrode is immerged in a solution, the targeted ions diffuse through the membrane, and the ion concentration gradient generates an electrochemical potential. The potential difference between the two electrodes (E) can then be measured and follows the Nerst equation:

$$E = E_0 + \frac{2.303 * R * T}{n * Fa} * log\ (a) \quad (5.1)$$

Where E_0 is the standard electrode potential (constant at a given temperature), R is the gas constant (8.314 J/K/mol), T the temperature (K), n is the charge of the ion measured, Fa is

the Faraday constant (96480 C/mol) and *a* is ion activity (equal to ion concentration in diluted solutions; Potts 1987). Thus, the Cl and F electrodes are expected to respond linearly to the logarithm of Cl and F concentration. As the measured ions are Cl^- and F^-, *n* will be -1 and electrode potential will be negatively correlated to the chlorine or fluorine concentration. The electrode is connected to a voltmeter from which the measured electrode potential is recorded.

5.4.1 Rock powder leaching

Chorine and fluorine concentrations were measured using a Cole-Parmer® chlorine and fluorine selective electrode respectively. To measure the halogen content of a rock using ISE, the halogens must first be exacted from the rock matrix into a leachate. Here we perform a leachate preparation adapted from and combining the method outlined by Stecher (1998) for F analysis, and the approaches of Haynes and Clark (1972) and Olade (1976) for Cl analysis. Combining these methods allows the use of the same leachate for both Cl and F concentration measurements. The sample preparation was made in a crucible, in which 500 mg of rock powder were mixed with 3 g of 5:1 Na_2CO_3-ZnO mixture as a fluxing agent. One gram of Na_2CO_3-ZnO flux was then added to cover the crucible content. Following this, the platinum crucible was set in a furnace heated gradually (100 °C every 20 minutes) up to 950 °C for 30-40 minutes and then cooled at room temperature.

To leach the cooled mixture, 30 mL of deionised (DI) water were poured into the crucibles. A couple of clean ethanol drops were added to avoid extracting chemicals affecting the leachate colour, which complicate the subsequent titration process. The crucibles were then left in the oven overnight at 80 °C for complete leaching. The day after, the crucibles were cooled down to room temperature and their content was poured through a Whatman® filter into a polyethylene bottle. The residue was rinsed repeatedly with DI water and filtered into the bottle. The solution was consequently slowly acidified to pH 5, using concentrated HNO_3 in order to eliminate CO_2. Finally, DI water was added to dilute the solution to 50 or 30 mL.

5.4.2 Fluorine measurement

The instrumental calibration of the F^- electrode is obtained from measurements of a series of fluorine standard solutions ranging from 0.3 to 10 ppm made by dilution of a *Trace*CERT® 1000 mg/L fluorine in water standard solution. Before measuring the rock powder leachates and the F standards concentrations, a Total Ionic Strength Adjustment Buffer (TISAB) was added 1:1, permitting both to maintain a constant ionic strength and to decomplex fluorine. Two TISAB solutions were prepared and tested, one following Stecher (1998) and the other Nicholson (1983). The first one is made if 57 mL glacial acetic acid, 58 g sodium chloride 12 g trisodium citrate dehydrate dissolved in one litre of DI water. The second buffer contains 24 g of tri-ammonium dehydrate (instead of trisodium) and 4 g of CDTA (trans-l,2-diaminocyclohexane-N,N,N',N'-tetra-acetic acid). Once the TISAB was added, it was necessary to wait for a couple of hours for the relevant reaction to complete and to obtain stable measurements with the F^- electrode.

During measurement sessions, the F^- electrode was immerged in each solution to be analysed, starting with the F standards in increasing concentration order and followed by the leachates, rinsing carefully with DI water the electrode between every measurement to avoid contamination and memory effects. The calibration curve was then constructed based on the

voltage measured for each F standard solution. The leachate voltage is then converted to fluorine concentration using the curve, corresponding to the calibration method F concentration.

As a result of matrix effect and interference of OH^- (of similar radius than F^-), the value obtained by direct leachate analysis underestimates the actual F concentration of the leachates. To correct such effect, the standard addition method described in Troll et al. (1977) and Stecher (1983) was used. After measuring the leachate, a small amount of concentrated F solution (mixed 1:1 with TISAB) was added to each sample, targeting approximately 30 mV difference. The F-doped leachate was left to homogenise (at least one hour was needed) before being reanalysed and the measured potential could be converted to fluorine "standard addition" concentration using the following equation (Troll et al. 1977; Stecher 1998) :

$$C_x = C_s * \frac{V_s}{V_X+V_s} * (10^{\frac{\Delta E}{S}} - \frac{V_S}{V_S+V_S})^{-1} \quad (5.2)$$

where C_x is the concentration of the analysed leachate and V_x its volume, C_s is the concentration of the added standard, V_s is its volume, ΔE is the difference in electrode potential between the solution before and after adding concentrated solution and S is the slope of the calibration curve in mV per ten-fold increase in fluoride concentration. As explained by Stecher (1998), the matrix effect will result in overestimation of the actual F concentrations by the standard addition method to the same extent as the underestimation by the calibration method (Fig. 5.1). Thus, the actual F concentration of the leachate is obtained by averaging the result from the calibration method and that of the standard addition method.

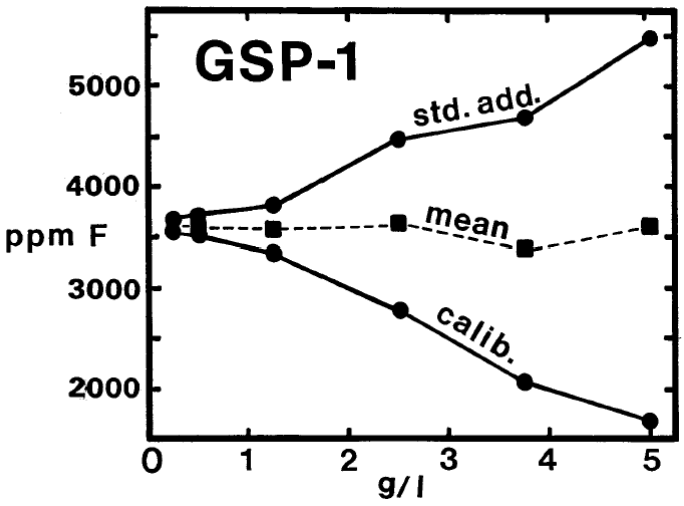

Figure 5.1. Figure taken from Stecher (1998) illustrating the difference in calculated F concentration by the calibration method and the standard addition method. *As the dilution factor decreases, the difference between the calibration and standard addition methods F concentration increases. The average of the two methods is however stable, corresponding to the actual F concentration*

5.4.3 Chlorine measurement

Quantification of the leachate chlorine concentration was also based on the use of a calibration curve, with Cl standards ranging from 0.625 to 20 ppm, obtained from dilution of a *Trace*CERT® 10000 mg/L chlorine in water standard solution. Before measurements,

the Cl standards were acidified to pH similar to the leachate (pH ~ 5), which allows much more stable potential measured by the Cl electrode. The measurement procedure was the same as for fluorine with first immersion of the standards and then the leachates. Unlike fluorine, the electrode response was very sensitive to exact reading conditions (steering speed, electrode placement, volume of solution analysed… etc.) which were kept as constant as possible. The electrode potential of the leachate could however not be converted directly to Cl concentration using the calibration curve as measured potential did not plot always on it (details in the next section).

5.5 Results and discussion

5.5.1 First results and revision of the method

Calibration curves

A stable electrochemical potential was quickly reached (< 2 minutes) when the F- selective electrode was immerged into the prepared F standard solutions (mixed with TISAB). The calibration curve obtained from the standards was logarithmic over the whole range of concentrations (0.3 to 10 ppm). Results using the buffer proposed by Nicholson (1983) and Stecher (1998) gave similar results, but the latter yielded systematically more consistent results and was thus favoured over the former. Negligeable drift (< 0.5 mV) was observed in replicate analyses of the standard solutions over a measurement session. Between sessions, the drift was low but not negligeable (0.31 ppm = 165-171 mV, 10 ppm = 77-82 mV, slope of -24 to -27). Measurements on DI water (+ TISAB) gave electrode potential at least 100 mV above the least concentrated samples (0.3 ppm), typically around 300 mV, indicating very high sensitivity of the F^- electrode.

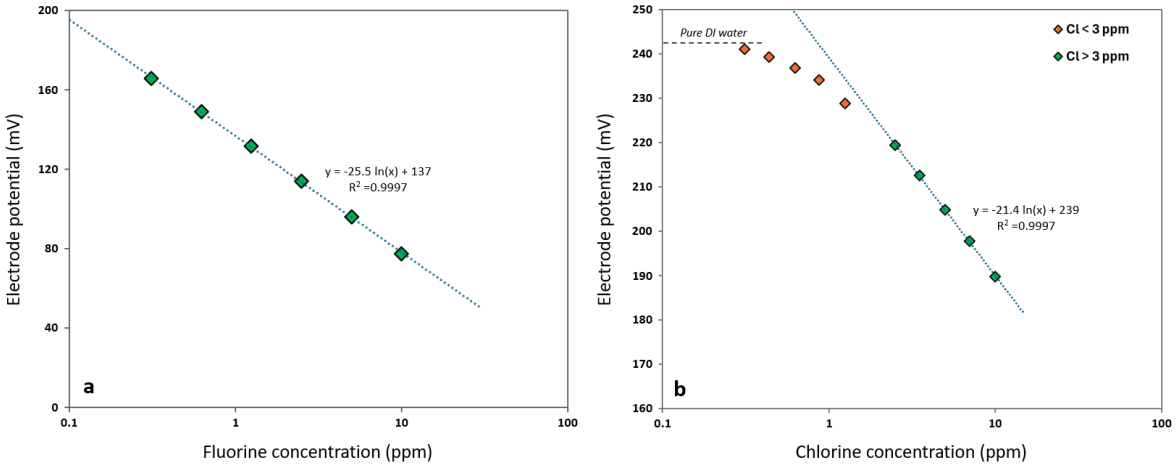

Figure 5.2. Example of F^- and Cl^- selective electrode calibration curves obtained from analyses of standards. *The calibration is linear over the whole range of concentrations for fluorine (a) but not for chlorine (b), which has a linear behaviour only above approximately 3 ppm. Below that concentration threshold, the electrode potential is less and less sensitive to Cl concentration change and DI water has an electrode potential close to the least concentrated solutions (0.6 ppm).*

Once the Cl^- electrode was immerged into the Cl standard solutions, a few minutes delay were needed to stabilize the potential, but significant fluctuations (3 mV) remained and affected the exact reading conditions. Decreasing the pH of the Cl standard solutions to values similar to that of the leachate (pH ~ 5) decreased the fluctuation to 0.5 mV, thus stabilising the reading conditions. The calibration curves obtained from the standards were linear (with Cl concentration on a logarithmic scale) for values above a certain concentration threshold. The exact threshold value appeared to be variable between sessions, ranging from 2 and 5 ppm, similar to what observed by Haynes and Clark (1972). Above the threshold, a fine calibration curve was obtained (r^2 around 0.99; Fig. 5.2). The calibration for chlorine concentration showed limited drift within each analysis session (< 2 mV), but large drift between sessions (1.25 ppm = 215-233 mV, 10 ppm = 180-190 mV, the slope of the calibration generally ranging from -21 to -24). The variable potential for the 1.25 ppm standard solution is both due to instrumental drift and unstable sensitivity (i.e., concentration at which the curve becomes nonlinear).

Since Cl^- electrode response to low Cl concentrations is more complex, its behaviour was investigated in more details by preparing and analysing standard solutions of 0.1, 0.3, 1, 3, 10, 30, 100, 300 and 1000 ppm Cl. The measurement confirmed the two zones of distinct calibration curves, with standards over 3 ppm Cl concentration forming a clear linear curve (on a logarithmic scale) with r^2 above 0.99 (Fig. 5.3). In contrast, the standard solution with less than 3 ppm Cl forms a nonlinear curve, and the electrode potential response decreases with diminishing Cl concentrations. Pure DI water was also analysed and displayed electrode potential ranging from 242 to 245 mV, sometimes indistinguishable from the 0.1 ppm Cl standard solution (236.5 to 242.6 mV).

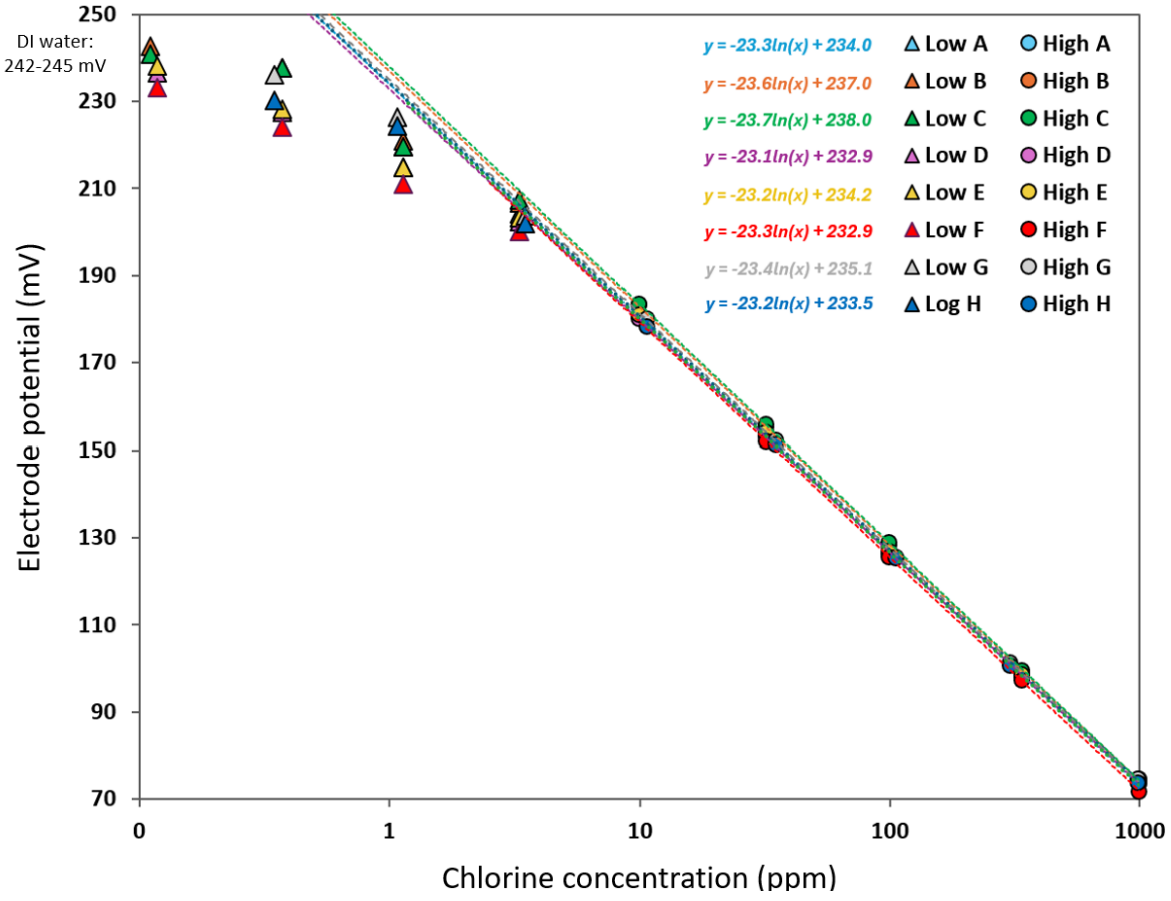

Figure 5.3. Measured potential by the Cl^- electrode on Cl standard solutions of concentrations ranging from 0.3 to 1000 ppm. *Measurements were conducted 8 times, the series A to D corresponding to the same standards measured at a different time, E and F a second set of standards and G and H a third one. The slight variability of Cl concentration originates from preparation inconsistences. The calibration curve obtained using the standards over 10 ppm (circles) remains relatively constant, but more fluctuations are observed in solutions ≤ 3 ppm (triangles).*

The calibration curves thus strongly suggest that the F^- electrode sensitivity is orders of magnitude higher than that of the Cl^-. Concentrations below 3 ppm Cl in a solution are thus less well quantified, with precision degenerating as the concentration decreases. Given the dilution factor used for sample preparation and leaching, 3 ppm in the analysed leachate corresponds to 100-160 ppm Cl in the rock powder, which is above the concentration of many samples from Reykjanes (Sigvaldason and Óskarsson 1976).

Leaching method testing and revision

To assess and adapt the leaching method, several parameters were examined and/or modified: the flux used, heating and cooling rate of the sample-flux mixture, leaching conditions (time, temperature and amount of DI water) and the acidification of the solutions.

Following first results that suggested Cl contamination on order of ppm level, the Na_2CO_3 with < 200 ppm Cl flux used initially was replaced with ultra-pure sodium carbonate decahydrate (Na_2CO_3* 10 H_2O) with < 1 ppm Cl. The sodium carbonate decahydrate was fully dried (by setting it in an over at 80 °C for a couple of days) before use. The potential effect of exact heating condition was minimised by employing constant rate: 100 °C every 20 minutes from 550 °C to 950 °C, temperature at which the samples were left to fuse for 30 minutes. The effect of cooling rate of the cake after fusion was tested by preparing two crucibles of the same samples, removing quickly one crucible from the furnace after the heating process and letting the other cool down with the oven (over few hours). No significant difference in either Cl or F measurement was observed in the two leachates. Consequently, all samples were removed 15-30 minutes after turning of the furnace.

Leaching conditions, including duration, temperature, and DI water volume, are key parameters. A temperature of 80°C was the minimum for effective leaching. Comparing Cl and F concentrations from overnight and 36-hour leachates showed up to 15% higher values for the latter. Instead of leaching for two nights, breaking the cake with a clean spatula, adding DI water, and leaching for an additional 3-4 hours also resulted in complete leaching. This method was thus used for our leachate preparation, and analyses of the residue from that leachate showed negligible F and Cl concentrations, confirming that the leaching process was effective.

Finally, the effect of exact pH was tested by measuring a leachate and a standard solution repeatedly with progressive addition of diluted acid. Though acidifying the sample initially creates a peak in potential measured by the Cl^- electrode, the values slowly decrease until stabilising at the same potential as before acidification. No change in potential was seen on the F^- electrode, most likely because the pH is buffered by the TISAB. The exact pH of the analysed solution is thus not expected to have significant effect on the electrode potential measurements.

5.5.2 Rock standard analyses using the revised method

A series of Icelandic (B-ALK, B-THO, A-THO, I-ICE) and international rock standards (JB-3, JA-2, JR-1, BIR-1, BCR-1, BHVO) were prepared and their leachates analysed using the revised method. The international rock standards generally have well constrained halogen concentrations, as they were measured using various techniques and the results obtained in literature are compiled in the database GeoREM (Jochum et al. 2005; https://georem.mpch-mainz.gwdg.de; 29/01/2025). Regarding the Icelandic rock standards, chlorine concentrations were measured by Óskarsson et al. (1982) using X-ray fluorescence and fluorine concentrations by Sigvaldason and Óskarsson (1986) using ISE. Based on this literature data, the F concentrations of the selected standards should span over an order of magnitude, from 42 ppm in B-THO and 55 ppm in BIR-1 to 945-1070 ppm in JR-1 and 1185 ppm in I-ICE. With a dilution factor of 60 to 65 (0.5 g of sample in 30 mL of DI water), which results in leachate concentration of 0.5 to 20 ppm F approximately. The rock standards cover a similar range of chlorine concentrations, ranging from 7.7-26 ppm in JA-2 to JR-1 which has a concentration of 817-1042 ppm, corresponding respectively to leachate concentration of < 0.5 ppm to > 15 ppm Cl.

Table 5.1. Fluorine and chlorine concentration (in ppm) of the selected international and Icelandic rock standards. *International standards data from the GeoREM database (Jochum et al. 2005; https://georem.mpch-mainz.gwdg.de; 29/01/2025), Icelandic standards Cl concentration from Óskarsson et al. (1982) and F concentration from Sigvaldason and Óskarsson (1986).*

	JB-3	JA-2	JR-1	BHVO	BCR-1	BIR-1	I-ICE	B-THO	A-THO	B-ALK
F (ppm)	210-261	226	945-1070	413	490	55	1185	42.5	770	752
Cl (ppm)	220-336	7.7-26	817-1042	90-95	59	44	225	90	530	130

Fluorine results

The rock standard leachates mixed with TISAB were first directly measured by the F^- electrode to obtain F concentrations with the calibration method. The measured electrode potential ranged from values similar to that of the 0.625 ppm standard solution to values corresponding to that of the 10 ppm standard solution (typically 150 and 80 mV respectively; Fig. 5.4a). As expected, the highest potential was measured from the leachate of F-poor rock standards (BTHO and BIR-1) and the lowest potential from the rocks with known high F concentration (JR-1, ATHO and I-ICE; Fig. 5.4b; supplementary Table 5.1). There is however significant scatter around the trend (B-ALK with higher potential and A-THO and JR-1 lower potential), most likely associated with distinct matrix effect.

All the leachates were remeasured after being doped in fluorine in order to obtain the standard addition method concentration of the leachate. The difference in measured fluorine concentrations between the calibration and the standard addition methods is large and variable, the latter being 1.5 to 4 times higher than the former. Such large difference is expected given the low dilution of our samples (generally around 1:64 or 1:107), which should result in larger interferences, as observed by Stecher (1983). The influence of dilution was visible for BHVO-1 (Supplementary Table 5.1), which has a standard addition method

concentration 1.9 to 2.1 times higher when 0.5 gram of powders was used (1:64 dilution) but 2.5 to 2.6 when 1 g of powder was used (1:32 dilution). This effect is not visible in the case of JR-1, with ratios ranging from 1.5 to 2, whether 0.15, 0.5 or 1 g was used. The concentration ratio between the two methods was stable when a leachate was analysed several times. When several leachates were prepared of the same standard, similar ratios are generally observed, except for I-ICE for which one duplicate (analysed 3 times) has a ratio of 2.4 to 2.7 and the other (analysed twice) 3.5 and 3.7. The high variability between samples most likely reflects the different matrix of the standards, creating variable degrees of interference.

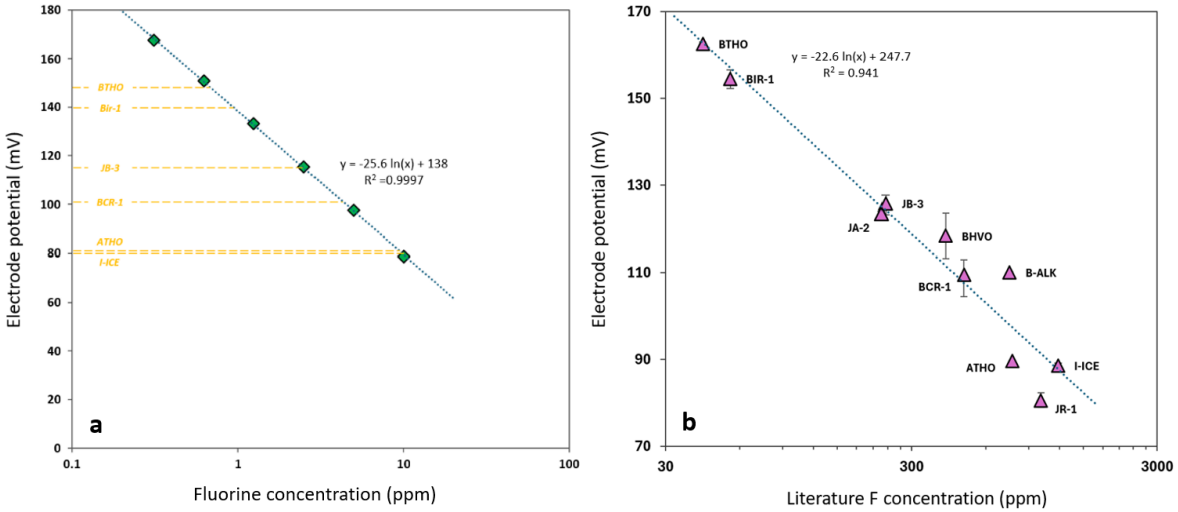

Figure 5.4. Electrode potential measured in the fluorine standard solutions and rock standard leachates. *(a) is an example of an analysis session including a series of F standard solutions building a calibration curve and several leachates from rock standards. The calibration curve remains linear over the whole F range of concentrations and the rock standard leachates display similar concentrations to the F standard solutions. (b) is the average electrode potential measured in the rock standard leachate (with a dilution factor of 64) as a function of their literature fluorine concentration.*

Repeated measurements on the same leachate gives similar results, with a relative standard deviation (RSD) around 10 % (ranging from 0 to 16 %; 2σ). The repeatability between different leachates of the same standard sample was more variable and ranged from 0 to 26 %. The range of measured concentrations for each rock standard are BIR-1: 42-55 ppm, JA-2: 173-180, JB-3: 186-201 ppm, BHVO-1: 194-236 ppm, BCR-1: 333-366 ppm, B-ALK: 371-373 ppm, A-THO: 755-762 ppm, JR-1: 846-942 ppm and I-ICE: 822-1040 ppm.

When compared to the data from the literature (Table 1), our results for the international standards are similar for JB-3, JA-2, JR-2 and BIR-1, whereas results are significantly lower for BCR-1 (28 %) and BHVO (47 %). With respect to measurements conducted by Sigvaldason and Óskarsson (1986), our F concentrations for Icelandic standards are very similar for A-THO, B-THO and to a lesser extent I-ICE, but distinct for B-ALK (50 % lower).

Chlorine results

The rock standard leachates analysis by the Cl^- electrode revealed a wide range of measured potential (over 50 mV). As expected, the least concentrated rock standards (JA-1, BCR-1 and BIR-1) display the highest potentials whereas those most concentrated showed the

lowest. The measured potential ranged from 265 mV to 186 mV (Supplementary Table 5.2) with decreasing average potential: JA-2 (251-265 mV), BIR-1 (241-244), BHVO-1 (236-247 mV), BCR-1 (223-240), JB-3 (209-223), I-ICE (215-216), B-ALK (212-217), A-THO (201-202) and JR-1 (186-191 mV). The analysis can thus differentiate concentrations of different samples and a correlation between the literature Cl concentrations from literature and the measured electrode potential (r^2 = 0.930, Fig. 5.5a) indicates semi-quantitative Cl concentration assessment.

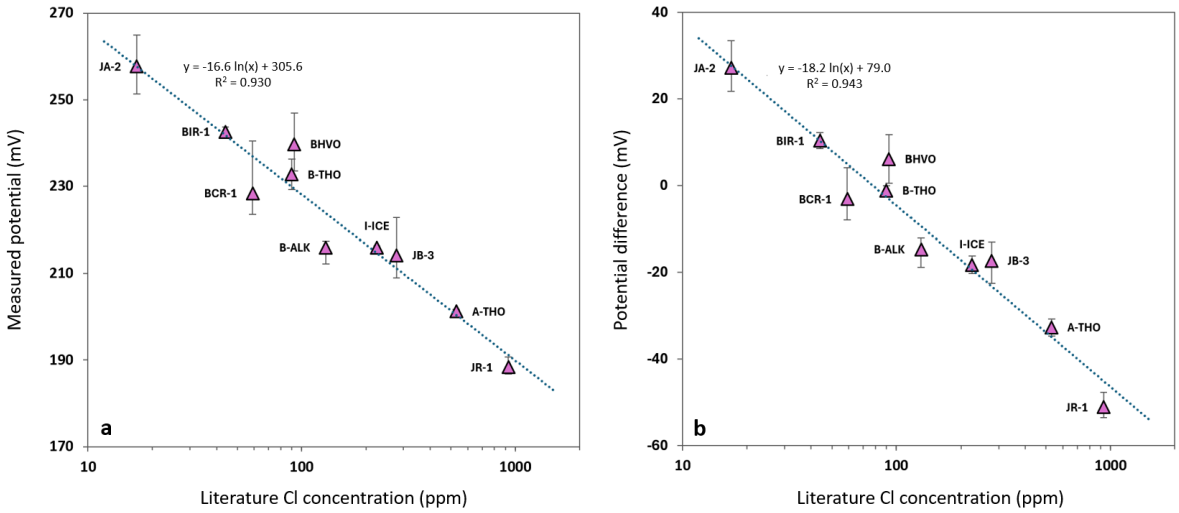

Figure 5.5. Relationship between Cl concentration in the rock standards and measured potential in their leachates. *(a) Measured potential by the Cl^- electrode on the rock standard leachate as a function of their literature Cl concentration. There is a correlation between the potential and the expected concentration (R^2 = 0.93) but significant scatter around the trend, especially for BCR-1, BHVO-1 and B-ALK. (b) Potential difference between the measured voltage from the leachate and the intercept from the calibration curve as a function of the literature Cl concentration. Marginally better correlation is observed (R^2 = 0.943) but BCR-1, BHVO-1 and B-ALK remain slightly off the trend.*

Given the temporally variable response of the Cl^- electrode for the same Cl concentration, the measured electrode potential must be corrected to account for such variation. This can be done by subtracting the measured potential to the origin found for the calibration curve measured during the same session. The potential difference for each sample is plotted on figure 5.5b. Such correction marginally improves the correlation between the Cl concentration (log scale) and the electrode response (R^2 = 0.943).

The range of measured potentials obtained is however not consistent with the calibration curve built from standard solutions. Indeed, the leachate from low Cl samples display electrode potentials higher than the least concentrated standards and often higher than pure DI water (Fig. 5.6). For example, the two leachates from JA-2 had potential 10 to 20 mV higher than DI water. The calibration curve can thus not be used to convert the electrode potential to Cl concentration. Electrode potential higher than pure DI water suggests significant matrix effect, shifting to higher potential. Such matrix effect could either result from the rock powder, or the flux (Na_2CO_3-ZnO) used. Haynes and Clark (1972) identified interference from other volatiles, mainly sulphur (in the form of sulphide), iodine and bromine. In order to assess which major elements could interfere with the Cl^- electrode measurement, several leachates (of BIR-1, JA-1 and BHVO) were analysed for major

element concentrations by ICP-MS. The leachate had significant concentrations of Si, Al, Ti, K, Ca in addition to Na and Zn (being part of the flux), but negligible Mg and Fe.

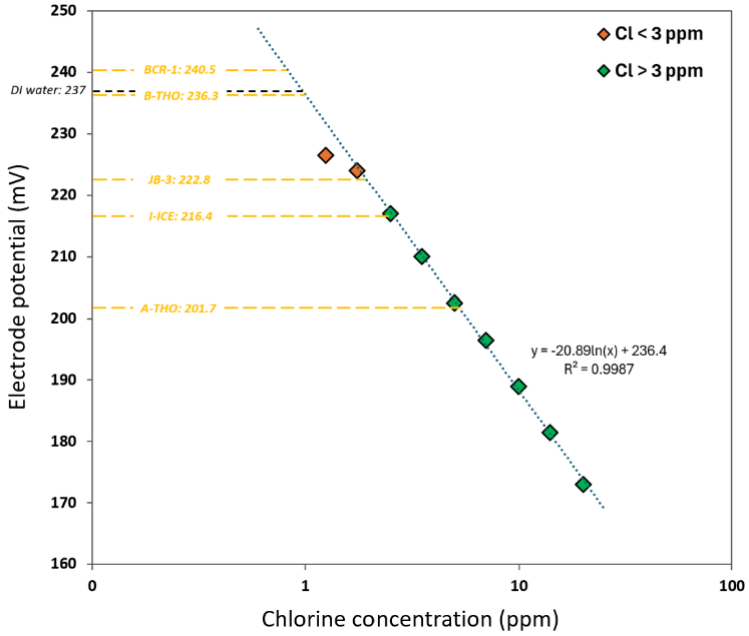

Figure 5.6. Example of an analysis session including a series of Cl standard drawing a calibration curve and several leachates from rock standards. *As previously shown on figure 5.2, the calibration curve becomes non-linear below 3 ppm Cl. The leachates prepared from rock standards spans a wide range of electrode potential, from equivalent to the 7 ppm standard to higher potential than pure DI water.*

Tests were thus conducted to investigate the matrix effect by adding to Cl standard solutions (typically 10 ppm) different quantity of volatile elements (S, F and Br) and major elements present in the leachate (Si, Al, Ti, K, Ca and Na). The addition of sulphur and fluorine had no visible effect on the electrode potential of the Cl solution. In contrast, addition of bromine resulted in electrode response similar to addition of Cl, suggesting similar interaction with the membrane, which is in line with observations by Elsheimer (1987). However, since bromine concentration should be lower, by orders of magnitude, than that of chlorine, its effect is expected to be minimal. Apart from Na, none of the major elements were found to influence electrode potential measured (variation < 1 eV). Interestingly, adding any element to the Cl standard solution stabilised the electrode measurement.

Important effect of Na addition (which has concentrations in the leachate orders of magnitude higher than other elements) was observed. Test were made using standards of different chlorine (0 to 25 ppm) and sodium concentrations (up to 0.9 %) and are plotted in figure 5.7. The measurements reveal clear shift to higher electrode potential with increasing Na content. For concentrations lower than 5 ppm Cl, the effect of Na addition decreases. Using the 10 and 25 ppm standard solutions, a similar slope can be observed at different Na concentration (-22 ± 1), but with an increase of about 10 mV. Such results indicate an electrode response to change in Cl concentration (above 10 ppm) independent from Na content, at concentration above 10 ppm Cl.

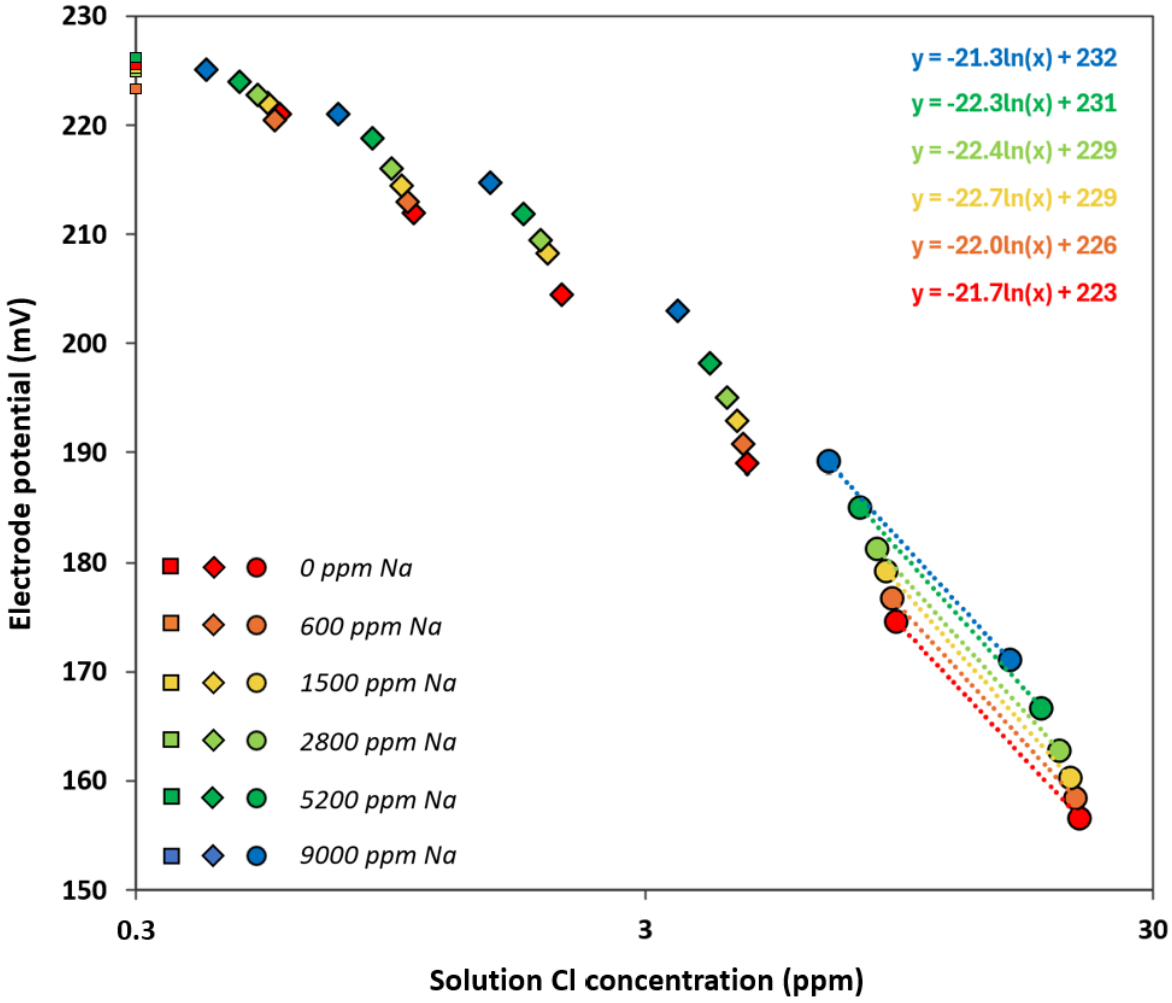

Figure 5.7. A series of calibration curves based on repeated measurement of the same Cl standard solutions with progressive addition of sodium dissolved in DI water. *A logarithmic scale is used as electrode potential should responds linearly with the logarithm of Cl concentration. Circles correspond to Cl concentrations of 10 and 25 ppm, used to draw the regression lines, diamonds correspond to Cl concentrations of 0.5 to 5 ppm and squares to Cl-free DI water. The Cl concentration decrease with increasing Na content results from the slight dilution associated with Na solution addition. The addition of Na clearly affects the electrode increasing the measured potential (beyond the effect of dilution). Such shift to higher potential is less consequent at lower Cl concentrations. Regression lines display constant slopes meaning that the electrode response to change Cl concentration (above 10 ppm) is independent from Na content.*

The shift induced by adding Na in the solution is however not constant. As the Cl concentration decreases, the effect of Na addition lessens significantly. For example, adding 0.9 % of Na increases the electrode potential of 15 mV for the 25-ppm standard solution but only 4 mV for the 0.5 ppm standard solution (Fig. 5.7).

Thus, given the incertitude in determination of the Cl concentration in an unknown leachate with the use of the calibration curve of the Cl standard solutions, a pragmatic approach is to apply the empiric calibration based on the rock standard (Fig. 5.4). In order to account for the change in electrode response with time, the use of the potential difference curve is favoured ($R^2 = 0.94$; Fig. 5.5b). Interestingly, the fact that the rock standard calibration curve

remains linear for the least concentrated rock standards (mainly JA-2) suggest increased electrode sensitivity in the leachate with respect to the Cl standard solution.

The correlation between the electrode potential and the Cl concentration of the rock standards (Fig. 5.5b) is however not perfect, inducing measurement uncertainties. The uncertainty associated with that calibration curve is estimated to be around 4 mV (the average difference between the measured potential of the standards and their expected concentration). The difference ranges from - 9 mV for BCR-1 to + 9 mV for BHVO-1. Nevertheless, significant Cl concentration difference should remain resolvable in a set of samples having similar matrix such as the Reykjanes tholeiites.

5.5.3 Halogens in the Reykjanes volcanic products

Fluorine and Chlorine concentration range

The Fagradalsfjall and Sundhnúksgígar lava and tephra (sample details in supplementary Table 5.5) leachates have fluorine selective electrode potential spanning 108 to 137 mV, which is in the range of what was measured for both standard solutions and rock standards. The concentration ratios between the standard addition and the calibration methods range from 1.5 to 2 for the leachates of 50 mL and 2 to 3 for those of 30 mL (Supplementary Table 5.3), which is similar to the rock standards. Averaging the concentrations calculated using both methods gives lava F concentrations ranging from 180 to 390 ppm (Table 5.2). The concentration range found here is in good agreement with the previous studies conducted on Icelandic rocks, plotting on the lower end of Icelandic products (Sigvaldason and Óskarsson 1986), but on the upper end for studied tholeiites (Stecher 1998).

The Cl^- electrode measurements of the Reykjanes product leachates revealed potentials ranging from 210 to 265 mV (Supplementary Table 5.4). The measured potential can be converted using the correlation between the potential difference of rock standards having known Cl concentrations (Fig. 5.5b):

$$[Rock\ Cl] = exp^{(\Delta V - y(calib)/S(calib))} \quad (5.3)$$

Where ΔV is the potential difference (mV) between the measured potential and the intercept of the Cl standard calibration curve, $y(calib)$ is the intercept of the rock standard leachates calibration curve (79 mV) and $S(calib)$ is the slope of the same curve (-18.17 mV/log(ppm) Cl).

Using equation 5.3, the measured potentials of the Reykjanes lava leachates give concentrations ranging from 50 to 200 ppm Cl (Table 2, supplementary Table 5.4). Such range of Cl concentration is in line with what was measured on Reykjanes by Sigvaldason and Óskarsson (1986) and the groundmass glass analyses from Caracciolo et al. (2024)

To better understand the behaviour of chlorine and fluorine in the Reykjanes products, and since they are known to be incompatible elements in the early stage of basaltic lava crystallisation (Webster et al. 2018), comparison with other incompatible elements is of interest. At least three mechanisms could influence the fluorine and chlorine concentration: fractional crystallisation (FC), loss through degassing and magma mixing, in addition to magma source heterogeneity.

Table 5.2. Halogen and incompatible oxide concentrations together with Sr and Nd isotope ratios in 2021-2024 Reykjanes products.

Sample name	Short name	Sample type	F(ppm)	Cl (ppm)	K_2O (%)	TiO_2 (%)	P_2O_5 (%)	$^{87}Sr/^{86}Sr$	$^{143}Nd/^{144}Nd$
G20210321-2	G1	Quenched lava	184 (± 4.6)	-	0.161	0.987	0.102	0.70311	0.51301
G20210330-2	G2	Glassy crust	186 (± 28)	104 (± 24)	0.194	1.01	0.105	0.70312	0.51299
G20210404-1	G3	Tephra	297 (± 44)	69.2 (± 1.1)	0.213	1.03	0.109	0.70316	0.51297
G20210405-1	G4	Quenched lava	203 (± 30)	96.8 (± 19)	0.193	1.01	0.104	0.70314	0.51298
G20210412-1	G5	Quenched lava	-	117 (± 13)	0.259	1.08	0.130	0.70318	0.51295
G20210424-6	G6	Quenched lava	248 (± 37)	100 (± 4,7)	0.244	1.05	0.116	0.70317	0.51296
G20210511-2	G7	Cooled lava	294 (± 44)	92.8 (± 2.5)	0.301	1.14	0.132	0.70321	0.51295
G20210525-1	G8	Quenched lava	-	71.1 (± 6.9)	0.250	1.09	0.130	0.70319	0.51296
G20210616-1	G9	Quenched lava	-	75.2 (± 4.1)	0.247	1.05	0.129	0.70318	0.51297
G20210707-1	G10	Glassy crust	188 (± 28)	84.4 (± 6.6)	0.274	1.14	0.128	0.70320	0.51296
G20210729-1	G11	Glassy crust	-	94.3 (± 1.5)	0.288	1.13	0.126	0.70318	0.51297
G20210808-1	G12	Glassy crust	228 (± 34)	102 (± 4.5)	0.221	0.989	0.109	0.70317	0.51298
G20210817-3	G13	Glassy crust	-	199 (± 0.9)	0.272	1.16	0.134	0.70320	0.51297
G20210924-1	G14	Glassy crust	284 (± 43)	112 (± 1.3)	0.28	1.10	0.12	0.70319	0.51297
20220812-2	M1	Quenched lava	250 (± 16)	119 (± 16)	0.317	1.17	0.137	0.70322	0.51295
20230710-2	L1	Cooled lava	257 (± 39)	59.4 (± 11)	0.289	1.11	0.132	0.70319	0.51295
20230719-3	L2	Tephra	225 (± 7.5)	65.5 (± 10)	0.277	1.13	0.127	0.70320	0.51295
20231219-2	S1	Cooled lava	326 (± 30)	154 (± 27)	0.406	1.77	0.208	0.70321	0.51296
20231221-3	S2	Cooled lava	341 (± 10)	155 (± 20)	0.315	2.08	0.235	0.70316	0.51300
20240103-7	S3	Tephra	388 (± 32)	149 (± 16)	0.371	1.88	0.215	0.70319	0.51298
20240105-1	S4	Cooled lava	375 (± 18)	139 (± 3.6)	0.365	1.89	0.213	0.70319	0.51298
20240105-16	S5	Tephra	357 (± 11)	165 (± 17)	0.404	1.79	0.207	-	-
20240110-109	S6	Cooled lava	319 (± 13)	-	0.327	2.06	0.226	-	-
20240110-112	S7	Tephra	355 (± 7.0)	-	0.412	1.77	0.205	-	-
20240110-114	S8	Cooled lava	268 (± 28)	163 (± 11)	0.431	1.74	0.206	-	-
20240110-116	S9	Tephra	266 (± 29)	113 (± 9.6)	0.438	1.75	0.206	-	-
20240117-12	S10	Tephra	232 (± 19)	128 (± 7.8)	0.407	1.81	0.210	0.70321	0.51297
20240117-13	S11	Cooled lava	285 (± 36)	154 (± 16)	0.414	1.81	0.212	-	-
20240117-6	S12	Cooled lava	308 (± 46)	-	0.444	1.81	0.212	0.70322	0.51296
20240117-8	S13	Cooled lava	309 (± 46)	-	0.307	2.13	0.231	0.70316	0.51301
20240209-208	S14	Tephra	341 (± 5.0)	110 (± 1.2)	0.414	1.85	0.214	-	-
20240209-210	S15	Tephra	292 (± 4.6)	113 (± 9.0)	0.414	1.84	0.216	0.70322	0.51297
20240208-2	S16	Quenched lava	231 (± 11.8)	96.4 (± 9.8)	0.401	1.87	0.216	0.70321	0.51298
20240209-2	S17	Cooled lava	271 (± 10.9)	110 (± 13)	0.394	1.90	0.218	-	-

Oxide and isotopic composition from Matthews et al. (2024) for Sundhnúksgígar samples and from Marshall et al. (2024) and Halldórsson et al. (2022) for Geldingadalir samples. Details regarding sampling location and time are given in supplementary figure 5.5.

Fractional crystallisation effect

The fluorine concentration of the historical and newly erupted material from Reykjanes correlate with the incompatible oxide concentrations, such as P_2O_5 (Fig. 5.8a), K_2O (Fig. 5.8b) or TiO_2. A variable extent of FC explains such correlation with intercept at the origin and the large concentration range in incompatible oxides and fluorine, spanning over an order of magnitude (K_2O = 0.01-0.47 %, P_2O_5 = 0.02-0.46, TiO_2 = 0.23-3.68 and F = 18-390 ppm). The most primitive (poor in incompatible elements) products are picrites from early Holocene small lava shields (Jakobsson et al. 1978; Stecher 1998). The most evolved

products are the Sundhnúksgígar lava and tephra, belonging to the Svartsengi volcanic system, known to produce relatively evolved tholeiite (Caracciolo et al. 2023). Fagradalsfjall and Sundhnúksgígar samples have P_2O_5 (0.10-0.14 and 0.20-0.24 % respectively) and TiO_2 (1-1.2 and 1.7-2.1 %) content highly distinct, as shown by Matthews et al. (2024), whereas the difference is signficant but less marked for K_2O (0.16-0.32 and 0.31-0.44) and F (184-294 and 232-388 ppm respectively).

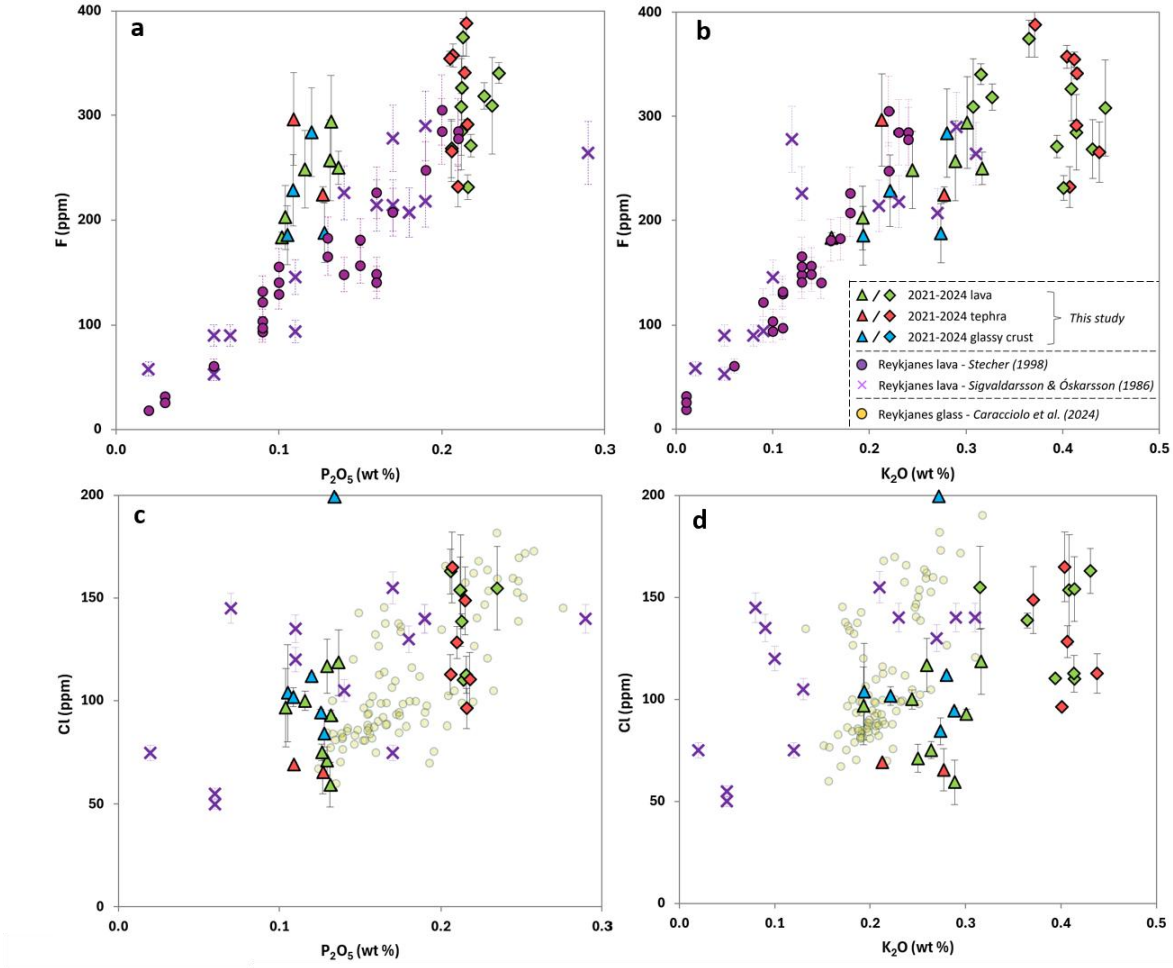

Figure 5.8. Comparison between the measured F and Cl concentrations and incompatible oxide concentrations in Reykjanes products. *The triangles and diamonds represent Fagradalsfjall and Sundhnúksgígar products respectively, lava being in green, glassy selvage in blue and tephra in red. The purple circles corresponds to Holocene lavas analysed by Stecher (1998). Purple crosses are products of diverse age (interglacial, subglacial and postglacial) analysed by Sigvaldason and Óskarsson (1976, 1986). Fluorine concentrations from both studies were measured using ISE whereas Cl concentrations were measured by X-ray fluorescence spectrometry. The glass analyses of medieval products from Caracciolo et al. (2023) are shown as yellow circle and were conducted using EPMA. The shown uncertainties are the 2σ standard deviations from repeated measurement on rock standards. Uncertainties from Caracciolo et al. (2023) glass measurements are larger (≈ 25 %) and not shown for clarity. The fluorine concentration is plotted against P_2O_5 (a) and K_2O (b). Cl is also shown as a function of P_2O_5 (c) and K_2O (d). The error shown on F and Cl concentrations is based on the standard deviation measured for each sample. For clarity, uncertainties associated with major oxides are not indicated as they are below 5 % (Marshall et al. 2024; Matthews et al. 2024).*

Compared to fluorine, the chlorine concentrations are less well correlated with those of the incompatible elements (Fig 5.8c and d). Chlorine reaches higher concentration in basalt from Sundhnúksgígar despite considerable overlap with that of Fagradalsfjall. The results align with those from Sigvaldason and Óskarsson (1986) and the Reykjanes groundmass glass analyses from Caracciolo et al. (2024) when Cl is plotted against P_2O_5 (Fig 5.8c). Despite the overall correlation between Cl and incompatible oxide concentrations, Cl displays a large concentration range at any oxide concentration and in all datasets (whether whole rock or groundmass glass).

Taken together, both Cl and F appear to have concentration largely affected by the fractional crystallisation magma differentiation mechanism. The correlations between concentrations in both halogens and those of incompatible oxides are however imperfect, Cl and F displaying significant concentration variation at a given oxide concentration. Such variability is well illustrated by the F concentration in the Fagradalsfjall and Sundhnúksgígar products which are higher than to published results when plotted against P_2O_5 (Fig. 5.8a) or TiO_2, while it is not the case when plotted against K_2O (Fig. 5.8b). To explain the halogen concentration variability, other mechanisms than fractional crystallisation must thus be taken into consideration such as degassing and magma source heterogeneity.

Halogen loss through degassing?

In addition to factional crystallisation, the halogen concentration heterogeneity could originate from a variable extent of degassing of the erupted magma. Regarding fluorine, its known low volatility in pre-eruptive conditions should result in minimal influence of pre- and syn-eruptive magma degassing on magma fluorine concentration (Villemant and Boudon 1999; Wallace et al. 2015). Such lack of F loss through degassing is supported by the absence of F depletion in the Icelandic basalt with respect to MORBs of the mid-Atlantic ridge (Rowe and Schilling 1979).

One context more favourable for F degassing is the secondary degassing, richer in halogens (see Chapter 3; Sigmarsson et al. 2020; Wainman et al. 2024). The potential effect of fluorine escape through this secondary degassing can be investigated by comparing the fluorine concentration in three types of samples: tephra, glassy crust and lava. Óskarsson et al. (1984) and Thordarson et al. (1996) revealed distinct halogen concentrations in the different products of the Laki 1783-1784 AD eruption. They identified higher F and Cl concentrations in the tephra compared to the glassy crust of the lava, which in turn had higher concentration than the crystalline lava. Such variable halogen concentrations were related to progressive loss through lava degassing, the tephra being the least degassed and the crystalline lava the most degassed product at Laki.

In the 2021-2024 Reykjanes products, no systematic difference in F concentration can be observed between the lava, glassy crust and tephra (Fig 5.8). The limited resolution of our results, associated both with measurement uncertainties (of typically 10 %) and the analysed sample set, may hinder the detection of small-scale variation of fluorine concentration. However, the fact that the range of F concentration in the tephra, glassy crust and lava does not only overlap but is virtually the same suggesting that only a limited proportion of fluorine escaped during the lava emplacement. Nevertheless, all lava/glassy crust being collected at the front of lava field, either during or shortly after the lava emplacement (Halldórsson et al. 2022; Marshall et al. 2024; Matthews et al. 2024; see details in supplementary figure 5.5),

the potential loss of fluorine from the lava core during crystallisation (Chapter 4) cannot be investigated through our dataset.

As chlorine is known to have lower solubility and thus be more volatile than fluorine in basaltic melt (Zelenski et al. 2021; Edmonds et al. 2022), the effect of pre- and syn-eruptive degassing must be considered. Investigating the Cl/TiO_2 and Cl/K_2O from melt inclusion (MI) and groundmass glass (GG) can give indication about the extent of chlorine loss during pre- and syn-eruptive degassing. Results on Cl concentration in MI and GG from the different volcanic systems of the Reykjanes peninsula were recently published by Caracciolo et al. (2024), analysing products from the last eruptive cycle (800-1240 CE). Comparing the average Cl concentrations reveals 10 to 30 % lower relative Cl content in the GG with respect to MI (Supplementary Fig. 5.1), suggesting an escape of chlorine around 20 ± 10 % through pre and syn-eruptive degassing. The variable Cl concentration at a given incompatible oxide concentration could thus result from variable degree of degassing pre- and syn-eruptively. Thus, the range of Cl concentration at a given oxide content can be partially explained by variable degree of pre/syn-eruptive Cl degassing, resulting in Cl loss. Such chlorine degassing indication is consistent with the proposed impoverishment of Cl in Icelandic volcanics with respect to the surrounding basalts of the Mid-Atlantic ridge (Unni and Schilling 1978).

As for fluorine, the comparison of Cl concentrations in the tephra, glassy surface and lava from the Fagradalsfjall and Sundhnúksgígar eruptions could reveal Cl loss through post-eruptive degassing. No systematic enrichment or depletion in chlorine of each sample type can be observed. In particular, the Cl concentration range in Sundhnúksgígar tephra is undistinguishable from that of the lava. Such a lack of resolvable Cl concentration difference suggests negligible Cl degassing during the early stage of lava degassing.

Thus, both fluorine and chlorine display a variable composition that cannot be solely explained by fractional crystallisation and loss through degassing even considering the pre-eruptive outgassing of Cl. Involvement of multiple magma source thus appear necessary to explain the observed halogen concentration variability in the Reykjanes 2021-2024 products.

Source heterogeneity and magma mixing.

The effect of fractional crystallisation (FC) on the halogen concentration is readily removed by normalising their concentrations against another incompatible element, the ratio of two incompatible elements being unaffected by FC. Normalising both fluorine and potassium oxide concentrations against titanium oxide reveals a correlation between the two ratios (Fig. 5.9a). The large variability of F/TiO_2 and K_2O/TiO_2 values confirms that both K_2O and F concentrations are not only controlled by fractional crystallisation. The general correlation between the two ratios, with a linear trend that includes most results from Stecher (1998), a large part of those from Sigvaldason and Óskarsson (1986) and ours, suggest that the same process affect both ratios. A few samples have significantly higher F/TiO_2: the two postglacial shield volcanoes RSG-26 and RSG-54 from Sigvaldason and Óskarsson (1986) and one Fagradalsfjall tephra, G20210404-1. These occasional high F concentrations however do not seem to be associated with a specific sample nature (many other samples are from shield volcanoes and tephra) or composition (distinct P_2O_5, K_2O and K_2O/TiO_2).

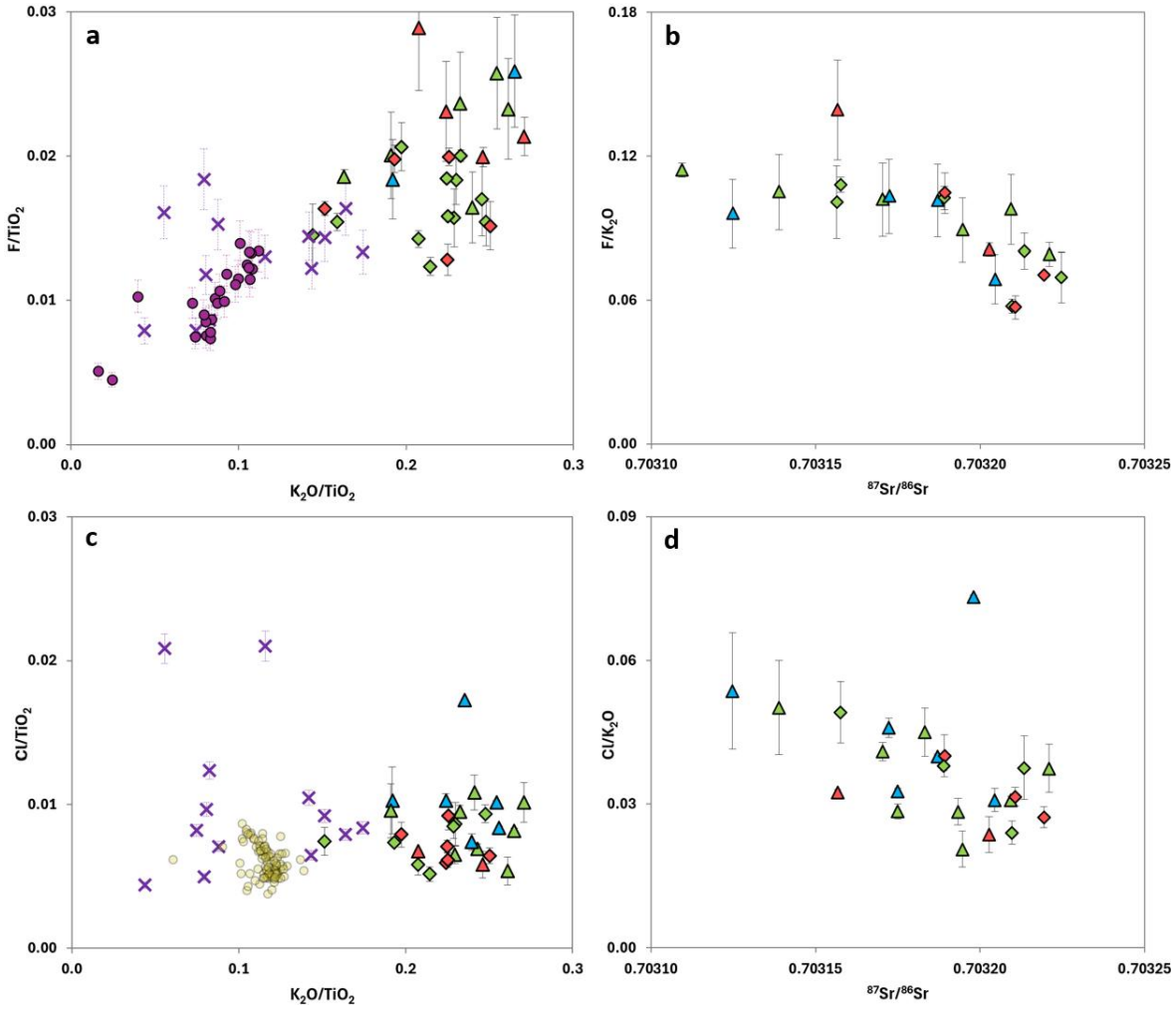

Figure 5.9. Comparison between normalised F and Cl concentrations and incompatible oxide concentration ratios and Sr isotope ratios in Reykjanes products. *The triangles and diamonds represent Fagradalsfjall and Sundhnúksgígar products respectively, lava being in green, glassy selvage in blue and tephra in red. The purple circles corresponds to Holocene lavas analysed by Stecher (1998). Purple crosses are products of diverse age (interglacial, subglacial and postglacial) analysed by Sigvaldason and Óskarsson (1986). Fluorine concentrations from both studies were measured using ISE whereas Cl concentrations were measured by X-ray fluorescence spectrometry. The glass analyses of medieval products from Caracciolo et al. (2023) are shown as yellow circle and were conducted using EPMA. The shown uncertainties are 2σ standard deviations from repeated measurement on rock/glass standards. Uncertainties from Caracciolo et al. (2023) glass measurements are larger (≈ 25 %) and not shown for clarity. The ratio F/TiO_2 is shown as a function K_2O/TiO_2 (a) and F/K_2O is plotted against the isotopic ratios $^{87}Sr/^{86}Sr$ (b). Cl/TiO_2 is plotted against K_2O/TiO_2 (c) and Cl/K_2O is plotted against the isotopic ratios $^{87}Sr/^{86}Sr$ (d). The error shown on F and Cl concentrations is based on the standard deviation measured for each sample. For clarity, uncertainties associated with major oxides and Sr isotopic ratio are not indicated as they are below 5 % and 0.00001 respectively (Marshall et al. 2024; Matthews et al. 2024).*

The ratio K_2O/TiO_2 has been demonstrated to correlate well with the isotopic ratio $^{143}Nd/^{144}Nd$, translating heterogeneous mantle source composition (Matthews et al. 2024). Such covariation was observed both in Fagradalsfjall and Sundhnúksgígar products and demonstrated to originate from mixing of compositionally distinct magmas, with important

temporal changes in their relative contributions (Halldórsson et al. 2022; Matthews et al. 2024). Thus, the correlation between F/TiO_2 and K_2O/TiO_2 may be explained by a general binary mixture of two magma endmembers. The Holocene Reykjanes lavas have significantly lower ratios than both Fagradalsfjall and Sundhnúksgígar products, suggesting that the 2021-2024 products present a higher contribution of the enriched magma. The F/TiO_2 variability can however not be fully explained by a binary magma mixture, as not all samples align on a single linear trend.

Such variation may be explained by the presence of more magma sources of distinct composition, especially regarding the 2021-2024 products. Based on the figure 5.9a, the contribution of an additional source with low F/TiO_2 and intermediate K_2O/TiO_2 would readily explain the products compositional variation. This third magma source can be further characterised by comparing the ratio F/K_2O to the isotopic ratio $^{87}Sr/^{86}Sr$ (Fig. 5.9b).

The F/K_2O variability visible in the Fagradalsfjall/Sundhnúksgígar products (0.06 to 0.12 excluding the sample G20210404-1) is comparable to what is observed in Mid-Atlantic ridge basalts (Supplementary Fig. 5.2a; Schilling et al. 1980). In contrast, only a small fraction of the of the $^{87}Sr/^{86}Sr$ variability in the Mid-Atlantic ridge basalts (0.7026 to 0.7035; White and Schilling 1978) is visible in the Reykjanes products. In our data, limited F/K_2O variation is observed in the range of $^{87}Sr/^{86}Sr$ from 0.70310 to 0.70318, but at more radiogenic Sr-isotope values there is clear negative correlation between F/K_2O and $^{87}Sr/^{86}Sr$. Such results support the contribution of at least three magma sources, two with distinct $^{87}Sr/^{86}Sr$ but similar F/K_2O (around 0.1) and the third one both radiogenic (high $^{87}Sr/^{86}Sr$) and poorer in fluorine ($F/K_2O \leq 0.06$). Interestingly, the products presenting contribution of this third magma source comes both from Fagradalsfjall and Sundhnúksgígar eruptions. This observation suggests that similar magma sources fed both eruptive systems, but in variable proportion.

Chlorine concentrations can also be normalised to TiO_2 and compared to the source indicator K_2O/TiO_2. Such normalisation reveals that Cl/TiO_2 display significant variability (Fig. 5.9c), both in the 2021-2024 products and published results for the Reykjanes peninsula. The lack of significant change of Cl/TiO_2 over a large range of K_2O/TiO_2 suggest that the different magma sources (with distinct K_2O/TiO_2) have similar Cl concentration normalised to TiO_2 (unlike what was observed for fluorine). The glass analyses by Caracciolo et al. (2024) also show no correlation between K_2O/TiO_2 and Cl/TiO_2 in the historical Reykjanes products. Two lavas from Sigvaldason and Óskarsson (1976), RSG-13 and RSG-29, and one newly erupted glassy crust, G20210817-3, have significantly higher Cl/TiO_2. Notably, such high values cannot be related to specific K_2O/TiO_2, sample nature or fluorine concentration (Fig. 5.10a).

The ratio Cl/K_2O vary significantly within the 2021-2024 products (Fig. 5.9d), recovering most of the mid-Atlantic ridge basalt variability (Supplementary Fig. 5.1b; Schilling et al. 1980). As Cl and K_2O have similar incompatible behaviour, the ratio Cl/K_2O of mid oceanic ridge basalts is frequently used to identify the assimilation of hydrothermally altered crust, strongly enriched in chlorine from seawater (Michael and Schilling 1989). If assimilation of the altered crust was responsible for higher Cl concentrations, the effect should also increase $^{87}Sr/^{86}Sr$, as it is substantially higher in the seawater (close to 0.709; e.g. Elderfield and Greaves 1981) with respect to basalt. In marked contrast, the 2021-2024 basalt has Cl/K_2O that is inversely correlated with the isotope ratio $^{87}Sr/^{86}Sr$. Furthermore, the absence of Cl enrichment in samples from Sundhnúksgígar with respect to Fagradalsfjall rule out the idea of hydrothermal contamination of the Sundhnúksgígar newly erupted magma. Such absence of seawater component is in agreement with the observation from Halldórsson et al. (2016),

who concluded that Cl enrichment in Icelandic products result from mantle source heterogeneity. The negative correlation between Cl/K_2O and $^{87}Sr/^{86}Sr$ thus more likely reflect the impact of the magma source compositional heterogeneity, with the radiogenic magma component being either poorer in Cl or increasingly outgassed on its way to surface.

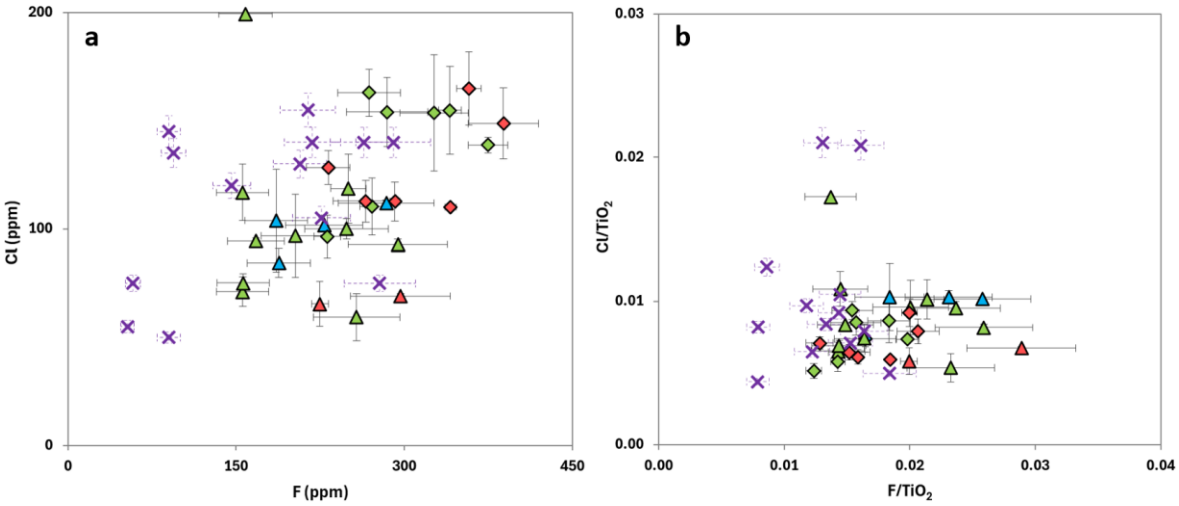

Figure 5.10. Comparison between the F and Cl concentrations in the Reykjanes basalts. *The triangles and diamonds represent Fagradalsfjall and Sundhnúksgígar products respectively, lava being in green, glassy selvage in blue and tephra in red. Purple crosses are products of diverse age (interglacial, subglacial and postglacial) analysed by Sigvaldason and Óskarsson (1976, 1986). Fluorine concentrations were measured using ISE whereas Cl concentrations were measured by X-ray fluorescence spectrometry. The shown uncertainties are 2σ standard deviations from repeated measurement on rock standards. (a) Chlorine concentration in the historical Reykjanes products (Sigvaldason and Óskarsson 1976, 1986) and in the newly erupted lava and tephra as a function of their F concentration. (b) Cl/TiO_2 as a function of F/TiO_2. A rough correlation can be observed between the Cl and F concentrations, but such correlation disappears once normalised by TiO_2.*

Thus, chlorine and fluorine exhibit distinct features in the Fagradalsfjall and Sundhnúksgígar volcanic products. Unlike fluorine, no obvious source heterogeneity in terms of Cl/TiO_2 content can be resolved. Though small variations could be hindered by the significant uncertainties associated with Cl electrode measurement and potential Cl loss through degassing, chlorine concentrations clearly do not vary as much as fluorine. Variation of Cl/K_2O with changing $^{87}Sr/^{86}Sr$ does however suggest some level of Cl source heterogeneity rather than ad hoc differential Cl degassing. Chlorine and fluorine heterogeneity thus seem distinct in the sources, as illustrated by the lack of correlation between Cl/TiO_2 and F/TiO_2 (Fig. 5.10b). These distinct features of chlorine and fluorine implies that significant change in the magma contribution from variable mantle sources to the erupted product controlled the relative halogen concentration. Such changes will in turn affect the proportion of F and Cl in the emitted gas phase as observed in the ratio of F over Cl in the different secondary gas types (post-eruptive crater gas versus gas from the crystallising lava; see Chapter 3).

5.6 Conclusions:

- Simultaneous leaching of chlorine and fluorine is possible, allowing synchronous measurement by ISE. The method however requires adaptation to ensure complete leaching and no contamination for both halogens and has limited resolution, particularly for Cl.

- The fluorine ISE is more sensitive that of the chlorine ISE, which respond nonlinearly to Cl concentration below 1-5 ppm. Measurements on low Cl concentration leachates reveal higher potential than pure DI water, implying important matrix effect.

- Matrix effect on the Cl ISE makes impossible to use in-house calibration standards to convert electrode potential to Cl leachate concentrations. Instead, building up a calibration curve, based on leachate from rock standards allows to calculate the Cl concentration in an unknown leachate. The response of the Cl ISE appears to have higher sensitivity for leachate than for Cl in pure water, the correlation remaining linear for Cl-poor leachates.

- Precise and accurate measurements of Cl concentration thus seem to require further development of the use of the ISE or using another method. However, rapid approximate Cl quantification can be conducted on a leachate prepared for F analysis.

- Both F and Cl concentration in the newly erupted Reykjanes products are correlated to incompatible element concentrations, highlighting their incompatible behaviour. Indications of loss through pre-/syn- eruptive degassing are observed for chlorine and but not for fluorine. In contrast, no lava degassing can be resolved by comparing the F and Cl concentration in the tephra, glassy surface and lava.

- To explain the variable F concentrations in the newly erupted Reykjanes products, at least three magma sources should be involved, contributing both to Fagradalsfjall and Sundhnúksgígar eruptions. These magma sources are characterised by distinct F content, K_2O/TiO_2 value and $^{87}Sr/^{86}Sr$ isotope ratio.

- Chlorine concentrations in the different products suggest some level of source heterogeneity but distinct from what is observed for fluorine. The negative correlation between Cl/K_2O and $^{87}Sr/^{86}Sr$ rules out the significant contribution of a geothermally altered component in the Fagradalsfjall and Sundhnúksgígar magmas.

- The distinct relative F and Cl concentrations in the different magma sources implies that change in relative source contribution should result in variable proportion of Cl and F in the magma. In that case, the change of source contribution could be tracked by measuring Cl/F either in the erupted product or in the escaping gas phase. However, variable pre-eruptive Cl degassing may compromise such approach.

Acknowledgements

We acknowledge Jóhann Gunnarsson Robin whose help and advice permitted to develop the methods associated with the use of the Ion Selective Electrodes. We also thank Severian Darmois Guennou, who greatly helped with preparing and analysing some of the samples used in this study. This work was supported by the Icelandic Research Found (Rannís).

5.7 Supplementary information

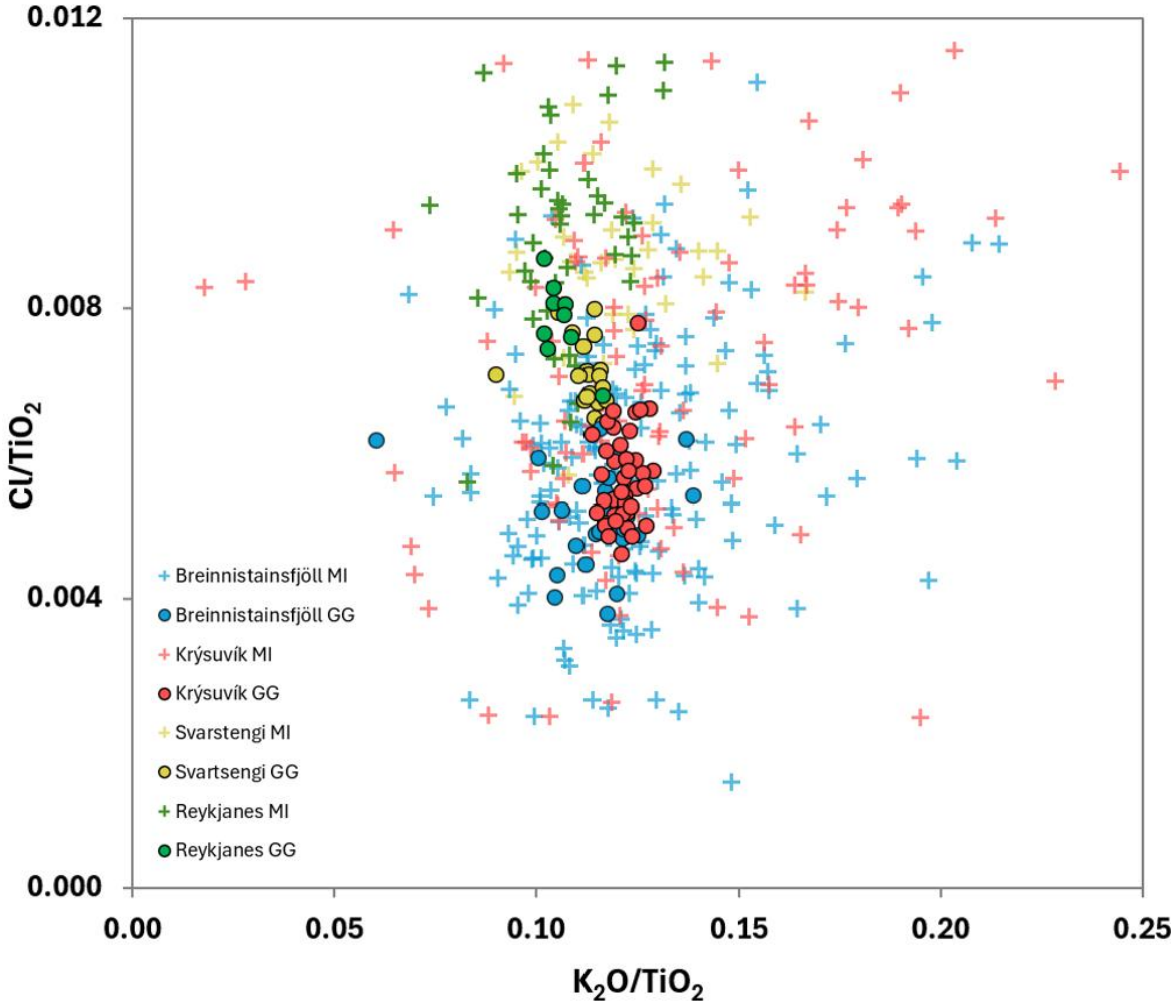

Supplementary Figure 5.1. Melt inclusion (MI) and groundmass glass (GG) Cl/TiO_2 as a function of K_2O/TiO_2 in the different Reykjanes volcanic systems. Both halogen and oxide concentrations are from Caracciolo et al. (2024) *Though both MI and GG exhibit significant range of Cl/TiO_2 in each system (Brennisteinsfjöll, Krýsuvík, Svartsengi and Reykjanes), average values are systematically higher in the MI, from 10 to 30 more than in the GG.*

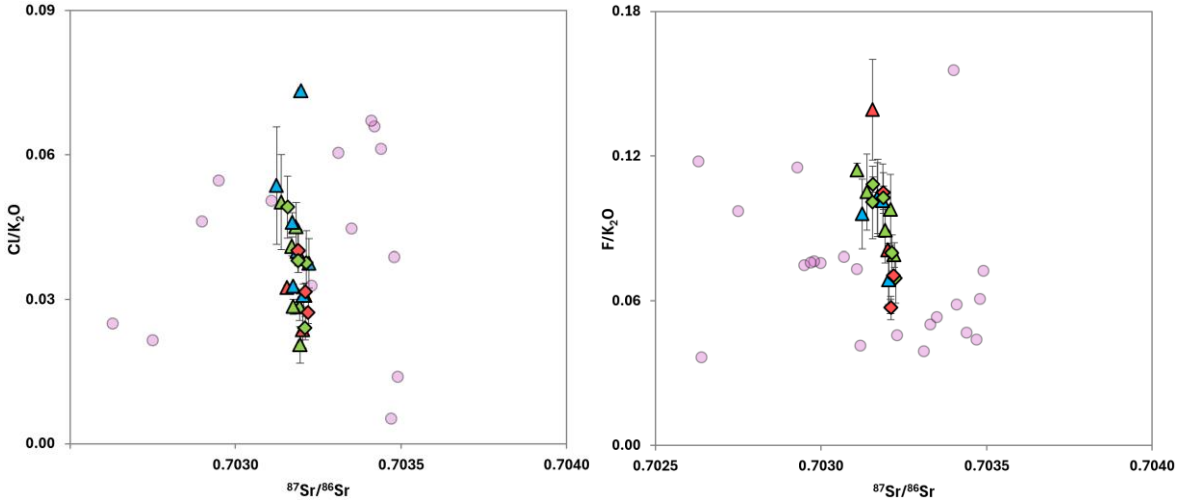

Supplementary Figure 5.2. Fluorine and chlorine concentration normalised by K_2O as a function of $^{87}Sr/^{86}Sr$ in the Reykjanes products and the Reykjanes ridge MORBs.

Supplementary Table 5.1. Florine measurement information and results on the rock standard leachates.

Prep date	Analysis date	Name sample	Dilution factor	Potential measured (mV)	Calib F (ppm)	SAM F (ppm)	Average F concentration (ppm)	Ratio methods
29/05/2024	31/05/2024	JR-1 1g (1)	32.0	67.8	575.0	889.5	732.2	1.55
29/05/2024	04/06/2024	JR-1 1g (1)	32.0	68.2	515.3	844.4	679.9	1.64
07/06/2024	11/06/2024	JR-1 0.15g (1)	213.3	105.9	851.3	1614.9	1233.1	1.90
07/06/2024	14/06/2024	JR-1 0.15g (1)	213.3	104.8	837.0	1493.6	1165.3	1.78
07/06/2024	14/06/2024	JR-1 0.15g (2)	213.3	103.8	870.7	1450.7	1160.7	1.67
07/06/2024	11/06/2024	JR-1 0.15g (2)	213.3	104.7	891.2	1607.5	1249.4	1.80
29/05/2024	31/05/2024	JR-1 0.5g (1)	64.0	82.3	646.3	1115.7	881.0	1.73
29/05/2024	04/06/2024	JR-1 0.5g (1)	64.0	81.4	605.4	1243.6	924.5	2.05
07/06/2024	11/06/2024	JR-1 (2)	64.0	80.8	666.1	1217.0	941.6	1.83
07/06/2024	14/06/2024	JR-1 (2)	64.0	80.0	668.6	1097.3	882.9	1.64
07/06/2024	11/06/2024	JR-1 (3)	64.0	79.7	694.7	1100.4	897.5	1.58
07/06/2024	14/06/2024	JR-1 (3)	64.0	79.0	695.5	1022.7	859.1	1.47
08/06/2024	11/06/2024	BHVO-1 1g (1)	32.0	106.8	123.4	326.2	224.8	2.64
08/06/2024	14/06/2024	BHVO-1 1g (1)	32.0	105.6	121.7	307.6	214.6	2.53
12/06/2024	14/06/2024	BHVO-1 1g (2)	32.0	106.6	117.0	302.5	209.7	2.59
12/06/2024	20/06/2024	BHVO-1 1g (2)	32.0	106.8	111.8	295.2	203.5	2.64
08/06/2024	11/06/2024	BHVO-1 (1)	64.0	123.5	130.4	271.6	201.0	2.08
08/06/2024	14/06/2024	BHVO-1 (1)	64.0	122.4	125.4	268.8	197.1	2.14
12/06/2024	14/06/2024	BHVO-1 (2)	64.0	116.1	160.8	312.8	236.8	1.95
12/06/2024	20/06/2024	BHVO-1 (2)	64.0	116.5	152.4	295.1	223.7	1.94
21/10/2024	13/11/2024	BHVO-1 (3)	63.4	113.2	163.5	308.9	236.2	1.89
11/06/2024	11/06/2024	BIR-1 (1)	64.0	156.6	35.5	59.0	47.3	1.66
11/06/2024	14/06/2024	BIR-1 (1)	64.0	155.7	33.7	53.9	43.8	1.60
11/06/2024	03/07/2024	BIR-1 (1)	64.0	155.9	32.2	53.9	43.0	1.67
18/06/2024	20/06/2024	BIR-1 (2)	64.0	152.3	37.0	74.2	55.6	2.01
18/06/2024	03/07/2024	BIR-1 (2)	64.0	152.3	37.1	67.6	52.3	1.82
06/08/2024	03/09/2024	B-ALK	63.4	109.9	184.5	561.1	372.8	3.04
06/08/2024	13/11/2024	B-ALK	63.4	110.3	183.0	559.0	371.0	3.05
06/08/2024	14/08/2024	JA-2 (1)	64.4	123.2	110.6	241.9	176.3	2.19
06/08/2024	03/09/2024	JA-2 (1)	64.4	124.0	107.4	239.7	173.5	2.23
21/10/2024	13/11/2024	JA-2 (2)	64.4	122.8	113.5	247.0	180.2	2.18
11/06/2024	11/06/2024	I-ICE (1)	64.0	88.5	485.8	1318.2	902.0	2.71
11/06/2024	14/06/2024	I-ICE (1)	64.0	88.0	487.5	1181.8	834.7	2.42
11/06/2024	03/07/2024	I-ICE (1)	64.0	88.0	471.2	1256.8	864.0	2.67
18/06/2024	20/06/2024	I-ICE (2)	64.0	89.2	448.3	1663.6	1056.0	3.71
18/06/2024	03/07/2024	I-ICE (2)	64.0	89.0	453.0	1587.9	1020.4	3.51
19/06/2024	20/06/2024	JB-3 (1)	64.0	127.7	97.9	302.6	200.3	3.09
19/06/2024	21/06/2024	JB-3 (1)	64.0	127.0	98.2	292.6	195.4	2.98
19/06/2024	03/07/2024	JB-3 (1)	64.0	127.6	98.5	286.5	192.5	2.91
30/07/2024	06/08/2024	JB-3 (2)	63.0	123.4	108.0	264.7	186.4	2.45
30/07/2024	14/08/2024	JB-3 (2)	63.0	123.2	108.2	292.9	200.6	2.71
19/06/2024	20/06/2024	BCR-1 (1)	64.0	113.0	175.0	500.9	337.9	2.86
19/06/2024	21/06/2024	BCR-1 (1)	64.0	112.2	180.6	513.8	347.2	2.84
19/06/2024	03/07/2024	BCR-1 (1)	64.0	112.7	177.5	560.8	369.2	3.16
30/07/2024	06/08/2024	BCR-1 (2)	62.4	105.2	220.6	485.0	352.8	2.20
30/07/2024	14/08/2024	BCR-1 (2)	62.4	104.5	224.9	506.5	365.7	2.25
20/06/2024	21/06/2024	B-THO	66.2	162.2	25.4	52.2	38.8	2.06
20/06/2024	03/07/2024	B-THO	66.2	163.0	25.1	49.6	37.4	1.97
20/06/2024	21/06/2024	A-THO	64.0	89.5	443.0	1105.7	774.4	2.50
20/06/2024	03/07/2024	A-THO	64.0	89.7	440.6	1093.8	767.2	2.48

Supplementary Table 5.2. Chlorine measurement information and results on the rock standard leachates.

Leaching date	Analysis session	Name sample	Dilution factor	Potential measured (mV)	Calibration curve slope (mV/ppm)	Calibration curve intercept (mV)	Potential difference (mV)
29/05/2024	06/06/2024	JR1 1g	32	176.9	-21.38	238.85	-62.0
29/05/2024	05/06/2024	JR1 1g	32	178.2	-21.02	237.04	-58.8
07/06/2024	10/06/2024	JR-1 0.15g (1)	213.3	218.1	-21.35	239.18	-21.1
07/06/2024	17/06/2024	JR-1 0.15g (1)	213.3	213.7	-20.21	233.00	-19.3
07/06/2024	07/06/2024	JR-1 0.15g (1)	213.3	214.0	-22.16	241.40	-27.4
07/06/2024	07/06/2024	JR-1 0.15g (2)	213.3	214.1	-22.16	241.40	-27.3
07/06/2024	10/06/2024	JR-1 0.15g (2)	213.3	216.2	-21.35	239.18	-23.0
07/06/2024	17/06/2024	JR-1 0.15g (2)	213.3	210.6	-20.21	233.00	-22.4
05/06/2024	05/06/2024	JR-1 (1)	64	189.3	-21.02	237.04	-47.7
05/06/2024	06/06/2024	JR-1 (1)	64	190.7	-21.38	238.85	-48.2
05/06/2024	07/06/2024	JR-1 (1)	64	189.1	-22.16	241.40	-52.3
05/06/2024	05/06/2024	JR-1 (2)	64	188.9	-21.02	237.04	-48.1
05/06/2024	06/06/2024	JR-1 (2)	64	188.0	-21.38	238.85	-50.9
05/06/2024	07/06/2024	JR-1 (2)	64	188.6	-22.16	241.40	-52.8
07/06/2024	10/06/2024	JR-1 (3)	64	186.8	-21.35	239.18	-52.4
07/06/2024	10/06/2024	JR-1 (3)	64	187.5	-21.35	239.18	-51.7
07/06/2024	07/06/2024	JR-1 (3)	64	188.6	-22.16	241.40	-52.8
07/06/2024	10/06/2024	JR-1 (4)	64	187.8	-21.35	239.18	-51.4
07/06/2024	10/06/2024	JR-1 (4)	64	186.9	-21.35	239.18	-52.3
07/06/2024	07/06/2024	JR-1 (4)	64	187.9	-22.16	241.40	-53.5
08/06/2024	10/06/2024	BHVO-1 (1)	64	246.9	-21.35	239.18	7.7
08/06/2024	17/06/2024	BHVO-1 (1)	64	238.5	-20.21	233.00	5.5
08/06/2024	21/06/2024	BHVO-1 (1)	64	236.5	-20.04	231.53	5.0
12/06/2024	17/06/2024	BHVO-1 (2)	64	233.5	-20.21	233.00	0.5
12/06/2024	21/06/2024	BHVO-1 (2)	64	243.3	-20.04	231.53	11.8
08/06/2024	10/06/2024	BHVO-1 1g (1)	64	257.2	-21.35	239.18	18.0
08/06/2024	17/06/2024	BHVO-1 1g (1)	64	239.1	-20.21	233.00	6.1
08/06/2024	21/06/2024	BHVO-1 1g (1)	64	241.9	-20.04	231.53	10.4
12/06/2024	17/06/2024	BHVO-1 1g (2)	64	251.3	-20.21	233.00	18.3
12/06/2024	21/06/2024	BHVO-1 1g (2)	64	237.9	-20.04	231.53	6.4
11/06/2024	17/06/2024	BIR-1	64	241.5	-20.21	233.00	8.5
18/06/2024	21/06/2024	BIR-1	64	243.7	-20.04	231.53	12.2
06/08/2024	07/08/2024	B-ALK	64	212.2	-21.75	231.08	-18.9
06/08/2024	29/08/2024	B-ALK	64	217.50	-21.60	229.59	-12.1
06/08/2024	29/08/2024	B-ALK	64	216.40	-21.60	229.59	-13.2
06/08/2024	22/10/2024	B-ALK	64	217.5	-22.83	231.50	-14.0
06/08/2024	22/10/2024	B-ALK	64	216.4	-22.83	231.50	-15.1
06/08/2024	22/10/2024	JA-2 (1)	65	264.9	-22.83	231.50	33.4
06/08/2024	22/10/2024	JA-2 (1)	65	261.1	-22.83	231.50	29.6
06/08/2024	29/08/2024	JA-2 (1)	65	253.40	-21.60	229.59	23.8
06/08/2024	29/08/2024	JA-2 (1)	65	251.30	-21.60	229.59	21.7
11/06/2024	17/06/2024	I-ICE (1)	64	216.2	-20.21	233.00	-16.8
11/06/2024	05/07/2024	I-ICE (1)	64	216.1	-20.89	236.40	-20.3
18/06/2024	21/06/2024	I-ICE (2)	64	215.3	-20.04	231.53	-16.2
18/06/2024	05/07/2024	I-ICE (2)	64	216.4	-20.89	236.40	-20.0
19/06/2024	21/06/2024	JB-3 (1)	64	216.5	-20.04	231.53	-15.0
19/06/2024	05/07/2024	JB-3 (1)	64	222.8	-20.89	236.40	-13.6
30/07/2024	22/10/2024	JB-3 (2)	62.4	209.0	-22.83	231.50	-22.5
30/07/2024	22/10/2024	JB-3 (2)	62.4	209.9	-22.83	231.50	-21.6
30/07/2024	29/08/2024	JB-3 (2)	62.4	209.00	-21.60	229.59	-20.6
30/07/2024	29/08/2024	JB-3 (2)	62.4	209.90	-21.60	229.59	-19.7
30/07/2024	07/08/2024	JB-3 (2)	62.4	210.6	-21.75	231.08	-20.5
30/07/2024	06/08/2024	JB-3 (2)	62.4	217.9	-20.06	231.43	-13.5
19/06/2024	05/07/2024	BCR-1 (1)	64	240.5	-20.89	236.40	4.1
19/06/2024	21/06/2024	BCR-1 (1)	64	230.1	-20.04	231.53	-1.4
30/07/2024	22/10/2024	BCR-1 (2)	63	223.8	-22.83	231.50	-7.7
30/07/2024	22/10/2024	BCR-1 (2)	63	223.5	-22.83	231.50	-8.0
30/07/2024	29/08/2024	BCR-1 (2)	63	223.80	-21.60	229.59	-5.8
30/07/2024	29/08/2024	BCR-1 (2)	63	223.50	-21.60	229.59	-6.1
30/07/2024	07/08/2024	BCR-1 (2)	63	225.6	-21.75	231.08	-5.5
30/07/2024	06/08/2024	BCR-1 (2)	63	230.8	-20.06	231.43	-0.6
20/06/2024	05/07/2024	B-THO	64	236.3	-20.89	236.40	-0.1
20/06/2024	21/06/2024	B-THO	64	229.2	-20.04	231.53	-2.3
20/06/2024	05/07/2024	A-THO	64	201.7	-20.89	236.40	-34.7
20/06/2024	21/06/2024	A-THO	64	200.8	-20.04	231.53	-30.7

Supplementary Table 5.3. Florine measurement information and results in 2021-2024 Reykjanes products.

Prep date	Analysis date	Name sample	Dilution factor	Potential measured (mV)	Calib F (ppm)	SAM F (ppm)	Average F concentration (ppm)	Ratio methods
25/01/2024	01/02/2024	S1 (1)	106.7	120.4	235.4	407.2	321.3	1.73
25/01/2024	13/02/2024	S1 (1)	106.7	119.1	229.9	510.7	370.3	2.22
30/01/2024	01/02/2024	S1 (2)	106.7	123.0	212.5	411.5	312.0	1.94
30/01/2024	13/02/2024	S1 (2)	106.7	121.6	208.3	395.0	301.6	1.90
25/01/2024	01/02/2024	S2 (1)	106.7	117.5	263.8	391.3	327.5	1.48
25/01/2024	13/02/2024	S2 (1)	106.7	116.2	257.9	427.0	342.5	1.66
30/01/2024	01/02/2024	S2 (2)	106.7	117.3	265.9	414.8	340.3	1.56
30/01/2024	13/02/2024	S2 (2)	106.7	116.1	258.9	444.6	351.8	1.72
31/01/2024	01/02/2024	S4	106.7	117.1	268.0	456.0	362.0	1.70
31/01/2024	13/02/2024	S4	106.7	115.5	265.1	509.1	387.1	1.92
31/01/2024	01/02/2024	S3	106.7	118.5	253.6	437.7	345.7	1.73
31/01/2024	13/02/2024	S5	106.7	116.8	251.9	482.9	367.4	1.92
31/01/2024	29/05/2024	S5	106.7	117.8	284.3	434.1	359.2	1.53
05/02/2024	13/02/2024	S3 (1)	106.7	115.5	265.1	466.8	366.0	1.76
07/02/2024	13/02/2024	S3 (2)	106.7	113.6	285.8	535.3	410.6	1.87
08/02/2024	13/02/2024	G2	106.7	131.6	140.2	231.1	185.7	1.65
08/02/2024	13/02/2024	G10	106.7	131.2	142.5	233.5	188.0	1.64
12/02/2024	13/02/2024	G1 (1)	106.7	132.0	138.0	235.8	186.9	1.71
19/02/2024	26/02/2024	G1 (2)	106.7	131.4	145.8	214.9	180.4	1.47
12/02/2024	13/02/2024	M1 (1)	106.7	123.6	192.5	329.7	261.1	1.71
22/02/2024	26/02/2024	M1 (2)	106.7	125.8	181.7	296.0	238.8	1.63
13/02/2024	26/02/2024	G12	106.7	127.3	171.3	285.6	228.4	1.67
13/02/2024	26/02/2024	L1	106.7	125.3	185.3	329.2	257.2	1.78
15/02/2024	26/02/2024	G4	106.7	128.9	160.8	244.5	202.6	1.52
15/02/2024	26/02/2024	L2 (1)	106.7	126.2	178.8	280.9	229.9	1.57
22/02/2024	26/02/2024	L2 (2)	106.7	130.1	153.4	285.1	219.3	1.86
20/02/2024	26/02/2024	G3	106.7	123.1	202.0	391.1	296.6	1.94
20/02/2024	26/02/2024	G6	106.7	123.5	198.9	298.1	248.5	1.50
21/02/2024	26/02/2024	G7	106.7	120.7	222.0	366.3	294.2	1.65
21/02/2024	26/02/2024	G14	106.7	121.0	219.4	348.3	283.8	1.59
16/05/2024	29/05/2024	G13	106.7	134.9	144.5	171.9	158.2	1.19
16/05/2024	29/05/2024	G5	106.7	136.6	135.1	176.1	155.6	1.30
22/05/2024	29/05/2024	G8	106.7	128.1	113.5	198.1	155.8	1.75
24/05/2024	29/05/2024	G11	106.7	124.4	131.3	203.7	167.5	1.55
24/05/2024	29/05/2024	G9	106.7	127.1	118.0	194.3	156.2	1.65
30/05/2024	04/06/2024	S17 (1)	64	113.9	163.4	360.5	261.9	2.21
27/05/2024	04/06/2024	S17 (2)	64	112.5	172.8	372.8	272.8	2.16
27/05/2024	29/05/2024	S17 (2)	64	115.0	190.5	380.9	285.7	2.00
06/06/2024	14/06/2024	S17 (3)	64	123.0	122.4	405.0	263.7	3.31
27/05/2024	29/05/2024	S16 (1)	60	124.2	132.4	293.4	212.9	2.22
06/06/2024	11/06/2024	S16 (2)	64	117.3	165.2	320.5	242.9	1.94
06/06/2024	14/06/2024	S16 (2)	64	116.3	159.5	314.8	237.2	1.97
29/06/2024	03/07/2024	S10 (1)	64.6	122.6	121.2	301.0	211.1	2.48
29/06/2024	10/07/2024	S10 (1)	64.6	122.0	120.7	299.6	210.1	2.48
04/07/2024	25/07/2024	S10 (2)	62.6	116.4	146.3	314.7	230.5	2.15
04/07/2024	10/07/2024	S10 (2)	62.6	116.4	146.4	320.4	233.4	2.19
01/08/2024	14/08/2024	S10 (3)	63.6	117.8	135.3	379.5	257.4	2.80
01/08/2024	06/08/2024	S10 (3)	63.6	118.4	133.0	367.4	250.2	2.76
29/06/2024	10/07/2024	S11 (1)	64.2	109.3	199.6	448.5	324.1	2.25
29/06/2024	03/07/2024	S11 (1)	64.2	110.3	195.8	421.5	308.6	2.15
04/07/2024	25/07/2024	S11 (2)	61.3	115.4	151.6	315.8	233.7	2.08
04/07/2024	10/07/2024	S11 (2)	61.3	115.7	149.9	345.8	247.8	2.31
01/08/2024	06/08/2024	S11 (3)	64.2	111.6	176.0	410.6	293.3	2.33
01/08/2024	14/08/2024	S11 (3)	64.2	111.0	178.9	436.0	307.4	2.44
26/06/2024	03/07/2024	S8 (1)	63.2	120.9	126.8	347.1	236.9	2.74
26/06/2024	10/07/2024	S8 (1)	63.2	120.0	127.9	378.5	253.2	2.96
31/07/2024	06/08/2024	S8 (2)	63.2	114.3	155.6	418.9	287.2	2.69
31/07/2024	14/08/2024	S8 (2)	63.2	114.0	156.3	436.8	296.6	2.79
26/06/2024	03/07/2024	S9 (1)	63	120.0	130.9	363.9	247.4	2.78
26/06/2024	10/07/2024	S9 (1)	63	119.7	129.1	371.3	250.2	2.88
31/07/2024	06/08/2024	S9 (2)	64.2	112.7	168.4	430.0	299.2	2.55
31/07/2024	14/08/2024	S9 (2)	64.2	112.3	169.9	614.6	392.2	3.62
24/06/2024	03/07/2024	S7	65	108.7	211.2	507.9	359.5	2.41
24/06/2024	10/07/2024	S7	65	108.1	212.1	487.2	349.6	2.30
24/06/2024	03/07/2024	S6	64.4	111.2	189.5	429.7	309.6	2.27
24/06/2024	10/07/2024	S6	64.4	110.5	190.8	463.9	327.4	2.43
21/06/2024	03/07/2024	S14	64	113.4	172.7	502.6	337.6	2.91
21/06/2024	10/07/2024	S14	64	113.1	170.9	518.5	344.7	3.03
21/06/2024	03/07/2024	S15	64	119.1	137.8	438.7	288.3	3.18
21/06/2024	10/07/2024	S15	64	118.6	137.0	452.5	294.8	3.30
02/07/2024	10/07/2024	S12	64	112.2	177.1	439.3	308.2	2.48
02/07/2024	10/07/2024	S13	64.8	108.1	211.4	407.0	309.2	1.93

Supplementary Table 5.4. Chlorine measurement information and results in 2021-2024 Reykjanes products

Leaching date	Analysis session	Name sample	Dilution factor	Potential measured (mV)	Potential difference (mV)	Rock Cl concentrations (ppm)
25/01/2024	05/02/2024	S1 (1)	106.7	253.1	-5.8	175.3
30/01/2024	07/02/2024	S1 (2)	106.7	251.2	-4.4	162.1
30/01/2024	05/02/2024	S1 (2)	106.7	259.5	0.6	123.3
25/01/2024	05/02/2024	S2 (1)	106.7	254.1	-4.8	166.0
25/01/2024	07/02/2024	S2 (1)	106.7	249.7	-5.9	176.0
30/01/2024	05/02/2024	S2 (2)	106.7	258.5	-0.4	130.3
30/01/2024	07/02/2024	S2 (2)	106.7	253.0	-2.6	146.8
31/01/2024	05/02/2024	S4	106.7	257.7	-1.3	136.2
31/01/2024	07/02/2024	S4	106.7	253.7	-1.9	141.3
31/01/2024	07/02/2024	S5	106.7	249.6	-6.0	177.0
31/01/2024	05/02/2024	S5	106.7	255.6	-3.3	152.8
05/02/2024	07/02/2024	S3 (1)	106.7	254.0	-1.6	139.0
05/02/2024	14/02/2024	S3 (1)	106.7	252.5	-1.6	139.0
07/02/2024	07/02/2024	S3 (2)	106.7	253.4	-2.2	143.6
07/02/2024	19/02/2024	S3 (2)	106.7	247.0	-5.6	173.1
08/02/2024	14/02/2024	G2	106.7	261.0	6.9	87.1
08/02/2024	19/02/2024	G2	106.7	253.6	1.0	120.5
08/02/2024	19/02/2024	G10	106.7	259.1	6.5	89.0
08/02/2024	14/02/2024	G10	106.7	262.6	8.5	79.8
12/02/2024	14/02/2024	G1 (1)	106.7	251.1	-3.0	150.1
12/02/2024	19/02/2024	G1 (1)	106.7	241.0	-11.6	240.7
19/02/2024	19/02/2024	G1 (2)	106.7	244.0	-8.6	204.1
19/02/2024	11/03/2024	G1 (2)	106.7	254.9	11.3	68.4
?	23/02/2024	G1 (3)	106.7	246.4	-1.2	135.9
?	23/02/2024	G1 (3)	106.7	244.0	-3.6	155.1
12/02/2024	14/02/2024	M1 (1)	106.7	252.3	-1.8	140.5
12/02/2024	23/02/2024	M1 (1)	106.7	249.6	2.0	114.0
22/02/2024	11/03/2024	M1 (2)	106.7	247.6	4.0	102.2
22/02/2024	23/02/2024	M1 (2)	106.7	249.0	1.4	117.8
13/02/2024	23/02/2024	G12	106.7	252.6	5.0	96.7
13/02/2024	14/02/2024	G12	106.7	258.0	3.9	102.7
13/02/2024	11/03/2024	G12	106.7	247.0	3.4	105.6
13/02/2024	14/02/2024	L1	106.7	264.5	10.4	71.9
13/02/2024	23/02/2024	L1	106.7	263.9	16.3	52.0
13/02/2024	11/03/2024	L1	106.7	259.1	15.5	54.3
15/02/2024	19/02/2024	G4	106.7	254.0	1.4	117.8
15/02/2024	23/02/2024	G4	106.7	253.5	5.9	92.0
15/02/2024	11/03/2024	G4	106.7	251.9	8.3	80.7
15/02/2024	19/02/2024	L2 (1)	106.7	264.2	11.6	67.3
15/02/2024	11/03/2024	L2 (1)	106.7	260.0	16.4	51.7
15/02/2024	23/02/2024	L2 (1)	106.7	261.0	13.4	60.9
22/02/2024	23/02/2024	L2 (2)	106.7	256.0	8.4	80.2
22/02/2024	11/03/2024	L2 (2)	106.7	255.2	11.6	67.3
20/02/2024	23/02/2024	G3	106.7	258.9	11.3	68.4
20/02/2024	11/03/2024	G3	106.7	254.5	10.9	69.9
20/02/2024	23/02/2024	G6	106.7	252.6	5.0	96.7
20/02/2024	11/03/2024	G6	106.7	247.4	3.8	103.3
21/02/2024	23/02/2024	G7	106.7	253.7	6.1	91.0
21/02/2024	11/03/2024	G7	106.7	249.0	5.4	94.6
21/02/2024	23/02/2024	G14	106.7	250.1	2.5	110.9
21/02/2024	11/03/2024	G14	106.7	245.8	2.2	112.8
16/05/2024	06/06/2024	G13	106.7	230.6	-8.3	200.0
16/05/2024	05/06/2024	G13	106.7	228.9	-8.1	198.8
16/05/2024	05/06/2024	G5	106.7	237.2	0.2	126.0
16/05/2024	06/06/2024	G5	106.7	241.9	3.1	107.5
22/05/2024	06/06/2024	G8	64	241.4	2.6	66.3
22/05/2024	05/06/2024	G8	64	237.1	0.1	76.0
24/05/2024	06/06/2024	G11	64	234.8	-4.0	95.3
24/05/2024	05/06/2024	G11	64	233.4	-3.6	93.1
24/05/2024	06/06/2024	G9	64	239.8	1.0	72.4
24/05/2024	05/06/2024	G9	64	236.6	-0.4	78.1
27/05/2024	05/06/2024	S16 (1)	64	235.8	-1.2	81.6
27/05/2024	06/06/2024	S16 (1)	64	236.0	-2.8	89.2
30/05/2024	06/06/2024	S16 (2)	64	234.4	-4.4	97.4
30/05/2024	05/06/2024	S16 (2)	64	232.4	-4.6	98.4
06/06/2024	10/06/2024	S16 (3)	64	233.7	-5.5	103.0
06/06/2024	07/06/2024	S16 (3)	64	234.9	-6.5	109.0
27/05/2024	05/06/2024	S17 (1)	64	231.1	-5.9	105.7

27/05/2024	06/06/2024	S17 (1)	64	234.7	-4.2	95.8
30/05/2024	06/06/2024	S17 (2)	64	229.5	-9.3	127.5
30/05/2024	05/06/2024	S17 (2)	64	230.0	-7.0	112.3
21/06/2024	05/07/2024	S14	64	229.6	-6.8	110.8
21/06/2024	21/06/2024	S14	64	225.0	-6.5	109.2
21/06/2024	05/07/2024	S15	64	228.3	-8.1	119.0
21/06/2024	21/06/2024	S15	64	225.5	-6.0	106.2
24/06/2024	11/07/2024	S6	64.4	228.7	-3.3	91.8
24/06/2024	05/07/2024	S6	64.4	232.0	-4.4	97.7
24/06/2024	11/07/2024	S7	65	225.0	-7.0	113.5
24/06/2024	05/07/2024	S7	65	223.7	-12.7	155.6
31/07/2024	22/10/2024	S9	64.2	222.3	-9.2	126.8
31/07/2024	22/10/2024	S9	64.2	224.0	-7.5	115.5
31/07/2024	29/08/2024	S9	64.2	222.30	-7.3	114.2
31/07/2024	29/08/2024	S9	64.2	224.00	-5.6	104.0
31/07/2024	07/08/2024	S9	64.2	225.6	-5.5	103.4
31/07/2024	22/10/2024	S8	63.2	216.3	-15.2	173.6
31/07/2024	22/10/2024	S8	63.2	216.1	-15.4	175.5
31/07/2024	29/08/2024	S8	63.2	216.30	-13.3	156.3
31/07/2024	29/08/2024	S8	63.2	216.10	-13.5	158.0
31/07/2024	07/08/2024	S8	63.2	218.4	-12.7	151.1
04/07/2024	12/07/2024	S10 (1)	62.6	229.7	-10.5	132.9
04/07/2024	12/07/2024	S10 (1)	62.6	228.9	-11.3	138.8
04/07/2024	11/07/2024	S10 (1)	62.6	223.1	-8.9	121.4
01/08/2024	22/10/2024	S10 (2)	63.6	221.0	-10.5	134.9
01/08/2024	22/10/2024	S10 (2)	63.6	221.8	-9.7	129.1
01/08/2024	29/08/2024	S10 (2)	63.6	221.00	-8.6	121.5
01/08/2024	29/08/2024	S10 (2)	63.6	221.80	-7.8	116.3
01/08/2024	07/08/2024	S10 (2)	63.6	221.0	-10.1	131.8
26/06/2024	05/07/2024	S11 (1)	64.2	225.5	-10.9	139.2
26/06/2024	12/07/2024	S11 (1)	64.2	225.5	-14.7	171.6
26/06/2024	11/07/2024	S11 (1)	64.2	222.2	-9.8	130.8
01/08/2024	22/10/2024	S11 (2)	64.2	218.4	-13.1	157.1
01/08/2024	22/10/2024	S11 (2)	64.2	216.3	-15.2	176.3
01/08/2024	29/08/2024	S11 (2)	64.2	218.40	-11.2	141.5
01/08/2024	29/08/2024	S11 (2)	64.2	216.30	-13.3	158.8
01/08/2024	07/08/2024	S11 (2)	64.2	218.0	-13.1	156.9
02/07/2024	11/07/2024	S12	64.8	236.3	4.3	60.8
02/07/2024	05/07/2024	S12	64.8	237.4	1.0	73.1
02/07/2024	11/07/2024	S13	64	224.8	-7.2	113.0
02/07/2024	05/07/2024	S13	64	227.7	-8.7	123.0

Supplementary Table 5.5 Sample and sampling details

Sample name	Sample type	Associated eruption	Sampling location	Collection date	Eruption date
G20210321-2	Quenched lava	Fagradalsfjall 2021 (Geldingadalir)	Unknown	21/03/2021	21/03/2021
G20210330-2	Glassy crust	Fagradalsfjall 2021 (Geldingadalir)	63.8932; -22.2734	30/03/2021	30/03/2021
G20210404-1	Tephra	Fagradalsfjall 2021 (Geldingadalir)	63.8904; -22.2678	04/04/2021	Unknown
G20210405-1	Quenched lava	Fagradalsfjall 2021 (Geldingadalir)	63.8936; -22.2449	05/04/2021	05/04/2021
G20210412-1	Quenched lava	Fagradalsfjall 2021 (Geldingadalir)	63.8933; -22.2506	12/04/2021	12/04/2021
G20210424-6	Quenched lava	Fagradalsfjall 2021 (Geldingadalir)	63.8849; -22.2631	04/24/2021	Unknown
G20210511-2	Cooled lava	Fagradalsfjall 2021 (Geldingadalir)	63.8806; -22.2598	11/05/2021	06/05/2021
G20210525-1	Quenched lava	Fagradalsfjall 2021 (Geldingadalir)	63.8835; -22.2697	11/05/2021	11/05/2021
G20210616-1	Quenched lava	Fagradalsfjall 2021 (Geldingadalir)	63.8646; -22.2897	06/16/2021	Unknown
G20210707-1	Glassy crust	Fagradalsfjall 2021 (Geldingadalir)	63.8896; -22.2416	07/07/2021	03/07/2021
G20210729-1	Glassy crust	Fagradalsfjall 2021 (Geldingadalir)	63.8971; -22.2359	29/07/2021	28/07/2021
G20210808-1	Glassy crust	Fagradalsfjall 2021 (Geldingadalir)	63.8884; -22.2342	08/08/2021	05/08/2021
G20210817-3	Glassy crust	Fagradalsfjall 2021 (Geldingadalir)	63.8983; -22.2208	17/08//2021	11/08//2021
G20210924-1	Glassy crust	Fagradalsfjall 2021 (Geldingadalir)	63.8860; -22.2785	24/09/2021	17/09/2021
20220812-2	Quenched lava	Fagradalsfjall 2022 (Meradalir)	63.8994; -22.2464	08/12/2022	08/12/2022
20230710-2	Cooled lava	Fagradalsfjall 2023 (Litli Hrútur)	63.912; -22.21	07/10/2023	07/10/2023
20230719-3	Tephra	Fagradalsfjall 2023 (Litli Hrútur)	63.9189; -22.2092	07/19/2023	07/19/2023
20231219-2	Cooled lava	Sundhnúksgígar I (December 2023)	63.8819; -22.3897	19/12/2023	19/12/2023
20231221-3	Cooled lava	Sundhnúksgígar I (December 2023)	63.8816; -22.3729	21/12/2023	21/12/2023
20240103-7	Tephra	Sundhnúksgígar I (December 2023)	63.8793; -22.3882	03/01/2024	19/12/2023
20240105-1	Cooled lava	Sundhnúksgígar I (December 2023)	63.9067; -22.3626	05/01/2024	19/12/2023
20240105-16	Tephra	Sundhnúksgígar I (December 2023)	63.8817; -22.3858	05/01/2024	19-21/12/2023
20240110-109	Cooled lava	Sundhnúksgígar I (December 2023)	63.8817; -22.3738	10/01/2024	19-21/12/2023
20240110-112	Tephra	Sundhnúksgígar I (December 2023)	63.8824; -22.3594	10/01/2024	19-21/12/2023
20240110-114	Cooled lava	Sundhnúksgígar I (December 2023)	63.8892; -22.3597	10/01/2024	19-21/12/2023
20240110-116	Tephra	Sundhnúksgígar I (December 2023)	63.8890; -22.3586	10/01/2024	19-21/12/2023
20240117-12	Tephra	Sundhnúksgígar II (January 2024)	63.8506; -22.4203	17/01/2024	14/01/2024
20240117-13	Cooled lava	Sundhnúksgígar II (January 2024)	63.8493; -22.4213	17/01/2024	14/01/2024
20240117-6	Cooled lava	Sundhnúksgígar II (January 2024)	63.8589; -22.4027	17/01/2024	14/01/2024
20240117-8	Cooled lava	Sundhnúksgígar II (January 2024)	63.8559; -22.4077	17/01/2024	14/01/2024
20240209-208	Tephra	Sundhnúksgígar III (February 2024)	63.8794; -22.3872	09/02/2024	08/02/2024
20240209-210	Tephra	Sundhnúksgígar III (February 2024)	63.8805; -22.3872	09/02/2024	08/02/2024
20240208-2	Quenched lava	Sundhnúksgígar III (February 2024)	63.8738; -22.3732	08/02/2024	08/02/2024
20240209-2	Cooled lava	Sundhnúksgígar III (February 2024)	63.8894; -22.4355	09/02/2024	08/02/2024

6 Conclusion and perspectives

The approach presented in this thesis allowed to conduct a rigorous investigation about the lava degassing process as a whole, not only focusing on the characterisation of the gas composition, but also the mechanisms behind the gas formation and escape in the context of lava emplacement, cooling and solidification. The research highlights the value of examining lava degassing from multiple angles, not only due to its potential impacts but also as a tool for understanding broader geological processes, such as silicate melt differentiation and degassing under various conditions. Nevertheless, several aspects regarding lava differentiation and degassing were identified as crucial but remain to be investigated in more depth. In this final chapter are summarised the main findings of this research, along with its limitations and suggestions for future work, first discussing individual chapters and then the thesis as a whole.

6.1 Characterising the secondary gas emissions and associated hazard

- In Chapter 3 was presented the results of a gas sampling campaign at Fagradalsfjall, with particular attention put on the degassing of the crystallising lava field. The measured gas composition from the crystallising lava along with an eruptive vent and an extinct crater enabled the characterisation and comparison of the different gas types. Such comparison revealed the halogen-rich nature of the post-eruptive gas, particularly from the crystallising lava, with halogen/S mass ratios exceeding 10. The comparison of the different gas phases also revealed the compositional variability between gases emitted at the syn-eruptive lava (investigated by Wainman et al. 2024), crystallising lava and extinct crater.

- This shift in major volatile relative proportions is accompanied by large variation in trace element composition of the gas, most likely associated with volatility changes. Such volatility change is readily explained by the speciation of the trace volatile elements as the halogen-rich secondary gas is enriched in the elements degassing as halide, whereas those degassing as sulphide or free elements are depleted. Comparing these trends to what observed Wainman et al. (2024) in the gas emitted by the syn-eruptive lava reveals a progressive differentiation of the emitted gas by Rayleigh distillation. The initial secondary gas from the syn-eruptive lava displays a moderate increase in halogen proportion (with respect to the primary gas) which is associated with large change in trace volatile element composition. The differentiation continues until the final gas is liberated from the crystallising lava, exhibiting a virtual absence of sulphur and sulphur-affine elements, such as Te, correlated with a particular enrichment in elements forming chlorine species at cooler temperature (e.g., Zn, Sn).

- The gas differentiation results in the emissions of a gas phase distinct from the well-known primary gas. Additionally, this degassing is characterised by its long-term and more localised nature. The potential hazard associated with this degassing was

approached by constraining the trace volatile fluxes, particularly heavy metal, released from the crystallising lava. Using estimates from Thordarson et al. (1996) on halogen release from Laki crystallising lava, each elements flux was calculated revealing important emissions from the crystallising lava for a few elements, Zn being of particular concern.

The findings associated with Chapter 3 thus underscore the interest of studying the crystallising lava secondary gas composition. Nevertheless, many aspects remain to be characterised about the secondary degassing and its consequences.

First, the use of filter packs for gas sampling circumscribes our knowledge about major volatile composition to sulphur, chlorine and fluorine. While using S/halogen ratios is common in volcanic gas studies, it could hinder large changes in the proportion of other major volatiles. Additionally, the oxidation state of the gas cannot be studied with such tool. This information is crucial for understanding the evolving volatility of some trace volatile elements. Sampling the whole gas phase using Giggenbach bottles in parallel to using filter pack would permit further characterisation of the secondary gas in terms of all major volatiles. However, such sampling is challenging because of the air contamination of the gas, largely diluted before reaching the surface. If undiluted gas is successfully sampled with Giggenbach bottles, the dilution factor for each gas sample could be calculated. This would allow to compare undiluted gas composition rather than normalised by one element and could permit estimation of the partition coefficient between the lava and the post-eruptive lava gas.

Another aspect to consider to exhaustively characterise the secondary gas emissions is the quick precipitation of part of the gas, as visible around each degassing crack (Fig. 3.2a) which could result in depletion in the collected post-eruptive lava gas. To have a better understanding of the overall degassing and precipitation processes along with its impacts, studying the precipitates on crystallising lava fields would thus be of interest. Given the nature of the deposits, their analysis would require techniques distinct from routine analysis of rocks, with would involve specific and preparation and analytical methods.

Finally, in light of the estimated flux from the crystallising lava degassing calculated in Chapter 3, it would be of interest to consider and study better this gas phase. Particularly, the emissions of a few elements could be of concern when degassing takes place from a source richer in trace elements and halogens, i.e., from subduction volcanism. Though subduction volcanoes tend to be more explosive, significant effusive activity also exist giving birth to large degassing lava bodies. Emissions of chlorine affine elements at low temperature would thus be boosted both by their higher concentration in the silicate melt and the higher concentration of Cl in the case which could increase even more their volatility. Investigating the trace element fluxes from a degassing lava field associated with a subduction zone volcano thus appears crucial to known whether significant hazard is posed to the surrounding population and ecosystem. The range of which such hazard could exist could be assessed by investigating the transport and environmental lifetime of these elements.

6.2 Understanding the process of segregation formation and its role in lava degassing

- The research regarding the segregation material collected on the Reykjanes peninsula, from a lava flow at Hekla and from the Eldgjá lava field were presented in chapter 4. All the segregations showed chemical composition distinct from the surrounding host lava, in terms of major elements, trace elements and volatile elements (H, S and F).

- As was previously identified by several studies, whose results are summed up in Chapter 1, the segregation evolved composition is readily explained by the fact that it originates from fractional crystallisation of the host lava. Fractional crystallisation also explains the overall enrichment in volatiles, generally behaving as incompatible elements. Variability in composition between segregations was attributed to continuous crystallisation within the segregation melt, giving birth to progressively more evolved segregations. To explain the composition of a vesicle cylinder, it is however necessary to account for host lava macrocryst contamination, consistent with the presence of large primitive crystal observed in this segregation. All these observations allowed the develop of a segregation formation model based on the gas filter pressing model from Anderson et al. (1984) adapted to our current understanding of the segregation system.

- The role of the gas phase in segregation formation was investigated using the volatile elements. The volatile trace elements were found to be enriched in most segregation as other incompatible elements, with the notable exception of Cd and Zn, identified as significantly partitioning in at least one crystallising mineral. A few segregations showed higher enrichment in volatile metals than all non-volatile incompatible elements. Such enrichment, associated with higher water content was interpreted as originating from the gas phase. This gas, which initiated the residual melt segregation, would thus occasionally (partially) condensate to give birth to volatile trace elements enriched segregations. The excess of volatile elements in these segregations was used as an insight into the composition of the gas circulating in the emplacing lava and similarities are found with the gas sampled at the surface.

Chapter 4 thus highlighted both the large heterogeneity in segregation compositional features and demonstrated the particular behaviour of elements known to be volatile. Such findings translate both that the segregation formation is complex and that it is closely tied to lava degassing. Because of the high level of segregation compositional heterogeneity, our interpretations were however hindered by the limited number of samples and lava field investigated.

In order to assess in detail all of the processes taking place during segregation formation and their prevalence, a more complete dataset is required. Sampling of numerous segregations of different types (VC, HVS, MV) from the same lava could permit to estimate statistically the frequency of different phenomenon taking place (host lava crystal assimilation, gas condensation, etc.). A sampling of numerous MV could for example highlight if their composition can be related to their feature on the field (thickness of the segregation pod, size of the overlying void, connexion to a fracture network, etc.).

On the other hand, given the role of the major volatiles in the gas phase formation and behaviour, measuring their concentrations in the lava and segregations in a precise, rigorous and systematic manner should give additional insight on segregation formation. Precise

quantification of major volatiles concentrations could be obtained by X-ray fluorescence, ion chromatography, ICP-MS, ICP-OES, radiochemical, instrumental and/or prompt-gamma neutron activation analysis depending on the element. Sulphur low concentrations, particularly in Reykjanes lavas, could however complexify its precise quantification. The loss of ignition could be measured and used to assess the total volume concentration of the segregations and thus identify volatile redissolution or precipitation. Finally, our understanding of volatile behaviour would greatly benefit the measurements of volatiles concentrations in the different phases of the lava and segregation, using for example an electron microprobe for sulphur and chlorine.

6.3 Using Ion Selective Electrode to characterise halogen heterogeneity in the Reykjanes lavas

- The repeated preparation of rock standards along with newly erupted lavas presented in Chapter 5 allowed to assess the potential and limitations associated with halogen measurements in lavas using ion selective electrode. To allow synchronous Cl and F quantification, constrains associated with both halogens must be considered. Overall, satisfying results could be obtained for fluorine measurements, though the leaching conditions must be conducted rigorously to ensure complete F leaching. Challenges associate with Cl are more numerous, both associated with low sensitivity of the Cl selective electrode and matrix effect. It was thus necessary to build a calibration curve based on the rock standard instead of artificial standards, leading to larger uncertainties.

- The obtained F and Cl concentrations in the 2021-2024 volcanic products from Reykjanes were both correlated to the incompatible element concentrations. Once the effect of crystallisation was removed, both Cl and F concentrations were still variable, but not in the same manner. Most of the halogen concentration variability can be explained by mixing of multiple (at least three) magmas, which have distinct Cl and F concentrations (normalised to incompatible oxides and also distinct Cl/F). The lack of differences between the products collected at Fagradalsfjall and Sundhnúksgígar (beyond FC effect) suggest magmas with similar halogen characteristics are feeding both eruptions.

- Regardless of the fractional crystallisation effect and variable mantle source, it seems that both halogens displayed significant variations. Such variability could be related to degassing. However, samples with specific Cl or F concentrations (either high or low) are distinct, which makes less likely that their depletion is associated with degassing. Furthermore, the sample nature (tephra, lava and glassy crust) did not display significant correlation with element halogen concentrations, which could be expected. No lava degassing could thus be resolved using our sample set.

The results presented in Chapter 5 indicate that simultaneous Cl and F measurements by ISE is possible. However, to obtain precise data that could allow resolution of small change in Cl or F concentration, the use of ISE requires rigorous and constant sample preparation and leaching. In particular, the use of Cl electrode for low concentration rocks and thus leachate is very sensitive to multiple parameters and the quantification using the method presented here is approximative. Separating Cl from the matrix using diffusion cells or Cl^- selective resins could help quantifying chlorine concentration with more precision. Alternatively, the

conception and use of a buffer adapted to Cl which would he mixed with both standard solution and leachates (as was done for F) could improve Cl quantification.

To investigate in detail the volatile concentrations in volcanic products and the associated degassing, a sampling campaign targeting the sample of interest for degassing would be necessary. Bias in the sampling is very likely since all lava collected correspond (for accessibility reasons) to the superficial part of the lava flow, which has most likely undergone distinct degassing from the lava core, with no effect of the segregation formation. Combining targeted sampling to more precise halogen measurements should allow to resolve the small-scale Cl and F variability that is expected to be associated with syn- and post-eruptive lava degassing.

The ideal manner to use halogens to study both magmatic processes and degassing would be to compare their features to other volatile elements. In particular, studying water, carbon dioxide and sulphur would give extensive information on pre-eruptive and syn-eruptive crater degassing, permitting better interpretation of the halogen results. Additionally, the mantle source heterogeneity could also apply to these volatiles and might affect major volatile ratios such as S/Cl and S/F. Including other volatiles would also permit a better characterisation of the halogen behaviour by comparing it to better understood elements. Having such data, along with the major and trace elements concentrations would permit to distinguish better the effect of the magma source, fractional crystallisation, assimilation and degassing.

6.4 Overall thesis conclusions

Throughout the thesis, a comprehensive picture of the basalt lava degassing was presented along with the associated processes. Syn- and post-eruptive gas composition analyses from the Fagradalsfjall eruptions (Reykjanes) revealed the diversity of degassing associated with basaltic eruptions (Chapter 3). The difference in gas composition was explained by a Rayleigh distillation process and variable trace element volatility depending on gas composition and temperature. The syn-eruptive crater and post-eruptive lava do, however, not only differ in terms of composition but also in origin and formation conditions. Gas emitted during eruptions is mostly formed by exsolution following decompression of the ascending magma which reduce element solubility. The crystallising lava gas on the other hand displays similar compositions to segregation veins (Chapter 4, Fig. 4.8), suggest that its connection with segregation developments. As such, the gas formation should be related to fractional crystallisation and volatile accumulation/saturation in the residual melt.

The distinct mechanism behind gas formation (resulting from decompression or fractional crystallisation) could have significant consequences. If gas exsolution (and escape) takes place after crystallisation of several minerals, some elements would be fractioned in the minerals before they could enter the gas phase. Though volatile elements are generally viewed as incompatible, this is not always the case, and such process would reduce emissions of a few volatile metals partitioning in minerals such as Cd, In and Zn (Chapter 4). As an example, extensive crystallisation iron oxide (rich in Zn), before melt segregation could strongly limit the liberation of Zn, identified as one of potential hazard in Chapter 3.

Once the gas is formed (after or not fractional crystallisation), element partitioning depends on the gas features. The study of secondary gas emissions from Fagradalsfjall highlighted the role of both chlorine and fluorine (particularly present in the secondary gas) in the liberation of multiple elements (Chapter 3). It was thus of interest to investigate to what extend the halogen concentration in the silicate melt vary and the origin of such variation. As highlighted in Chapter 5, both F and Cl concentrations in Reykjanes volcanic products largely dependent on fractional crystallisation, highlighting their incompatibility in early crystallising minerals (plagioclases, olivine and clinopyroxene). Additionally, a large influence of magma source contribution was found to affect the halogen (and particularly fluorine) content. This would ultimately impact the relative proportion of major volatiles in the emitted lava and gas, affecting the volatility of numerous trace elements. In contrast, the comparison between Reykjanes tephra and lava halogen concentrations did not permit to identify any halogen loss through syn-eruptive lava degassing, unlike what was observed at Laki by Thordarson et al. (1996).

Though no impact of lava degassing could be identified in the investigation conducted in Chapter 5, this does not mean that halogen loss is negligeable. As stated previously, the lack of samples coming from the core of the lava flow, which takes a long time to crystallise after the lava emplacement (and is thus currently not available from the recent Reykjanes eruptions), hinders any post-eruptive lava degassing, associated with segregation formation discussed in Chapter 4. Instead, our comparison of tephra and lava halogen concentrations only give information about syn-eruptive lava degassing. As lavas from Reykjanes eruptions flowed much lower distance than that of Laki, a lesser syn-eruptive lava degassing component is expected. Thus, it is not surprising that the halogen loss through syn-eruptive degassing, which resulted in significant lower halogens content in the lava with respect to tephra at Laki, could not be observed from Fagradalsfjall and Sundhnúksgígar.

Beyond perspectives associated with individual chapters discussed above, the thesis results rose several questions and drew perspectives of future work that could enhance our understanding of lava degassing and its consequences. First, though we presented arguments in favour of a link between the segregation process and post-eruptive lava degassing, such relationship remains to be confirmed. As segregation process is associated with extensive crystallisation before gas formation, one manner to verify our hypothesis would be to confirm that gas formed from a residual melt. Identifying how crystallisation affect the composition of the residual melt and of the exsolved gas could allow to track the origin of such gas. Such crystallisation effect (or absence of crystallisation effect) may perhaps be tracked by investigating the isotopic composition of volatile elements (which partition differently in minerals, melt and gas) in the lava gas.

Several aspects of the lava degassing described in this thesis were shown dependent on magma/lava composition. Basaltic magmas of distinct composition could be characterised by distinct crystallising minerals (such as iron oxide as visible for Eldgjá), and thus different element partitioning during the segregation process. Additionally depending on the volcanic system, the relative proportion of major volatiles vary, and Cl-rich subduction volcanoes could emit secondary gas even richer in elements degassing as chloride. Thus, investigating the post-eruptive lava degassing from other volcanic systems would be of great interest. Such study would both help to constrain better all the parameters involved in post-eruptive lava

degassing and assess if increased secondary degassing hazard could be associated with particular magma features.

Overall, this thesis underscores the importance of examining the origin, characteristics, and consequences of lava degassing to comprehensively understand volcanic degassing from effusive basaltic eruptions and flood lavas. The unique processes involved in post-eruptive lava degassing, along with its compositional features distinct from primary degassing are worth further investigation. Additionally, the role of halogens as ligands in the release of certain volatile metals, along with their varying concentrations in magma sources, emphasises the need to consider these elements in studies of volcanic degassing. If potential hazards associated with lava degassing are to be studied, all the aspects raised above are to be taken into consideration.

References

Adam J, Green T (2006) Trace element partitioning between mica- and amphibole-bearing garnet lherzolite and hydrous basanitic melt: 1. Experimental results and the investigation of controls on partitioning behaviour. Contrib Mineral Petrol 152:1–17. https://doi.org/10.1007/s00410-006-0085-4

Africano F, Van Rompaey G, Bernard A, Le Guern F (2002) Deposition of trace elements from high temperature gases of Satsuma-Iwojima volcano. Earth Planet Sp 54:275–286. https://doi.org/10.1186/BF03353027

Aiuppa A (2009) Degassing of halogens from basaltic volcanism: Insights from volcanic gas observations. Chemical Geology 263:99–109. https://doi.org/10.1016/j.chemgeo.2008.08.022

Aiuppa A, Allard P, D'Alessandro W, et al (2000) Mobility and fluxes of major, minor and trace metals during basalt weathering and groundwater transport at Mt. Etna volcano (Sicily). Geochimica et Cosmochimica Acta 64:1827–1841. https://doi.org/10.1016/S0016-7037(00)00345-8

Aiuppa A, Baker DR, Webster JD (2009) Halogens in volcanic systems. Chemical Geology 263:1–18. https://doi.org/10.1016/j.chemgeo.2008.10.005

Aiuppa A, Dongarrà G, Valenza M, et al (2003) Degassing of trace volatile metals during the 2001 eruption of Etna. Washington DC American Geophysical Union Geophysical Monograph Series 139:41–54. https://doi.org/10.1029/139GM03

Aiuppa A, Federico C, Paonita A, et al (2002) S, Cl and F degassing as an indicator of volcanic dynamics: The 2001 eruption of Mount Etna. Geophysical Research Letters 29:54–1. https://doi.org/10.1029/2002GL015032

Allard P, Aiuppa A, Bani P, et al (2016) Prodigious emission rates and magma degassing budget of major, trace and radioactive volatile species from Ambrym basaltic volcano, Vanuatu island Arc. Journal of Volcanology and Geothermal Research 322:119–143. https://doi.org/10.1016/j.jvolgeores.2015.10.004

Allard P, Carbonnelle J, Dajlevic D, et al (1991) Eruptive and diffuse emissions of CO2 from Mount Etna. Nature 351:387–391. https://doi.org/10.1038/351387a0

Allen AG, Baxter PJ, Ottley CJ (2000) Gas and particle emissions from Soufrière Hills Volcano, Montserrat, West Indies: characterization and health hazard assessment. Bull Volcanol 62:8–19. https://doi.org/10.1007/s004450050287

Anderson AT, Swihart GH, Artioli G, Geiger CA (1984) Segregation Vesicles, Gas Filter-Pressing, and Igneous Differentiation. The Journal of Geology 92:55–72. https://doi.org/10.1086/628834

Ármannsson H, Benjamínsson J, Jeffrey AWA (1989) Gas changes in the Krafla geothermal system, Iceland. Chemical Geology 76:175–196. https://doi.org/10.1016/0009-2541(89)90089-2

Armstrong JT (1991) Quantitative Elemental Analysis of Individual Microparticles with Electron Beam Instruments. In: Heinrich KFJ, Newbury DE (eds) Electron Probe Quantitation. Springer US, Boston, MA, pp 261–315

Aruscavage PJ, Campbell EY (1983) An ion-selective electrode method for determination of chlorine in geological materials. Talanta 30:745–749. https://doi.org/10.1016/0039-9140(83)80171-4

Bali E, Hartley ME, Halldórsson SA, et al (2018) Melt inclusion constraints on volatile systematics and degassing history of the 2014–2015 Holuhraun eruption, Iceland. Contrib Mineral Petrol 173:9. https://doi.org/10.1007/s00410-017-1434-1

Barsotti S, Parks MM, Pfeffer MA, et al (2023) The eruption in Fagradalsfjall (2021, Iceland): how the operational monitoring and the volcanic hazard assessment contributed to its safe access. Nat Hazards 116:3063–3092. https://doi.org/10.1007/s11069-022-05798-7

Bindeman I, Gurenko A, Sigmarsson O, Chaussidon M (2008) Oxygen isotope heterogeneity and disequilibria of olivine crystals in large volume Holocene basalts from Iceland: Evidence for magmatic digestion and erosion of Pleistocene hyaloclastites. Geochimica et Cosmochimica Acta 72:4397–4420. https://doi.org/10.1016/j.gca.2008.06.010

Bindeman IN, Davis AM (2000) Trace element partitioning between plagioclase and melt: investigation of dopant influence on partition behavior. Geochimica et Cosmochimica Acta 64:2863–2878. https://doi.org/10.1016/S0016-7037(00)00389-6

Bindeman IN, Davis AM, Drake MJ (1998) Ion Microprobe Study of Plagioclase-Basalt Partition Experiments at Natural Concentration Levels of Trace Elements. Geochimica et Cosmochimica Acta 62:1175–1193. https://doi.org/10.1016/S0016-7037(98)00047-7

Bodkin JB (1977) Determination of fluorine in silicates by use of an ion-selective electrode following fusion with lithium metaborate. Analyst 102:409–413. https://doi.org/10.1039/AN9770200409

Bougault H, Hekinian R (1974) Rift Valley in the Atlantic Ocean near 36°50'N: petrology and geochemistry of basaltic rocks. Earth and Planetary Science Letters 24:249–261. https://doi.org/10.1016/0012-821X(74)90103-4

Burton MR, Sawyer GM, Granieri D (2013) Deep Carbon Emissions from Volcanoes. Reviews in Mineralogy and Geochemistry 75:323–354. https://doi.org/10.2138/rmg.2013.75.11

Caracciolo A, Bali E, Halldórsson SA, et al (2023) Magma plumbing architectures and timescales of magmatic processes during historical magmatism on the Reykjanes Peninsula, Iceland. Earth and Planetary Science Letters 621:118378. https://doi.org/10.1016/j.epsl.2023.118378

Caracciolo A, Bali E, Ranta E, et al (2024) Medieval and recent SO2 budgets in the Reykjanes Peninsula: implication for future hazard. Geochemical Perspectives Letters 30:20–27. https://doi.org/10.7185/geochemlet.241710.31223/x5tx05

Caroff M, Ambrics C, Maury RenéC, Cotten J (1997) From alkali basalt to phonolite in hand-size samples: vapor-differentiation effects in the Bouzentès lava flow (Cantal, France). Journal of Volcanology and Geothermal Research 79:47–61. https://doi.org/10.1016/S0377-0273(97)00023-1

Caroff M, Maury RC, Cotten J, Clément J-P (2000) Segregation structures in vapor-differentiated basaltic flows. Bull Volcanol 62:171–187. https://doi.org/10.1007/s004450000077

Carroll MR, Webster JD (2018) Chapter 7. SOLUBILITIES OF SULFUR, NOBLE GASES, NITROGEN, CHLORINE, AND FLUORINE IN MAGMAS. In: Chapter 7. SOLUBILITIES OF SULFUR, NOBLE GASES, NITROGEN, CHLORINE, AND FLUORINE IN MAGMAS. De Gruyter, pp 231–280

Carroll MR, Webster JD (1994) Chapter 7. Solubilities of sulfur, noble gases, nitrogen, chlorine, and fluorine in magmas. In: Carroll MR, Holloway JR (eds) Volatiles in Magmas. pp 231–280

Cashman KV, Mangan MT, Newman S (1994) Surface degassing and modifications to vesicle size distributions in active basalt flows. Journal of Volcanology and Geothermal Research 61:45–68. https://doi.org/10.1016/0377-0273(94)00015-8

Chekol TA, Kobayashi K, Yokoyama T, et al (2011) Timescales of magma differentiation from basalt to andesite beneath Hekla Volcano, Iceland: Constraints from U-series disequilibria in lavas from the last quarter-millennium flows. Geochimica et Cosmochimica Acta 75:256–283. https://doi.org/10.1016/j.gca.2010.10.001

Cole-Dai J (2010) Volcanoes and climate. WIREs Climate Change 1:824–839. https://doi.org/10.1002/wcc.76

Costa A, Blake S, Self S (2006) Segregation processes in vesiculating crystallizing magmas. Journal of Volcanology and Geothermal Research 153:287–300. https://doi.org/10.1016/j.jvolgeores.2005.12.006

Crowe BM, Finnegan DL, Zoller WH, Boynton WV (1987) Trace element geochemistry of volcanic gases and particles from 1983–1984 eruptive episodes of Kilauea Volcano. Journal of Geophysical Research: Solid Earth 92:13708–13714. https://doi.org/10.1029/JB092iB13p13708

Day AL, Shepherd ES (1913) Water and volcanic activity. GSA Bulletin 24:573–606. https://doi.org/10.1130/GSAB-24-573

De Rita D, Cremisini C, Cinnirella A, Spaziani F (2012) Fluorine in the rocks and sediments of volcanic areas in central Italy: total content, enrichment and leaching processes and a hypothesis on the vulnerability of the related aquifers. Environ Monit Assess 184:5781–5796. https://doi.org/10.1007/s10661-011-2381-3

Delmelle P, Maters EC, Calkins JA, et al (2021) Eruptive style controls the formation of silicon hexafluoride salts on volcanic ash: The case of the 2010 eruption of Eyjafjallajökull volcano, Iceland. Chemical Geology 579:120327. https://doi.org/10.1016/j.chemgeo.2021.120327

Dixon J, Stolper E, Holloway J (1995) An Experimental Study of Water and Carbon Dioxide Solubilities in Mid-Ocean Ridge Basaltic Liquids. Part I: Calibration and Solubility Models. Journal of Petrology. https://doi.org/10.1093/oxfordjournals.petrology.a037267

Edmonds M, Gerlach TM (2007) Vapor segregation and loss in basaltic melts. Geology 35:751–754. https://doi.org/10.1130/G23464A.1

Edmonds M, Gerlach TM, Herd RA (2009) Halogen degassing during ascent and eruption of water-poor basaltic magma. Chemical Geology 263:122–130. https://doi.org/10.1016/j.chemgeo.2008.09.022

Edmonds M, Mason E, Hogg O (2022) Volcanic Outgassing of Volatile Trace Metals. Annual Review of Earth and Planetary Sciences 50:79–98. https://doi.org/10.1146/annurev-earth-070921-062047

Edmonds M, Mather TA, Liu EJ (2018) A distinct metal fingerprint in arc volcanic emissions. Nature Geosci 11:790–794. https://doi.org/10.1038/s41561-018-0214-5

Edmonds M, Wallace PJ (2017) Volatiles and Exsolved Vapor in Volcanic Systems. Elements 13:29–34. https://doi.org/10.2113/gselements.13.1.29

Edmonds M, Woods AW (2018) Exsolved volatiles in magma reservoirs. Journal of Volcanology and Geothermal Research 368:13–30. https://doi.org/10.1016/j.jvolgeores.2018.10.018

Elderfield H, Greaves MJ (1981) Strontium isotope geochemistry of Icelandic geothermal systems and implications for sea water chemistry. Geochimica et Cosmochimica Acta 45:2201–2212. https://doi.org/10.1016/0016-7037(81)90072-7

Elsheimer H n. (1987) Application of an Ion-Selective Electrode Method to the Determination of Chloride in 41 International Geochemical Reference Materials. Geostandards Newsletter 11:115–122. https://doi.org/10.1111/j.1751-908X.1987.tb00014.x

Fei J, Zhou J (2006) The Possible Climatic Impact in China of Iceland's Eldgjá Eruption Inferred from Historical Sources. Climatic Change 76:443–457. https://doi.org/10.1007/s10584-005-9012-3

Fiantis D, Ginting F, Nelson M, Minasny B (2019) Volcanic Ash, Insecurity for the People but Securing Fertile Soil for the Future. Sustainability 11:3072

Finnegan DL (1984) Chemistry of trace elements and acidic species in fumarolic emissions. Univ. of Maryland,College Park, MD

Finnegan DL, Kotra JP, Hermann DM, Zoller WH (1989) The use of7LiOH-impregnated filters for the collection of acidic gases and analysis by instrumental neutron activation analysis. Bull Volcanol 51:83–87. https://doi.org/10.1007/BF01081977

Fischer TP (2008) Fluxes of volatiles (H_2O, CO_2, N_2, Cl, F) from arc volcanoes. Geochemical Journal 42:21–38. https://doi.org/10.2343/geochemj.42.21

Fischer TP, Mandon CL, Nowicki S, et al (2024) CO2 emissions during the 2023 Litli Hrútur eruption in Reykjanes, Iceland: δ13C tracks magma degassing. Bull Volcanol 86:60. https://doi.org/10.1007/s00445-024-01751-7

Fowler AC, Rust AC, Vynnycky M (2015) The formation of vesicular cylinders in pahoehoe lava flows. Geophysical & Astrophysical Fluid Dynamics 109:39–61. https://doi.org/10.1080/03091929.2014.955799

Gauthier P-J, Le Cloarec M-F (1998) Variability of alkali and heavy metal fluxes released by Mt. Etna volcano, Sicily, between 1991 and 1995. Journal of Volcanology and Geothermal Research 81:311–326. https://doi.org/10.1016/S0377-0273(98)00002-X

Gauthier P-J, Sigmarsson O, Gouhier M, et al (2016) Elevated gas flux and trace metal degassing from the 2014–2015 fissure eruption at the Bárðarbunga volcanic system, Iceland. Journal of Geophysical Research: Solid Earth 121:1610–1630. https://doi.org/10.1002/2015JB012111

Geist D, Harpp K, Oswald P, et al (2021) Hekla Revisited: Fractionation of a Magma Body at Historical Timescales. Journal of Petrology 62:egab001. https://doi.org/10.1093/petrology/egab001

Gerlach TM (2004) Volcanic sources of tropospheric ozone-depleting trace gases. Geochemistry, Geophysics, Geosystems 5:. https://doi.org/10.1029/2004GC000747

Gerlach TM (1980) Evaluaion of volcanic gas analyses from Kilauea Volcano. J Volcanol Geotherm Res; (Netherlands) 7:3/4: https://doi.org/10.1016/0377-0273(80)90034-7

Gerlach TM (1986) Exsolution of H2O, CO2, and S during eruptive episodes at Kilauea Volcano, Hawaii. Journal of Geophysical Research: Solid Earth 91:12177–12185. https://doi.org/10.1029/JB091iB12p12177

Giggenbach WF (1975) A simple method for the collection and analysis of volcanic gas samples. Bull Volcanol 39:132–145. https://doi.org/10.1007/BF02596953

Giggenbach WF (1989) Collection and Analysis of Geothermal and Volcanic Water and Gas Discharges. New Zealand 81:

Giggenbach WF (1996) Chemical Composition of Volcanic Gases. In: Scarpa R, Tilling RI (eds) Monitoring and Mitigation of Volcano Hazards. Springer, Berlin, Heidelberg, pp 221–256

Glauser J, Hermann P, Mitchell SA (2018) Handbook of Pre-Modern Nordic Memory Studies: Interdisciplinary Approaches. Walter de Gruyter GmbH & Co KG

Goff FE (1996) Vesicle cylinders in vapor-differentiated basalt flows. Journal of Volcanology and Geothermal Research 71:167–185. https://doi.org/10.1016/0377-0273(95)00073-9

Goff FE (1977) Vesicle cylinders in vapor-differentiated basalt flows. University of California, Santa Cruz

Greenland LP (1984) Gas composition of the January 1983 eruption of Kilauea Volcano, Hawaii. Geochimica et Cosmochimica Acta 48:193–195. https://doi.org/10.1016/0016-7037(84)90361-2

Greenland LP, Rose WI, Stokes JB (1985) An estimate of gas emissions and magmatic gas content from Kilauea volcano. Geochimica et Cosmochimica Acta 49:125–129. https://doi.org/10.1016/0016-7037(85)90196-6

Greenough JD, Lee C-Y, Fryer BJ (1999) Evidence for volatile-influenced differentiation in a layered alkali basalt flow, Penghu Islands, Taiwan. Bull Volcanol 60:412–424. https://doi.org/10.1007/s004450050241

Gudmundsson A (2000) Dynamics of Volcanic Systems in Iceland: Example of Tectonism and Volcanism at Juxtaposed Hot Spot and Mid-Ocean Ridge Systems. Annual Review of Earth and Planetary Sciences 28:107–140. https://doi.org/10.1146/annurev.earth.28.1.107

Halldórsson SA, Barnes JD, Stefánsson A, et al (2016) Subducted lithosphere controls halogen enrichments in the Iceland mantle plume source. Geology 44:679–682. https://doi.org/10.1130/G37924.1

Halldórsson SA, Marshall EW, Caracciolo A, et al (2022) Rapid shifting of a deep magmatic source at Fagradalsfjall volcano, Iceland. Nature 609:529–534. https://doi.org/10.1038/s41586-022-04981-x

Hart SR, Schilling J-G, Powell JL (1973) Basalts from Iceland and Along the Reykjanes Ridge: Sr Isotope Geochemistry. Nature Physical Science 246:104–107. https://doi.org/10.1038/physci246104a0

Hartley ME, Thordarson T (2009) Melt segregations in a Columbia River Basalt lava flow: A possible mechanism for the formation of highly evolved mafic magmas. Lithos 112:434–446. https://doi.org/10.1016/j.lithos.2009.04.003

Haynes SJ, Clark AH (1972) A rapid method for the determination of chlorine in silicate rocks using ion-selective electrodes. Economic Geology 67:378–382. https://doi.org/10.2113/gsecongeo.67.3.378

Haynes WM, Lide DR, Bruno TJ (eds) (2016) Physical Constants of Organic Compounds. In: CRC Handbook of Chemistry and Physics, 97th edn. CRC Press

Helz R (1987) Differentiation behaviour of Kilauea Iki lava lake, Kilauea volcano, Hawaii: an overview of past and current work. Magmatic Processes: Physicochemical Principles 1:241–258

Helz RT (1980) Crystallization history of Kilauea Iki lava lake as seen in drill core recovered in 1967–1979. Bull Volcanol 43:675–701. https://doi.org/10.1007/BF02600365

Helz RT, KIRSCHENBAUM H, MARINENKO JW (1989) Diapiric transfer of melt in Kilauea Iki lava lake, Hawaii: A quick, efficient process of igneous differentiation. GSA Bulletin 101:578–594. https://doi.org/10.1130/0016-7606(1989)101<0578:DTOMIK>2.3.CO;2

Helz RT, Wright TL (1983) Drilling report and core logs for the 1981 drilling of Kilauea Iki lava lake, Kilauea volcano, Hawaii, with comparative notes on earlier (1967-1979) drilling experiences. Geological Survey, Reston, VA (USA)

Hinkley TK, Lamothe PJ, Wilson SA, et al (1999) Metal emissions from Kilauea, and a suggested revision of the estimated worldwide metal output by quiescent degassing of volcanoes. Earth and Planetary Science Letters 170:315–325. https://doi.org/10.1016/S0012-821X(99)00103-X

Hon K, KAUAHIKAUA J, DENLINGER R, MACKAY K (1994) Emplacement and inflation of pahoehoe sheet flows: Observations and measurements of active lava flows on Kilauea Volcano, Hawaii. GSA Bulletin 106:351–370. https://doi.org/10.1130/0016-7606(1994)106<0351:EAIOPS>2.3.CO;2

Iacono-Marziano G, Morizet Y, Le Trong E, Gaillard F (2012) New experimental data and semi-empirical parameterization of H2O–CO2 solubility in mafic melts. Geochimica et Cosmochimica Acta 97:1–23. https://doi.org/10.1016/j.gca.2012.08.035

Ilyinskaya E, Martin RS, Oppenheimer C (2012) Aerosol formation in basaltic lava fountaining: Eyjafjallajökull volcano, Iceland. Journal of Geophysical Research: Atmospheres 117:. https://doi.org/10.1029/2011JD016811

Ilyinskaya E, Mason E, Wieser PE, et al (2021) Rapid metal pollutant deposition from the volcanic plume of Kīlauea, Hawai'i. Commun Earth Environ 2:1–15. https://doi.org/10.1038/s43247-021-00146-2

Ilyinskaya E, Schmidt A, Mather TA, et al (2017) Understanding the environmental impacts of large fissure eruptions: Aerosol and gas emissions from the 2014–2015 Holuhraun eruption (Iceland). Earth and Planetary Science Letters 472:309–322. https://doi.org/10.1016/j.epsl.2017.05.025

Ingram BL (1970) Determination of fluoride in silicate rocks without separation of aluminum using a specific ion electrode. Analytical Chemistry 42:1825–1827. https://doi.org/10.1021/ac50160a067

Jakobsson SP (1979) Petrology of recent basalts of the eastern volcanic zone, Iceland. Petrology of recent basalts of the eastern volcanic zone, Iceland

Jakobsson SP, Jónsson J, Shido F (1978) Petrology of the Western Reykjanes Peninsula, Iceland. Journal of Petrology 19:669–705. https://doi.org/10.1093/petrology/19.4.669

Jochum KP, Nohl U, Herwig K, et al (2005) GeoReM: A New Geochemical Database for Reference Materials and Isotopic Standards. Geostandards and Geoanalytical Research 29:333–338. https://doi.org/10.1111/j.1751-908X.2005.tb00904.x

Johnson A, Canil D (2011) The degassing behavior of Au, Tl, As, Pb, Re, Cd and Bi from silicate liquids: Experiments and applications. Geochimica et Cosmochimica Acta 75:1773–1784. https://doi.org/10.1016/j.gca.2010.12.023

Júlíusdóttir R, Óladóttir BA, Gudmundsson MT, et al (2024) Nýtt gosskeið hafið á Reykjanesskaga. nfr 94:. https://doi.org/10.33112/nfr.94.3.4

Kerrick DM (2001) Present and past nonanthropogenic CO2 degassing from the solid earth. Reviews of Geophysics 39:565–585. https://doi.org/10.1029/2001RG000105

Kjartanasson G (1957) Some secondary effects of the Hekla eruption. Exhalations of carbon dioxide, contamination of ground-water and lowering of water table. Societas Scientarum Islendica

Kling GW, Clark MA, Wagner GN, et al (1987) The 1986 Lake Nyos Gas Disaster in Cameroon, West Africa. Science 236:169–175. https://doi.org/10.1126/science.236.4798.169

Kokfelt TF, Hoernle K, Hauff F, et al (2006) Combined Trace Element and Pb-Nd–Sr-O Isotope Evidence for Recycled Oceanic Crust (Upper and Lower) in the Iceland Mantle Plume. Journal of Petrology 47:1705–1749. https://doi.org/10.1093/petrology/egl025

Kuno H (1965) Fractionation Trends of Basalt Magmas in Lava Flows. Journal of Petrology 6:302–321. https://doi.org/10.1093/petrology/6.2.302

Kuno H, Yamasaki K, IIda C, Nagashima K (1957) Differentiation of Hawaiian magmas. Jap J Geol Geogr, 28, 179-218 28:179–218

Kuritani T, Yoshida T, Nagahashi Y (2010) Internal differentiation of Kutsugata lava flow from Rishiri Volcano, Japan: Processes and timescales of segregation structures' formation. Journal of Volcanology and Geothermal Research 195:57–68. https://doi.org/10.1016/j.jvolgeores.2010.06.003

Kurz MD, Meyer PS, Sigurdsson H (1985) Helium isotopic systematics within the neovolcanic zones of Iceland. Earth and Planetary Science Letters 74:291–305. https://doi.org/10.1016/S0012-821X(85)80001-7

Langenauer M, Krähenbühl U, Furrer V, Wyttenbach A (1992) Determination of Fluorine, Chlorine, Bromine and Iodine in Seven Geochemical Reference Samples. Geostandards Newsletter 16:41–44. https://doi.org/10.1111/j.1751-908X.1992.tb00485.x

Larsen G (2000) Holocene eruptions within the Katla volcanic system, south Iceland: Characteristics and environmental impact. Jökull 49:

Larsen G (1979) Um aldur Eldgjárhrauna. Náttúrufræðingurinn 49:

Larsen G, Dugmore A, Newton A (1999) Geochemistry of historical-age silicic tephras in Iceland. The Holocene 9:463–471. https://doi.org/10.1191/095968399669624108

Lee H-F, Yang TF, Lan TF, et al (2005) Fumarolic Gas Composition of the Tatun Volcano Group,Northern Taiwan. Terr Atmos Ocean Sci 16:843. https://doi.org/10.3319/TAO.2005.16.4.843(GIG)

Lerner AH, Wallace PJ, Shea T, et al (2021) The petrologic and degassing behavior of sulfur and other magmatic volatiles from the 2018 eruption of Kīlauea, Hawai'i: melt concentrations, magma storage depths, and magma recycling. Bull Volcanol 83:43. https://doi.org/10.1007/s00445-021-01459-y

Maclennan J, Jull M, McKenzie D, et al (2002) The link between volcanism and deglaciation in Iceland. Geochemistry, Geophysics, Geosystems 3:1–25. https://doi.org/10.1029/2001GC000282

Mandon CL, Christenson BW, Schipper CI, et al (2019) Metal transport in volcanic plumes: A case study at White Island and Yasur volcanoes. Journal of Volcanology and Geothermal Research 369:155–171. https://doi.org/10.1016/j.jvolgeores.2018.11.024

Mandon CL, Kaasalainen H, Calabrese S, et al (2025) Trace element transport by volcanic gases at Vulcano (Sicily, Italy) – Speciation, deposition and fluxes. Journal of Volcanology and Geothermal Research 458:108235. https://doi.org/10.1016/j.jvolgeores.2024.108235

Marshall EW, Caracciolo A, Bali E, et al (2024) The Petrology and Geochemistry of the 2021 Fagradalsfjall Eruption, Iceland: An Eruption Sourced From Multiple, Compositionally Diverse, Near-Moho Sills. AGU Advances 5:e2024AV001310. https://doi.org/10.1029/2024AV001310

Martin E, Sigmarsson O (2007) Low-pressure differentiation of tholeiitic lavas as recorded in segregation veins from Reykjanes (Iceland), Lanzarote (Canary Islands) and Masaya (Nicaragua). Contributions to Mineralogy and Petrology 154:559–573. http://dx.doi.org/10.1007/s00410-007-0209-5

Martin E, Sigmarsson O (2005) Trondhjemitic and granitic melts formed by fractional crystallization of an olivine tholeiite from Reykjanes Peninsula, Iceland. Geological Magazine 142:651–658. https://doi.org/10.1017/S0016756805001160

Mason E, Wieser PE, Liu EJ, et al (2021) Volatile metal emissions from volcanic degassing and lava–seawater interactions at Kīlauea Volcano, Hawai'i. Commun Earth Environ 2:1–16. https://doi.org/10.1038/s43247-021-00145-3

Mason EM, Edmonds M, Hammond S, et al (2024) Chalcophile element degassing at an active continental arc volcano. Geochimica et Cosmochimica Acta 367:72–86. https://doi.org/10.1016/j.gca.2023.12.014

Mather TA, Witt MLI, Pyle DM, et al (2012) Halogens and trace metal emissions from the ongoing 2008 summit eruption of Kīlauea volcano, Hawai`i. Geochimica et Cosmochimica Acta 83:292–323. https://doi.org/10.1016/j.gca.2011.11.029

Matthews SW, Caracciolo A, Bali E, et al (2024) A dynamic mid-crustal magma domain revealed by the 2023 to 2024 Sundhnúksgígar eruptions, Iceland. Science 0:eadp8778. https://doi.org/10.1126/science.adp8778

Mazziotti-Tagliani S, Angelone M, Armiento G, et al (2012) Arsenic and fluorine in the Etnean volcanics from Biancavilla, Sicily, Italy: environmental implications. Environ Earth Sci 66:561–572. https://doi.org/10.1007/s12665-011-1265-8

Michael PJ, Schilling J-G (1989) Chlorine in mid-ocean ridge magmas: Evidence for assimilation of seawater-influenced components. Geochimica et Cosmochimica Acta 53:3131–3143. https://doi.org/10.1016/0016-7037(89)90094-X

Morison CAG, Oppenheimer C, Thordarson T, et al (2024) Disparate impacts of the Eldgjá and Laki flood-lava eruptions. https://journals.sagepub.com/doi/full/10.1177/09596836241254478. Accessed 30 Aug 2024

Moune S, Gauthier P-J, Gislason SR, Sigmarsson O (2006) Trace element degassing and enrichment in the eruptive plume of the 2000 eruption of Hekla volcano, Iceland. Geochimica et Cosmochimica Acta 70:461–479

Moune S, Sigmarsson O, Thordarson T, Gauthier P-J (2007) Recent volatile evolution in the magmatic system of Hekla volcano, Iceland. Earth and Planetary Science Letters 255:373–389. https://doi.org/10.1016/j.epsl.2006.12.024

Moussallam Y, Rose-Koga EF, Fischer TP, et al (2024) Kinetic Isotopic Degassing of CO2 During the 2021 Fagradalsfjall Eruption and the δ13C Signature of the Icelandic Mantle. Geochemistry, Geophysics, Geosystems 25:e2024GC011997. https://doi.org/10.1029/2024GC011997

Mroz EJ, Zoller WH (1975) Composition of Atmospheric Particulate Matter from the Eruption of Heimaey, Iceland. Science 190:461–464. https://doi.org/10.1126/science.190.4213.461

Muehlenbachs K, Anderson AT, Sigvaldason GE (1974) Low-O18 basalts from Iceland. Geochimica et Cosmochimica Acta 38:577–588. https://doi.org/10.1016/0016-7037(74)90042-8

Naughton JJ, Lewis V, Thomas D, Finlayson JB (1975) Fume compositions found at various stages of activity at Kilauea Volcano, Hawaii. Journal of Geophysical Research (1896-1977) 80:2963–2966. https://doi.org/10.1029/JC080i021p02963

Nicholson K (1983) Fluorine determination in geochemistry: Errors in the electrode method of analysis. Chemical Geology 38:1–22. https://doi.org/10.1016/0009-2541(83)90042-6

Nikkola P, Thordarson T, Rämö OT, Heikkilä P (2019) Formation of segregation structures in Hafnarhraun pāhoehoe lobe, SW Iceland: a window into crystal–melt separation in basaltic magma. Bull Volcanol 81:70. https://doi.org/10.1007/s00445-019-1330-9

Nriagu JO (1989) A global assessment of natural sources of atmospheric trace metals. Nature 338:47–49. https://doi.org/10.1038/338047a0

Olade MA (1976) Rapid and simultaneous determination of chlorine and fluorine in rocks and an application in detailed geochemical exploration. Journal of Mining and Geology 13:28–32

Óladóttir BA, Sigmarsson O, Larsen G, Thordarson T (2008) Katla volcano, Iceland: magma composition, dynamics and eruption frequency as recorded by Holocene tephra layers. Bull Volcanol 70:475–493. https://doi.org/10.1007/s00445-007-0150-5

Olmez I, Finnegan DL, Zoller WH (1986) Iridium emissions from Kilauea Volcano. Journal of Geophysical Research: Solid Earth 91:653–663. https://doi.org/10.1029/JB091iB01p00653

O'Nions RK, Hamilton PJ, Evensen NM (1977) Variations in143Nd/144Nd and87Sr/86Sr ratios in oceanic basalts. Earth and Planetary Science Letters 34:13–22. https://doi.org/10.1016/0012-821X(77)90100-5

Oppenheimer C, Fischer TP, Scaillet B (2014) Volcanic Degassing: Process and Impact. 4:111. https://doi.org/10.1016/B978-0-08-095975-7.00304-1

Oppenheimer C, Orchard A, Stoffel M, et al (2018) The Eldgjá eruption: timing, long-range impacts and influence on the Christianisation of Iceland. Climatic Change 147:369–381. https://doi.org/10.1007/s10584-018-2171-9

Oppenheimer C, Pyle DM, Barclay J (2003) Volcanic Degassing. Geological Society of London

Óskarsson N (1984) Monitoring of fumarole discharge during the 1975–1982 rifting in Krafla volcanic center, north Iceland. Journal of Volcanology and Geothermal Research 22:97–121. https://doi.org/10.1016/0377-0273(84)90036-2

Óskarsson N (1980) The interaction between volcanic gases and tephra: Fluorine adhering to tephra of the 1970 hekla eruption. Journal of Volcanology and Geothermal Research 8:251–266. https://doi.org/10.1016/0377-0273(80)90107-9

Óskarsson N (1981) The chemistry of icelandic lava incrustations and the latest stages of degassing. Journal of Volcanology and Geothermal Research 10:93–111. https://doi.org/10.1016/0377-0273(81)90057-3

Óskarsson N, Sigvaldason GE, Steinthórsson S (1982) A Dynamic Model of Rift Zone Petrogenesis and the Regional Petrology of Iceland. Journal of Petrology 23:28–74. https://doi.org/10.1093/petrology/23.1.28

Pagli C, Sigmundsson F (2008) Will present day glacier retreat increase volcanic activity? Stress induced by recent glacier retreat and its effect on magmatism at the Vatnajökull ice cap, Iceland. Geophysical Research Letters 35:. https://doi.org/10.1029/2008GL033510

Parks M, Sigmundsson F, Drouin V, et al (2023) Deformation, seismicity, and monitoring response preceding and during the 2022 Fagradalsfjall eruption, Iceland. Bull Volcanol 85:60. https://doi.org/10.1007/s00445-023-01671-y

Peacock MA (1925) VIII. A Contribution to the Petrography of Iceland. Transactions of the Geological Society of Glasgow 17:271–333. https://doi.org/10.1144/transglas.17.2.271

Peate DW, Baker JA, Jakobsson SP, et al (2009) Historic magmatism on the Reykjanes Peninsula, Iceland: a snap-shot of melt generation at a ridge segment. Contrib Mineral Petrol 157:359–382. https://doi.org/10.1007/s00410-008-0339-4

Pedersen GBM, Belart JMC, Óskarsson BV, et al (2022) Volume, Effusion Rate, and Lava Transport During the 2021 Fagradalsfjall Eruption: Results From Near Real-Time Photogrammetric Monitoring. Geophysical Research Letters 49:e2021GL097125. https://doi.org/10.1029/2021GL097125

Pétursson G, Pálsson PA, Georgsson G (1984) Um eituráhrif af völdum Skaftárelda (On the poisoning effect of the Skaftá Fires (Laki eruption).

Pfeffer MA, Arellano S, Barsotti S, et al (2024) SO2 emission rates and incorporation into the air pollution dispersion forecast during the 2021 eruption of Fagradalsfjall, Iceland. Journal of Volcanology and Geothermal Research 449:108064. https://doi.org/10.1016/j.jvolgeores.2024.108064

Pfeffer MA, Bergsson B, Barsotti S, et al (2018) Ground-Based Measurements of the 2014–2015 Holuhraun Volcanic Cloud (Iceland). Geosciences 8:29. https://doi.org/10.3390/geosciences8010029

Philpotts AR, CARROLL M, HILL JM (1996) Crystal-Mush Compaction and the Origin of Pegmatitic Segregation Sheets in a Thick Flood-Basalt Flow in the Mesozoic Hartford Basin, Connecticut. Journal of Petrology 37:811–836. https://doi.org/10.1093/petrology/37.4.811

Potts PJ (1987) Ion-selective electrodes. In: Potts PJ (ed) A Handbook of Silicate Rock Analysis. Springer Netherlands, Dordrecht, pp 213–225

Puffer JH, Horter DL (1993) Origin of pegmatitic segregation veins within flood basalts. GSA Bulletin 105:738–748. https://doi.org/10.1130/0016-7606(1993)105<0738:OOPSVW>2.3.CO;2

Pyle DM, Mather TA (2009) Halogens in igneous processes and their fluxes to the atmosphere and oceans from volcanic activity: A review. Chemical Geology 263:110–121. https://doi.org/10.1016/j.chemgeo.2008.11.013

Raible CC, Brönnimann S, Auchmann R, et al (2016) Tambora 1815 as a test case for high impact volcanic eruptions: Earth system effects. WIREs Climate Change 7:569–589. https://doi.org/10.1002/wcc.407

Rampino MR, Self S (1992) Volcanic winter and accelerated glaciation following the Toba super-eruption. Nature 359:50–52. https://doi.org/10.1038/359050a0

Rampino MR, Self S, Stothers RB (1988) Volcanic Winters. Annual Review of Earth and Planetary Sciences 16:73–99. https://doi.org/10.1146/annurev.ea.16.050188.000445

Regenspurg S, Virchow L, Wilke FDH, et al (2022) Origin and migration of fluoride in the area of the Aluto Volcanic Complex (Main Ethiopian Rift). Applied Geochemistry 146:105403. https://doi.org/10.1016/j.apgeochem.2022.105403

Renggli CJ, Klemme S (2020) Experimental constraints on metal transport in fumarolic gases. Journal of Volcanology and Geothermal Research 400:106929. https://doi.org/10.1016/j.jvolgeores.2020.106929

Robock A (2000) Volcanic eruptions and climate. Reviews of Geophysics 38:191–219. https://doi.org/10.1029/1998RG000054

Rowe EC, Schilling J-G (1979) Fluorine in Iceland and Reykjanes Ridge basalts. Nature 279:33–37. https://doi.org/10.1038/279033a0

Saal AE, Hauri EH, Langmuir CH, Perfit MR (2002) Vapour undersaturation in primitive mid-ocean-ridge basalt and the volatile content of Earth's upper mantle. Nature 419:451–455. https://doi.org/10.1038/nature01073

Sæmundsson K, Sigurgeirsson MÁ, Friðleifsson GÓ (2020) Geology and structure of the Reykjanes volcanic system, Iceland. Journal of Volcanology and Geothermal Research 391:106501. https://doi.org/10.1016/j.jvolgeores.2018.11.022

Salters VJM, Stracke A (2004) Composition of the depleted mantle. Geochemistry, Geophysics, Geosystems 5:. https://doi.org/10.1029/2003GC000597

Scaillet B, Clemente B, Evans BW, Pichavant M (1998) Redox control of sulfur degassing in silicic magmas. Journal of Geophysical Research: Solid Earth 103:23937–23949. https://doi.org/10.1029/98JB02301

Scaillet B, Luhr JF, Carroll MR (2004) Petrological and Volcanological Constraints on Volcanic Sulfur Emissions to the Atmosphere. In: Volcanism and the Earth's Atmosphere. American Geophysical Union (AGU), pp 11–40

Schiano P, Bourdon B, Clocchiatti R, et al (1998) Low-degree partial melting trends recorded in upper mantle minerals. Earth and Planetary Science Letters 160:537–550. https://doi.org/10.1016/S0012-821X(98)00109-5

Schilling J-G (1973) Iceland Mantle Plume: Geochemical Study of Reykjanes Ridge. Nature 242:565–571. https://doi.org/10.1038/242565a0

Schilling J-G, Bergeron MB, Evans R (1980) Halogens in the mantle beneath the North Atlantic. Philosophical Transactions of the Royal Society of London Series A, Mathematical and Physical Sciences. https://doi.org/10.1098/rsta.1980.0208

Schoeberl MR, Wang Y, Ueyama R, et al (2023) The Estimated Climate Impact of the Hunga Tonga-Hunga Ha'apai Eruption Plume. Geophysical Research Letters 50:e2023GL104634. https://doi.org/10.1029/2023GL104634

Scholtysik R, Canil D (2021) The effects of S, Cl and oxygen fugacity on the sublimation of volatile trace metals degassed from silicate melts with implications for volcanic emissions. Geochimica et Cosmochimica Acta 301:141–157. https://doi.org/10.1016/j.gca.2021.02.018

Scholtysik R, Canil D (2020) Investigation of the effect of Cl on the transport and sublimation of volatile trace metals in volcanic gases using benchtop fumarole experiments. Journal of Volcanology and Geothermal Research 395:106838. https://doi.org/10.1016/j.jvolgeores.2020.106838

Scott S, Pfeffer M, Oppenheimer C, et al (2023) Near-surface magma flow instability drives cyclic lava fountaining at Fagradalsfjall, Iceland. Nat Commun 14:6810. https://doi.org/10.1038/s41467-023-42569-9

Self S, Thordarson Th, Keszthelyi L, et al (1996) A new model for the emplacement of Columbia River basalts as large, inflated Pahoehoe Lava Flow Fields. Geophysical Research Letters 23:2689–2692. https://doi.org/10.1029/96GL02450

Sheth H, Patel V, Samant H (2017) Control of early-formed vesicle cylinders on upper crustal prismatic jointing in compound pāhoehoe lavas of Elephanta Island, western Deccan Traps, India. Bull Volcanol 79:63. https://doi.org/10.1007/s00445-017-1147-3

Shinohara H (2009) A missing link between volcanic degassing and experimental studies on chloride partitioning. Chemical Geology 263:51–59. https://doi.org/10.1016/j.chemgeo.2008.12.001

Shoji S, Takahashi T (2002) Environmental and agricultural significance of volcanic ash soils. Global Environmental Research-English Edition 6:113–135

Sigmarsson O, Condomines M, Fourcade S (1992) A detailed Th, Sr and O isotope study of Hekla: differentiation processes in an Icelandic Volcano. Contrib Mineral Petrol 112:20–34. https://doi.org/10.1007/BF00310953

Sigmarsson O, Moune S, Gauthier P-J (2020) Fractional degassing of S, Cl and F from basalt magma in the Bárðarbunga rift zone, Iceland. Bull Volcanol 82:54. https://doi.org/10.1007/s00445-020-01391-7

Sigmarsson O, Steinthórsson S (2007) Origin of Icelandic basalts: A review of their petrology and geochemistry. Journal of Geodynamics 43:87–100. https://doi.org/10.1016/j.jog.2006.09.016

Sigmarsson O, Thordarson T, Jakobsson S (2009) Segregations in Surtsey lavas (Iceland) reveal extreme magma differentiation during late stage flow emplacement. IAVCEI 2:84–104. https://doi.org/10.1144/IAVCEI002.5

Sigmundsson F, Parks M, Hooper A, et al (2022) Deformation and seismicity decline before the 2021 Fagradalsfjall eruption. Nature 609:523–528. https://doi.org/10.1038/s41586-022-05083-4

Sigurdardottir S, Gudmundsson M, Hreinsdottir S (2015) Mapping of the Eldgja lava flow on Myrdalssandur with magnetic surveying. Jokull 65:61–72. https://doi.org/10.33799/jokull2015.65.061

Sigurgeirsson MÁ, Þorbergsson A (2021) Gosskeið á Reykjanesskaga fyrir 1900-2500 árum – yfirlit - ISOR.IS. https://isor.is/gosskeid-a-reykjanesskaga-fyrir-1900-2500-arum-yfirlit/. Accessed 6 Aug 2025

Sigvaldason GE, Elísson G (1968) Collection and analysis of volcanic gases at Surtsey Iceland. Geochimica et Cosmochimica Acta 32:797–805. https://doi.org/10.1016/0016-7037(68)90095-1

Sigvaldason GE, Óskarsson N (1976) Chlorine in basalts from Iceland. Geochimica et Cosmochimica Acta 40:777–789. https://doi.org/10.1016/0016-7037(76)90030-2

Sigvaldason GE, Óskarsson N (1986) Fluorine in basalts from Iceland. Contr Mineral and Petrol 94:263–271. https://doi.org/10.1007/BF00371435

Stecher O (1998) Fluorine geochemistry in volcanic rock series: examples from Iceland and Jan Mayen. Geochimica et Cosmochimica Acta 62:3117–3130. https://doi.org/10.1016/S0016-7037(98)00210-5

Stecher O (1983) Fluorine in Twenty-Two International Reference Rock Samples and a Compilation of Fluorine Values for the USGS Reference Samples. Geostandards Newsletter 7:283–287. https://doi.org/10.1111/j.1751-908X.1983.tb00384.x

Stefánsson A, Stefánsdóttir G, Keller NS, et al (2017) Major impact of volcanic gases on the chemical composition of precipitation in Iceland during the 2014–2015 Holuhraun eruption. Journal of Geophysical Research: Atmospheres 122:1971–1982. https://doi.org/10.1002/2015JD024093

Stephenson PJ, Zhang M, Spry M (2000) Fractionation modelling of segregations in the Toomba Basalt, north Queensland. Australian Journal of Earth Sciences 47:291–300. https://doi.org/10.1046/j.1440-0952.2000.00780.x

Stewart C, Damby DE, Horwell CJ, et al (2022) Volcanic air pollution and human health: recent advances and future directions. Bull Volcanol 84:11. https://doi.org/10.1007/s00445-021-01513-9

Sun S-S, Tatsumoto M, Schilling J-G (1975) Mantle Plume Mixing Along the Reykjanes Ridge Axis: Lead Isotopic Evidence. Science 190:143–147. https://doi.org/10.1126/science.190.4210.143

Symonds RB, Reed MH (1993) Calculation of multicomponent chemical equilibria in gas-solid-liquid systems: Calculation methods, thermochemical data, and applications to studies of high-temperature volcanic gases with examples from Mt. St. Helens. American Journal of Science; (United States) 293:8: https://doi.org/10.2475/ajs.293.8.758

Symonds RB, Reed MH, Rose WI (1992) Origin, speciation, and fluxes of trace-element gases at Augustine volcano, Alaska: Insights into magma degassing and fumarolic processes. Geochimica et Cosmochimica Acta 56:633–657. https://doi.org/10.1016/0016-7037(92)90087-Y

Symonds RB, Rose WI, Bluth GJS, Gerlach TM (1994) Volcanic-gas studies: Methods, results and applications. In: Volatiles in Magmas. Mineralogical Society of America, pp 1–66

Tam E, Miike R, Labrenz S, et al (2016) Volcanic air pollution over the Island of Hawai'i: Emissions, dispersal, and composition. Association with respiratory symptoms and lung function in Hawai'i Island school children. Environment International 92–93:543–552. https://doi.org/10.1016/j.envint.2016.03.025

Taran YA, Bernard A, Gavilanes J-C, et al (2001) Chemistry and mineralogy of high-temperature gas discharges from Colima volcano, Mexico. Implications for magmatic gas–atmosphere interaction. Journal of Volcanology and Geothermal Research 108:245–264. https://doi.org/10.1016/S0377-0273(00)00289-4

Thorarinsson S (1969) The Lakagígar eruption of 1783. Bull Volcanol 33:910–929. https://doi.org/10.1007/BF02596756

Thorarinsson S (1967) The Eruptions of Hekla in historical times : a tephrochronological study. (No Title)

Thorarinsson S, Saemundsson K (1979) Volcanic activity in historical time

Thordarson T (1995) Volatile release and atmospheric effects of basaltic fissure eruptions. PhD Thesis

Thordarson T (2010) Perception of Volcanic Eruptions in Iceland. In: Martini IP, Chesworth W (eds) Landscapes and Societies: Selected Cases. Springer Netherlands, Dordrecht, pp 285–296

Thordarson T, Larsen G (2007) Volcanism in Iceland in historical time: Volcano types, eruption styles and eruptive history. Journal of Geodynamics 43:118–152. https://doi.org/10.1016/j.jog.2006.09.005

Thordarson T, Miller DJ, Larsen G, et al (2001) New estimates of sulfur degassing and atmospheric mass-loading by the 934 AD Eldgjá eruption, Iceland. Journal of Volcanology and Geothermal Research 108:33–54. https://doi.org/10.1016/S0377-0273(00)00277-8

Thordarson T, Self S (1998) The Roza Member, Columbia River Basalt Group: A gigantic pahoehoe lava flow field formed by endogenous processes? Journal of Geophysical Research: Solid Earth 103:27411–27445. https://doi.org/10.1029/98JB01355

Thordarson T, Self S (1993) The Laki (Skaftár Fires) and Grímsvötn eruptions in 1783–1785. Bull Volcanol 55:233–263. https://doi.org/10.1007/BF00624353

Thordarson T, Self S (2003) Atmospheric and environmental effects of the 1783–1784 Laki eruption: A review and reassessment. Journal of Geophysical Research: Atmospheres 108:AAC 7-1-AAC 7-29. https://doi.org/10.1029/2001JD002042

Thordarson T, Self S, Óskarsson N, Hulsebosch T (1996) Sulfur, chlorine, and fluorine degassing and atmospheric loading by the 1783–1784 AD Laki (Skaftár Fires) eruption in Iceland. Bull Volcanol 58:205–225. https://doi.org/10.1007/s004450050136

Thordarson T, Sigmarsson O (2009) Effusive activity in the 1963–1967 Surtsey eruption, Iceland: flow emplacement and growth of small lava shields. In: Thordarson T, Self S, Larsen G, et al. (eds) Studies in Volcanology: The Legacy of George Walker. Geological Society of London, p 0

Toutain JP, Aloupogiannis P, Delorme H, et al (1990) Vapor deposition of trace elements from degassed basaltic lava, Piton de la Fournaise volcano, Reunion Island. Journal of Volcanology and Geothermal Research 40:257–268. https://doi.org/10.1016/0377-0273(90)90124-X

Troll G, Farzaneh A, Cammann K (1977) Rapid determination of fluoride in mineral and rock samples using an ion-selective electrode. Chemical Geology 20:295–305. https://doi.org/10.1016/0009-2541(77)90054-7

Tyrrell GW, Peacock MA (1927) III.—The Petrology of Iceland. Earth and Environmental Science Transactions of The Royal Society of Edinburgh 55:51–76. https://doi.org/10.1017/S0080456800016240

Unni CK, Schilling J-G (1978) Cl and Br degassing by volcanism along the Reykjanes Ridge and Iceland. Nature 272:19–23. https://doi.org/10.1038/272019a0

Vigneri R, Malandrino P, Gianì F, et al (2017) Heavy metals in the volcanic environment and thyroid cancer. Molecular and Cellular Endocrinology 457:73–80. https://doi.org/10.1016/j.mce.2016.10.027

Villemant B, Boudon G (1999) H2O and halogen (F, Cl, Br) behaviour during shallow magma degassing processes. Earth and Planetary Science Letters 168:271–286. https://doi.org/10.1016/S0012-821X(99)00058-8

Wager LR (1939) The petrology of the Skeargaard intrusion, kangerdlugssuag, East Greenland. Medd Gronland 105:1–352

Wahrenberger C (1997) Some aspects of the chemistry of volcanic gases. PhD Thesis

Wainman L, Ilyinskaya E, Pfeffer M, et al (2024) Trace Element Emissions Vary With Lava Flow Age and Thermal Evolution During the Fagradalsfjall 2021–2023 Eruptions, Iceland. Geochemistry, Geophysics, Geosystems 25:e2024GC011822. https://doi.org/10.1029/2024GC011822

Walker GPL, Cañón-Tapia E, Herrero-Bervera E (1999) Origin of vesicle layering and double imbrication by endogenous growth in the Birkett basalt flow (Columbia river plateau). Journal of Volcanology and Geothermal Research 88:15–28. https://doi.org/10.1016/S0377-0273(98)00112-7

Wallace PJ, Plank T, Edmonds M, Hauri EH (2015) Chapter 7 - Volatiles in Magmas. In: Sigurdsson H (ed) The Encyclopedia of Volcanoes (Second Edition). Academic Press, Amsterdam, pp 163–183

Webster JD (2004) The exsolution of magmatic hydrosaline chloride liquids. Chemical Geology 210:33–48. https://doi.org/10.1016/j.chemgeo.2004.06.003

Webster JD, Baker DR, Aiuppa A (2018) Halogens in Mafic and Intermediate-Silica Content Magmas. In: Harlov DE, Aranovich L (eds) The Role of Halogens in Terrestrial and Extraterrestrial Geochemical Processes: Surface, Crust, and Mantle. Springer International Publishing, Cham, pp 307–430

Wedepohl KH (1995) The composition of the continental crust. Geochimica et Cosmochimica Acta 59:1217–1232. https://doi.org/10.1016/0016-7037(95)00038-2

White WM, Schilling J-G (1978) The nature and origin of geochemical variation in Mid-Atlantic Ridge basalts from the Central North Atlantic. Geochimica et Cosmochimica Acta 42:1501–1516. https://doi.org/10.1016/0016-7037(78)90021-2

Williams SN, Schaefer SJ, Marta Lucia Calvache V, Lopez D (1992) Global carbon dioxide emission to the atmosphere by volcanoes. Geochimica et Cosmochimica Acta 56:1765–1770. https://doi.org/10.1016/0016-7037(92)90243-C

Wilmoth RA, Walker GPL (1993) P-type and S-type pahoehoe: a study of vesicle distribution patterns in Hawaiian lava flows. Journal of Volcanology and Geothermal Research 55:129–142. https://doi.org/10.1016/0377-0273(93)90094-8

Witham CS, Oppenheimer C, Horwell CJ (2005) Volcanic ash-leachates: a review and recommendations for sampling methods. Journal of Volcanology and Geothermal Research 141:299–326. https://doi.org/10.1016/j.jvolgeores.2004.11.010

Wood DA, Joron J-L, Treuil M, et al (1979) Elemental and Sr isotope variations in basic lavas from Iceland and the surrounding ocean floor. Contr Mineral and Petrol 70:319–339. https://doi.org/10.1007/BF00375360

World Health Organization (2007) Health risks of heavy metals from long-range transboundary air pollution. In: Health risks of heavy metals from long-range transboundary air pollution

Wright TJ, Sigmundsson F, Pagli C, et al (2012) Geophysical constraints on the dynamics of spreading centres from rifting episodes on land. Nature Geosci 5:242–250. https://doi.org/10.1038/ngeo1428

Zelenski M, Fischer TP, de Moor JM, et al (2013) Trace elements in the gas emissions from the Erta Ale volcano, Afar, Ethiopia. Chemical Geology 357:95–116. https://doi.org/10.1016/j.chemgeo.2013.08.022

Zelenski M, Malik N, Taran Yu (2014) Emissions of trace elements during the 2012–2013 effusive eruption of Tolbachik volcano, Kamchatka: enrichment factors, partition coefficients and aerosol contribution. Journal of Volcanology and Geothermal Research 285:136–149. https://doi.org/10.1016/j.jvolgeores.2014.08.007

Zelenski M, Simakin A, Taran Y, et al (2021) Partitioning of elements between high-temperature, low-density aqueous fluid and silicate melt as derived from volcanic gas geochemistry. Geochimica et Cosmochimica Acta 295:112–134. https://doi.org/10.1016/j.gca.2020.12.011

Zhang W, Hu Z, Liu Y, et al (2012) Total rock dissolution using ammonium bifluoride (NH4HF2) in screw-top Teflon vials: a new development in open-vessel digestion. Anal Chem 84:10686–10693. https://doi.org/10.1021/ac302327g

Zreda MG, Phillips FM, Elmore D, et al (1991) Cosmogenic chlorine-36 production rates in terrestrial rocks. Earth and Planetary Science Letters 105:94–109. https://doi.org/10.1016/0012-821X(91)90123-Y